

UNIVERSITY OF OKLAHOMA
GRADUATE COLLEGE

THE EARLY INSTABILITY SCENARIO FOR
PLANET FORMATION IN THE SOLAR SYSTEM

A DISSERTATION
SUBMITTED TO THE GRADUATE FACULTY
in partial fulfillment of the requirements for the
Degree of
DOCTOR OF PHILOSOPHY

By
MATTHEW SCOTT CLEMENT
Norman, Oklahoma
2019

THE EARLY INSTABILITY SCENARIO FOR
PLANET FORMATION IN THE SOLAR SYSTEM

A DISSERTATION APPROVED FOR THE
HOMER L. DODGE DEPARTMENT OF PHYSICS
ASTRONOMY

BY

Dr. Nathan Kaib, Chair

Dr. Edward Baron

Dr. Megan Elwood Madden

Dr. Kieran Mullen

Dr. John Wisniewski

Acknowledgements

I am extremely grateful to have received tremendous support during graduate school from my wife Carolyn; my Mom, Dad and sister Kristen; and in-laws Bob, Cheryl and Katherine.

A special thanks to my advisor Nate, for teaching me everything I needed to know, I wouldn't have gotten past step one without you. Sean Raymond also provided invaluable advise and expertise throughout three years of collaboration, and a semester in France directly supervising the development of my thesis. I am also thankful for support from all my fellow graduate students and past office-mates.

A final shout-out to all my Naval Academy class of 2010 and first company classmates, fellow divers in class 10-80-SC, my past shipmates on the Defender of the Heartland USS TOPEKA (SSN-754), and all those who continue serve in the Submarine Force.

In memory of Tommy Dyer

5/8/87 - 2/26/19

Contents

1	Introduction	1
1.1	Background	3
1.1.1	The solar system's fragile state	3
1.1.2	The Nice Model	5
1.1.3	Timing the instability	8
1.1.4	Terrestrial planet formation	11
1.2	Shortcomings of conventional terrestrial planet formation models	15
1.2.1	Collisional fragmentation	16
1.2.2	Mercury's peculiar composition	16
1.2.3	Accurately modeling the asteroid belt	19
1.3	Dissertation outline	21
2	Prevalence of Chaos in Planetary Systems Formed Through Embryo Accretion	24
2.1	Introduction	24
2.2	Methods	27
2.2.1	System Formation and Evolution	27
2.2.2	Numerical Analysis	28
2.2.3	Simulation Parameters	32
2.2.4	Detecting Mean Motion Resonances	33
2.3	Results	33
2.3.1	System Evolution Beyond 200 Myr	33
2.3.2	Prevalence of Chaos	41
2.3.3	Angular Momentum Deficit and Last Loss Analysis	47
2.3.4	Mass Concentration Statistic and Center of Mass Analysis	47
2.3.5	Systems of Particular Interest	48
2.4	Discussion and Conclusions	52
2.5	Acknowledgements	53
3	Mars' Growth Stunted by an Early Giant Planet Instability	54
3.1	Introduction	54
3.2	Methods	61
3.2.1	Instability Timing	67
3.3	Success Criteria	68
3.3.1	The Inner Solar System	69

3.3.2	The Formation Timescales of Earth and Mars	70
3.3.3	The Asteroid Belt	71
3.3.4	Water Delivery to Earth	73
3.3.5	Angular Momentum Deficit	74
3.3.6	The Outer Solar System	74
3.4	Results and Discussion	75
3.4.1	Formation of a Small Mars	76
3.4.2	Strengths of an Early Instability	81
3.4.3	Weaknesses of an Early Instability	87
3.4.4	Varied Initial Conditions	89
3.4.5	Excitation of Jupiter's g_5 Mode	91
3.4.6	Impact Velocities	92
3.5	Conclusions	94
3.6	Acknowledgments	96
4	The Early Instability Scenario: Terrestrial Planet Formation During the Giant Planet Instability, and the Effect of Collisional Fragmentation	98
4.1	Introduction	98
4.2	Methods	103
4.2.1	Collisional Algorithm	103
4.2.2	Giant Planet Configurations	104
4.2.3	Terrestrial Disks	105
4.2.4	Success Criteria	109
4.3	Results and Discussion	112
4.3.1	The Small Mars Problem	114
4.3.2	Mars' Formation Timescale	119
4.3.3	Collisional Evolution of the Asteroid Belt	121
4.3.4	AMDs and RMCs	123
4.3.5	Annulus Initial Conditions	126
4.4	Future Work	129
4.4.1	Late Terrestrial Bombardment	129
4.4.2	Extended Simulations	130
4.4.3	Late Impacts	131
4.4.4	HSE Constraints	132
4.5	Conclusions	133
4.6	Acknowledgments	135
5	Dynamical Constraints on Mercury's Collisional Origin	136
5.1	Introduction	136
5.2	Methods	140
5.2.1	Control Simulations	141
5.2.2	Instability Scenario	142
5.2.3	Annulus Scenario	143
5.2.4	Analysis Metrics	144
5.3	Results and Discussion	145

5.3.1	High CMF Objects	145
5.3.2	Prevalence of Mercury Analogs	148
5.3.3	Dynamical Barriers to the Single Impact Scenario	150
5.4	Conclusions	159
6	Excitation and Depletion of the Asteroid Belt in the Early Instability Scenario	161
6.1	Introduction	161
6.2	Methods	166
6.3	Results and Discussion	170
6.3.1	Depletion	170
6.3.2	Radial Mixing	175
6.3.3	Orbital Structure	178
6.3.4	Seeded Embryos	184
6.3.5	The formation of Veneneia	185
6.4	Conclusions	186
6.5	Acknowledgments	188
7	Conclusions	189
A	Chapter 2 Supplemental Data	206

List of Tables

2.1	Run 1 simulates each fully evolved 4.5 Gyr system discussed in § 2.2.1. Runs a and b evaluate the effect of removing outer planets. Runs c–e investigate the result of inflating the giant planet’s eccentricities. Run e is re-performed for cjs and ann systems using the MERCURY hybrid integrator for 1 Gyr in order to detect close encounters (see § 2.3.2)	32
2.2	The percentage of ann and cjs systems which lost a given number of planets when integrated with inflated giant planet eccentricities in run e for 1 Gyr.	44
2.3	Comparison of non-chaotic 5 terrestrial planet systems (cjs10 and cjs13) mass and semi-major axis distributions. The fifth body for the solar system is taken to be Ceres.	50
3.1	Giant Planet Initial Conditions: The columns are: (1) the name of the simulation set, (2) the number of giant planets, (3) the mass of the planetesimal disk exterior to the giant planets, (4) the distance between the outermost ice giant and the planetesimal disks inner edge, (5) the semi-major axis of the outermost ice giant (commonly referred to as Neptune, however not necessarily the planet which completes the simulation at Neptune’s present orbit), (6) the resonant configuration of the giant planets starting with the Jupiter/Saturn resonance, and (7) the masses of the ice giants from inside to outside.	62
3.2	Summary of initial conditions for terrestrial planetary formation simulations.	66
3.3	Summary of success criteria for the solar system. The columns are: (1) the semi-major axis of Mars, (2-4) The masses of Mars, Venus and Earth, (5-6) the time for Mars and Earth to accrete 90% of their mass, (7) the final mass of the asteroid belt, (8) the ratio of asteroids above to below the ν_6 secular resonance between 2.05-2.8 au, (8) the water mass fraction of Earth, (9) the angular momentum deficit (AMD) of the inner solar system, (10) the final number of giant planets, (11-13) the semi-major axes, time-averaged eccentricities and inclination of the giant planets, (14) the orbital period ratio of Jupiter and Saturn. A complete discussion of the success criteria, background information and justifications is provided in the Supplementary Information.	69
3.4	Summary of percentages of systems which meet the various terrestrial planet success criteria established in Table 3.3. It should be noted that, because runs beginning with a disk mass of $3M_{\oplus}$ were not successful at producing appropriately massed Earth and Venus analogs, criterion A and A1 are only calculated for $5M_{\oplus}$ systems. The subscripts TP and AB indicate the terrestrial planets and asteroid belt respectively.	76

3.5	Summary of percentages of systems which meet the various giant planet success criteria established in Table 3.3. The subscript GP indicates the giant planets.	77
3.6	Summary of percentages of systems which meet the various terrestrial planet success criteria established in Table 3.3 <i>AND</i> finish with Jupiter and Saturn’s period ratio less than 2.8 (criterion J). It should be noted that, because runs beginning with a disk mass of $3M_{\oplus}$ were not successful at producing appropriately massed Earth and Venus analogs, criterion A and A1 are only calculated for $5M_{\oplus}$ systems. The subscripts TP and AB indicate the terrestrial planets and asteroid belt respectively.	77
4.1	Table of giant planet initial resonant configurations from Chapter 3. The columns are: (1) the name of the simulation set, (2) the number of giant planets, (3) the mass of the planetesimal disk exterior to the giant planets, (4) the distance between the outermost ice giant and the planetesimal disks inner edge, (5) the semi-major axis of the outermost ice giant (commonly referred to as Neptune, however not necessarily the planet which completes the simulation at Neptune’s present orbit), (6) the resonant configuration of the giant planets starting with the Jupiter/Saturn resonance, and (7) the masses of the ice giants from inside to outside.	104
4.2	Summary of initial conditions for complete sets of terrestrial planet formation simulations. The columns are (1) the name of the simulation set, (2) the inner edge of the terrestrial forming disk, (3) the disk’s outer edge, (4) the total disk mass, (5) the number of equal-mass embryos used and (6) the number of equal-mass planetesimals used, (7) the number of giant planets, (8) the instability timing in Myr, and (9) the total number of integrations comprising the set (Note that each set begins with 100 calculations, however instability runs where Jupiter and Saturn exceed a period ratio of 2.8 or an ice giant is not ejected within 5 Myr are removed). In the subsequent text, we often refer to the 6 standard/XGP/XMyr (rows 3-8) collectively as our instability sets. It should also be noted that the “standard” set was referred to as the “control” set in Chapter 3.	108
4.3	Summary of success criteria for the inner solar system from Chapter 3. The rows are: (1) the semi-major axis of Mars, (2-4) The masses of Mars, Venus and Earth, (5-6) the time for Mars and Earth to accrete 90% of their mass, (7) the final mass of the asteroid belt, (8) the ratio of asteroids above to below the ν_6 secular resonance between 2.05-2.8 au, (8) the water mass fraction of Earth, and (9) the angular momentum deficit (AMD) of the inner solar system.	109
4.4	Summary of percentages of systems which meet the various terrestrial planet success criteria established in Table 4.3. Values in parenthesis indicate the change from the same simulation set in Chapter 3 (where fragmentation was not considered). The subscripts TP and AB indicate the terrestrial planets and asteroid belt respectively.	113

5.1	Summary of initial conditions for complete sets of terrestrial planet formation simulations. The columns are (1) the name of the simulation set, (2) the inner edge of the terrestrial forming disk, (3) the disk's outer edge, (4) the total disk mass, (5) the number of equal-mass embryos used, and (6) the number of equal-mass planetesimals used.	143
5.2	Summary of initial conditions for simulations to produce Mercury as suggested by Asphaug & Reufer (2014). The columns are (1) the scenario number, (2-4) the semi-major axis, eccentricity and inclination ranges from which the projectiles orbit is selected, (5) the fragment ejection velocity with respect to the mutual two-body escape velocity (6) the total number of integrations performed, and (7) the total number of integrations where fragmenting collisions occurred.	155
6.1	Summary of our three different simulation batches. The columns are as follows; (1) the name of the set of simulations, (2) the numbering scheme for the set's runs, (3) the number of $0.006 M_{\oplus}$ asteroids, and (4) the number of $0.055 M_{\oplus}$ embryos.	169
6.2	Table of results for our 18 runs. The columns are as follows: (1) the run number, (2) the AMD of the Jupiter/Saturn system, (3) Jupiter and Saturn period ratio, (4) the run's AB depletion fraction, and (5) the ratio of asteroids above to below the ν_6 resonance. Only asteroids not on planet crossing orbits are considered.	179
A.1	Simulation Results	206

List of Figures

2.1	Upper: Fractional Energy ($\delta E/E$) change for the innermost planet in the system ann21, the body with the smallest pericenter ($q = 0.136$ au) in all of our systems. Lower: Fractional Energy change ($\delta E/E$) for all bodies in ann21.	30
2.2	Cumulative Distribution of the absolute value of Fractional Energy change ($\delta E/E$) over the duration of the simulation for all WHFAST integrations performed in this project.	31
2.3	A shows clear libration between 2 resonant angles. These 2 terrestrial planets are locked in a 2:1 MMR for the duration of the simulation. B: depicts occasional libration where 2 rocky planets are going in and out of a 5:3 MMR. C shows slow circulation of a resonant angle for 2 inner planets. These objects are close to a 2:1 MMR. Finally, D is an example of a uniform distribution of resonant angles where the objects are not in a MMR.	34
2.4	Cumulative distribution of the last times at which systems lose a planet more massive than $0.055 M_{\oplus}$ via collision or ejection. The distributions for cjs, eejs, and ann are shown with the blue, red, and green lines, respectively.	36
2.5	For systems that lose a planet after $t = 200$ Myr (more massive than $0.055 M_{\oplus}$), the distribution of masses for the last lost planet is shown. The distributions for cjs, eejs, and ann are shown with the blue, red, and green lines, respectively.	37
2.6	A: Time evolution of a 5-planet system from the cjs simulation batch. The pericenter, apocenter, and semi-major axis of each terrestrial planet is shown vs time. B: Time evolution of a 3-planet system from the eejs simulation batch. The pericenter, apocenter, and semi-major axis of each terrestrial planet is shown vs time.	39
2.7	A–C: The distribution of the number of planets in each system at $t = 200$ Myr are shown for our cjs, eejs, and ann simulation batches in panels A, B, and C, respectively. The unfilled histograms show the distribution for all systems, and the filled histograms shown the distribution for systems that lose at least 1 planet more massive than $0.055 M_{\oplus}$ after $t = 200$ Myr. D–F: The distribution of the number of planets in each system at $t = 4.5$ Gyr are shown for our cjs, eejs, and ann simulation batches in panels D, E, and F, respectively. The unfilled histograms show the distribution for all systems, and the filled histograms shown the distribution for systems that lose at least 1 planet more massive than $0.055 M_{\oplus}$ after $t = 200$ Myr.	40

2.8	A–C: The distribution of terrestrial AMD values (normalized to the solar system’s modern terrestrial AMD) at $t = 200$ Myr are shown for our cjs, eejs, and ann simulation batches in panels A, B, and C, respectively. The unfilled histograms show the AMD values for all systems, and the filled histograms shown the AMD values for systems that lose at least 1 planet more massive than $0.055 M_{\oplus}$ after $t = 200$ Myr. D–F: The distribution of terrestrial AMD values (normalized to the solar system’s modern terrestrial AMD) at $t = 4.5$ Gyr are shown for our cjs, eejs, and ann simulation batches in panels A, B, and C, respectively. The unfilled histograms show the AMD values for all systems, and the filled histograms shown the AMD values for systems that lose at least 1 planet more massive than $0.055 M_{\oplus}$ after $t = 200$ Myr.	42
2.9	Comparison of the prevalence of chaos for runs 1, a and b.	44
2.10	This figure compares the behavior of MEGNO in two separate simulations of our own solar system, run using the same settings described in § 2.2.3. With the giant planets in place (red line), the system is chaotic, and when they are removed (green line) the chaos disappears. Though Jupiter is the source of the chaos in our own solar system, when only Saturn, Uranus and Neptune are removed the system is non-chaotic because the precession of Jupiter’s orbit due to the outer planets stops. This result is different than the vast majority of the systems in this Chapter, which remain chaotic when only Saturn is removed.	45
2.11	Comparison of the prevalence of chaos for runs 1, c, d and e.	46
2.12	Cumulative distribution of the last times at which systems’ with inflated eccentricities lose a planet more massive than $0.055 M_{\oplus}$ via collision or ejection. The distributions for cjs and ann are shown with the blue and green lines, respectively.	46
2.13	A–C: S_c ’s affect on chaos for simulation batches cjs, eejs and ann (A, B and C respectively). S_c ’s for 1-planet systems are infinite, and therefore omitted in these graphs. D–F: Relationship between center of mass and chaos in simulation batches cjs, eejs and ann (D, E and F respectively). Chaotic systems are designated by green plus signs and non-chaotic systems are represented by red circles.	49
2.14	Comparison of eejs25’s innermost planet’s (E0) inclination and eccentricity with Jupiter’s eccentricity. The periods of oscillation match, indicating a strong secularly driven resonance. Interestingly, this interaction does not drive any chaos in the system.	51
3.1	An example of the resonant evolution of a system of outer planets in the 5GP batch. With the forcing function mimicking interactions with the gaseous disk in place, once a set of planets falls in to a MMR, they remain locked in resonance for the remainder of the evolution.	65

3.2	Cumulative distribution of Mars analog masses formed in instability systems and our control batch (note that some systems form multiple planets in this region, here we only plot the largest planet). The vertical line corresponds to Mars' actual mass. All control runs with a Mars analog smaller than $0.3 M_{\oplus}$ ($\sim 20\%$ of the batch) were unsuccessful in that they also formed a large planet in the asteroid belt	78
3.3	Cumulative mass distribution of embryos and planetesimals at the beginning of the control simulations (black line), 10 Myr after the early instability delay times (.01 and 0.1 Myr; red line), 100 Myr after the early instability delay times (orange line), 10 Myr after the late instability delay times (1 and 10 Myr; cyan line) and 100 Myr after the late instability delay times (blue line). The green line represents the current mass distribution of the inner solar system.	80
3.4	Distribution of semi-major axes and masses for all planets formed using $5 M_{\oplus}$ massed planetesimal disks. The red squares denote the actual solar system values for Mercury, Venus, Earth and Mars. The vertical dashed line separates the Earth and Venus analogs (left side of the line) and the Mars analogs (right side). The top panel shows our control runs and each of the 4 lower plots depict a different instability delay time.	82
3.5	Semi-Major Axis/Eccentricity plot depicting the evolution of a successful system in the 5GP/10Myr batch. The size of each point corresponding to the mass of the particle (because Jupiter and Saturn are hundreds of times more massive than the terrestrial planets, we use separate mass scales for the inner and outer planets). The final planet masses are 0.37, 1.0, 0.69 and $0.15 M_{\oplus}$ respectively.	84
3.6	The upper plot shows the inclination distribution of the modern asteroid belt (only bright objects with absolute magnitude $H < 9.7$, approximately corresponding to $D > 50$ km, are plotted). The bottom plot combines all planetesimals remaining in the asteroid belt region from all instability simulations that form a Mars analog less massive than 3 times Mars' actual mass, and finish with Jupiter and Saturn's period ratio less than 2.8. Grey points correspond to high-eccentricity asteroids on Mars crossing orbits which will be naturally removed during subsequent evolution up to the solar system's present epoch. The vertical dashed lines represent the locations of the important mean motion resonances with Jupiter. The bold dashed lines indicate the current location of the ν_6 secular resonance.	86
3.7	Values of the amplitudes of Jupiter's g_5 mode versus the mass of Mars analogs formed for 10 Myr delayed instability systems where the orbital period ratio of Saturn to Jupiter completing the integration less than 2.8. The red stars correspond with the present solar system values.	90
3.8	The AMD of Jupiter and Saturn (normalized to the actual solar system value) versus the mass of Mars analogs formed for all instability systems. The red star denotes the solar system values.	92

3.9	Values of the total mass of Earth and Venus analogs versus the mass of Mars analogs formed in instability systems where the value of Jupiter and Saturn’s period ratio finished the simulation less than 2.8. The color of each point corresponds to the amplitude of Jupiter’s g_5 mode. The blue star denotes actual solar system values.	93
4.1	Distribution of semi-major axes and masses for all planets formed in all simulation sets. The red squares denote the actual solar system values for Mercury, Venus, Earth and Mars. The vertical dashed line separates the Earth and Venus analogs (left side of the line) and the Mars analogs (right side). Planets from Chapter 3 simulations that do not include collisional fragmentation (control (standard) sets, 1.0 Myr and 10.0 Myr instability delays) are denoted with open circles.	115
4.2	The top panel depicts the cumulative distribution of Mars analog masses formed in our various fragmentation simulation sets (solid lines) compared with our results from Chapter 3 (dashed lines). The bottom panel depicts the same data for the various instability delay times tested in this work (solid lines), and in Chapter 3 (dashed lines). The grey vertical lines corresponds to Mars actual mass. Note that some systems may form multiple planets in this region, but here we only plot the most massive planet. Systems that do not form a Mars analog via embryo accretion are plotted as having zero mass.	116
4.3	Comparison of disk properties in our instability simulations that include fragmentation (this work) and those performed using a conventional integration scheme (Chapter 3). The red and black lines in the upper panel plot an exponential fit of the average total particle number in the terrestrial forming disk with respect to time. The red and black points denote mean eccentricities (middle panel) and inclinations (bottom panel) for growing Earth and Venus analogs.	118
4.4	Semi-Major Axis/Eccentricity plot depicting the evolution of a successful system in the standard/5GP/1Myr batch. The size of each point corresponds to the mass of the particle (because Jupiter and Saturn are hundreds of times more massive than the terrestrial planets, we use separate mass scales for the inner and outer planets). The final terrestrial planet masses are 0.52, 0.68, 0.76 and 0.08 M_{\oplus} respectively.	120
4.5	Cumulative distribution of normalized AMDs (top panel) and RMCs (bottom panel) for the terrestrial systems formed in our various fragmentation simulation sets (solid lines) compared with our results from Chapter 3 (dashed lines). The grey vertical line corresponds to the solar system value (1 by normalization). Each statistic is calculated utilizing all terrestrial objects that complete the simulation with $a < 2.0$ au and $m > 0.055 M_{\oplus}$, and normalized to the modern solar system value.	125

4.6	Semi-Major Axis/Eccentricity plot depicting a successful system in the annulus/5GP/10Myr batch (bottom panel), compared with the actual solar system (top panel). The size of each point corresponds to the mass of the particle (because Jupiter and Saturn are hundreds of times more massive than the terrestrial planets, we use separate mass scales for the inner and outer planets). The final terrestrial planet masses are 0.73, 1.04 and 0.076 M_{\oplus} respectively.	128
4.7	Relative late impact rates with respect to time on Venus, Earth and Mars analogs in our 1 Gyr extended annulus and instability integrations.	131
5.1	Distribution of all objects with masses greater than 0.01 M_{\oplus} and CMFs greater than 0.5 surviving 200 Myr of terrestrial planet formation. The colors black, red and green correspond to the control, instability and annulus simulations respectively. The yellow star plots the actual planet Mercury.	147
5.2	Cumulative distribution of the difference between the perihelion of Venus analogs and aphelion of Mercury analogs (top panel), and relative period ratios (bottom panel), produced in our complete simulations of terrestrial planet formation. The figure only depicts systems that finish with a planet (Mercury) with $a < 0.5$ au and $m < 0.2 M_{\oplus}$, interior to a larger body (Venus) with $a < 1.3$ au and $m > 0.6 M_{\oplus}$. The red vertical lines corresponds to the solar system values for Mercury and Venus. The different line styles denote our different simulation sets.	149
5.3	Semi-Major Axis/Eccentricity plot of selected successful simulations. The size of each point is proportional to the mass of the planet. The color of each point indicates the planet's CMF. The top 6 panels show examples from each of our 3 simulation sets (Control, Annulus and Instability). The bottom panel shows the actual solar system.	151
5.4	Giant planet instability evolutionary schemes for the two instability systems from Figure 5.3. The perihelia and aphelia are plotted for each outer planet in the simulation. The horizontal dashed lines correspond to the modern semi-major axes of Jupiter, Saturn, Uranus and Neptune. The top panel corresponds to "Instability 1" and the bottom panel plots "Instability 2."	152
5.5	Cumulative distribution of the difference between the perihelion of Venus and aphelion of fragments (top panel), and relative period ratios (bottom panel), in all simulation batches after 1 Gyr of evolution. The red vertical lines correspond to the solar system values for Mercury and Venus. The different line styles denote the fragment ejection speed (percentage greater than the mutual escape speed; denoted as subsets a, b and c in Table 5.2, column 5).	155
5.6	Cumulative distribution of system AMDs after 1 Gyr of evolution, normalized to the solar system value for Mercury, Venus, Earth and Mars. The different line styles represent the different initial projectile orbital parameter space tested (Table 5.2). The red vertical line corresponds to the solar system value.	158

5.7	Example evolution of a successful simulation in the scenario 1b set (Table 5.2, column 5) . The perihelia and aphelia are plotted for each body in the simulation. After the projectile (color coded black) smashes into the proto-Venus at 131 Myr, five fragments are ejected. Four more fragments are formed over the next 25 Myr in four different collisions between the original fragments. Each fragment is coded a different non-greyscale color.	158
6.1	Pre-instability, self-stirred eccentricity (top panel) and inclination (bottom panel) distribution of our simulated AB after 1 Myr of evolution in the presence of a static Jupiter and Saturn.	168
6.2	Dependence of AB depletion on the AMD of Jupiter and Saturn (top panel), the excitation of Jupiter's g_5 mode (e_{55} , middle panel) and Saturn's forced eccentricity (e_{56} , bottom panel). Runs 1-8 (fully self gravitating AB) are plotted in red. Runs 1a-8a (test particle AB) are plotted with black. Runs 1b and 2b (embedded planet embryos) are plotted in green. The red line denotes the solar system value for each statistic and the grey region denotes the area within a factor of 5 of a 10^{-3} depletion factor. Note, run 4a is not plotted since Saturn was ejected.	171
6.3	Semi-Major Axis/Eccentricity plot depicting the final planets from run 2a (bottom panel), compared with the actual solar system (top panel). The size of each point corresponds to the mass of the particle (because Jupiter and Saturn are hundreds of times more massive than the terrestrial planets, we use separate mass scales for the inner and outer planets). The final terrestrial planet masses are 0.20, 0.75, 0.86, 0.23 and 0.23 M_{\oplus} respectively.	174
6.4	Radial mixing of silicate rich (S-type; dashed line) and carbonaceous (C-type; solid line) bodies in the actual AB (top left panel; all known asteroids with spectral classifications and $D > 50$ km) and our various simulation sets. The different curves in the other three plots (Interact, Test Particle and Embryos) compare the final distributions of all asteroids that began the integration with $a < 2.8$ au (dashed lines) to those that started with $a > 2.8$ au (solid lines). Only asteroids not on planet crossing orbits are considered.	176
6.5	Histograms of semi-major axis (top panel), eccentricity (middle panel), and inclination (bottom panel) distributions for the modern asteroid belt (solid lines; $H < 9.7$, $D > 50$ km), run 1 (dashed lines) and all interaction systems with $P_S/P_J < 2.8$ (dot-dashed lines). Only asteroids not on planet crossing orbits are considered.	180
6.6	Semi-major axis/inclination plot for the modern asteroid belt (top panel; $H < 9.7$, $D > 50$ km), run 1, and all interaction systems with $P_S/P_J < 2.8$. Only asteroids not on planet crossing orbits are considered. The vertical dashed lines represent the locations of the important mean motion resonances with Jupiter. The bold dashed lines indicate the current location of the ν_6 secular resonance.	181

6.7 Semi-major axis/eccentricity plot for the modern asteroid belt (top panel; $H < 9.7$, $D > 50$ km), run 1, and all interaction systems with $P_S/P_J < 2.8$. Only asteroids not on planet crossing orbits are considered. The vertical dashed lines represent the locations of the important mean motion resonances with Jupiter. 183

Acronyms and Abbreviations

1. a : Orbital semi-major axis.
2. AB: Asteroid Belt.
3. AMD: Angular Momentum Deficit; the degree to which a system of orbits' deviates from being circular and co-planar.
4. ann: Annulus; refers to the terrestrial planets forming out of a narrow annulus of material extending from ~ 0.7 - 1.0 au.
5. AU: Astronomical Unit; the Earth-Sun distance.
6. CAI: Calcium-Aluminum-rich Inclusion; the oldest samples in the solar system.
7. cjs: Circular Jupiter and Saturn.
8. CMF: Core Mass Fraction; fraction of a planet's total mass contained in its Iron core.
9. CPU: Central Processing Unit.
10. C-type: Carbonaceous asteroid type dominant in the outer asteroid belt.
11. e : Orbital eccentricity.
12. e_{55} : Amplitude of the g_5 eigenmode in the secular theory of solar system dynamics (related to the precession of Jupiter's eccentricity vector).
13. e_{56} : Amplitude of the g_6 eigenmode's forcing on g_5 in the secular theory of solar system dynamics (related to the precession of Saturn's eccentric forcing on Jupiter's orbit).

14. eejs: Extra Eccentric Jupiter and Saturn.
15. Frag: Fragmentation.
16. g_5 : Dominant secular precession frequency in the solar system; strongly driven by the precession of Jupiter's eccentricity vector.
17. g_6 : Significant secular precession frequency in the solar system; strongly driven by the precession of Saturn's eccentricity vector.
18. GPU: Graphics Processing Unit.
19. GENGA: Gravitational Encounters with GPU Accerleration; simulation package used in Chapter 6.
20. GP: Giant Planets.
21. Gyr: Billion years.
22. HSE: Highly Siderophile Elements; Metal-rich silicates used to trace accretion and differentiation in growing planets.
23. i : Orbital inclination.
24. inst: Instability.
25. KBO: Kuiper Belt Objects; a circumstellar ring of icy, comet-like bodies past the orbit of Neptune similar to Pluto.
26. LHB: Late Heavy Bombardment; hypothesized spike in the Moon's cratering record several hundred million years after the planets formed.
27. M_{\oplus} : Earth Mass; 3.285×10^{23} kg.
28. M_f : Mercury Mass; 5.972×10^{24} kg.

29. MB: Main Belt; the classical section of the asteroid belt extending from ~ 2.0 - 3.2 au that excludes other asteroids such as Near-Earth asteroids and the Hildas.
30. MEGNO: Mean Exponential Growth of Nearby Orbits; statistic used to quantify orbital chaos.
31. MFM: Minimum Fragment Mass.
32. MMR: Mean Motion Resonance; when two objects' orbital periods are in integer ratio.
33. MVEM: Mercury, Venus, Earth and Mars.
34. Myr: Million years.
35. ν_6 : Dominant secular resonance for orbital precessions in the asteroid belt driven by the solar system's g_6 eigenfrequency
36. P : Orbital period.
37. q : Orbital perihelion.
38. Q : Orbital aphelion.
39. RMC: Radial Mass Concentration Statistic (Chapter 4 only, S_C in Chapter 2).
40. S_C : Radial Mass Concentration Statistic (Chapter 2 only, RMC in Chapter 4).
41. std: Standard.
42. S-type: Silicate-rich asteroid type dominant in the inner asteroid belt.
43. τ_L : Lyapunov Timescale.
44. TP: Terrestrial Planets.
45. WHFast: Wisdom-Holman symplectic integrator used in Chapters 2 and 5.

46. WMF: Water Mass Fraction
47. 5GP: Primordial configuration of the outer solar system containing five giant planets (Jupiter, Saturn, Uranus, Neptune and an additional primordial ice giant that is subsequently lost).
48. 6GP: Primordial configuration of the outer solar system containing five giant planets (Jupiter, Saturn, Uranus, Neptune and two additional primordial ice giants that are subsequently lost).

Chapter 1

Introduction

In this thesis we use numerical modeling to develop a robust, self-consistent evolutionary model for the solar system. Doing so requires reconciling the formation and evolution of four broadly unique regimes of objects that orbit the Sun alongside our Earth. The four terrestrial planets (Mercury, Venus, Earth and Mars) lie on mostly circular orbits with semi-major axes between ~ 0.4 and 1.5 au (Astronomical Unit; the Earth-Sun distance). Each terrestrial planet is composed of an iron-rich core, a layer of silicate mantle material, and a solid crust. Earth and the slightly smaller Venus are the most massive of the terrestrial worlds, while Mercury and Mars are each about ten times smaller.

Further away from the Sun past Mars' orbit lie hundreds of thousands of small, rocky asteroids. The majority of the asteroid belt's (AB) mass is concentrated in the semi-major axis range of ~ 2.0 - 3.2 au known as the main belt (MB). However, the total amount of material in the entire asteroid belt (about $\sim 10^{-4}M_{\oplus}$; Earth masses) is curiously small. In contrast to the solar system's planetary regimes, most orbits in the asteroid belt are eccentric and significantly inclined. Because many asteroids are thought to be composed of the raw, unprocessed materials present in the solar system's infancy ([Bottke et al., 2006b](#)), understanding their nature is a vital step in developing a theoretical framework for the planet formation process.

The solar system's giant planets; Jupiter, Saturn, Uranus and Neptune, make up the next

regime of objects. Jupiter is the largest and closest of these worlds with a semi-major axis of 5.2 au and a mass of over $300 M_{\oplus}$. Because of this, Jupiter and (albeit to a lesser degree) Saturn largely regulate and drive the dynamical state and evolution of the solar system. The gas giants Jupiter and Saturn are primarily composed of hydrogen and helium, while the ice giants Uranus and Neptune contain larger concentrations of compounds like water and methane. Furthermore, the ice giants are also smaller ($\sim 14\text{-}17 M_{\oplus}$) and more distant from the Sun than the gas giants (Uranus and Neptune’s semi-major axes are 19.2 and 30.1 au, respectively).

Finally, the Kuiper Belt is a circumstellar disk of icy, comet-like bodies outside Neptune’s orbit. The classical Kuiper Belt’s outer edge is at around 48 au, and its total mass has been estimated to only be a few percent that of the Earth (Gladman et al., 2001). Furthermore, nearly all Kuiper Belt objects (KBOs) are dynamically excited (large orbital eccentricities and inclinations), and many are in resonant orbits with Neptune (Malhotra, 1995). Constraining the Kuiper Belt’s detailed orbital distribution has been a crucial step in developing our modern understanding of the solar system’s evolution (Levison et al., 2008).

The solar system’s structure is not only complex, but also rather peculiar within the context of discovered systems of exoplanets. Around 30-50% of main sequence stars host at least one “Super-Earth” (larger than the Earth but less massive than the ice giants) at a semi-major axis closer than that of Mercury (Fressin et al., 2013; Mulders et al., 2015). Furthermore, around a percent of stars possess at least one planet similar in size to Jupiter with an orbital period of just a few days (“Hot Jupiters;” Wang et al., 2015). The apparent uniqueness of our own solar system within the greater galactic community of planetary systems provides the motivation for this thesis. Developing a theoretical picture of how the solar system formed and evolved is thus a supremely important step in understanding the conditions that might give rise to life elsewhere in the cosmos.

1.1 Background

1.1.1 The solar system’s fragile state

Broadly speaking, the planets are thought to have formed out of the proto-stellar disk of material that surrounded the newly born Sun, over Myr timescales. In conjunction with the late stages of star formation (~ 4.5 Gyr ago), dust grains slowly grow within the nebula into a distribution of small pebbles and slightly larger boulders via adhesive forces, aggregation and compaction (Dominik et al., 2007). These objects orbit at sub-Keplerian velocities due to aerodynamic drag from the nebular gas, which restricts their growth beyond the meter-scale (Whipple, 1972). How these small bodies eventually grow into larger, asteroid-like “planetesimals” is still an active field of research and debate (see further discussion in § 1.1.4; Levison et al., 2015a; Drążkowska et al., 2016; Raymond et al., 2018). Irregardless, once planetesimals reach the km-scale, runaway growth ensues, and larger planetary “embryos” begin to take shape (Kokubo & Ida, 1996, 1998, 2000). The entire process of planetesimal and embryo formation must take place in just a few Myr, while nebular gas still persists in the planet-forming disk (Haisch et al., 2001). After gas disk dispersal, the terrestrial planets finally take shape over ~ 100 Myr timescales, as Moon-Mars massed embryos combine and grow within a sea of planetesimals (Wetherill, 1996; Chambers, 2001). This final phase of terrestrial accretion is referred to as the “giant impact” phase, and occurs after the giant planets are fully formed (discussed in greater detail in § 1.1.4).

The solar system’s terrestrial planets now exist in a peculiar state where their orbits evolve chaotically, and are only marginally stable over Gyr timescales (Laskar, 1996, 2008; Laskar & Gastineau, 2009). Dynamical modeling utilizing N-body integration algorithms specifically designed for studying planetary systems (Wisdom & Holman, 1991; Duncan et al., 1998; Chambers, 2001; Rein & Tamayo, 2015) has shown that this chaos is largely driven by perturbations from the giant planets (Sussman & Wisdom, 1988; Laskar, 1989; Sussman & Wisdom, 1992; Laskar, 2008).

At this point we must concretely define the difference between “stability” and “chaos” in a planetary system. In general, a system that is non-chaotic is also stable, but a chaotic system might be either stable or unstable (Milani & Nobili, 1992; Deck et al., 2013). The term “chaos” is used to imply prominent mixing across all energetically accessible points in phase space, and a particular sensitivity to initial conditions (Deck et al., 2013). Changing the initial location of a body in a chaotic system like our own by just a few centimeters can lead to a radical change in the system’s evolution. Occasionally these chaotic conditions can give rise to orbital “instabilities;” specific dynamical events or episodes such as collisions, ejections, or the rapid evolution of the orbital elements (most notably a, e and i) of one or more planets.

Mercury and (to a lesser degree) the other terrestrial planets are most affected by chaos in the solar system. Long duration modeling of terrestrial dynamics has shown the real possibility of planet ejections and collisions in the solar system’s future (Clement & Kaib, 2017). Specifically, Laskar (2008) demonstrated a 1-2% probability of Mercury being excited on to a Venus-crossing orbit in the next 5 Gyr. Laskar (2000) used planet formation models of our own solar system to show that orbital chaos is connected to the particular initial mass distribution function selected. Since these systems were evolved in a semi-analytic fashion, without the presence of the giant planets, it is still unclear whether the solar system’s chaotic state is a natural outcome of the planet formation process as we understand it. Understanding how unusual our state is, and sorting out the potential sources of chaos in the solar system might therefore provide insight in to whether other systems of exoplanets exist in a marginally stable, chaotic state. In Chapter 2 (a reproduction of Clement & Kaib, 2017), we perform a detailed investigation into the prevalence of chaos in numerically evolved planetary systems.

1.1.2 The Nice Model

The giant planets' complex dynamics have a massive effect on the fragile terrestrial system, and our understanding of the early evolution of the solar system's outer planets has changed drastically over the last quarter century. In a study that went largely unnoticed for about a decade, [Fernandez & Ip \(1984\)](#) showed that the individual giant planets' orbits behave differently when they interact dynamically with objects in the Kuiper Belt. In short, Saturn, Uranus and Neptune tend to scatter objects on to orbits that routinely bring them closer to the Sun. Thus, the three outermost giant planets “pass” comets inward from one to another until the small bodies eventually attain orbits where they interact heavily with Jupiter. Unlike the smaller three giant planets, Jupiter preferentially ejects these icy worlds from the solar system entirely. In order to conserve angular momentum through this process, Jupiter's orbit moves inward (towards the Sun) and the other three giant planets' move outward over time ([Hahn & Malhotra, 1999](#); [Gomes, 2003](#)).

[Malhotra \(1993\)](#) and [Malhotra \(1995\)](#) argued that this process of orbital migration driven by momentum exchange with small bodies (often referred to as “planetesimal driven migration”) could explain the resonant orbit of Pluto and other objects in the Kuiper Belt. Pluto is one of many similar KBOs in a mean motion resonance (MMR) with Neptune. Pluto, for example, completes exactly 2 orbits for every 3 of Neptune's; and the pair of planets are said to be in a 3:2 MMR.

When taken to its logical conclusion, the concept of planetesimal driven migration in the outer solar system implies that the giant planets must have formed closer to the Sun, in a more compact configuration. [Thommes et al. \(1999\)](#) demonstrated that an orbital instability in a primordially compact outer solar system could simultaneously excite the orbits of KBOs, all while moving the giant planets to their modern semi-major axes.

These ideas were finally formalized into a comprehensive evolutionary model for the outer solar system ([Gomes et al., 2005](#); [Tsiganis et al., 2005](#); [Morbidelli et al., 2005](#)). The so-called Nice (as in Nice, France) Model invokes an orbital instability in the outer solar system

to explain much of its observed modern architecture. In the model’s original form, this instability is generated when Jupiter and Saturn’s initially compact orbital configuration broadens to the point where a mutual 2:1 MMR is crossed (Tsiganis et al., 2005). The periodic perturbations caused by the regular alignment of the solar system’s two most massive planets routinely destabilizes the entire planetary system in numerical simulations, resulting in rapid erosion of a primordially massive Kuiper Belt (Gomes et al., 2005), and a swift reshuffling of the giant planets into their modern configuration (Tsiganis et al., 2005). The Nice Model has since been further expanded to explain the broad orbital distributions within the Kuiper Belt (Levison et al., 2008; Nesvorný, 2015a,b), Jupiter’s capture of co-orbital Trojan asteroids (Morbidelli et al., 2005; Nesvorný et al., 2013), the orbital structure of the asteroid belt (O’Brien et al., 2007; Roig & Nesvorný, 2015; Deienno et al., 2016; Clement et al., 2019c), and the capture of so-called irregular satellites (such as Triton) by the giant planets (Nesvorný et al., 2007).

The Nice Model has been substantially modified since it was first proposed. Simulations using hydrodynamical codes designed for studying giant planet formation in the Sun’s primordial gas disk demonstrate that the outer planets likely emerged in a mutual resonant configuration (Snellgrove et al., 2001; Papaloizou & Nelson, 2003; Nelson & Papaloizou, 2003; Papaloizou et al., 2004; Nelson & Papaloizou, 2004). In the most common scenarios, Jupiter and Saturn are “born” out of the disk in either a 3:2 (Masset & Snellgrove, 2001; Morbidelli & Crida, 2007; Pierens & Nelson, 2008) or 2:1 MMR (Morbidelli et al., 2007). To accommodate these new initial conditions, the current version of the Nice Model’s instability is triggered when two planets fall out of resonance. Such an evolutionary scheme is also enticing because multiple systems of giant exoplanets have been discovered in marginally-stable resonant configurations (eg: HD 60532b, GJ 876b, HD 45364b, HD 27894, Kepler 223 and HR 8799; Holman et al., 2010; Fabrycky & Murray-Clay, 2010; Rivera et al., 2010; Delisle et al., 2015; Mills et al., 2016; Trifonov et al., 2017).

Simulations of the original Nice Model also over-excited the terrestrial planets’ eccen-

tricies and inclinations (Brasser et al., 2009), and often completely annihilated the inner asteroid belt’s orbital structure (O’Brien et al., 2007). Specifically, the rapid and chaotic migration of Jupiter and Saturn’s semi-major axes within the instability causes powerful secular resonances to “sweep” violently across the belt (Walsh & Morbidelli, 2011). In the secular theory of solar system evolution (Tisserand, 1882; Poincare, 1892) the precession rate of each planet’s pericenter location (orientation of the orbital ellipse) can be deconstructed into a sum of the solar system’s eight dominant eigenfrequencies. Each eigenfrequency (g_1 - g_8) is driven by one of the eight planets’ intrinsic precessions. Any object that precesses at a rate equal to one of these eigenfrequencies is said to be in a secular resonance. Studies focusing on the original Nice Model’s effect on the inner solar system found that secular resonance sweeping results in the ejection and over-excitation of nearly all inner main belt asteroids (O’Brien et al., 2007; Brasser et al., 2009; Roig & Nesvorný, 2015; Deienno et al., 2016). To resolve this, the “Jumping Jupiter” style Nice Model instability requires that Jupiter and Saturn “jump” across their mutual 2:1 MMR almost instantaneously, rather than migrate smoothly across it (Brasser et al., 2009; Roig & Nesvorný, 2015; Roig et al., 2016). This style of evolution is typically achieved by invoking the formation of either 1 or 2 additional ice giants in the young solar system (Nesvorný, 2011; Batygin et al., 2012). In successful dynamical simulations, the extra planet (or planets) scatter off the Jupiter-Saturn system, and transfer sufficient energy to “jump” the gas giant’s orbital spacing to close to its modern value (Nesvorný & Morbidelli, 2012). This new scheme is also advantageous because the loss of either Uranus or Neptune is common in simulations of the original, four giant planet Nice Model (Tsiganis et al., 2005; Nesvorný & Morbidelli, 2012). Simply put, beginning an integration with more ice giants increases the likelihood of finishing with four giant planets in the outer solar system.

1.1.3 Timing the instability

Our knowledge of the infant solar system’s dynamical history was strongly shaped by the Lunar materials returned by the latter Apollo missions (most notably Apollo 17; [Schmitt, 2014](#)). In particular, all of the large basins sampled returned geological ages close to ~ 3.9 Gyr ([Tera et al., 1974](#); [Zellner, 2017](#)); close to 400 Myr after the Earth and Moon are thought to have finished forming ([Touboul et al., 2007](#); [Kleine et al., 2009](#)). The Late Heavy Bombardment (LHB, also referred to as lunar cataclysm) hypothesis ([Tera et al., 1974](#)) accounts for this peculiarity by arguing that some cataclysmic event triggered a delayed spike of impacts on the Moon and the terrestrial planets. Because the giant planets’ unstable orbits can routinely scatter asteroids and comets into the inner solar system, the original version of the Nice Model asserted that the solar system’s instability occurred around 3.9 Gyr ago, in conjunction with the LHB. However, multiple recent studies have cast the LHB’s very existence in to doubt, and forced planetary dynamicists to consider the possibility that the Nice Model instability might have occurred when the solar system was much younger. We summarize these new ideas below:

Dynamical fine tuning

Preventing the compact, resonant giant planet configuration from destabilizing for ~ 600 Myr following the disappearance of the primordial gas disk ([Haisch et al., 2001](#); [Pascucci et al., 2009](#)) is challenging for N-body simulations of the event ([Quarles & Kaib, 2019](#)). Most notably, the instability’s timing is rather sensitive to the simulated primordial Kuiper Belt’s total mass and orbital offset from Neptune ([Gomes et al., 2005](#)). Because of limits in computing power, most dynamical investigations of the instability are forced to approximate the primordial Kuiper Belt’s complex structure with $\sim 1,000$ Moon-massed objects (each around an order of magnitude larger than the largest known KBOs) that do not interact gravitationally with one another ([Gomes et al., 2005](#); [Levison et al., 2008](#); [Nesvorný & Morbidelli, 2012](#)). However, simulations utilizing graphics processing units (GPUs, [Grimm](#)

& Stadel, 2014) and more realistic, fully-self-gravitating KBOs (Quarles & Kaib, 2019) have found that instabilities typically occur much quicker than required by the late instability scenario (Gomes et al., 2005).

Highly Siderophile Elements

Highly Siderophile Elements (HSEs; Greek for “iron-loving”) are elements that have a tendency to partition into metals. Therefore, it is expected that nearly all HSEs present in the Earth’s mantle prior to the formation of the iron-core were removed, and incorporated into the core (Morbidelli et al., 2012; Raymond et al., 2013). The modern abundance of HSEs in the Earth’s mantle is thus evidence for delivery (referred to as the “late veneer”) after the final core-forming event (Day et al., 2007; Walker, 2009). Since the closure of Earth’s core is thought to have coincided with the Moon-forming impact (see further discussion in § 1.1.4; Canup, 2012), comparing the HSE inventories of both worlds can inform our knowledge of the tail-end of bombardment in the inner solar system. HSE concentrations obtained from lunar samples indicate that the young Earth accreted 1200 times more material than the Moon (Walker et al., 2004; Day et al., 2007; Walker, 2009), far more than would be expected given their relative geometric cross-sections (different by a factor of only 20). This disparity implies a top-heavy distribution of material impacting the newly formed planets (Bottke et al., 2010). Such a distribution is quite dissimilar from what is observed in the modern asteroid belt, and would seemingly favor the LHB hypothesis (Morbidelli et al., 2012, 2018). However, Rubie et al. (2016) showed that the HSE disparity can be explained by sulfur and iron segregating in the young Moon’s magma ocean. Through this process, HSEs can still drag towards the core for some time after the last giant impact. Since the Moon’s magma ocean crystalized much faster than the Earth’s (Morbidelli et al., 2018), a substantial difference in HSE inventories would be expected, and therefore not the result of the LHB.

Updated dating techniques and imagery

Further analysis of the lunar impactites gathered by the Apollo missions indicated a larger dispersion in the ages of basins (Zellner, 2017) than the initial measurements from the 1970s (Tera et al., 1974, the original motivation for the LHB hypothesis). Several recent studies utilizing $^{40}\text{Ar}/^{39}\text{Ar}$ dating of melt clasts have returned ages significantly different from the original U/Pb values that were clustered around ~ 3.9 Gyr (Fernandes et al., 2000; Chapman et al., 2007; Boehnke & Harrison, 2016). Since these new dates cover a larger range of possible lunar basin ages, they imply a smoother decline in the young Moon’s cratering history than in the LHB hypothesis. Furthermore, modern high-resolution imagery from spacecraft like the Lunar Reconnaissance Orbiter (LRO) and the Gravity Recovery and Interior Laboratory (GRAIL) have revealed larger numbers of old (>3.9 Gyr) impact basins (Spudis et al., 2011; Fassett et al., 2012; Zellner, 2017). For example, Apollo 17 samples thought to be from the Serenitatis basin are now believed to be highly contaminated with material from the younger Irbrium basin (Spudis et al., 2011). Therefore, the Serenitatis basin is likely older than ~ 4 Gyr, and the samples returned by Apollo 17 are simply material from the younger 3.9 Gyr Irbrium event.

The survivability of the terrestrial planets

Multiple studies have shown that the dynamical excitement induced in a late Nice Model instability can be catastrophic for the terrestrial planets (Brasser et al., 2009; Agnor & Lin, 2012; Brasser et al., 2013). Specifically, Kaib & Chambers (2016) demonstrated only a $\sim 1\%$ probability of simultaneously reproducing the orbital structure of both the inner and outer planetary systems. Even in simulations where the Jupiter-Saturn orbital period “jump” (Brasser et al., 2009) is ideal, the giant planets’ orbital excitation can bleed into the terrestrial regime via stochastic diffusion. Common terrestrial outcomes in simulations of a late Nice Model instability include over-exciting the eccentricities of the inner planets (though this might explain Mercury’s modern elevated eccentricity; Roig et al., 2016), planet

ejections, and collisions (Agnor & Lin, 2012; Brasser et al., 2013; Kaib & Chambers, 2016). These results, and those of the other studies mentioned in this section, suggest that the instability likely occurred much earlier. If so, the Nice Model event might have coincided with the epoch of terrestrial planet formation (discussed further in § 1.1.4). An instability of arbitrary timing is still highly successful at explaining many aspects of the outer solar system (Morbidelli et al., 2018). These include the orbital structure of the Kuiper Belt (Thommes et al., 1999; Tsiganis et al., 2005; Levison et al., 2008; Nesvorný, 2015a,b), Jupiter’s co-orbital Trojan asteroids (Morbidelli et al., 2005; Nesvorný et al., 2013), Jupiter’s moons Ganymede and Callisto’s dissimilar differentiation states (Barr & Canup, 2010) and irregular satellite capture by the giant planets (Nesvorný et al., 2007). Incorporating the terrestrial planets into the Nice Model’s framework is thus a vital step, and the major subject of this thesis.

1.1.4 Terrestrial planet formation

The so-called “classic” model of terrestrial planet formation began to take shape alongside advancements in N-body integration algorithms in the 1990s (Wisdom & Holman, 1991; Duncan et al., 1998; Chambers, 1999, 2001). Since then, the late stages of terrestrial planet formation have been the subject of numerous computational studies. Many of these papers only consider the giant impact phase of planet formation in the inner solar system; where a population of Moon-Mars massed planetary embryos combine and grow among a sea of smaller planetesimals. The terrestrial disk initial conditions chosen by most authors (Chambers, 2001; Raymond et al., 2009b; Clement et al., 2018) come from studies of oligarchic growth of embryos and planetesimals embedded in the Sun’s primordial gas disk (Kokubo & Ida, 1996, 1998, 2000). The total mass and distribution of objects assumed is largely consistent with numerical studies and observations of proto-planetary disks (Weidenschilling, 1977; Hayashi, 1981; Bitsch et al., 2015).

The presence of the giant planets is of utmost importance in numerical simulations of the giant impact phase (Wetherill, 1996; Chambers & Cassen, 2002; Levison & Agnor, 2003a).

Observations of gaseous proto-stellar disks (Haisch et al., 2001; Pascucci et al., 2009) indicate that their decay timescales ($\sim 1\text{-}10$ Myr) are far quicker than the timescales of terrestrial planet formation ($\sim 50\text{-}150$ Myr) inferred from isotopic dating (Halliday, 2008; Kleine et al., 2009; Touboul et al., 2007). In order to have built their massive gaseous envelopes, the giant planets must have formed rapidly, before the terrestrial worlds, while the gas disk was still present.

Early N-body integrations using classic initial conditions were reasonably successful at producing the correct number of inner planets at close to their modern semi-major axes (Chambers & Wetherill, 1998; Chambers, 2001). However, these simulations fell short in depleting (by a factor of $\sim 10^4$) and dynamically exciting the asteroid belt, and producing a system of dynamically cold (unexcited; low eccentricities and inclinations) terrestrial planets (Morishima et al., 2010) with the proper mass ratios (recall that Mercury and Mars are $\sim 5\%$ and $\sim 10\%$ the mass of Earth respectively). While accounting for the dynamical friction generated by a sea of small planetesimals helps lower the eccentricities of the fully formed terrestrial planets (Raymond et al., 2006; O’Brien et al., 2006), dynamically cold systems similar to our own are unlikely outcomes in nearly all subsequent studies (Clement et al., 2019b). Worse still, the inability to replicate the low mass of Mars (most simulations build Earth-massed planets where Mars should be) and the asteroid belt seems to be a systematic failure of the classic initial conditions (Raymond et al., 2009b). Fischer & Ciesla (2014) argued that Mars’ small mass could simply be the result of a low probability event. However, while several of the simulations in Fischer & Ciesla (2014) did produce a proper Mars analog, all of these “semi-successful” systems were poor replicas of the solar system for other reasons (for example an extra large planet forming in the asteroid belt; Jacobson & Walsh, 2015). There are multiple compelling solutions to the so-called “small Mars problem.” We summarize the different classes of models and evolutionary schemes below:

Truncated initial conditions

Hansen (2009) found that the four terrestrial planets’ masses and orbits could be consistently replicated when the initial planet-forming disk of material is confined within a narrow annulus between ~ 0.7 - 1.0 au. The “Grand Tack” hypothesis (Walsh et al., 2011; Walsh & Levison, 2016) provides a mechanism for generating these initial conditions by postulating that, during the gas disk phase, Jupiter and Saturn migrated into and out of the terrestrial disk. In the Grand Tack scenario, the inward migration phase is the result of gas disk interactions (Snellgrove et al., 2001; Papaloizou & Nelson, 2003; Nelson & Papaloizou, 2003; Papaloizou et al., 2004; Nelson & Papaloizou, 2004), and the outward migration ensues when the two gas giants fall into resonance with one another (Walsh et al., 2011; D’Angelo & Marzari, 2012; Brasser et al., 2016a). In simulations where Jupiter “tacks” (as in sailing jargon) at the correct semi-major axis, the terrestrial disk is effectively truncated at ~ 1.0 au; thereby replicating an annulus. The Grand Tack model also provides a compelling explanation for the asteroid belt’s bimodal distribution of spectral classes (Walsh et al., 2011). Carbonaceous, low albedo C-types are scattered into the belt from the outer solar system while silicate-rich, moderate albedo S-types are the remnants of the region’s primordial bodies (Chapman et al., 1975; Gradie & Tedesco, 1982; Gradie et al., 1989; Bus & Binzel, 2002; DeMeo & Carry, 2013). Furthermore, the modern asteroid belt’s complex orbital structure is broadly consistent with a Grand Tack and follow-on Nice Model evolutionary scheme (Deienno et al., 2016). The weakness of the scenario lies in the strong dependence of Jupiter’s tack location on the particular disk parameters selected (for a critical review consult Raymond & Morbidelli, 2014).

While the classic model of terrestrial planet formation assumes a fairly uniform disk mass profile (Wetherill, 1996), Mars’ small mass can be generated more consistently from a steep radial distribution of material (Izidoro et al., 2014). The “low-mass asteroid belt” model (Izidoro et al., 2015; Raymond & Izidoro, 2017b) supposes that the primordial asteroid belt and Mars-forming regions never contained much mass to begin with. In that scenario, the belt’s compositional dichotomy is explained by aerodynamic destabilization and scattering

of planetesimals during the giant planets’ growth phase (Raymond & Izidoro, 2017a). The model’s weakness is that it is unclear whether such a steep initial radial mass distribution is realistic (Raymond et al., 2018; Clement et al., 2019c). However, a steeper distribution of material is fairly consistent with the results “pebble accretion” simulations that model embryo and planetesimal growth past the meter barrier from “pebbles” in the gas disk phase (Levison et al., 2015b; Walsh & Levison, 2016; Drażkowska et al., 2016; Drażkowska & Dullemond, 2018). Kenyon & Bromley (2006) performed the first such simulations with a multi-annulus coagulation code and kilometer-scale planetesimals. Subsequent investigations (Levison et al., 2015b; Drażkowska et al., 2016) have taken advantage of rapid advancements in high performance computing and found that particle drift induced by dust growth tends to result in a steeper inner disk radial mass distribution. While simulations of pebble accretion are still in their infancy, these new algorithms are beginning to call the classic initial conditions validity into question.

Direct influence from the giant planets

Raymond et al. (2009b) noted that Mars’ mass can be limited if Jupiter and Saturn’s primordial eccentricities and inclinations are elevated (eejs; Extra Eccentric Jupiter and Saturn). However, such excited primordial giant planet orbits are difficult to justify because interactions between the gas disk and the growing giants tend to circularize their orbits (Papaloizou & Larwood, 2000; Tanaka & Ward, 2004). Nevertheless, the fully formed outer solar system’s influence on the forming terrestrial planets presents a compelling solution to the small Mars problem. Several studies have demonstrated that Mars’ growth can be limited by giant planet migration-driven resonance sweeping (Nagasawa et al., 2005; Thommes et al., 2008). While similar to the Grand Tack scenario, the migration scheme proposed in the so-called “dynamical shake-up” model (Bromley & Kenyon, 2017) is appealing because it is not as drastic and specific. However, the final mass of Mars is strongly tied to the migration speed selected. Furthermore, the major weakness of the dynamical shake-up scenario is that it

also requires a primordially excited outer solar system that is inconsistent with the results of disk models (similar to the eejs configuration of [Raymond et al., 2009b](#)).

The work presented in this thesis is largely motivated by the aforementioned studies ([Raymond et al., 2009b](#); [Nagasawa et al., 2005](#); [Bromley & Kenyon, 2017](#)) of the fully formed giant planets influence on the growing terrestrial system. In particular, [Lykawka & Ito \(2013\)](#) found that a low massed Mars can be produced when Jupiter and Saturn smoothly migrate across their mutual 2:1 MMR with artificial forces and elevated eccentricities. In Chapter 3 we investigate whether an early Nice Model instability, occurring in conjunction with the epoch of terrestrial planet formation, can limit the mass of Mars in a simple, unified model.

1.2 Shortcomings of conventional terrestrial planet formation models

In § 1.1.4, we outlined the systematic problems encountered by studies of the classic model of terrestrial planet formation ([Chambers, 2001](#); [Raymond et al., 2009b](#); [Clement et al., 2018](#)). These included the inability of numerical simulations of the process to produce a dynamically cold system of terrestrial planets, substantially deplete the asteroid belt’s total mass, and regularly yield small Mars and Mercury analogs. While the small Mars problem has been the subject of numerous previous investigations ([Walsh et al., 2011](#); [Bromley & Kenyon, 2017](#); [Raymond & Izidoro, 2017b](#); [Clement et al., 2018](#)), terrestrial excitation, Mercury and the asteroid belt are often (but not always) neglected for a variety of reasons. In this section we summarize the difficulties faced by conventional N-body algorithms in confronting these issues. In Chapters 4-6, we approach these problems using new computational methods ([Chambers, 2013](#); [Grimm & Stadel, 2014](#)), and lay out a path forward for follow-on investigations of terrestrial planet formation.

1.2.1 Collisional fragmentation

N-body codes used in many of the aforementioned studies of terrestrial planet formation (eg: *Mercury* (Chambers, 1999) and *Symba* (Duncan et al., 1998)) save computational time by treating all collisions as perfectly accretionary. In short, when two objects collide, they stick together. While this can be a good first-order approximation for many accretion events (Chambers, 2013; Raymond et al., 2013), real encounters can either be perfectly merging, hit-and-run, partially, or totally fragmenting. Genda et al. (2012) and Leinhardt & Stewart (2012) mapped these various regimes of collisional parameter space, thus permitting traditional N-body algorithms to be modified for fragmenting collisions. Initial simulations performed by Chambers (2013) using such an integration scheme indicated that hit-and-run collisions often dissipate and carry away angular momentum. Often, this process can damp out the orbital eccentricities of the growing terrestrial planets. While this presents an enticing potential solution to the terrestrial over-excitation problem, very few subsequent studies (Dwyer et al., 2015; Bonsor et al., 2015; Carter et al., 2015; Leinhardt et al., 2015; Quintana et al., 2016; Wallace et al., 2017) utilizing this approach were dedicated to investigating terrestrial accretion in our solar system. Since the majority of the systems we present in Chapter 3 (Clement et al., 2018) are poor matches to the actual terrestrial system in terms of the planets' eccentricities and inclinations, we re-perform our study in Chapter 4 using a version of the *Mercury* integration package (Chambers, 1999) that is modified to include the effects of fragmentation (Chambers, 2013; Clement et al., 2019b).

1.2.2 Mercury's peculiar composition

Of the four terrestrial planets, Mercury is perhaps the most unique. Not only is Mercury the smallest of the terrestrial worlds ($0.055 M_{\oplus}$), both its eccentricity (0.21) and inclination (7.0°) are by far the larger than any of the other seven planets'. While the other three inner planets' iron cores makeup about $\sim 30\%$ of their total mass, $\sim 80\text{-}90\%$ of Mercury's mass is believed to reside in its core (Siegfried & Solomon, 1974; Hauck et al., 2013; Margot et al.,

2018). Furthermore, Mercury’s volatile content is substantially depleted compared to the other terrestrial planets’ (Nittler et al., 2017). Recent reviews about Mercury’s formation and composition can be found in Ebel & Stewart (2017), Nittler et al. (2017) and Margot et al. (2018).

Most numerical simulations of terrestrial planet formation rarely produce planets with masses and semi-major axes similar to Mercury (Chambers, 2001; Raymond et al., 2009b; Clement et al., 2018). These studies often truncate the inner terrestrial disk at ~ 0.5 au in order to inhibit the formation of additional massive planets on orbits interior to Mercury’s. These initial conditions are exceedingly difficult to justify given the growing number of discovered exoplanet systems that possess multiple Earth-massed planets on orbits smaller than Mercury’s (eg: Kepler-102, Kepler-11, Kepler-85 and TRAPPIST-1; Lissauer et al., 2013, 2014; Gillon et al., 2017). Some estimates for the preponderance of Main Sequence stars with close-in Super-Earths are as high as $\sim 90\%$ (Mulders et al., 2018). Volk & Gladman (2015) argued that the young inner solar system might have possessed a similar structure. In such a scenario, at some point in the solar system’s youth, this system of additional planets destabilized, and left behind Mercury as the sole survivor. However, the Volk & Gladman (2015) simulations only showed quasi-stability in known exoplanet systems with Super-Earths. Furthermore, they did not include realistic collisions (Wallace et al., 2017) or any of the other planets in our own solar system. Similarly, Lykawka & Ito (2017) studied planet formation in the 0.2-0.5 au region and found that the resulting planets tend to be over-massed and under-excited.

Other authors have speculated that the solar system’s lack of close-in planets might be a relic of the giant planet migration phase. Raymond et al. (2016) demonstrated that planetesimals in the Mercury forming region can be removed from the area during Jupiter’s outward migration phase. Furthermore, Batygin & Laughlin (2015) proposed that the interior terrestrial disk could be cleared out by resonant excitation driven by Jupiter’s inward migration in a Grand Tack scenario (though such a scheme is in direct conflict with the results of disc

models; [Kenyon & Bromley, 2009](#); [Raymond et al., 2016](#)).

Perhaps the most compelling scenario for Mercury’s formation is rooted in an attempt to explain its massive iron-rich core and depleted volatile inventory. Both of these unique features seem to be the result of a massive, energetic collision that occurred some time in the solar system’s infancy ([Benz et al., 1988](#); [Asphaug, 2010](#); [Asphaug & Reufer, 2014](#)). While the Moon’s collisional origin is well studied ([Hartmann & Davis, 1975](#); [Ćuk & Stewart, 2012](#); [Canup, 2012](#); [Herwartz et al., 2014](#); [Mastrobuono-Battisti et al., 2015](#); [Kaib & Cowan, 2015](#); [Quarles & Lissauer, 2015](#); [Citron et al., 2018](#)), the literature concerning a Mercury-forming impact is less extensive. To date, two different collisional scenarios have been proposed to explain Mercury’s origin. In the first, a primordially larger Mercury is eroded via repeated hit-and-run collisions with another proto-planet ([Asphaug et al., 2006](#); [Svetsov, 2011](#); [Chau et al., 2018](#)). Through this process of repeated impacts, much of Mercury’s original mantle is lost. The weakness of this hypothesis lies in explaining Mercury’s volatile content. Modern hydrodynamical simulations of giant impacts have found that ejected volatiles are typically re-accreted by the target object ([Marchi et al., 2014](#)). Therefore, we would expect Mercury’s modern volatile inventory to be much higher. The second proposed scenario suggests that Mercury is actually a collisional fragment that was ejected from another planet during the giant impact phase ([Benz et al., 2007](#); [Asphaug, 2010](#); [Asphaug & Reufer, 2014](#); [Chau et al., 2018](#)). Though the obvious origin world for such an event might seem to be the proto-Venus, [Jacobson et al. \(2017\)](#) proposed that the absence of an internally driven magnetic dynamo implies that Venus never experienced such a large impact.

Though several works have investigated the different Mercury-forming impact scenarios ([Asphaug et al., 2006](#); [Svetsov, 2011](#); [Asphaug & Reufer, 2014](#); [Jackson et al., 2018](#); [Chau et al., 2018](#)), the dynamical likelihood of such an event within the context of terrestrial planet formation is still largely unexplored. In Chapter 5, we approach this problem with the same collisional fragmentation algorithm we use in Chapter 4 ([Clement et al., 2019b](#)). We perform an extensive suite of numerical integrations designed to replicate the preferred

single giant-impact scenario of [Asphaug & Reufer \(2014\)](#), and utilize Chapter 4’s suite of early instability simulations to search for Mercury-like planets with boosted core mass fractions (CMF) ([Clement et al., 2019a](#)).

1.2.3 Accurately modeling the asteroid belt

While the modern asteroid belt is observationally well-constrained, the nature of the primordial belt is still poorly understood ([Clement et al., 2019c](#)). The total mass of the $\sim 100,000$ known objects in the main belt is estimated to be less than $\sim 5 \times 10^{-4} M_{\oplus}$ ([DeMeo & Carry, 2013](#); [Kuchynka & Folkner, 2013](#)), over half of which is concentrated in just four asteroids (in order of descending mass: Ceres, Vesta, Pallas, Hygiea). However, disk models predict that the primordial belt’s mass (before the giant impact phase) was around $\sim 1-5 M_{\oplus}$ ([Hayashi, 1981](#); [Bitsch et al., 2015](#)). The asteroid belt’s planetesimal and embryo mass distribution is most important from a dynamical standpoint, however the mass profiles predicted by planetesimal formation models are inconsistent ([Drażkowska et al., 2016](#); [Carrera et al., 2017](#); [Drażkowska & Dullemond, 2018](#)). Because the primordial belt is rather unconstrained, studying its formation and long term evolution is exceedingly difficult ([Bottke et al., 2015](#)).

Perhaps the most important two observational constraints on the young asteroid belt come from the belt’s second largest asteroid. Meteorites thought to have originated from Vesta suggest that it differentiated and finished forming only a few Myr ([Shukolyukov & Lugmair, 2002](#)) after Calcium Aluminum-rich Inclusion (CAI, the oldest samples in the solar system). This implies that the largest asteroids grew to their modern sizes rapidly; after which their buildup stagnated as the result of dynamical excitement lengthening accretion timescales in the belt. Additionally, collisional fragmentation and grinding have a tendency to break up large asteroids over time ([Bottke et al., 2005a](#)). This trend towards smaller diameters is fairly consistent with the large number of identified collisional families of asteroids ([Bottke et al., 2006a](#); [Walsh et al., 2013](#)). One study ([Dermott et al., 2018](#)) has even proposed that nearly all asteroids in the inner belt are the fragmented remains of just a

small number (a dozen or so) of primordial asteroids. Vesta’s two massive craters (the 505 km Rheasilvia crater on the south pole and the underlying 395 km Veneneia crater; [Schenk et al., 2012](#)) provide further constraints on the collisional evolution and long-term mass loss in the main belt. The probability of both events occurring in the last 2 Gyr given the current size distribution of asteroids is around 1% ([Bottke et al., 2005b](#)). Because there are no other ~ 100 km sized basins in the asteroid belt, it is highly unlikely that the belt has lost much mass over the last few Gyr ([Bottke et al., 2015](#)).

All of these constraints seem to imply that the vast majority of depletion (about three orders of magnitude worth) in the belt must have occurred in the solar system’s infancy. Unfortunately, extrapolating conclusions about the primordial belt from these constraints is inherently problematic since Vesta might have been implanted in the belt from another region of the solar system ([Bottke et al., 2006b](#); [Raymond & Izidoro, 2017a](#)). Indeed, there is a distinct mismatch between Vesta’s distance to the Sun and composition relative to the Earth and Mars ([Mastrobuono-Battisti & Perets, 2017](#)). However, dynamical studies also seem to corroborate this limited asteroidal mass loss over the last 3-4 Gyr. [Minton & Malhotra \(2010\)](#) concluded that the main belt has lost no more than half of all large asteroids since it attained its current dynamical state. The primary mechanism for this mass loss in the modern belt is excitation via MMR and secular resonances. The locations of the solar system’s two most powerful secular resonances (ν_5 and ν_6 ; driven respectively by the precession of Jupiter and Saturn’s ellipses) in a/e and a/i space ([Morbidelli & Henrard, 1991a,b](#)) intersect several prominent MMRs with Jupiter (of most importance are the 4:1, 3:1, 5:2, 7:3 and 2:1). Asteroids in these overlap regions are rapidly excited on to planet crossing orbits, and eventually removed from the belt ([Morbidelli et al., 1995](#)).

Studying the early evolution of a primordially massive asteroid belt is inherently challenging for N-body studies of planet formation because of the massive number of simulation particles required. It would require over 10,000 particles just to approximate the belt down to the mass resolution of the largest asteroid, Ceres. Many investigations of the classic model

of terrestrial planet formation assume a population of Moon-Mars massed embryos extending throughout the entire main belt (Wetherill, 1992; Chambers & Wetherill, 1998; Chambers, 2001; Chambers & Wetherill, 2001; Chambers, 2007; Raymond et al., 2009b). While the dynamical excitation induced by these large objects can lead to substantial mass loss in the belt (Petit et al., 2001; O’Brien et al., 2007), such systems also routinely form stable Mars-Earth massed planets at semi-major axes beyond ~ 2.0 au (Chambers, 2001; Raymond et al., 2009b; Clement et al., 2018). Indeed, the smallest particles used in the simulations we present in Chapters 3-5 are almost 20 times the mass of Ceres. Given the strong radial dependence of embryo growth (Kokubo & Ida, 1996, 1998, 2000), these initial conditions are extremely unrealistic. We address this problem for the early instability scenario in Chapter 6 with a state-of-the-art GPU accelerated integration scheme (Grimm & Stadel, 2014; Clement et al., 2019c).

1.3 Dissertation outline

In Chapter 2 (a reproduction of Clement & Kaib, 2017) we investigate the prevalence of orbital chaos in 145 planetary systems generated in Kaib & Cowan (2015). Our study probes three sets of terrestrial initial conditions: a configuration where Jupiter and Saturn begin on circular orbits (cjs), one where their initial eccentricities and inclinations are large (eejs; Raymond et al., 2009b), and a set where the inner planet-forming disk is confined to a narrow annulus (ANN; Hansen, 2009). We show that dynamical chaos is a common result of the planet formation process as we currently understand it. Furthermore, we find that this chaos disappears in the majority of systems when Jupiter is removed. Therefore, perturbations from the solar system’s largest planet appear to be the largest source of dynamical chaos in our systems. Chaos is also most prevalent in simulations that generate either 4 or 5 terrestrial planets, while systems with fewer planets are often quite stable. Additionally, sets of terrestrial planets with a center of mass highly concentrated between ~ 0.8 -1.2 au

are generally less susceptible to developing the symptoms of chaos than are more disperse systems.

Since we find that the fate of terrestrial systems is intrinsically tied to the dynamical evolution of the gas giants, and the evidence for a late Nice Model instability has recently weakened (see full discussion above), we begin to study the effects of an early instability on terrestrial planet formation in Chapter 3 (a reproduction of [Clement et al., 2018](#)). We present 800 simulations of this scenario to show that an early Nice Model instability strongly affects the forming terrestrial planets, and systematically produces Mars analogs of the correct mass. Our simulations where the terrestrial planets evolve for an additional 1-10 Myr after the gas disk's disappearance are most successful. In this preferred scenario, Mars' growth is effectively aborted upon the instability's onset. Perturbations from the giant planets' unstable orbits quickly remove large embryos from the asteroid belt and Mars-forming regions. While Mars is left behind as a stranded embryo, Earth and Venus continue to grow for another ~ 100 Myr or so. Therefore, an early instability provides a natural explanation for the dissimilarity between Earth and Mars' inferred geologic formation timescales ($\sim 1-5$ Myr for Mars ([Nimmo & Agnor, 2006](#); [Dauphas & Pourmand, 2011](#)) and over 50 Myr for Earth ([Touboul et al., 2007](#); [Kleine et al., 2009](#))).

In the final three chapters of this thesis, we continue to refine the early instability framework of [Clement et al. \(2018\)](#) and Chapter 3. We begin by considering the often neglected effects of collisional fragmentation on terrestrial growth in Chapter 4 (a reproduction of [Clement et al., 2019b](#)). We present close to 1,000 new simulations of the early instability scenario that incorporate a collisional fragmentation algorithm. We demonstrate that the total number of small objects in the terrestrial disk stays higher for longer when fragmentation is included. Because of the increased dynamical friction from these small bodies, and hit-and-run encounters that tend to dissipate angular momentum, our fully formed terrestrial systems are better solar system analogs in terms of their final orbital excitation. These same processes also have the added benefits of yielding better Earth-Venus orbital spacings,

shortening the growth timescales of Mars analogs, and lengthening those for Earth and Venus analogs.

In Chapter 5 (a reproduction of [Clement et al., 2019a](#)), we use this same fragmentation algorithm to perform a detailed dynamical investigation into the proposed collisional origin of Mercury ([Asphaug & Reufer, 2014](#)). We show that it is possible, albeit extremely unlikely, to replicate Mercury and Venus' modern dynamical separation following an energetic collision. However, when we scrutinize Chapter 4's suite of early instability simulations that include the effects of fragmentation, we find that high CMF planets like Mercury are common outcomes of the chaotic planet formation process.

The early instability scenario simulations we present in Chapters 3-5 lack the resolution to adequately model the complex dynamics within the asteroid belt. In Chapter 6 (a reproduction of [Clement et al., 2019c](#)), we utilize a GPU accelerated code ([Grimm & Stadel, 2014](#)) to probe the effects of an early Nice Model instability on a realistic asteroid belt. We present 18 high-resolution simulations to show that the instability can successfully deplete a primordially massive belt at the 99-99.9% level. We find that main belt depletion is strongly related to the giant planets' particular evolution within the Nice Model instability. When the giant planets' final orbital configuration best resembles that of the actual solar system, the asteroid belt is sufficiently depleted by two to three orders of magnitude. We also show that these simulated belts are reasonable matches to the solar system in terms of their broad dynamical structure and radial mixing.

Chapter 2

Prevalence of Chaos in Planetary Systems Formed Through Embryo Accretion

This Chapter is reproduced from [Clement & Kaib \(2017\)](#), which appeared in the journal *Icarus*, with only minor typographical and formatting alterations. The abstract has been removed to improve the flow and readability of this thesis.

2.1 Introduction

Our four terrestrial planets are in a curious state where they are evolving chaotically, and are only marginally stable over time ([Laskar, 1996, 2008](#); [Laskar & Gastineau, 2009](#)). This chaos is largely driven by interactions with the 4 giant planets. However our understanding of the dynamical evolution of the gas giants, particularly Jupiter and Saturn, has changed drastically since the introduction of the Nice Model ([Gomes et al., 2005](#); [Morbidelli et al., 2005](#); [Tsiganis et al., 2005](#)).

The classical model of terrestrial planetary formation, where planets form from a large number of small embryos and planetesimals that interact and slowly accrete, is the basis for numerous studies of planetary evolution (e.g. [Chambers, 2001](#); [O'Brien et al., 2006](#); [Chambers, 2007](#); [Raymond et al., 2009b](#); [Kaib & Cowan, 2015](#)). Using direct observations of proto-stellar disks ([Currie et al., 2009](#)), it is clear that free gas disappears long before the

epoch when Earth’s isotope record indicates the conclusion of terrestrial planetary formation (Halliday, 2008). For these reasons, a common initial condition taken when numerically forming the inner planets is a fully formed system of gas giants at their current orbital locations. Many numerical models have produced planets using this method. However, none to date have analyzed the chaotic nature of fully evolved accreted terrestrial planets up to the solar system’s current epoch. It should be noted that other works have modeled the outcome of terrestrial planetary formation up to 4.5 Gyr. Laskar (2000) evolved 5,000 such systems from 10,000 planetesimals and showed correlations between the resulting power-law orbital spacing and the initial mass distribution. Furthermore, many works have performed integrations of the current solar system, finding solutions that showed both chaos and a very real possibility of future instabilities (Laskar, 2008; Laskar & Gastineau, 2009). Our work is unique in that we take systems formed via direct numerical integration of planetary accretion, evolve them to the solar system’s age, probe for chaos and its source, and draw parallels to the actual solar system.

Although the classical terrestrial planet formation model has succeeded in replicating many of the inner solar systems features, the mass of Mars remains largely unexplained (Chambers, 2001; O’Brien et al., 2006; Chambers, 2007; Raymond et al., 2009b; Kaib & Cowan, 2015). Known as the Mars mass deficit problem, most simulations routinely produce Mars analogues which are too massive by about an order of magnitude. Walsh et al. (2011) argue for an early inward, and subsequent outward migration of a fully formed Jupiter, which results in a truncation of the proto-planetary disc at 1 AU prior to terrestrial planetary formation. If correct, this “Grand Tack Model” would explain the peculiar mass distribution observed in our inner solar system. Another interesting solution involves local depletion of the disc in the vicinity of Mars’s orbit (Izidoro et al., 2014). A detailed investigation of the Mars mass deficit problem is beyond the scope of this paper. It is important, however, to note that accurately reproducing the mass ratios of the terrestrial planets is a significant constraint for any successful numerical model of planetary formation.

Through dynamical modeling, we know chaos is prevalent in our solar system (Sussman & Wisdom, 1988; Laskar, 1989; Sussman & Wisdom, 1992; Laskar, 2008). It is important to note the difference between “stability” and “chaos.” While a system without “chaos” can generally be considered stable, a system with “chaos” is not necessarily unstable (Milani & Nobili, 1992; Deck et al., 2013). As is convention in other works, in this paper “chaos” implies both a strong sensitivity of outcomes to specific initial conditions, and a high degree of mixing across all energetically accessible points in phase space (Deck et al., 2013) Conversely “Instability” is used to describe systems which experience specific dynamical effects such as ejections, collisions or excited eccentricities.

The chaos in our solar system mostly affects the terrestrial planets, particularly Mercury, and can cause the system to destabilize over long periods of time. Laskar (2008) even shows a 1–2% probability of Mercury’s eccentricity being excited to a degree which would risk planetary collision in the next 5 Gyr. What we still don’t fully understand is whether these chaotic symptoms (highly excited eccentricities, close encounters and ejection) are an expected outcome of the planetary formation process as we presently understand it, or merely a quality of our particular solar system. The work of Laskar (2000) showed us that the outcomes of semi-analytic planetary formation models of our own solar system show symptoms of chaos, and are connected to the particular initial mass distribution which is chosen. However these systems were formed without the presence of the gas giants, and planetesimal interactions were simplified to minimize computing time. Perhaps our solar system is a rare outlier in the universe, with it’s nearly stable, yet inherently chaotic system of orbits occurring by pure chance. Of even greater interest, if it turns out that systems like our own are unlikely results of planetary formation, we may need to consider other mechanisms that can drive the terrestrial planets into their modern chaotic state.

This work takes 145 systems of terrestrial planets formed in Kaib & Cowan (2015) as a starting point. The systems are broken into three ensembles. The first set of 50 simulations, “Circular Jupiter and Saturn” (cjs), are formed with Jupiter and Saturn on nearly circular

($e < 0.01$) orbits, at their current semi-major axes. The simulations use 100 self-interacting embryos on nearly circular and coplanar orbits between 0.5 and 4.0 AU, and 1000 smaller non-self-interacting planetesimals. The smaller planetesimals interact with the larger bodies, but not with each other. Additionally, the initial embryo spacing is uniform and embryo mass decreases with semi-major axis to yield an $r^{-3/2}$ surface density profile. The second ensemble (containing 46 integrations), “Extra Eccentric Jupiter and Saturn” (eejs) evolve from the same initial embryo configuration as cjs, with Jupiter and Saturn initially on higher ($e=0.1$) eccentricity orbits. The final batch of integrations (49 systems), “Annulus” (ann), begin with Jupiter and Saturn in the same configuration as cjs, however no planetesimals are used. 400 Planetary embryos for ann are confined to a thin annulus between 0.7–1.0 AU, roughly representative of the conditions described following Jupiter’s outward migration in the Grand Tack Model (Walsh et al., 2011).

After advancing each system to $t=4.5$ Gyr, we perform detailed 100 Myr simulations and probe multiple chaos indicators. By careful analysis we aim to show whether chaotic systems naturally emerge from accretion models, and whether the source of the chaos is the same as has been shown for our own solar system.

2.2 Methods

2.2.1 System Formation and Evolution

We use the simulations modeling terrestrial planet formation in Kaib & Cowan (2015) as a starting point for our current numerical work. In Kaib & Cowan (2015), all simulations are stopped after 200 Myr of evolution, an integration time similar to previous studies of terrestrial planet formation (e.g. Chambers, 2001; Raymond et al., 2004; O’Brien et al., 2006; Walsh et al., 2011). Because we ultimately want to compare the dynamical state of our solar system (a 4.5 Gyr old planetary system) with the dynamical states of our simulated systems, we begin by integrating the systems from Kaib & Cowan (2015) from $t = 200$ Myr

to $t = 4.5$ Gyr. Since bodies can evolve onto crossing orbits and collide before $t = 4.5$ Gyr, accurately handling close encounters between massive objects is essential. Thus, we use the MERCURY hybrid integrator (Chambers, 1999) to integrate our systems up to $t = 4.5$ Gyr. During these integrations, we use a 6-day time-step and remove bodies if their heliocentric distance exceeds 100 au. Because we are unable to accurately integrate through very low pericenter passages, objects are also merged with the central star if their heliocentric distance falls below 0.1 au. Though by no means ideal, the process of removing objects at 0.1 au is commonplace in direct numerical models of planetary formation due to the limitations of the integrators used for such modeling. Chambers (2001) showed that this does not affect the ability to accurately form planets in the vicinity of the actual inner solar system, since objects crossing 0.1 au must have very high eccentricities. These excited objects interact weakly when encountering forming embryos due to their high relative velocity, and rarely contribute to embryo accretion. It should be noted that many discovered exoplanetary systems have planets with semi-major axis interior to 0.1 au. However, we are not interested in studying such systems since we aim to draw parallels to our actual solar system. The WHFAST integrator used in the second phase of this work (§ 2.2.2), however, can integrate the innermost planet to arbitrarily high eccentricities, so the 0.1 au filter is no longer used. Finally, to assess the dynamical chaos among planetary-mass bodies, any “planetesimal” particles (low-mass particles that do not gravitationally interact with each other) that still survive after 4.5 Gyr are manually removed from the final system.

2.2.2 Numerical Analysis

Numerical simulations for detailed analysis of the fully evolved systems are performed using the WHFAST integrator in the Python module Rebound (Rein & Liu, 2012). WHFAST (Rein & Tamayo, 2015) is a freely available, next generation Wisdom Holman symplectic integrator (Wisdom, 1981; Wisdom & Holman, 1991; Kinoshita et al., 1991) ideal for this project due to its reduction on the CPU hours required to accurately simulate systems of

planets over long timescales. WHFAST’s reduction in error arising from Jacobi coordinate transformations, incorporation of the MEGNO (Mean Exponential Growth factor of Nearby Orbits) parameter, improved energy conservation error and tunable symplectic corrector up to order 11 motivate the integrator choice. The accuracy of many mixed variable symplectic integration routines are degraded by integrating orbits through phases of high eccentricity and low pericenter. For this reason, in [Figure 2.1](#) we plot the variation in energy from our simulation with the lowest pericenter ($q = 0.136$ au). In the upper panel, we plot the energy of the innermost planet, since this should be fixed in the secular regime. We see that energy variations stay well below one part in 10^3 . In the lower panel, we plot the fractional change in the total energy of this system. Again, we find that energy variations rarely exceed one part in 10^4 . Finally, in [Figure 2.2](#) we show a histogram of the fractional energy change between the start and end of the integration for all of our simulations. For the vast majority of systems, the fractional energy change is far less than one part in 10^4 , and no simulations exceed 10^3 . Values in excess of 10^4 are from simulations where the eccentricities of the giant planets were artificially inflated and the performance of the integrator is degraded by close encounters. These systems with frequent close encounters are obviously chaotic, so our chaos determination is not affected.

MEGNO is the primary tool for identifying chaotic systems. Introduced in [Cincotta et al. \(2003\)](#), MEGNO represents the time averaged ratio of the derivative of the infinitesimal displacement of an arc of orbit in N-dimensional phase space to the infinitesimal displacement. For quasi-periodic (stable) motion, MEGNO will converge to a value of 2 in the infinite limit. For chaotic systems, however, MEGNO will diverge ([Cincotta et al., 2003](#)). [Maffione et al. \(2013\)](#) showed that MEGNO is an extremely useful and accurate tool for detecting chaos. Systems which are non-chaotic will maintain stable MEGNO values of ~ 2 for the duration of the simulation, while chaotic systems diverge from 2. For this project, systems which attained a maximum value of $\text{MEGNO} \geq 3.0$ were classified as chaotic.

For use in certain analyses, the Lyapunov Timescale (τ_L) is also output. WHFAST

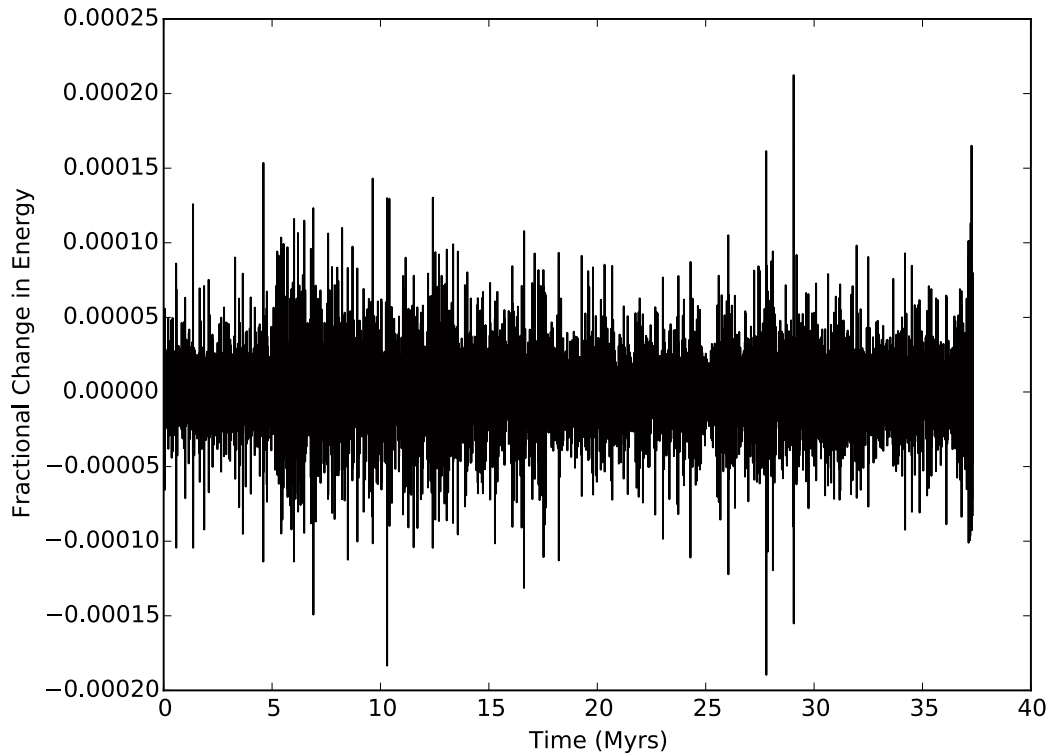
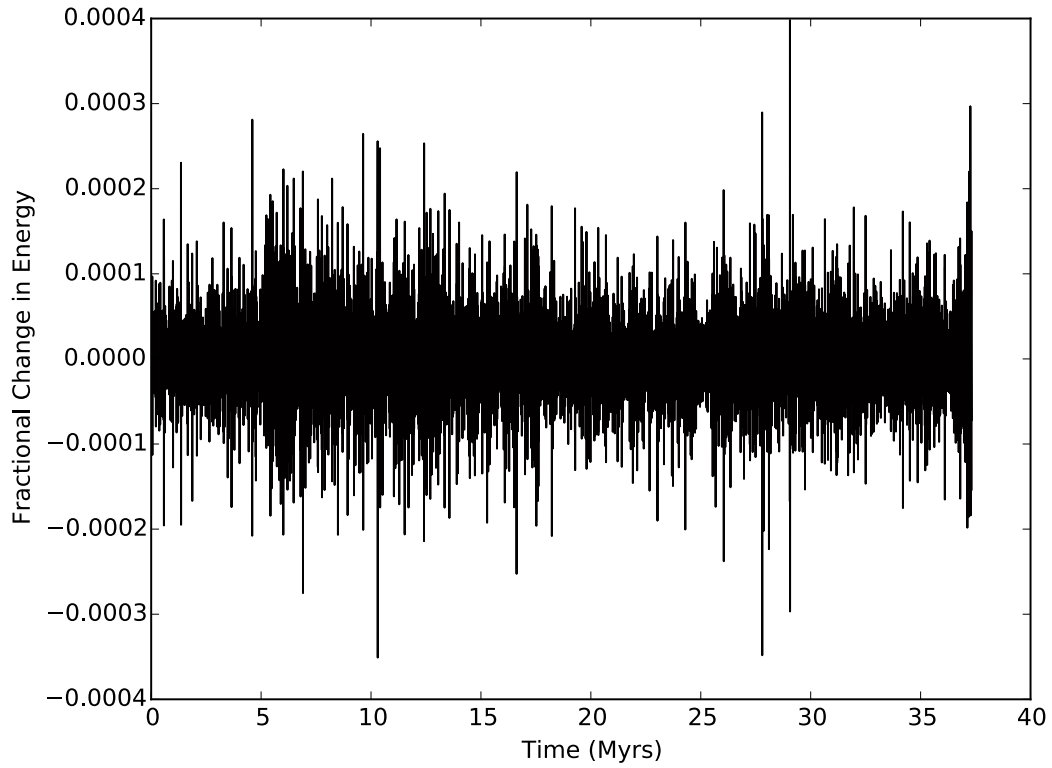


Figure 2.1: **Upper:** Fractional Energy ($\delta E/E$) change for the innermost planet in the system ann21, the body with the smallest pericenter ($q = 0.136$ au) in all of our systems. **Lower:** Fractional Energy change ($\delta E/E$) for all bodies in ann21.

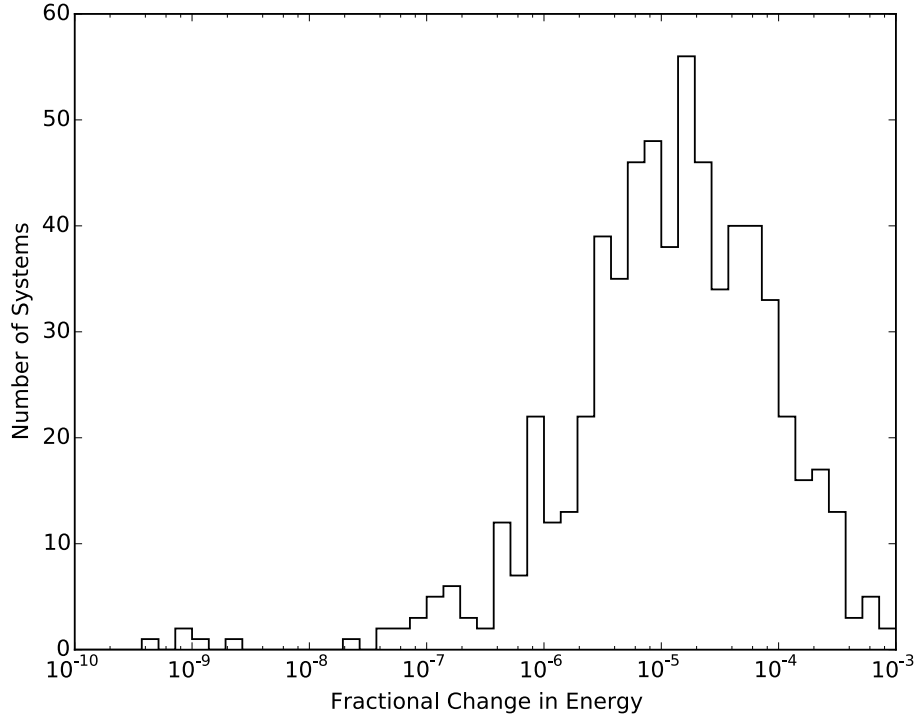


Figure 2.2: Cumulative Distribution of the absolute value of Fractional Energy change ($\delta E/E$) over the duration of the simulation for all WHFAST integrations performed in this project.

calculates the inverse of τ_L by least squares fitting the time evolution of MEGNO (Rein & Tamayo, 2015). Systems classified as chaotic tended to have a τ_L less than ~ 10 – 100 Myr.

Some simulations which quickly displayed chaos were terminated early to save computing time. Terminating these simulations early did not affect the chaos determination since MEGNO had already clearly diverged, nor did shorter simulations affect follow on data analysis and reduction (such as the detection of resonances described in § 2.2.4).

Another tool we use to characterize the chaos in our systems is Angular Momentum Deficit (AMD) (Laskar, 1997). AMD (Eq. 2.1) measures the difference between the z-component of the angular momentum of a given system to that of a zero eccentricity, zero inclination system with the same masses and semi-major axes. Evaluating the evolution of AMD over the duration of a simulation will probe whether angular momentum is being exchanged between giant planets and terrestrial planets as orbits excite and de-excite due

Run Name	Run Time	Jupiter	Saturn	Outer Planet eccentricity shift
1	100 Myr			unchanged
a	100 Myr	removed	removed	unchanged
b	100 Myr		removed	unchanged
c	100 Myr			150%
d	100 Myr			200%
e	100 Myr/1 Gyr			+ 0.05

Table 2.1: Run 1 simulates each fully evolved 4.5 Gyr system discussed in § 2.2.1. Runs a and b evaluate the effect of removing outer planets. Runs c–e investigate the result of inflating the giant planet’s eccentricities. Run e is re-performed for cjs and ann systems using the MERCURY hybrid integrator for 1 Gyr in order to detect close encounters (see § 2.3.2)

to induced chaos (Chambers, 2001).

$$AMD = \frac{\sum_i m_i \sqrt{a_i [1 - \sqrt{(1 - e_i^2)} \cos i_i]}}{\sum_i m_i \sqrt{a_i}} \quad (2.1)$$

2.2.3 Simulation Parameters

Simulations are run for 100 Myr, with an integration time-step of 3.65 days. Orbital data is output every 5000 years. The order of the symplectic corrector is the order to which the symplectic correction term in the interaction Hamiltonian (ϵdt in Rein & Tamayo, 2015) is expanded. Here, we set this to order 1 (WHFAST allows for corrections up to order 11) (Rein & Tamayo, 2015). 10 sample systems were integrated at different corrector values in order to determine the lowest corrector order necessary to accurately detect chaos. Additionally, a total of 16 1 Gyr simulations consisting of both chaotic and non-chaotic systems of 3, 4 and 5 terrestrial planets were performed to evaluate long-term behavior and verify the adequacy of 100 Myr runs. Finally, 6 sets of 145 simulations are performed, results and findings for which are reported in § 2.3. In these six sets of runs, the configurations of giant planets exterior to our terrestrial planets are augmented in various ways to study their influence on the chaos and stability of the systems. These 6 runs and their differences in giant planet configurations are summarized in Table 2.1.

2.2.4 Detecting Mean Motion Resonances

A MMR occurs when the periods of orbital revolution of 2 bodies are in integer ratio to one another. For a given MMR, the resonant angle will librate between 2 values (Àngel Jorba, 2012). Many possible resonant angles exist. In this Chapter, however, we only consider 4 of the more common planar resonant angles (Elliot et al., 2005). Only planar resonances are considered because our systems typically have very low inclinations.

To detect MMRs, the average Keplerian period is calculated for all bodies in the simulation. 4 resonant angles are calculated for all sets of bodies with period ratios within 5% of a given integer ratio. 21 different MMRs (all possible permutations of integer ratios between 2:1 and 8:7) are checked for. Using a Komolgorov-Smirnov test, each resulting time-resonant angle distribution (e.g. Figure 2.3) is compared to a uniform distribution (e.g. Figure 2.3d), yielding a p-value. All distributions with p-values less than 0.01 are evaluated by eye for libration. Figure 2.3 shows 4 different example distributions and their classification.

2.3 Results

2.3.1 System Evolution Beyond 200 Myr

In Kaib & Cowan (2015), systems of terrestrial planets were generated via simulations of terrestrial planet accretion. These simulations were terminated after 200 Myr of evolution, as each simulation had evolved into a system dominated by 1–6 terrestrial planet-mass bodies. Terminating accretion simulations after 200–400 Myr of system evolution is common practice since the great majority of accretion events occur well before these final times are reached. However, it remains unknown how these newly formed systems evolve over the next several Gyr. Do planetesimals and embryos naturally accrete into indefinitely stable configurations of terrestrial planets? Or are the systems that arise from terrestrial planet accretion often only marginally stable, with major instabilities occurring hundreds of Myr or Gyr after

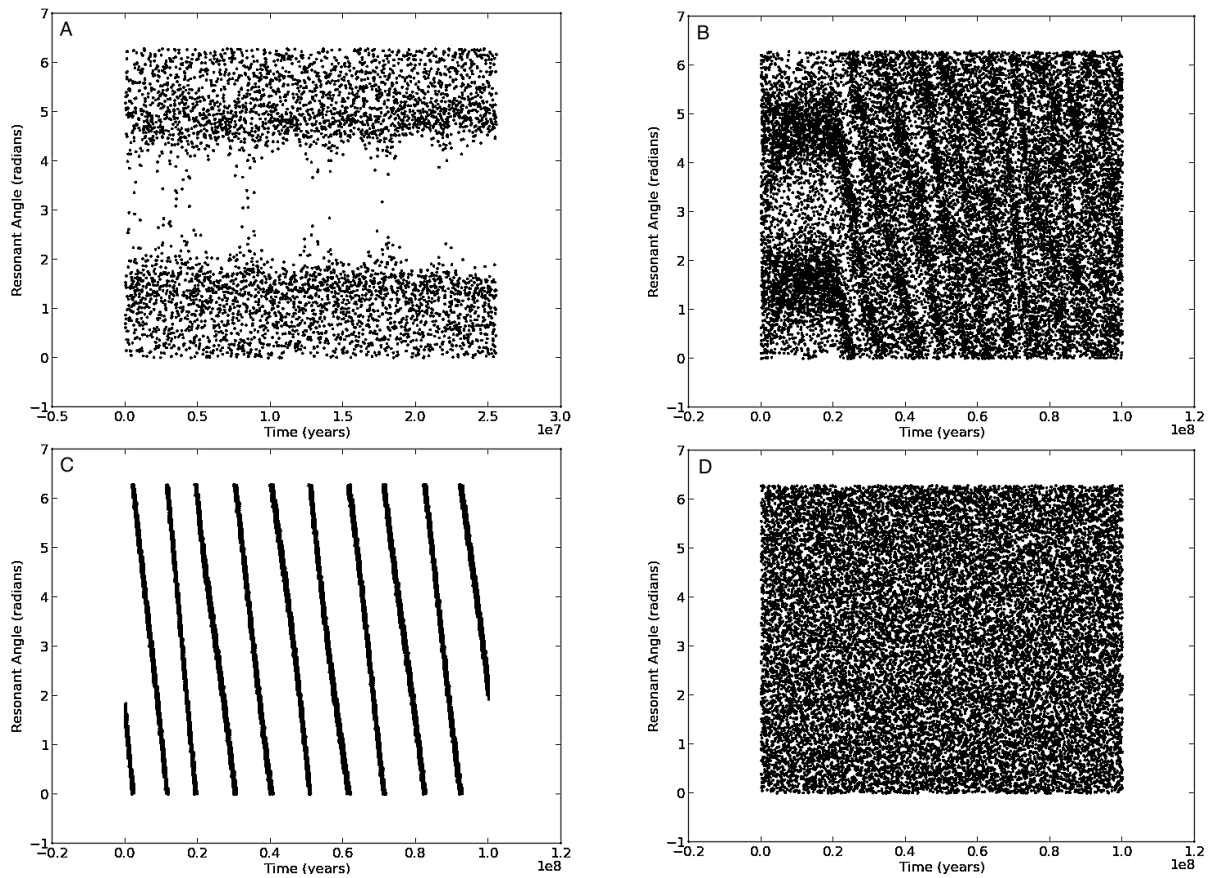


Figure 2.3: **A** shows clear libration between 2 resonant angles. These 2 terrestrial planets are locked in a 2:1 MMR for the duration of the simulation. **B**: depicts occasional libration where 2 rocky planets are going in and out of a 5:3 MMR. **C** shows slow circulation of a resonant angle for 2 inner planets. These objects are close to a 2:1 MMR. Finally, **D** is an example of a uniform distribution of resonant angles where the objects are not in a MMR.

formation?

To begin answering this question, we take the systems from [Kaib & Cowan \(2015\)](#) and integrate them for another 4.3 Gyr with MERCURY. In [Figure 2.4](#), we show the cumulative distributions of times at which these systems lose their last terrestrial planet mass body ($m > 0.055 M_{\oplus}$). These planets can be lost via collision with a larger planet, collision with the Sun, or ejection from the system ($r > 100$ au). We find that there are many systems that undergo substantial dynamical evolution after their first 200 Myr. As [Figure 2.4](#) shows, between 20 and 50% of systems lose at least 1 planet after $t = 200$ Myr. This fraction varies with the simulation batch. Systems in the cjs set are the most likely to lose planets at late times. This is likely due to the fact that these systems often form planets well beyond 2 au ([Raymond et al., 2009b](#)), where dynamical timescales are longer and planets require a longer time period to undergo ejections or final collisions compared to those at ~ 1 au. In eejs simulations, a smaller fraction of systems ($\sim 25\%$) lose a planet after their first 200 Myr of evolution. In these systems, the effects of an eccentric Jupiter and Saturn greatly deplete the mass orbiting beyond 1.5–2 au ([Raymond et al., 2009b](#)), and this absence of more distant material may explain the decrease in late instabilities. Finally, the conditions are even more extreme in the ann simulations, where the initial planetesimal region is truncated at 1 au. These simulations have the lowest rate of late ($t > 200$ Myr) instabilities at 18%.

It should also be noted that some systems lose planets at extremely late times. 8 out of 150 systems ($\sim 5\%$) lose planets after $t = 1$ Gyr. 5 of these systems are from cjs, while eejs and ann yield 1 and 2 systems, respectively. This small, yet non-negligible fraction of systems undergoing late instabilities may help explain the existence of transient hot dust around older main sequence stars ([Wyatt et al., 2007](#)). These very late instabilities in our systems occur even though the orbits of Jupiter and Saturn are effectively fixed for the entire integration. The rate of instabilities would likely be significantly higher if the orbits of the gas giants evolved substantially over time ([Brasser et al., 2009](#); [Agnor & Lin, 2012](#); [Brasser et al., 2013](#); [Kaib & Chambers, 2016](#)).

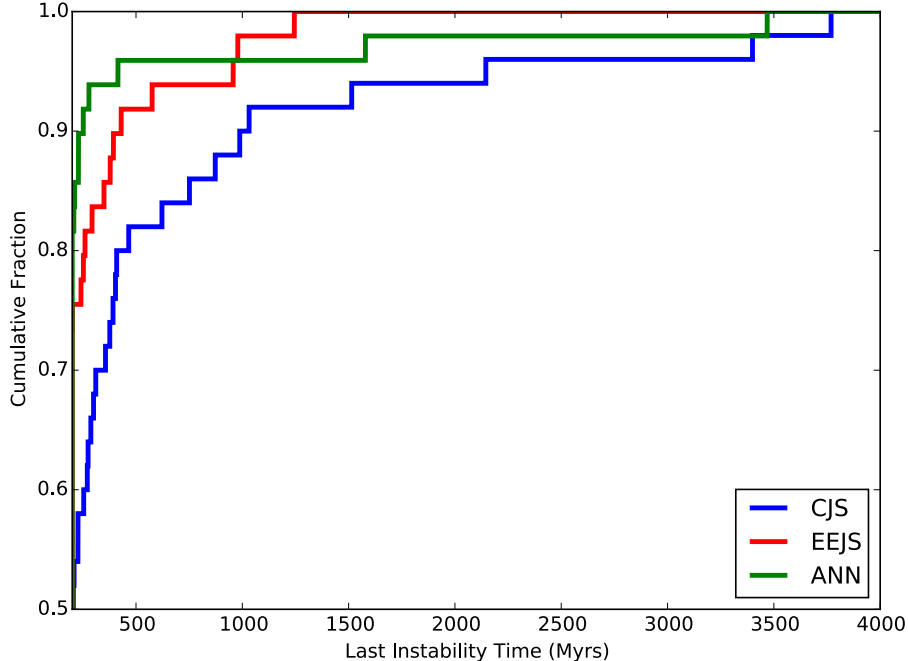


Figure 2.4: Cumulative distribution of the last times at which systems lose a planet more massive than $0.055 M_{\oplus}$ via collision or ejection. The distributions for cjs, eejs, and ann are shown with the blue, red, and green lines, respectively.

In Figure 2.5, we look at the mass distributions for the last planet lost from each system with an instability after $t = 200$ Myr. In general, we see that the last planets lost from systems with late instabilities have masses below $\sim 0.5 M_{\oplus}$. This is not surprising, since during an instability event it is typical for the smallest planets to be driven to the highest eccentricities, resulting in their collision or ejection (Rasio & Ford, 1996; Chatterjee et al., 2008; Jurić & Tremaine, 2008a; Raymond et al., 2009a). However, not all systems abide by this. In particular, 3 of the 13 eejs systems that undergo late instabilities lose planets with masses well over $1 M_{\oplus}$.

This suggests there may be a different instability mechanism in eejs systems. Indeed, when we look at *how* the last planets are lost from eejs systems, we find that 10 of the 13 systems with late instabilities lose their planets via collision with the Sun. This contrasts strongly with the cjs and ann systems, where there is only one instance of a planet-Sun collision among the 34 systems that have late instabilities. Moreover, there are 4 eejs systems

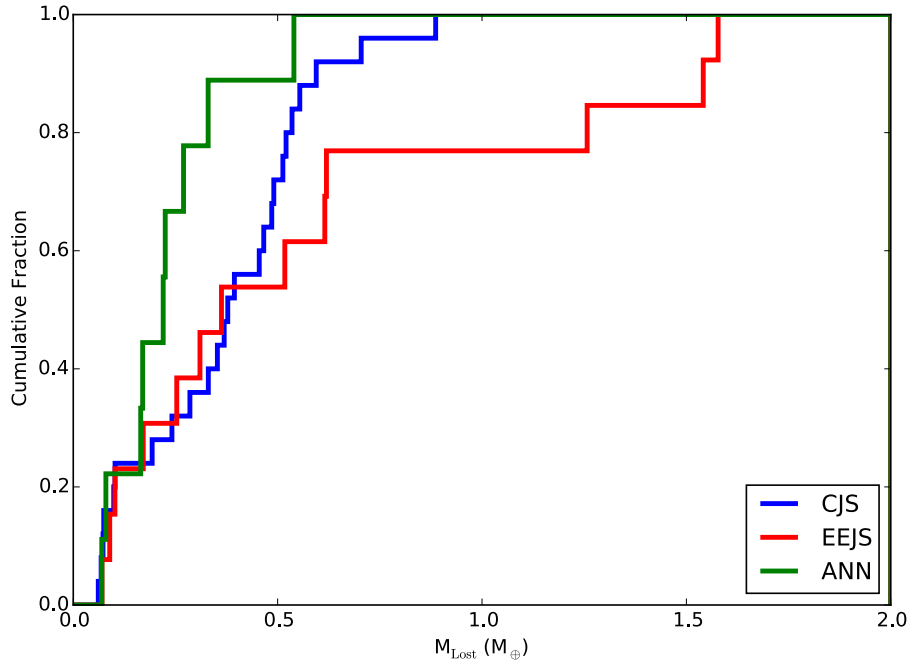


Figure 2.5: For systems that lose a planet after $t = 200$ Myr (more massive than $0.055 M_{\oplus}$), the distribution of masses for the last lost planet is shown. The distributions for cjs, eejs, and ann are shown with the blue, red, and green lines, respectively.

with only 1 planet at $t = 200$ Myr, which go on to have a planet-Sun collision before $t = 4.5$ Gyr. In these cases, the gas giants are clearly driving instabilities. This is not surprising, since the heightened eccentricities of Jupiter and Saturn will enhance the secular and resonant perturbations they impart on the terrestrial planets. When interactions between a gas giant and the terrestrial planets are the main driver of an instability, the relative masses of the terrestrial planets lose their significance because they are all so small relative to the gas giants. This allows for more massive planets to be lost from these systems.

Figure 2.6A shows an example of an instability within a cjs system. In this case, a system of 5 terrestrial planets are orbiting at virtually fixed semi-major axes for 3.8 Gyr when an instability develops between the inner 3 planets. The second and third planets collide and the resulting 4-planet system finishes the simulation with smaller orbital eccentricities than it began with. On the other hand, the evolution of an eejs system is shown in Figure 2.6B. Here we see the eccentricities of 3 relatively well separated planets driven up around 400–500 Myr,

leading to a collision between the second and third planets. After the collision, the outermost planet’s eccentricity is again quickly excited and eventually approaches 0.8. Shortly after this point, the planet collides with the Sun (after a scattering event with the inner planet). While the detailed dynamics of this system are undoubtedly complex, the behavior is clearly different from that of the cjs system, and is almost certainly a consequence of the enhanced gas giant perturbations produced from their increased eccentricities.

We also study how the properties of systems with late instabilities differ from systems that do not lose planet-mass bodies after $t = 200$ Myr. In [Figure 2.7](#) we look at the number of planets that each system has. In panels A–C, we see that after 200 Myr of evolution, cjs systems typically have 4–6 planet-mass bodies (an average of 4.68 planets per system). This is significantly higher than eejs and ann systems, which have an average of 2.45 and 3.00 planets per system, respectively. The differences can largely be attributed to the lack of distant planets in these systems, owing to their initial conditions. Panels A–C also show which systems go on to lose planets at later times. For cjs and ann simulations, these systems tend to have more planets than the overall distribution. In contrast, no such trend is seen among eejs systems. Regardless of planet number, the eejs systems all seem to have roughly the same probability of losing a planet at late times. This is again a symptom of the gas giants driving instabilities within these systems, unlike the cjs and ann systems, where interactions between terrestrial planets play a larger role in late instabilities. Finally, panels D–F show the distributions of planets per system after 4.5 Gyr of evolution. At the end of our integrations, the cjs, eejs, and ann systems have an average of 3.76, 2.12, and 2.78 planets per system respectively. For all of our simulation batches, we see that systems with late instabilities tend to have lower numbers of planets than the overall distribution of systems. Thus, in the case of cjs and ann systems, late instabilities tend to transform systems with relatively high numbers of planets into systems with relatively few planets. We also note that 4 eejs systems finish with no terrestrial planets whatsoever.

Finally, we show the AMD of each of our terrestrial planet systems at $t = 200$ Myr and

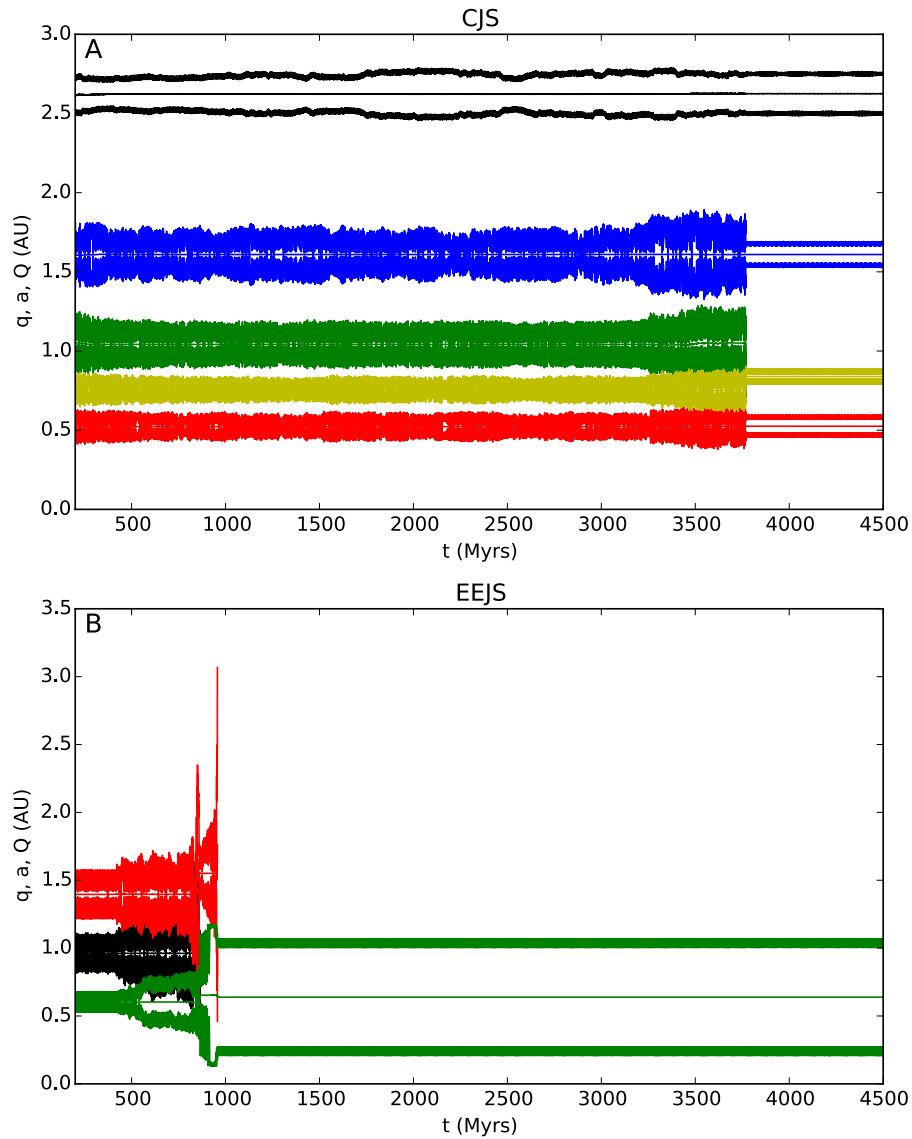


Figure 2.6: **A**: Time evolution of a 5-planet system from the cjs simulation batch. The pericenter, apocenter, and semi-major axis of each terrestrial planet is shown vs time. **B**: Time evolution of a 3-planet system from the eejs simulation batch. The pericenter, apocenter, and semi-major axis of each terrestrial planet is shown vs time.

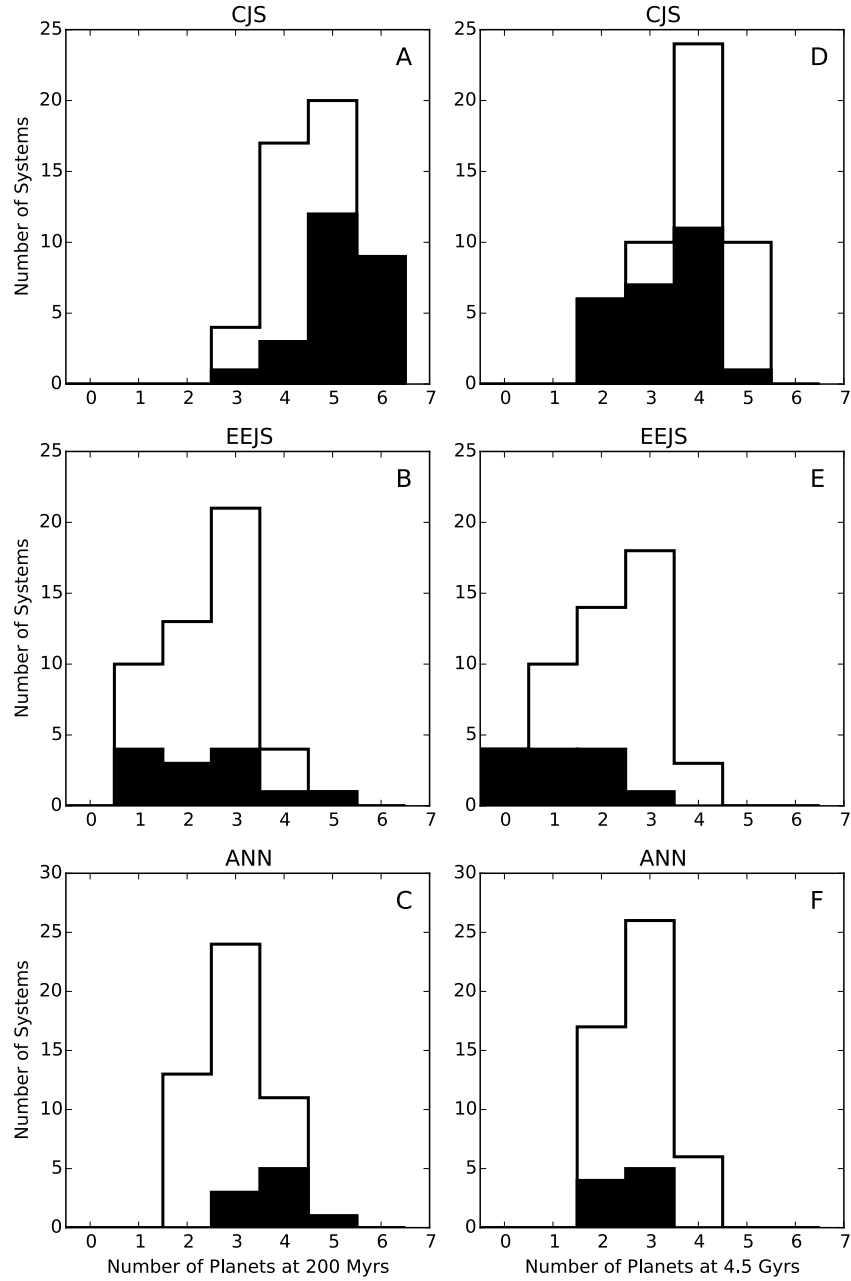


Figure 2.7: **A–C**: The distribution of the number of planets in each system at $t = 200$ Myr are shown for our cjs, eejs, and ann simulation batches in panels A, B, and C, respectively. The unfilled histograms show the distribution for all systems, and the filled histograms shown the distribution for systems that lose at least 1 planet more massive than $0.055 M_{\oplus}$ after $t = 200$ Myr. **D–F**: The distribution of the number of planets in each system at $t = 4.5$ Gyr are shown for our cjs, eejs, and ann simulation batches in panels D, E, and F, respectively. The unfilled histograms show the distribution for all systems, and the filled histograms shown the distribution for systems that lose at least 1 planet more massive than $0.055 M_{\oplus}$ after $t = 200$ Myr.

$t = 4.5$ Gyr in [Figure 2.8](#). Panels A–C show our systems’ AMD distribution at $t = 200$ Myr. For each of our simulation batches, the median AMD is greater than the solar system’s value. Our cjs, eejs and ann simulations have median AMD values of 2.9, 4.0, and 1.7 times the value of the modern inner solar system. Again, we also show the AMD distributions for systems that go on to have late instabilities. These systems tend to have larger AMD values. For the cjs, eejs and ann systems that undergo late instabilities the median AMD values at $t = 200$ Myr are 4.1, 14, and 4.3 times the solar system’s AMD, respectively. Interestingly, though, panels D–F demonstrate that these systems are not always destined to maintain a relatively large AMD. Systems in the cjs and ann batches that undergo late instabilities have median AMD values of 2.7 and 3.7 times the value of the solar system after 4.5 Gyr of evolution, respectively. Thus, a late instability does not necessarily increase the AMD of the system, and in some situations can result in moderate decreases. On the other hand, in eejs systems, the excited orbits of Jupiter and Saturn continue to wreak havoc on the terrestrial planets. Systems that experience late instabilities have a median AMD of 132 times that of the solar system!

2.3.2 Prevalence of Chaos

A selection of results from our simulations are provided in Appendix A ([Table A.1](#)). τ_L and MEGNO are listed for run 1 for all systems. Additionally, we provide our chaos determination (yes or no) for runs 1, a and b, as well as MMRs detected for run 1. [Figure 2.9](#) compares the fraction of all systems which are chaotic between runs 1, a and b. We find that removing Jupiter and Saturn has the greatest effect on reducing chaos in our systems. In general, $\sim 50\%$ of systems exhibit some form of chaos, when Saturn is removed only $\sim 40\%$ of systems are chaotic and when Jupiter is removed that number is only $\sim 20\%$. This indicates that the chaos in most of our systems is likely driven by perturbations from Jupiter. In fact, when Jupiter was removed, all systems but 1 had τ_L ’s which either increase, or are within 1.5 orders of magnitude of the original value.

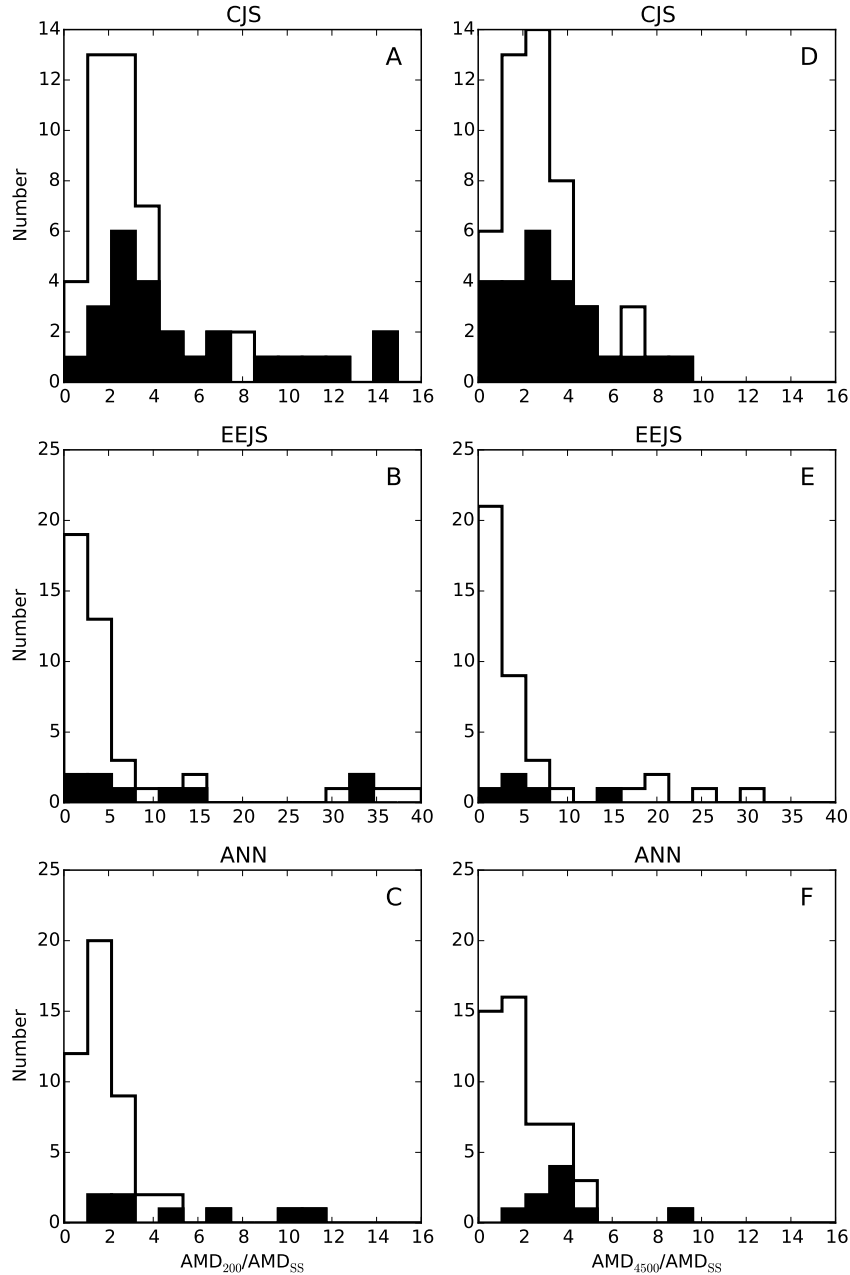


Figure 2.8: **A–C**: The distribution of terrestrial AMD values (normalized to the solar system’s modern terrestrial AMD) at $t = 200$ Myr are shown for our cjs, eejs, and ann simulation batches in panels A, B, and C, respectively. The unfilled histograms show the AMD values for all systems, and the filled histograms shown the AMD values for systems that lose at least 1 planet more massive than $0.055 M_{\oplus}$ after $t = 200$ Myr. **D–F**: The distribution of terrestrial AMD values (normalized to the solar system’s modern terrestrial AMD) at $t = 4.5$ Gyr are shown for our cjs, eejs, and ann simulation batches in panels A, B, and C, respectively. The unfilled histograms show the AMD values for all systems, and the filled histograms shown the AMD values for systems that lose at least 1 planet more massive than $0.055 M_{\oplus}$ after $t = 200$ Myr.

Figure 2.9 also clearly shows the disparity of chaos between systems with different numbers of terrestrial planets. This is most pronounced in 5-planet configurations, where only 2 such systems are free of chaos with the outer planets in place, and only 3 when they are removed. Having 4 terrestrial planets may not to be a significant source of chaos in our own solar system. This can be seen in Figure 2.10, which provides MEGNO plots for the solar system with and without the 4 outer planets. In fact, the solar system may better be described as a 3-planet configuration when compared to our results. Most 4 and 5-planet systems in our study differ greatly from our own since they typically contain only planets with masses comparable to Earth and Venus (see Table 2.3 for 2 such 5-planet examples). Mars analogues are rare in our systems, and Mercury sized planets are almost non-existent. If we consider our solar system a 3 terrestrial planet arrangement, it's inherent chaos fits in well with our results; where about half of systems show chaos with the giant planets in place, and only around 1 in 6 when they are removed. A shortcoming of this comparison is that many studies have shown that Mercury is a very important source of the chaos in our own solar system (Laskar, 2008; Laskar & Gastineau, 2009). However, when we integrate the solar system without Mercury, the system is still chaotic. Therefore, though the actual solar system does match our results, this comparison is limited by the fact that present models of the terrestrial planet formation systematically fail to produce Mercury analogs.

MMRs between planets are common features in many of our chaotic systems, implying that they are often important sources of the dynamical chaos. We detect 365 MMRs among all simulations in this phase of the project, 82% of which occur in chaotic systems. Further analysis shows that the MMRs which do occur in non-chaotic systems tend to be of higher order between smaller terrestrial planets. It should be noted that the vast majority of these MMRs are intermittent, and last only a fraction of the entire simulation duration.

Figure 2.11 shows the fraction of systems which are chaotic in runs 1, c, d and e. It is clear that an eccentric Jupiter and Saturn can quickly introduce chaos to an otherwise non-chaotic system. One interesting result from this batch of simulations is that when the eccentricities

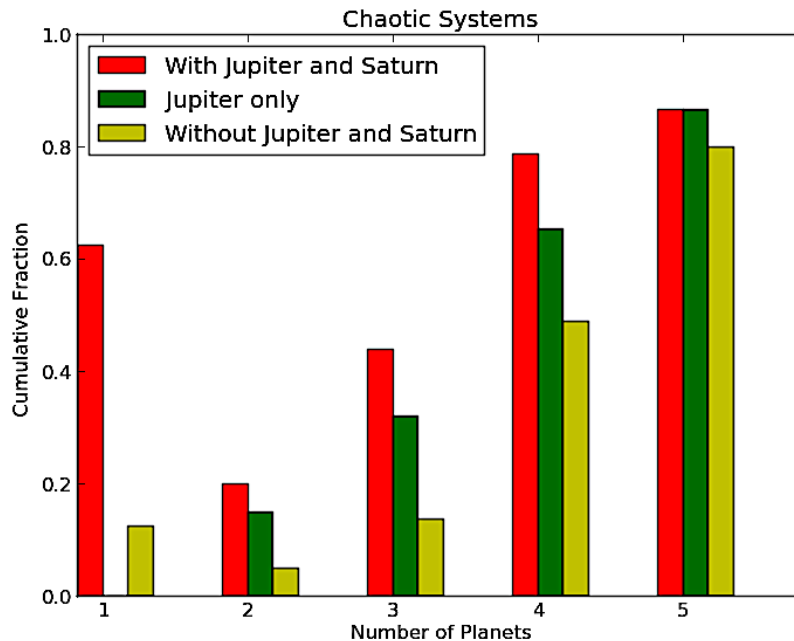


Figure 2.9: Comparison of the prevalence of chaos for runs 1, a and b.

system	0	1	2	3	4	5
ann	71%	12%	2%	12%	0%	4%
cjs	48%	18%	18%	14%	2%	0%

Table 2.2: The percentage of ann and cjs systems which lost a given number of planets when integrated with inflated giant planet eccentricities in run e for 1 Gyr.

of the outer planets are inflated, the likelihood of a 5:2 MMR between Jupiter and Saturn developing increases. In almost all systems, this resonant perturbation introduces chaos, and can possibly destabilize the system. Since systems labeled cjs were formed with the giant planets on near circular orbits, simply multiplying the already low eccentricity by 1.5 or 2 was not enough to produce a noticeable effect. For this reason, run e was performed using a step increase of 0.05. There is a clear parallel between the results of this scenario and a Nice Model instability (Gomes et al., 2005; Morbidelli et al., 2005; Tsiganis et al., 2005), where the outer planets rapidly transition from nearly circular to relatively eccentric orbits.

To further probe this effect, we repeat run e for cjs and ann systems using the MERCURY hybrid integrator in order to accurately detect collisions and ejections. Systems are

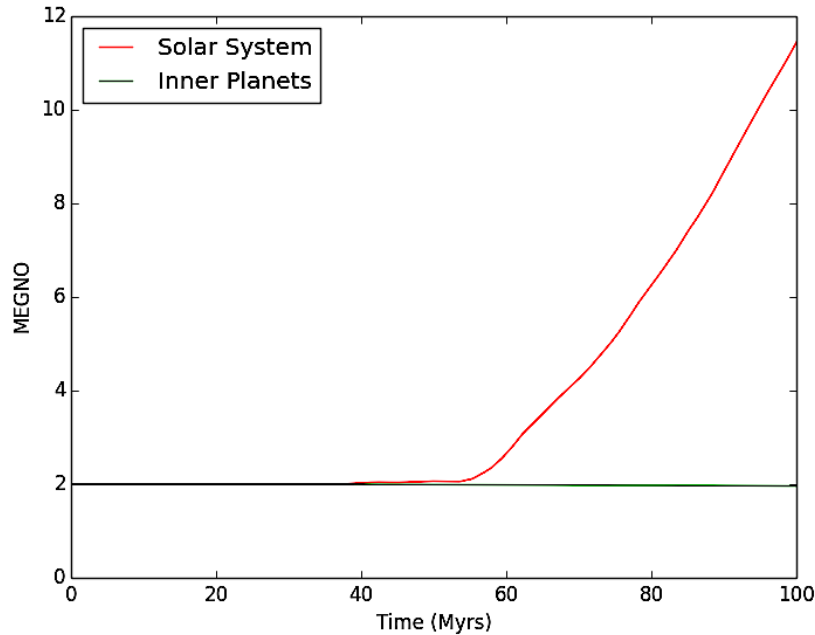


Figure 2.10: This figure compares the behavior of MEGNO in two separate simulations of our own solar system, run using the same settings described in § 2.2.3. With the giant planets in place (red line), the system is chaotic, and when they are removed (green line) the chaos disappears. Though Jupiter is the source of the chaos in our own solar system, when only Saturn, Uranus and Neptune are removed the system is non-chaotic because the precession of Jupiter’s orbit due to the outer planets stops. This result is different than the vast majority of the systems in this Chapter, which remain chaotic when only Saturn is removed.

integrated for 1 Gyr using simulation parameters similar to those discussed in § 2.2.1. We find instabilities are relatively common in these systems. 29% of ann systems and 52% of cjs systems lose one or more planets over the 1 Gyr integration. Table 2.2 shows the percentage of systems which lose a given number of terrestrial planets. In fact, the resulting systems are quite similar to those produced after integrating the eejs batch to the current epoch. A small fraction of systems lose all inner planets, and some can have instabilities occur very late in the simulations (Figure 2.12). Overall we show that an event similar to the Nice Model scenario, where the Giant planets eccentricities quickly inflate, can result in a non-negligible probability of inner planet loss.

If we again classify our solar system as a 3 terrestrial planet system, we can draw further

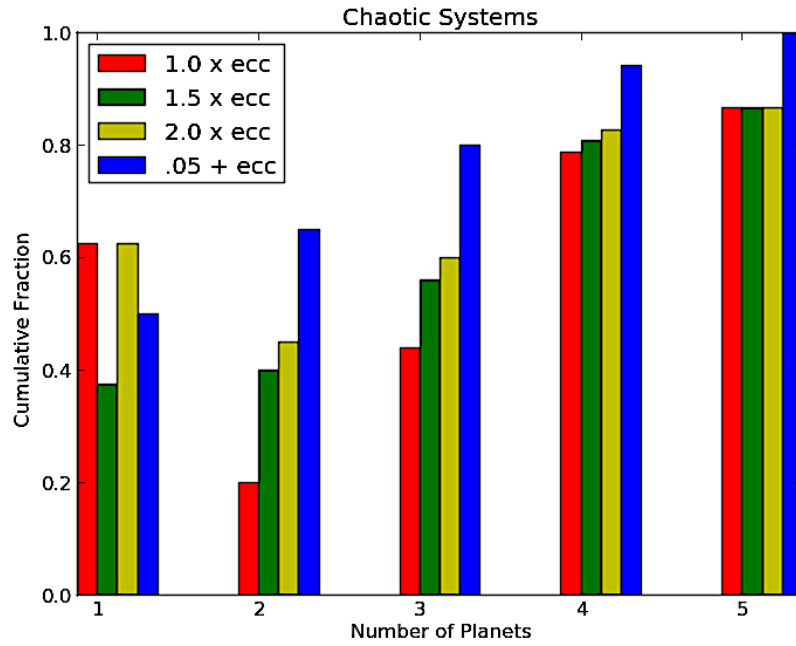


Figure 2.11: Comparison of the prevalence of chaos for runs 1, c, d and e.

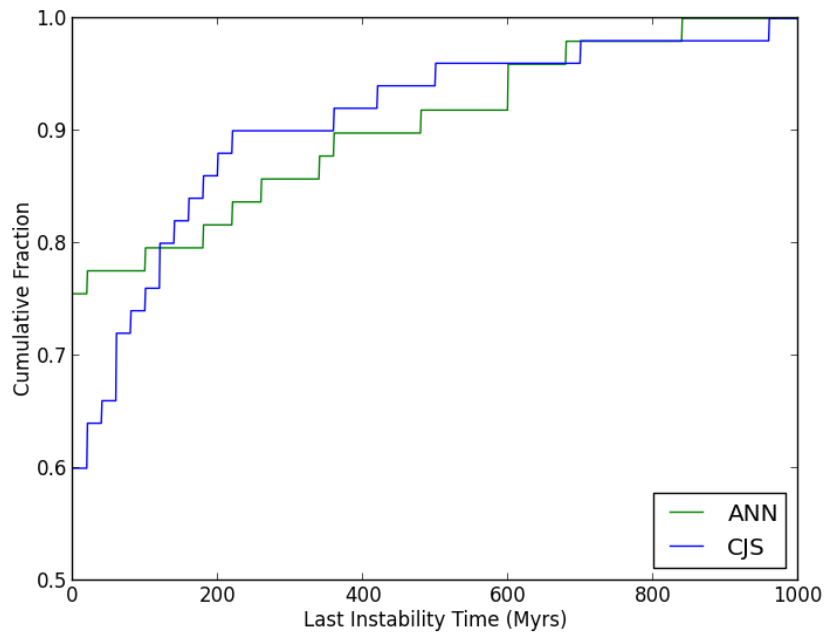


Figure 2.12: Cumulative distribution of the last times at which systems' with inflated eccentricities lose a planet more massive than $0.055 M_{\oplus}$ via collision or ejection. The distributions for cjs and ann are shown with the blue and green lines, respectively.

parallels between the results of such cjs run e configurations and the Nice Model instability, since Jupiter and Saturn begin on near circular orbits. In run e, 6 out of 8 such systems were chaotic, as compared to only 2 out of 8 in run 1. Indeed, we see that even a perturbation in the giant planet’s eccentricities of 0.05 is successful in rapidly making a system chaotic. In fact, when our own solar system is integrated with the outer planets on circular ($e < 0.001$, $i \sim 0$) orbits, the chaos disappears.

2.3.3 Angular Momentum Deficit and Last Loss Analysis

For our systems, we evaluate the difference between the average AMD of the inner planets over the first and last 3 Myr of our 100 Myr simulations. Taking the average removes the contributions from periodic forcing in the AMD from Jupiter and Saturn. We find a weak trend for chaotic 4 and 5 planet systems to have larger changes in AMD over the duration of the simulation than their non-chaotic counterparts. Of the 13 systems which had total changes in AMD greater than the actual solar system’s value, 9 were classified as chaotic. The largest outlier, a non-chaotic eejs 2 planet system (eejs25), is discussed further in § 2.3.5. We also search for any correlation between the time and mass of the last object ($m > 0.055 M_{\oplus}$) lost, and the chaos of a system. Though we show that some unstable, chaotic systems can stabilize after losing a planetary mass body, we are unable to identify any conclusive trends as to whether a late instability will shape the ultimate chaotic state of a system.

2.3.4 Mass Concentration Statistic and Center of Mass Analysis

To evaluate the degree to which mass is concentrated at a given distance away from the central star, we utilize a mass concentration statistic (S_c) (Chambers, 2001):

$$S_c = MAX \left(\frac{\sum_i m_i}{\sum_i m_i [\log_{10}(\frac{a}{a_i})]^2} \right) \quad (2.2)$$

The expression in parenthesis in (2.2) is essentially the level of mass concentration at

any point as a function of semi-major axis. [Chambers \(2001\)](#) utilizes a logarithm in the equation since, in our own solar system, the semi-major axes of the planets lie spaced in rough geometric series (the famous Titius-Bode law). S_c is the maximum value of the mass concentration function. A system where most of the mass is concentrated in a single, massive planet would have a very steep mass concentration curve, and a high value of S_c . A system of multiple planets with the same mass would have a smoother curve and yield a lower S_c . As a point of reference, the S_c value of the solar system’s 4 inner planets, where most of the mass is concentrated in Venus and Earth, is 90. S_c values are provided in the same format as AMD values in [Figure 2.13](#). A general, weak correlation can be seen between chaotic systems and slightly higher values of S_c , however this trend is not very conclusive. We also provide the center of mass for each system of terrestrial planets in [Figure 2.13](#). A clear trend is visible where non-chaotic systems tend to have a center of mass between ~ 0.8 – 1.2 au (the value being slightly greater as number of planets increases). In general, the more mass is concentrated closer to the central star, or closer to Jupiter, the greater the likelihood of chaos developing. This is likely related to Jupiter’s role in introducing chaos to systems. This trend is true for all three simulation subsets, but particularly strong in the cjs and eejs batches.

2.3.5 Systems of Particular Interest

eejs25

The system with the largest change in AMD over the duration of the simulation is surprisingly non-chaotic. This outlier (eejs25), is a system of just 2 inner planets. The innermost planet is $\sim 117\%$ the mass of Earth, residing at a semi-major axis of 0.62 au, and the second planet is $\sim 96\%$ the mass of Venus at a semi-major axis of 1.35 au. The innermost planet is locked in a strong, secularly driven resonance with Jupiter ([Figure 2.14](#)). This causes the eccentricity of the innermost planet to periodically oscillate between ~ 0.15 and ~ 0.7 over a period of ~ 8 Myr. These oscillations are remarkably stable. In fact, due to the fortuitous spacing

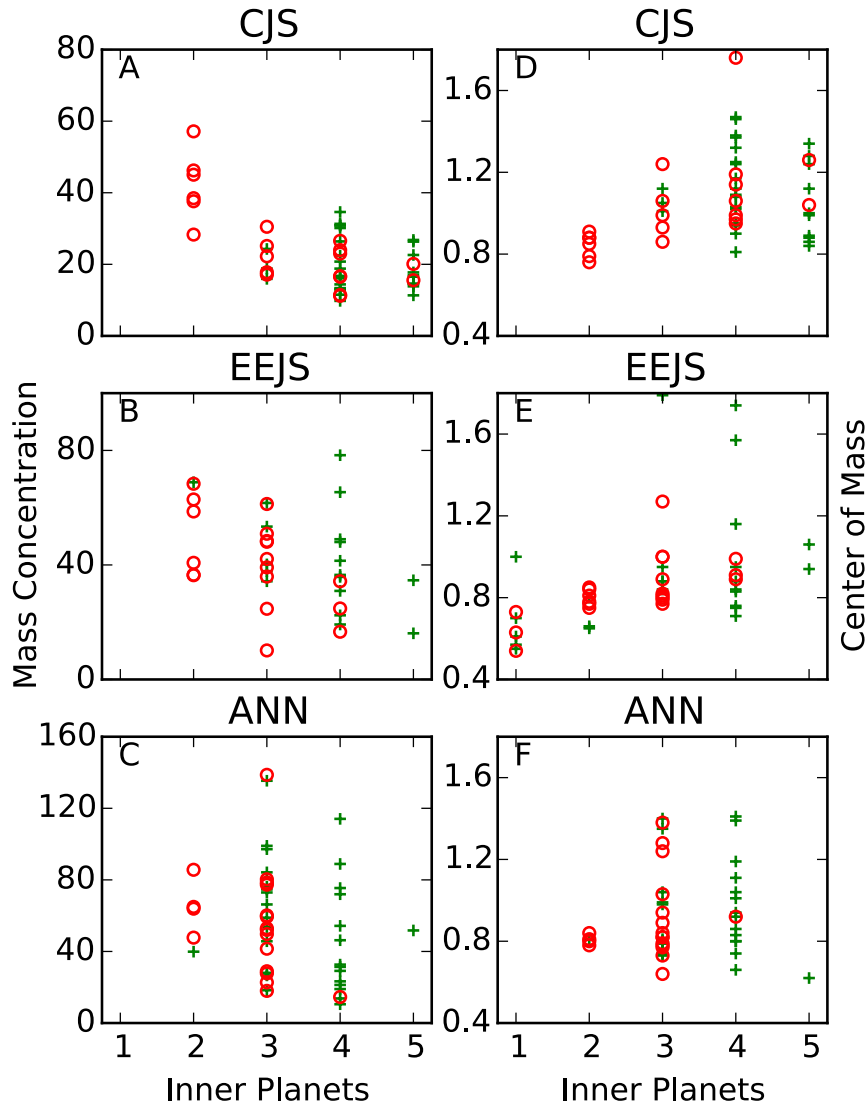


Figure 2.13: **A–C:** S_c 's affect on chaos for simulation batches cjs, eejs and ann (A, B and C respectively). S_c 's for 1-planet systems are infinite, and therefore omitted in these graphs. **D–F:** Relationship between center of mass and chaos in simulation batches cjs, eejs and ann (D, E and F respectively). Chaotic systems are designated by green plus signs and non-chaotic systems are represented by red circles.

body	cjs10 a (au)	cjs13 a (au)	sol a (au)	cjs10 m (M_{\oplus})	cjs13 m (M_{\oplus})	sol m (M_{\oplus})
1	0.51	0.54	0.39	0.61	0.68	0.055
2	0.76	0.78	0.72	0.63	0.18	0.82
3	1.1	1.1	1.0	1.0	0.77	1.0
4	1.9	1.6	1.5	0.46	0.59	0.11
5	2.5	2.7	2.8	0.32	0.80	0.00015

Table 2.3: Comparison of non-chaotic 5 terrestrial planet systems (cjs10 and cjs13) mass and semi-major axis distributions. The fifth body for the solar system is taken to be Ceres.

between of the Sun and inner 2 planets, this oscillation does not lead to interactions with other bodies in the system.

cjs10 and cjs13

The 2 most stable 5 planet configurations occurred in cjs10 and cjs13, with both systems classified as non-chaotic through runs 1, a and b. In the runs which vary eccentricity, cjs10 started to develop a weak 5:2 MMR between Jupiter and Saturn, causing mild chaos in run c (where eccentricities are increased by 150%). However, the chaos in this run was mild (MEGNO only rose to 3.703 and τ_L for this run was 1.57×10^9). A step increase of 0.05 to Jupiter and Saturn’s eccentricity in run e was required to fully introduce chaos (maximum MEGNO values 198.9 and 186.4 for cjs10 and cjs13 respectively) to both of these systems. This excitation of the eccentricities of the giant planets drove an occasional 3:1 MMR between the second and fourth inner planets in cjs13, possibly contributing to this chaos. The most remarkable similarity between these systems is their mass spacing and distribution (summarized in [Table 2.3](#)). Both have similarly low values of S_c (20.1 and 15.6). In fact, the planet spacing of both systems is somewhat reminiscent of a Titius-Bode Law series. For example, all orbital locations of cjs13 are within 6% of a Titius-Bode series beginning at the inner planet’s semi-major axis.

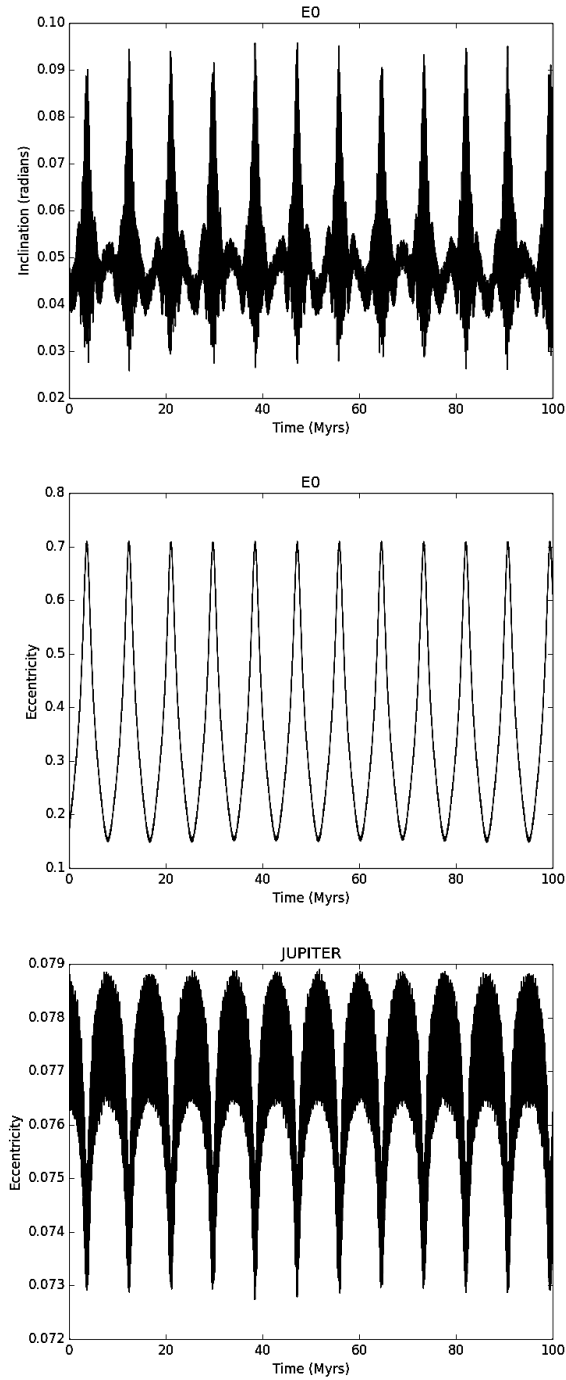


Figure 2.14: Comparison of eejs25’s innermost planet’s (E0) inclination and eccentricity with Jupiter’s eccentricity. The periods of oscillation match, indicating a strong secularly driven resonance. Interestingly, this interaction does not drive any chaos in the system.

2.4 Discussion and Conclusions

We have presented an analysis of systems of terrestrial planets formed through direct numerical integration of terrestrial accretion, fully evolved to the present epoch. Our work aims to assess whether our solar system, and its inherently chaotic dynamics, is a likely result of planetary formation as we currently understand it. We report that roughly half of our systems display some form of chaos. By far, the most common source of this dynamical chaos is perturbations from Jupiter. Additionally, we find that systems in our sample with greater numbers of terrestrial planets are far more prone to chaos than those with fewer inner planets. Unfortunately, systems formed through numerical integrations (including those of [Kaib & Cowan \(2015\)](#) which are used for this work) still routinely produce Mercury and Mars analogues which are far too massive ([Chambers, 2001](#); [O'Brien et al., 2006](#); [Chambers, 2007](#); [Raymond et al., 2009b](#)). Consequently, we find it best to consider our solar system a 3 terrestrial planet system for the purposes of comparison in this work. This classification of the solar system works well with our results that 3-planet systems have an $\sim 50\%$ chance of being chaotic, and a much lower probability when the giant planets are removed.

By varying the eccentricities of Jupiter and Saturn in 3 separate batches of simulations, we show that an eccentric system of outer planets can quickly introduce dynamical chaos and trigger instabilities in otherwise stable systems. This result confirms the findings in numerous previous works (e.g. [Gomes et al., 2005](#); [Morbidelli et al., 2005](#); [Tsiganis et al., 2005](#)). The inflation in eccentricity required to create such a chaotic system is surprisingly small. By varying the eccentricity of a batch of systems with Jupiter and Saturn on nearly circular orbits, we show that dynamical chaos quickly ensues. This sort of event is akin to a Nice Model-like instability ([Gomes et al., 2005](#); [Morbidelli et al., 2005](#); [Tsiganis et al., 2005](#)). We go on to show that in such an instability, the possibility of destabilizing the inner planets to the point where a terrestrial planet is lost by either collision or ejection is fairly high.

Additionally, we find that systems most immune to developing dynamical chaos tend to have centers of mass between ~ 0.8 – 1.2 au, though that range is by no means absolute. This

is an interesting result, and likely related to Jupiter’s role in driving chaos in many of these systems.

We consistently identified systems throughout our suite of simulations which displayed many of the same chaotic dynamics as our own solar system. It is clear that chaotic systems such as our own are common results of planetary formation. The largest source of chaos in our own system, perturbations from Jupiter, is the most common source of chaos observed in our work. The solar system, however, is akin to only a small fraction ($\sim 10\%$) of our simulations since removing just the planets beyond Jupiter turns our system non-chaotic. Additionally we show that late instabilities are common among these systems, and it is not far-fetched to imagine a late instability shaping dynamics within our own system. Finally, we find many systems with similar numbers of terrestrial planets, semi-major axis configurations, mass concentrations and chaos indicators (τ_L and MEGNO) as our own.

2.5 Acknowledgements

This Chapter is reproduced by permission of Elsevier and the American Astronomical Society’s Division of Planetary Sciences from the following publication: Clement, M. S. and Kaib, N.A. (May 2017). Prevalence of chaos in planetary systems formed through embryo accretion. In: *Icarus* 288: 88-98.

This work was supported by NSF award AST-1615975. Simulations in this paper made use of the REBOUND code which can be downloaded freely at <http://github.com/hannorein/rebound>. The bulk of our simulations were performed over a network managed with the HTCondor software package.

Chapter 3

Mars' Growth Stunted by an Early Giant Planet

Instability

This Chapter is reproduced from [Clement et al. \(2018\)](#), which appeared in the journal *Icarus*, with only minor typographical and formatting alterations. To improve the flow and readability of this thesis, the abstract and "Future Work" section have been removed.

3.1 Introduction

It is widely understood that the evolution of the solar system's giant planets play the most important role in shaping the dynamical system of bodies we observe today. When the outer planets interact with an exterior disk of bodies, Saturn, Uranus and Neptune tend to scatter objects inward ([Fernandez & Ip, 1984](#)). To conserve angular momentum through this process, the orbits of these planets move outward over time ([Hahn & Malhotra, 1999](#); [Gomes, 2003](#)). Thus, as the young solar system evolved, the three most distant planets' orbits moved out while Jupiter (which is more likely to eject small bodies from the system) moved in. To explain the excitation of Pluto's resonant orbit with Neptune, [Malhotra \(1993\)](#) proposed that Uranus and Neptune must have undergone significant orbital migration prior to arriving at their present semi-major axes. [Malhotra \(1995\)](#) later expanded upon this idea to explain the full resonant structure of the Kuiper belt. In the same manner, an orbital

instability in the outer solar system can successfully excite Kuiper belt eccentricities and inclinations, while simultaneously moving the giant planets to their present semi-major axes via planet-planet scattering followed by dynamical friction (Thommes et al., 1999).

These ideas culminated in the eventual hypothesis that, as the giant planets orbits diverged after their formation, Jupiter and Saturn’s orbits would have crossed a mutual 2:1 Mean Motion Resonance (MMR). Known as the Nice (as in Nice, France) Model (Tsiganis et al., 2005; Gomes et al., 2005; Morbidelli et al., 2005), this resonant configuration of the two most massive planets causes a solar system-wide instability, which has been shown to reproduce many peculiar dynamical traits of the solar system. This hypothesis has subsequently explained the overall structure of the Kuiper belt (Levison et al., 2008; Nesvorný, 2015a,b), the capture of trojan satellites by Jupiter (Morbidelli et al., 2005; Nesvorný et al., 2013), the orbital architecture of the asteroid belt (Roig & Nesvorný, 2015), and the giant planets’ irregular satellites, including Triton (Nesvorný et al., 2007).

The Nice Model itself has changed significantly since its introduction. In order to keep the orbits of the terrestrial planets dynamically cold (low eccentricities and inclinations), Brasser et al. (2009) proposed that Jupiter “jump” over its 2:1 MMR with Saturn, rather than migrate smoothly through it (Morbidelli et al., 2009, 2010). Otherwise, the terrestrial planets were routinely excited to the point where they were ejected or collided with one another in simulations. The probability of producing successful jumps in these simulations is greatly increased when an extra primordial ice giant was added to the model (Nesvorný, 2011; Batygin et al., 2012). In successful simulations, the ejection of an additional ice giant rapidly forces Jupiter and Saturn across the 2:1 MMR. Furthermore, hydrodynamical simulations (Snellgrove et al., 2001; Papaloizou & Nelson, 2003) show that a resonant chain of giant planets is likely to emerge from the dissipating gaseous circumstellar disk, with Jupiter and Saturn locked in an initial 3:2 MMR resonance (Masset & Snellgrove, 2001; Morbidelli & Crida, 2007; Pierens & Nelson, 2008). This configuration can produce the same results as the 2:1 MMR crossing model (Morbidelli et al., 2007). In this scenario, the instability ensues

when two giant planets fall out of their mutual resonant configuration. Such an evolutionary scheme seems consistent with the number of resonant giant exoplanets discovered (eg: HD 60532b, GJ 876b, HD 45364b, HD 27894, Kepler 223 and HR 8799; [Holman et al., 2010](#); [Fabrycky & Murray-Clay, 2010](#); [Rivera et al., 2010](#); [Delisle et al., 2015](#); [Mills et al., 2016](#); [Trifonov et al., 2017](#)).

Despite the fact that 5 and 6 primordial giant planet configurations are quite successful at reproducing the architecture of the outer solar system ([Nesvorný & Morbidelli, 2012](#)), delaying the instability ~ 400 Myr to coincide with the lunar cataclysm ([Gomes et al., 2005](#)) still proves problematic for the terrestrial planets. Indeed, [Kaib & Chambers \(2016\)](#) find only a $\sim 1\%$ chance that the terrestrial planets' orbits and the giant planets' orbits are reproduced simultaneously. Even in systems with an ideal “jump,” the eccentricity excitation of Jupiter and Saturn can bleed to the terrestrial planets via stochastic diffusion, leading to the over-excitation or ejection of one or more inner planets ([Agnor & Lin, 2012](#); [Brasser et al., 2013](#); [Roig & Nesvorný, 2015](#)). It should be noted, however, that Mercury's uniquely excited orbit (largest mean eccentricity and inclination of the planets) may be explained by a giant planet instability ([Roig et al., 2016](#)). Nevertheless, the chances of the entire solar system emerging from a late instability in a configuration roughly resembling its modern architecture are very low ([Kaib & Chambers, 2016](#)). This suggests that the instability is more likely to have not occurred in conjunction with the LHB, but rather before the terrestrial planets had fully formed. Fortunately, many of the dynamical constraints on the problem are fairly impartial to whether the instability happened early or late ([Morbidelli et al., 2018](#)). The Kuiper belt's orbital structure ([Levison et al., 2008](#); [Nesvorný, 2015a,b](#)), Jupiter's Trojans ([Morbidelli et al., 2005](#); [Nesvorný et al., 2013](#)), Ganymede and Callisto's different differentiation states ([Barr & Canup, 2010](#)) and the capture of irregular satellites in the outer solar system ([Nesvorný et al., 2007](#)) are still explained well regardless of the specific timing of the Nice Model instability. In addition to perhaps ensuring the survivability of the terrestrial system, there are several other compelling reasons to investigate an early

instability:

1. Uncertainties in Disk Properties: Since the introduction of the Nice Model, simplifying assumptions of the unknown properties of the primordial Kuiper belt have provided initial conditions for N-body simulations. The actual timing of the instability is highly sensitive to the particular disk structure selected (Gomes et al., 2005). Furthermore, numerical studies must approximate the complex disk structure with a small number of bodies in order to optimize the computational cost of simulations. In fact, most N-body simulations do not account for the affects of disk self gravity (Nesvorný & Morbidelli, 2012). When the giant planets are embedded in a disk of gravitationally self-interacting particles using a graphics processing unit (GPU) to perform calculations in parallel and accelerate simulations (Grimm & Stadel, 2014), instabilities typically occur far earlier than what is required for a late instability (Quarles & Kaib, 2019).

2. Highly Siderophile Elements (HSE): A late instability (the LHB) was originally favored because of the small mass accreted by the Moon relative to the Earth after the Moon-forming impact (for a review of these ideas see Morbidelli et al., 2012). The HSE record from lunar samples indicates that the Earth accreted almost 1200 times more material, despite the fact that its geometric cross-section is only about 20 times that of the Moon (Walker et al., 2004; Day et al., 2007; Walker, 2009). Thus, the flux of objects impacting the young Earth would have had a very top-heavy size distribution (Bottke et al., 2010, however Minton et al. (2015) showed that the pre-bombardment impactor size distribution may not be as steep as originally assumed). This distribution of impactors is greatly dissimilar from what is observed today, and favors the occurrence of a LHB. New results, however, indicate that the HSE disparity is actually a result of iron and sulfur segregation in the Moon’s primordial magma ocean causing HSEs to drag towards the core long after the moon-forming impact (Rubie et al., 2016). Because the crystallization of the lunar magma took far longer than on Earth, a large disparity between the HSE records is expected (Morbidelli et al., 2018).

3. Updated Impact Data: The LHB hypothesis gained significant momentum when

none of the lunar impactites returned by the Apollo missions were older than 3.9 Gyr (Tera et al., 1974; Zellner, 2017). However, recent $^{40}\text{Ar}/^{39}\text{Ar}$ age measurements of melt clasts in Lunar meteorites are inconsistent with the U/Pb dates determined in the 1970s (Fernandes et al., 2000; Chapman et al., 2007; Boehnke & Harrison, 2016). These new dates cover a broader range of lunar ages; and thus imply a smoother decline of the Moon’s cratering rate. Furthermore, new high-resolution images from the Lunar reconnaissance Orbiter (LRO) and the GRAIL spacecraft have significantly increased the number of old (>3.9 Gyr) crater basins used in crater counting (Spudis et al., 2011; Fassett et al., 2012). For example, samples returned by Apollo 17 that were originally assumed to be from the impactor that formed the Serenitatis basin are likely contaminated by ejecta from the Irbrium basin (Spudis et al., 2011). Because the Serenitatis basin is highly marred by young craters and ring structures, it is likely older than 4 Gyr, and the Apollo samples are merely remnants of the 3.9 Gyr Irbrium event.

Here we build upon the hypothesis of an early instability by systematically investigating the effects of the Nice Model occurring during the process of terrestrial planetary formation. Since advances in algorithms substantially decreased the computational cost of N-body integrators in the 1990s (Wisdom & Holman, 1991; Duncan et al., 1998; Chambers, 1999), many papers have been dedicated to modeling the late stages (giant impact phase) of terrestrial planetary formation. Observations of proto-stellar disks (Haisch et al., 2001; Pascucci et al., 2009) suggest that free gas disappears far quicker than the timescale radioactive dating indicates it took the terrestrial planets to form (Halliday, 2008; Kleine et al., 2009). Because the outer planets must clearly form first, the presence of Jupiter is supremely important when modeling the formation of the inner planets (Wetherill, 1996; Chambers & Cassen, 2002; Levison & Agnor, 2003a). Early N-body integrations of planet formation in the inner solar system in 3 dimensions from a disk of planetary embryos and a uniformly distributed sea of planetesimals reproduced the general orbital spacing of our 4 terrestrial planets (Chambers & Wetherill, 1998; Chambers, 2001). However, these efforts systematically failed to produce

an excited asteroid belt and 4 dynamically cold planets with the correct mass ratios (Mercury and Mars are $\sim 5\%$ and $\sim 10\%$ the mass of Earth respectively).

Numerous subsequent authors approached these problems using various methods and initial conditions. By accounting for the dynamical friction of small planetesimals, [O'Brien et al. \(2006\)](#) and [Raymond et al. \(2006\)](#) more consistently replicated the low eccentricities of the terrestrial planets. However, the so-called “Small Mars Problem” proved to be a systematic short-coming of N-body accretion models ([Wetherill, 1991](#); [Raymond et al., 2009b](#)). The vast majority of simulations produce Mars analogs roughly the same mass as Earth and Venus; a full order of magnitude too large ([Morishima et al., 2010](#)). However, Mars’ mass consistently stayed low when using a configuration of Jupiter and Saturn with present day mutual inclination and eccentricities twice their modern values ([Raymond et al., 2009b](#)). Because planet-disk interactions systematically damp the eccentricities of growing gas planets ([Papaloizou & Larwood, 2000](#); [Tanaka & Ward, 2004](#)), this result presented the problem of requiring a mechanism to adequately excite the orbits of the giant planets prior to terrestrial planetary formation. [Hansen \(2009\)](#) then demonstrated that a small Mars could be formed if the initial disk of planetesimals was confined to a narrow annulus between 0.7-1.0 au (interestingly, a narrow annulus might also explain the orbital distribution of silicate rich S-type asteroids [Raymond & Izidoro, 2017b](#)). The “Grand Tack” hypothesis provides an interesting mechanism to create these conditions whereby a still-forming Jupiter migrates inward and subsequently “tacks” backward once it falls into resonance with Saturn ([Walsh et al., 2011](#); [Brasser et al., 2016a](#)). When Jupiter “tacks” at the correct location, the disk of planetesimals in the still-forming inner solar system is truncated at 1.0 au, roughly replicating an annulus (for a critical review of the Grand Tack consult [Raymond & Morbidelli, 2014](#)).

Another potential solution to the small Mars problem is local depletion of the outer disk ([Izidoro et al., 2014, 2015](#)). However, systems in these studies that placed Jupiter and Saturn on more realistic initially circular orbits failed to produce a small Mars. Mars’ formation could have also been affected by a secular resonance with Jupiter sweeping across the inner

solar system as the gaseous disk depletes (Thommes et al., 2008; Bromley & Kenyon, 2017). The degree to which this process induces a dynamical shake-up of material in the vicinity of the forming Mars and asteroid belt is strongly tied to speed of the resonance sweeping. Furthermore, it is possible that Mars’ peculiar mass is simply the result of a low probability event. Indeed, there is a low, but non-negligible probability of forming a small Mars when using standard initial conditions and assuming no prior depletion of the disk (Fischer & Ciesla, 2014). However, on closer inspection, many of the “successful” systems in Fischer & Ciesla (2014) are poor solar system analogs for other reasons (such as an extra large planet in the asteroid belt, Jacobson & Walsh, 2015). Additionally, the large masses of Mars analogs produced in N-body integrations could be a consequence of the simplifications and assumptions made by such simulations. The process of how planetesimals form out of small, pebble to meter sized bodies is still an active field of research. Reevaluating the initial conditions used by N-body accretion models of the giant impact phase may potentially shed light on the origin of Mars’ small mass. Kenyon & Bromley (2006) considered this problem using a multi-annulus coagulation code to grow kilometer scale planetesimals. Subsequent authors (Levison et al., 2015b; Drazkowska et al., 2016; Raymond & Izidoro, 2017b) modeling the accretion of meter sized objects found that dust growth and drift cause solids in the inner disk to be redistributed in to a much steeper radial profile. Finally, multiple studies have demonstrated that more realistic, erosive collisions can significantly reduce the mass of embryos during the late stages of terrestrial planet accretion (Kokubo & Genda, 2010; Kobayashi & Dauphas, 2013; Chambers, 2013).

Here we investigate an alternative scenario wherein the still forming inner planets are subjected to a Nice Model instability. Though the effect of the Nice Model on the fully formed terrestrial planets is well studied (Brasser et al., 2009; Agnor & Lin, 2012; Brasser et al., 2013; Kaib & Chambers, 2016; Roig et al., 2016), no investigation to date has performed direct numerical simulations of the effect of the Nice Model instability on the still forming terrestrial planets. Furthermore, our work is motivated by simulations from Lykawka & Ito

(2013). The authors found that a low massed Mars could be formed when Jupiter and Saturn (with enhanced eccentricities) were artificially migrated across their mutual 2:1 MMR using fictitious forces. A downfall of this scenario, however, is that it overexcites the orbits of the forming terrestrial planets. Additionally, previous authors (Walsh & Morbidelli, 2011) have investigated whether smooth migration of Jupiter and Saturn (as opposed to the “jumping Jupiter” model) could produce a small Mars, however the speed of the process was found to be too slow with respect to Mars’ formation timescale (1-10 Myr; Dauphas & Pourmand, 2011). The work of Walsh & Morbidelli (2011) is perhaps the most similar to that of this paper. However, our work differs greatly in that we consider full instabilities directly, rather than modeling terrestrial evolution while migrating the giant planets with artificial forces. It should also be noted that we do not include the “Grand Tack” hypothesis in our study (in § 3.4 we argue that it is potentially compatible with the scenario we investigate).

3.2 Methods

Because the parameter space of possible giant planet configurations (number of planets, resonant configuration, planet spacing, disk mass and disk spacing) emerging from the primordial gas disk is substantial, as a starting point for this work we take two of the most successful five and six giant planet configurations from Nesvorný & Morbidelli (2012)¹. Both begin with Jupiter and Saturn in their 3:2 MMR. Though placing Jupiter and Saturn in an initial 2:1 configuration on circular orbits can be highly successful at replicating the correct planetary spacing of the outer solar system, only $\sim 0.2\%$ such simulations sufficiently excite Jupiter’s eccentricity (Nesvorný & Morbidelli, 2012). For this reason we focus on the scenario where Jupiter and Saturn emerge from the gas disk locked in a 3:2 MMR. Furthermore, Nesvorný & Morbidelli (2012) found advantages and disadvantages which are mutually exclusive to

¹It should be noted that, with the additional constraint of requiring that Neptune migrate to ~ 28 au prior to the onset of the instability, a 3:2,3:2,2:1,3:2 resonant configuration for 5 planet scenarios is more effective (Deienno et al., 2017). Because we are mostly interested in studying the excitation of the inner solar system, which is largely unaffected by the particular migration of Neptune, our results should be relatively independent of the particular ice giant resonant configuration selected.

Name	N_{Pln}	M_{disk} (M_{\oplus})	δr (au)	r_{out} (au)	a_{nep} (au)	Resonance Chain	M_{ice} (M_{\oplus})
5GP	5	35	1.5	30	17.4	3:2,3:2,3:2,3:2	16,16,16
6GP	6	20	1.0	30	20.6	3:2,4:3,3:2,3:2,3:2	8,8,16,16

Table 3.1: Giant Planet Initial Conditions: The columns are: (1) the name of the simulation set, (2) the number of giant planets, (3) the mass of the planetesimal disk exterior to the giant planets, (4) the distance between the outermost ice giant and the planetesimal disks inner edge, (5) the semi-major axis of the outermost ice giant (commonly referred to as Neptune, however not necessarily the planet which completes the simulation at Neptune’s present orbit), (6) the resonant configuration of the giant planets starting with the Jupiter/Saturn resonance, and (7) the masses of the ice giants from inside to outside.

both the five and six planet cases. Thus, for completeness we select one five and one six planet setup for our study. We summarize our chosen sets of giant planet initial conditions in [Table 3.1](#).

To create a mutual resonant chain of gas giants, we apply an external force to the giant planets which mimics the effects of a gas disk by modifying the equations of motion with forced migration (\dot{a}) and eccentricity damping (\dot{e}) terms ([Lee & Peale, 2002](#)). Though the precise underlying physics of the interaction between forming giant planets and a gas disk is not fully understood, this method is employed by many authors studying both the solar system, and observed resonant exoplanets because it consistently produces stable resonant chains ([Matsumura et al., 2010](#); [Beaugé & Nesvorný, 2012](#)). The exact functional forms of \dot{a} and \dot{e} depend on the timescale and overall distance of migration desired. We utilize a form of $\dot{a} = ka$ and $\dot{e} = ke/100$ ([Batygin & Brown, 2010a](#)), where the constant k is adjusted to achieve a migration timescale $\tau_{mig} \sim .1-1$ Myr. Because the actual migration rate is a complex function of the properties of the gas disk and relative masses of the planets, achieving a specific migration timescale is of less importance than placing the resonant planets on the proper orbits ([Kley & Nelson, 2012](#); [Baruteau et al., 2014](#))

We first evolve the gas giants (without terrestrial planets or a exterior disk of planetesimals) using the Mercury6 Bulirsch-Stoer integrator (as opposed to the faster hybrid integrator) with a 6.0 day time-step ([Chambers, 1999](#); [Stoer et al., 2002](#)). The Bulirish-Stoer

method is necessary when building resonant configurations because the force on a particle is a function of both the positions and momenta (Chambers, 1999; Batygin & Brown, 2010b). The planets are initially placed on orbits just outside their respective resonances, and then integrated until the outermost planet’s semi-major axis is at the appropriate location (Table 3.1). Figure 3.1 shows an example of this evolution for a simulation in the 5GP batch. To verify that the planets are in a MMR, libration about a series of resonant angles is checked for using the method described in Clement & Kaib (2017).

After the resonant chain is assembled, we add a disk of 1000 equal massed planetesimals (our primordial KBOs) using the inner and outer radii that Nesvorný & Morbidelli (2012) showed best meet dynamical constraints for the outer solar system (Table 3.1). The orbital distribution of the planetesimals is chosen in a manner consistent with previous authors (Batygin & Brown, 2010b; Nesvorný & Morbidelli, 2012; Kaib & Chambers, 2016), and follows an r^{-1} surface density profile. Angular orbital elements (arguments of pericenter, longitudes of ascending node and mean anomalies) for the planetesimals are selected randomly. Eccentricities and inclinations are drawn from near circular and co-planar Gaussian distributions (standard deviations: $\sigma_e = .002$ and $\sigma_i = .2^\circ$). These same distributions are utilized throughout our study to maintain all initial eccentricities less than 0.01, and inclinations within 1° . These systems are integrated using the Mercury6 hybrid integrator (Chambers, 1999) with a 20.0 day time-step up until the point when two giant planets first pass within 3 mutual Hill Radii. Because we wish to investigate specific instability times with respect to terrestrial planetary formation, and our resonant configurations can often last for tens of millions of years prior to experiencing an instability, we integrate these systems up until the onset of the instability with an empty inner solar system. Only after this point are the terrestrial planetary formation disks at various stages of evolution embedded in these systems. The method allows us to save computational time, and control at exactly what point the instability occurs during the giant impact phase. Though the giant planets are already on significantly eccentric orbits at this point (and therefore affecting the terrestrial

disk), we find that systems can last for millions of years before experiencing an instability if the simulation is stopped sooner. Moreover, the terrestrial planets are far more sensitive to the evolution of Jupiter and Saturn than that of the ice giants. We find that, in the vast majority of simulations, Jupiter and Saturn don't begin evolving substantially until after this first close encounter time. In the vast majority of our simulations, the instability ensues within several thousand years of the first close-encounter time. This is consistent with simulations of planet-planet scattering designed to reproduce giant exoplanet systems (Chatterjee et al., 2008; Jurić & Tremaine, 2008b; Raymond et al., 2010).

Because we want to embed terrestrial planetary disks at different stages of development into a giant planet instability, we begin by modeling terrestrial disk evolution in the presence of a static Jupiter and Saturn in a 3:2 MMR. We form 100 systems of terrestrial planets using the Mercury6 hybrid integrator (Chambers, 1999) and a 6.0 day time-step. Because of the integrator's inability to accurately handle low pericenter passages, objects are considered to be merged with the Sun at 0.1 au (Chambers, 1999, 2001). We choose the simplest initial orbital distributions for objects in the terrestrial forming disk in order to mirror previous studies which assumed no prior disk depletion (Chambers, 2001, 2007). Half of the disk mass is in 100 equal massed embryos, with the remainder in 1000 equal massed planetesimals. The spacing of the embryos and planetesimals is selected to achieve a surface density profile that falls off radially as $r^{-3/2}$ (Wetherill, 1996). Angular orbital elements are selected randomly, and eccentricities and inclinations are drawn from near circular, co-planar Gaussian distributions ($\sigma_e = .002$ and $\sigma_i = .2^\circ$). The initial disk mass in simulations numbered 0-49 is set to $5 M_\oplus$. Runs numbered 50-99 begin with $3 M_\oplus$ of material. Additionally, half of the simulations begin with the inner disk edge at 0.5 au (numbers 0-24 and 50-74) as opposed to 0.7 au. This gives us 25 simulations with each mass/edge permutation. Additionally, the embryo spacing varies between ~ 5 -12 mutual hill radii (depending on the simulation initial conditions and disk locations), and is consistent with simulations of oligarchic growth of embryos (Kokubo & Ida, 1998). Furthermore, terrestrial planet formation is a highly chaotic

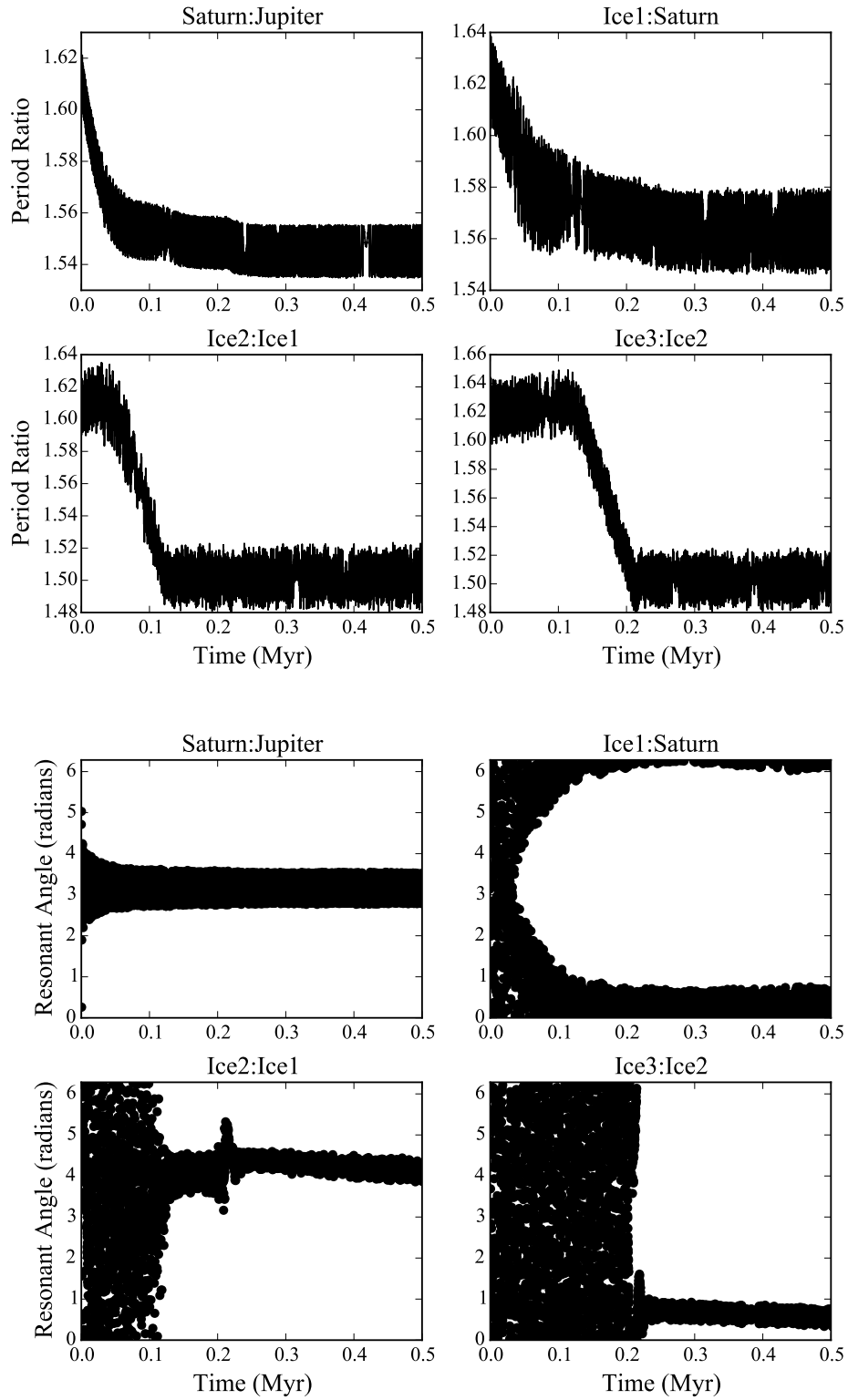


Figure 3.1: An example of the resonant evolution of a system of outer planets in the 5GP batch. With the forcing function mimicking interactions with the gaseous disk in place, once a set of planets falls in to a MMR, they remain locked in resonance for the remainder of the evolution.

Run Number	Disk Mass (M_{\oplus})	Disk Inner edge (au)
0-24	5.0	0.5
25-49	5.0	0.7
50-74	3.0	0.5
75-99	3.0	0.7

Table 3.2: Summary of initial conditions for terrestrial planetary formation simulations.

process in which the stochasticity of the actual process dominates over the effects of small changes to initial conditions such as embryo masses and spacing (Hoffmann et al., 2017). For a summary of these initial conditions, see Table 3.2. In all simulations the outer disk edge is set at 4.0 au. Furthermore, we place Jupiter and Saturn in a 3:2 MMR at roughly the same orbital locations as in the 5GP and 6GP configurations (ice giants are not included for this portion of the simulation). As in previous studies, we evolve each system for 200 Myr (Raymond et al., 2009b; Kaib & Cowan, 2015), outputting a snapshot of each system at 10^4 , 10^5 , 10^6 and 10^7 years (these times roughly correspond to the time elapsed following gas disk dispersal, which we loosely correlate with the onset of the giant impact phase). These snapshots are then input into the giant planet configurations 5GP and 6GP described above (therefore each output is used twice, Table 3.1), and integrated through the giant planet instability for an additional 200 Myr using the same integrator package and time-step.

This gives us 800 different instability simulations. We refer to the two different giant planet configurations (5GP and 6GP; each containing 400 individual systems) as the simulation “set.” We then denote each subset of 100 integrations with a unique instability delay time (10^4 , 10^5 , 10^6 and 10^7 years) as “batches.” And finally each unique simulation within a batch (100 each) is referred to as a “run.” The completed terrestrial formation simulations (with a static Jupiter and Saturn in their pre-instability 3:2 MMR) become our control batch (100 runs). Thus the control batch represents a sample of terrestrial formation outcomes in a late Nice Model scenario, where the giant planets remain locked in their mutual resonant configuration until the instability occurs ~ 400 Myr after the planets finish forming.

3.2.1 Instability Timing

We relate time zero in our simulations (the beginning of our control runs) with the epoch of gas dispersal, which loosely correlates with the beginning of the giant impact phase. However, the exact dynamical state of the terrestrial disk (for our purposes, the relative abundance of larger planet embryos within the planetesimal sea) at the time of gas disk dispersal is not exactly known. For this reason, the specific instability times we test, and draw conclusions about, are of less importance than the particular dynamical state of the disk. In the subsequent sections of this text, we compare broad characteristics of our early (0.01 and 0.1 Myr) and late (1 and 10 Myr) instability delay times. Though we can confidently make a general connection between these specific instability times and the time elapsed following gas dispersal in the solar system, relating the dynamical state of the terrestrial disk with the timing of the instability is the more important conclusion of our work. As we expand upon in the subsequent sections, the later two instability delays we test tend to be more successful than the earlier ones. Therefore our work correlates the giant planet instability timing with a terrestrial disk at a state of evolution that is mostly depleted of small planetesimals, with most of the mass concentrated in a handful of growing planet embryos. Subsequently overlaying this timeline on that of Mars' growth inferred from isotopic dating ([Dauphas & Pourmand, 2011](#)) is difficult because the relationship between gas disk dispersal and CAI (Calcium-Aluminum-rich inclusion) formation is not well known.

Furthermore, [Marty et al. \(2017\)](#) presented evidence that cometary bombardment accounted for $\sim 22\%$ of the noble gas concentration in Earth's atmosphere. At first glance, this constraint appears to be slightly at odds with the various delay times we examine in this Chapter (0.01-10 Myr). We choose to discuss this here in detail because it can potentially be construed to undermine the merit of our study. Because the noble gas makeup of the mantle is so different from that of the atmosphere, and that of comet 67P, this seems to imply that the onslaught of comets (the timing of which would correlate with the giant planet instability) occurred after the moon forming impact. Because the moon forming impact occurred

after Mars had completed forming (Kleine et al., 2009; Dauphas & Pourmand, 2011), the giant planet instability could not be the mass-depleting event in the Mars forming region. However this argument does not take in to account the timing of impacts with respect to the Earth’s magma ocean phase. It is reasonable to assume that some cometary delivery must have occurred prior to core closure. If fractionalization of Xenon occurred during the magma ocean phase, the preserved signature in the mantle could very well be different from that in the atmosphere. Because neither the distribution of impact times of primordial Kuiper belt objects (KBOs), nor the fractionalization of Xenon in the magma ocean are well known, drawing a broad conclusion of the timing of the instability from this constraint is difficult. Additionally, delivery itself may have been stochastic; in that an early instability might set the Xenon content of the mantle by delivering many small comets, and then a later impact of a large comet could boost the Xenon fraction in the atmosphere. Finally, Xenon isotope trends are not well known over a large enough sample of comets. It is reasonable to expect that comet 67P’s specific Xenon concentration would fall somewhere on a continuum when compared to other similar comets. A larger sample of such measurements must be made before these conclusions can be applied to the giant planet instability timeline. Therefore, as a starting point for our study, we argue that the most important constraint for instability timing is the survivability of the terrestrial planets, which no scenario to date can ensure.

3.3 Success Criteria

When analyzing the results of our simulations, the parameter space for comparison to the actual solar system is extensive. Furthermore, for many metrics our accuracy is strongly limited by the resolution of our simulations. For example, the planetary embryos used in the majority of our simulations begin the integration with a fourth of Mars’ present mass. Therefore, a “successful” Mars analog could be formed from as few as 2-3 impacts. For these reasons our criteria must be broad, because we are more interested in looking at statistical

Code	Criterion	Actual Value	Accepted Value	Justification
A	a_{Mars}	1.52 au	1.3-2.0 au	Inside AB
A,A1	M_{Mars}	$0.107 M_{\oplus}$	$> 0.025, < .3M_{\oplus}$	(Raymond et al., 2009b)
A,A1	M_{Venus}	$0.815 M_{\oplus}$	$> 0.6 M_{\oplus}$	Within $\sim 25\%$
A,A1	M_{Earth}	$1.0 M_{\oplus}$	$> 0.6 M_{\oplus}$	Match Venus
B	τ_{Mars}	1-10 Myr	< 10 Myr	
C	τ_{\oplus}	50-150 Myr	> 50 Myr	
D	M_{AB}	$\sim 0.0004 M_{\oplus}$	No embryos	(Chambers, 2001)
E	ν_6	~ 0.09	< 1.0	
F	WMF_{\oplus}	$\sim 10^{-3}$	$> 10^{-4}$	Order of magnitude
G	AMD	0.0018	< 0.0036	(Raymond et al., 2009b)
H	N_{GP}	4	4	(Nesvorný & Morbidelli, 2012)
I	a_{GP}	5.2/9.6/19/30au	20%	(Nesvorný & Morbidelli, 2012)
I	\bar{e}_{GP}	0.046/0.054/0.044/0.01	$< .11$	(Nesvorný & Morbidelli, 2012)
I	\bar{i}_{GP}	0.37/0.90/1.02/.67°	$< 2^{\circ}$	(Nesvorný & Morbidelli, 2012)
J	P_{Sat}/P_{Jup}	2.49	< 2.8	(Nesvorný & Morbidelli, 2012)

Table 3.3: Summary of success criteria for the solar system. The columns are: (1) the semi-major axis of Mars, (2-4) The masses of Mars, Venus and Earth, (5-6) the time for Mars and Earth to accrete 90% of their mass, (7) the final mass of the asteroid belt, (8) the ratio of asteroids above to below the ν_6 secular resonance between 2.05-2.8 au, (8) the water mass fraction of Earth, (9) the angular momentum deficit (AMD) of the inner solar system, (10) the final number of giant planets, (11-13) the semi-major axes, time-averaged eccentricities and inclination of the giant planets, (14) the orbital period ratio of Jupiter and Saturn. A complete discussion of the success criteria, background information and justifications is provided in the Supplementary Information.

consistencies and order of magnitude agreements than perfectly replicating every nuance of the actual solar system. Thus, we focus on 10 broad criteria for replication of both the inner and outer solar systems, which we summarize in [Table 3.3](#).

3.3.1 The Inner Solar System

Because our goal is to look for systems like our own, with particular emphasis on forming Mars analogs, we employ an analysis metric similar to [Chambers \(2001\)](#). A system is considered to meet criterion A if it forms a Mars sized body in the vicinity of Mars' semi-major axis, exterior to two Earth sized bodies. We first check for any planets formed in the region of 1.3-2.0 au, where the inner edge of this region is roughly equal to Mars' current pericenter (~ 1.38 au) and the outer limit lies at the inner edge of the asteroid belt. If this planet has a

mass less than $0.3 M_{\oplus}$, is immediately exterior to two planets each with masses greater than $0.6 M_{\oplus}$, and the system contains no planets greater than $0.3 M_{\oplus}$ in the asteroid belt, criterion A is satisfied. A separate success criteria (criterion D, § 3.3.3) filters out systems that finish with an embryo in the Asteroid Belt as unsuccessful. While some authors (Hansen, 2009) select $0.2 M_{\oplus}$ as the upper mass limit for Mars analogs, due to the previously discussed resolution limitation encountered when using $0.025 M_{\oplus}$ embryos, we follow the prescription in Raymond et al. (2009b) and use $0.3 M_{\oplus}$ as our limit. Additionally, because our simulations do not take collisional fragmentation in to account (for further discussion of this phenomenon, see § 3.4.6), it is possible that the masses of our Mars analogs are somewhat over-estimated. Because we set the Venus/Earth minimum mass to $0.6 M_{\oplus}$ (approximately 75% that of Venus’ present mass), this provides an adequate mass disparity of a factor of 2 between the Venus/Earth and Mars analogs. We also look at systems which form three planets of the correct mass (criterion A1), but do not have the correct semi major axes (eg: Mars formed at a semi-major axis greater than 2.0 au). For this criterion, we include systems which form no Mars, but do accrete appropriately sized Earth and Venus analogs in the correct locations as being successful.

3.3.2 The Formation Timescales of Earth and Mars

Mars is often thought to have been left behind as a “stranded embryo” (Morbidelli et al., 2000) during the process of planetary formation because the timescale for its accretion inferred from Hf/W dating (.1-10 Myr) is so quick (Nimmo & Agnor, 2006; Dauphas & Pourmand, 2011). Contrarily, Earth is believed to have formed much slower; of order 50-150 Myr (Touboul et al., 2007; Kleine et al., 2009). There is a significant amount of uncertainty in both of these timescales. The specific timing of the moon forming impact, which is thought to correlate with the last major accretion event on Earth, is still not well known. Unfortunately, these metrics are quite difficult to meet when using standard embryo accretion numerical models. In fact, planets with semi-major axes greater than 1.3 au in our control

simulation (which assume no gas giant evolution) almost always form far *slower* than interior planets. With these metrics in mind, we require our Mars analogs accrete 90% of their mass within 10 Myr of the beginning of our terrestrial planetary formation simulations (not the onset of the instability, criterion B). Additionally, we require our Earth analogs take at least 50 Myr to accrete 90% of their mass (criterion C)

3.3.3 The Asteroid Belt

Imposing strict constraints on the asteroid belt is difficult because, of the 1000 planetesimals that begin a given simulation, typically only 10 to 30 complete the integration in the asteroid belt region. Furthermore, because the smallest objects in our simulations have masses ~ 16 times greater than Ceres, our initial conditions are quite unrealistic for an appropriate study of the asteroid belt. Our ability to model the depletion of the asteroid belt is thus limited. Therefore, we cannot draw any conclusions about the total mass of the asteroid belt as all the particles in our simulation are simply too large. However, the dynamical behavior of our small planetesimals should be roughly similar to that of the larger asteroids in the belt (such as Ceres). Because there are only a few such large asteroids in the actual asteroid belt, it is important that we heavily deplete the region of such objects in our simulations. Several studies have already investigated the effects of the Nice Model on the asteroid belt (O'Brien et al., 2007; Walsh & Morbidelli, 2011; Roig & Nesvorný, 2015; Deienno et al., 2016). A similar study, using tens of thousands of smaller particles in the asteroid belt region will be required to study the particular dynamical constraints our scenario places on the asteroid belt. Furthermore, the most successful models for the asteroid belt (Walsh et al., 2011; Raymond & Izidoro, 2017b) successfully reproduce the compositional dichotomy between “S-types” (Silicate rich, moderate albedo asteroids) and “C-types” (low albedo, carbonaceous asteroids making up about 75% of the belt) (Gradie & Tedesco, 1982). Improving our mass resolution within the asteroid belt in the future will allow us to test this constraint as well.

For our purposes, we simply require that no embryos remain in the region ($a > 2.0$ au).

This method (criterion D) is similar to that employed in [Chambers \(2001\)](#) and [Raymond et al. \(2009b\)](#). The fact that there are no significant gaps between observed mean motion and secular resonances in the actual asteroid belt implies an upper limit (about a Mercury mass) for the mass of the largest object in the belt that could survive terrestrial planetary formation ([O’Brien & Sykes, 2011](#)). Because the total mass of the asteroid belt is thought to have depleted by about a factor of $\sim 10^4$ over the life of the solar system ([Petit et al., 2001](#)), a detailed calculation of the actual numerical value of what is left over is far beyond the scope of this Chapter. Moreover, because Gyr timescale modeling of test particles in the asteroid belt indicates that depletion is logarithmic over the life of the solar system, the majority of this depletion must happen during the first ~ 200 Myr of evolution because loss in the next 4 Gyr is only of order $\sim 50\%$ ([Minton & Malhotra, 2010](#)).

Additionally, we look at the number of remaining planetesimals above and below the ν_6 secular resonance between 2.05-2.8 au. In the actual solar system, this ratio is about $\sim .09$. Again, due to the small number statistics, the ratio inferred from an individual simulation will be very imprecise. Therefore we only require this ratio to be less than one (criterion E).

Furthermore, resonance sweeping during giant planet migration and evolution can drastically effect the dynamical structure of the asteroid belt ([Walsh & Morbidelli, 2011](#); [Minton & Malhotra, 2011](#); [Roig & Nesvorný, 2015](#)). In a slow migration scenario, as Saturn moves outward towards its current semi-major axis, the ν_{16} secular resonance excites inclinations as it sweeps through the asteroid belt. As Saturn continues to migrate, the ν_6 resonance erodes the remaining low inclination, low eccentricity component. Though the process of resonance sweeping can undoubtedly have an effect on the resulting mass of Mars ([Bromley & Kenyon, 2017](#)), the mechanism can also remove low inclination asteroids which are common ([Figure 3.6](#)) in today’s asteroid belt ([Walsh & Morbidelli, 2011](#)). To preserve the structure of the asteroid belt from the effects of resonance dragging, previous authors ([Roig & Nesvorný, 2015](#)) utilized a “jumping Jupiter” model instability (wherein Jupiter and Saturn “jump” toward their present orbital locations, ideally preserving the fragile terrestrial planets and

asteroid belt structure). In order for our model to be successful, it must heavily deplete the asteroid belt while still maintaining the low inclination component.

3.3.4 Water Delivery to Earth

Many models trace the origin of Earth’s water to the early depletion of the primordial asteroid belt (Raymond et al., 2007, 2009b). The actual topic of water delivery to Earth is extensive, with many competing models, and far beyond the scope of this Chapter (for a more complete discussion of various ideas see Morbidelli et al., 2000, 2012; Marty et al., 2016). Uncertainties in the initial disk properties and locations of various snow lines make it challenging for embryo accretion models like our own to confidently quantify the water mass fraction (WMF) of Earth analogs. In addition, the actual bulk water content of Earth is extremely uncertain. Estimates of the mantle’s water content range between 0 to tens of oceans (Lécuyer et al., 1998; Marty, 2012; Halliday, 2013), while the core may contain 0 to nearly 100 (Badro, 2014; Nomura et al., 2014). See the review by Hirschmann (2006) for a discussion of the difference between the capacity of Earth’s water reservoirs and geochemical evidence for the actual water contained in Earth’s interior. Furthermore, given the amount of planetesimal scattering which occurs when the giant planets grew and migrated during the gas disk phase, the material from which Earth formed during the giant impact phase may have already been sufficiently water rich (Raymond & Izidoro, 2017a). For our simulations, we first look at the bulk WMF of Earth analogs calculated using an initial water radial distribution similar to that used in Raymond et al. (2009b) (Eq. 3.1, this assumes that the primordial asteroid belt region was populated by water-rich objects from the outer solar system during the gas disk phase; Raymond & Izidoro, 2017a). Any system which boosts Earth’s WMF to greater than 10^{-4} is considered to satisfy criterion F. We also analyze the percentage of objects Earth analogs accrete from different sections of the disk.

$$WMF = \begin{cases} 10^{-5}, & r < 2au \\ 10^{-3}, & 2au < r < 2.5au \\ 10\%, & r > 2.5au \end{cases} \quad (3.1)$$

3.3.5 Angular Momentum Deficit

One defining aspect about our solar system is the remarkably low eccentricities and inclinations of the terrestrial planets. Over lengthy integrations, the orbits of all the inner planets but Mercury typically stay extremely low (Quinn et al., 1991; Laskar & Gastineau, 2009). This orbital constraint was very difficult for early accretion models to meet (Chambers & Wetherill, 1998; Chambers, 2001). O’Brien et al. (2006) used dynamical friction to explain how the orbits could stay cold through the standard process of planetary formation. However, it has proven even more challenging to keep eccentricities low when a giant planet instability is considered (Brasser et al., 2009; Kaib & Chambers, 2016). Any successful model of terrestrial planetary formation must maintain low orbital excitation in the inner solar system. To measure this in our systems, we measure the angular momentum deficit (AMD, criterion F) of each system (Laskar, 1997). AMD (Eq. 2.1; see § 2.2.2) quantifies the deviation of the orbits in a system from perfectly coplanar, circular orbits. We follow the same procedure as Raymond et al. (2009b) and require our systems maintain an AMD less than twice the value of the modern inner solar system ($\sim .0018$).

3.3.6 The Outer Solar System

When analyzing the success of our terrestrial planetary formation simulations, it is important to consider how dependent our results are on the fate of the outer solar system. Indeed, the chance of our chosen resonant chains reproducing all the important traits of the outer solar system after undergoing an instability is often low. For example, Nesvorný & Morbidelli (2012) report only a 33% chance of our 5GP configurations finishing the integration with the

correct number of outer planets. When all four success criteria in that work are considered, 5GP resonant chains only successfully match the outer solar system $\sim 4\%$ of the time. Given the computational cost of our integrations, we are less interested in how *often* we correctly replicate the orbital architecture of the giant planets, and more concerned with how *dependent* our results are on the fate of the outer solar system.

To quantify the outer solar system, we adopt the same success criteria as [Nesvorný & Morbidelli \(2012\)](#). First, criterion H requires that the simulation finish with 4 giant planets. If this is satisfied, criterion I stipulates that the final semi-major axis of each planet be within 20% of the modern location, and the time averaged eccentricity and inclination of each planet be less than twice the largest current value in the outer solar system. Finally, criterion J states that the period ratio of Jupiter and Saturn stay less than 2.8. It should be noted that, unlike [Nesvorný & Morbidelli \(2012\)](#), we check for criterion J independently of whether the other two standards are met. The dynamics of the forming terrestrial planets are far less sensitive to the behavior of the ice giants than they are to that of Jupiter and Saturn. Therefore, we are nearly just as interested in systems that correctly produce Jupiter and Saturn but eject too many ice giants as we are in those that replicate the outer solar system perfectly.

3.4 Results and Discussion

We provide complete summaries of our results in Tables [3.4](#), [3.5](#) and [3.6](#). It should be noted that a small number of our instabilities fail to properly eject an ice giant, and complete the integration with greater than four giant planets. Because we are only interested in systems similar to the solar system, we do not include these few outliers in any of our analyses. [Table 3.4](#) shows the total percentage of systems in each simulation batch which meet our success criteria for the inner solar system. [Table 3.5](#) summarizes the percentage of systems satisfying our giant planet success criteria. We find that our systems adequately

Set	A	A1	B	C	D	E	F	G
	a, m_{TP}	m_{TP}	τ_{mars}	τ_{\oplus}	M_{AB}	ν_6	WMF	AMD
Control	0	0	9	86	2	53	87	8
5GP/.01Myr	3	15	31	84	41	35	40	14
6GP/.01Myr	2	6	15	75	48	46	34	9
5GP/.1Myr	0	2	16	79	38	39	27	12
6GP/.1Myr	6	10	20	69	50	39	38	12
5GP/1Myr	13	13	6	90	38	31	47	13
6GP/1Myr	8	14	11	87	54	42	44	7
5GP/10Myr	12	20	3	73	48	26	47	16
6GP/10Myr	8	20	19	80	54	31	62	8

Table 3.4: Summary of percentages of systems which meet the various terrestrial planet success criteria established in Table 3.3. It should be noted that, because runs beginning with a disk mass of $3M_{\oplus}$ were not successful at producing appropriately massed Earth and Venus analogs, criterion A and A1 are only calculated for $5M_{\oplus}$ systems. The subscripts TP and AB indicate the terrestrial planets and asteroid belt respectively.

replicate the outer solar system with frequencies consistent with those reported in Nesvorný & Morbidelli (2012). In Table 3.6, we look at our success rates for systems with Jupiter/Saturn configurations most similar to the actual solar system (period ratios less than 2.8). Clearly, the fate of the terrestrial planets is highly dependent on the evolution of the solar system’s two giant planets. This is largely due to strong secular perturbations which result from the post-instability excitation of the giant planet orbits. Indeed, when we look at systems which eject all ice giants and finish with a highly eccentric Jupiter and Saturn outside a period ratio of 2.8, we find terrestrial planets which are too few in number, on excited orbits and systematically under-massed. Though we still see these symptoms in some of the systems summarized in Table 3.6, they are noticeably less frequent.

3.4.1 Formation of a Small Mars

An early instability is highly successful at producing a small Mars, regardless of instability timing and the particular evolution of the giant planets. 75% of all our instability systems form either no Mars or a small Mars (less than $0.3 M_{\oplus}$), as opposed to none of our control runs. Additionally, as shown in Table 3.4, most of our control systems leave at least one

Set	H	I	J
	N_{GP}	a,e, i_{GP}	S:J
5GP/.01Myr	27	14	47
6GP/.01Myr	18	6	41
5GP/.1Myr	14	7	42
6GP/.1Myr	18	3	38
5GP/1Myr	23	15	57
6GP/1Myr	22	9	38
5GP/10Myr	17	9	36
6GP/10Myr	16	8	36

Table 3.5: Summary of percentages of systems which meet the various giant planet success criteria established in Table 3.3. The subscript GP indicates the giant planets.

Set	A	A1	B	C	D	E	F	G
	a, m_{TP}	m_{TP}	τ_{mars}	τ_{\oplus}	M_{AB}	ν_6	WMF	AMD
Control	0	0	9	86	2	53	87	8
5GP/.01Myr	0	15	33	94	24	33	61	15
6GP/.01Myr	5	5	17	80	30	60	56	10
5GP/.1Myr	0	0	14	78	13	36	42	5
6GP/.1Myr	12	18	7	84	32	59	64	11
5GP/1Myr	26	26	12	95	20	29	65	14
6GP/1Myr	11	27	12	92	42	44	69	2
5GP/10Myr	9	18	7	92	16	29	53	25
6GP/10Myr	20	33	27	87	25	52	77	2

Table 3.6: Summary of percentages of systems which meet the various terrestrial planet success criteria established in Table 3.3 AND finish with Jupiter and Saturn’s period ratio less than 2.8 (criterion J). It should be noted that, because runs beginning with a disk mass of $3M_{\oplus}$ were not successful at producing appropriately massed Earth and Venus analogs, criterion A and A1 are only calculated for $5M_{\oplus}$ systems. The subscripts TP and AB indicate the terrestrial planets and asteroid belt respectively.

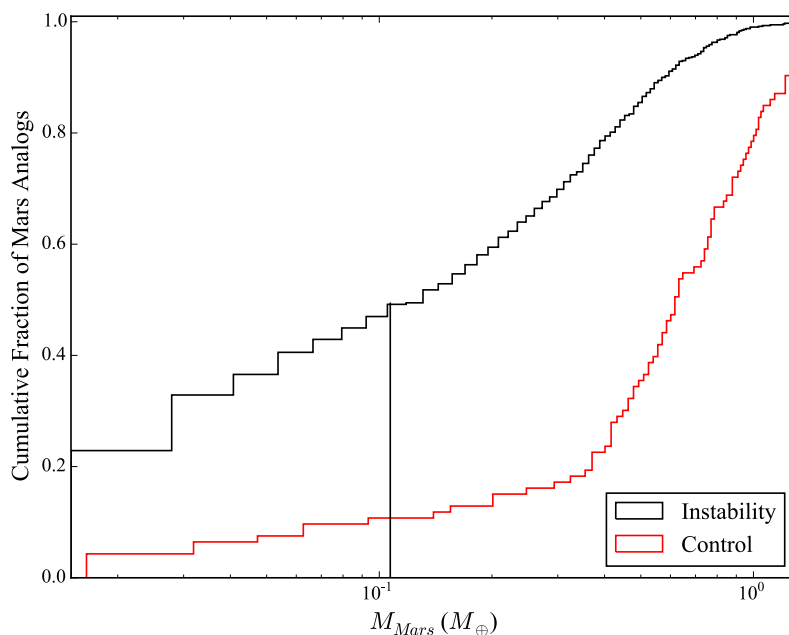


Figure 3.2: Cumulative distribution of Mars analog masses formed in instability systems and our control batch (note that some systems form multiple planets in this region, here we only plot the largest planet). The vertical line corresponds to Mars’ actual mass. All control runs with a Mars analog smaller than $0.3 M_{\oplus}$ ($\sim 20\%$ of the batch) were unsuccessful in that they also formed a large planet in the asteroid belt

embryo in the asteroid belt. In fact, many of these systems even form multiple small planets, or an Earth massed planet in the asteroid belt. Only 9% of our instability simulations form a planet more massive than Mars in the asteroid belt, as opposed to 65% of our control runs. Clearly a Nice Model instability is a highly efficient means of depleting the planetesimal disk region of material outside of 1.3 au.

Figure 3.2 shows the cumulative distribution of the largest planets in each system formed between 1.3 and 2.0 au for our instability sets versus the control batch. The solar system fits in well with this distribution, with slightly greater than half of our systems forming Mars analogs larger than the actual planet. Indeed, the instability consistently starves this region of material and produces a small planet. In fact, 22% of our systems produce no planet in the Mars region whatsoever. This is slightly lower for the two earliest instability delays (0.01 and 0.1 Myr) which we test, with 18% of such systems forming no Mars in the 1.3

to 2.0 au region. This is due to the fact that, when the instability occurs, the ratio of the number of planetesimals to embryos, and that of total planetesimal mass to total embryo mass is much higher. In the late instability cases, the majority of the system mass is trapped in several large embryos. The dynamical excitement of the additional planetesimals in the early instability delay cases allows the disk mass to disperse, thereby enhancing the mass of Mars analogs. We find that planets in the outer disk ($a > 1.3$ au) from early instability delay systems (0.01 and 0.1 Myr) where the outer planets meet criterion J accrete ~ 6 times more material from the inner disk than in late instabilities (1 and 10 Myr). Furthermore, dynamical friction from the higher number of planetesimals de-excites material in the outer disk. Indeed, our early instability delay systems which satisfy criterion J lose an average of $0.25 M_{\oplus}$ less mass in the outer disk ($a > 1.3$ au) to ejection or collisions with the Sun than the later delays. [Figure 3.3](#) shows how a late instability delay results in a dramatically steeper mass distribution profile.

In [Figure 3.4](#) we show the distributions of semi-major axes and masses for the planets we form, compared with our control simulations. Regardless of the instability delay time, there is a stark contrast between our simulations and the control set. Earth mass planets in the Mars region and beyond are very common in the control simulations, and rarely occur when the system undergoes a Nice Model instability. Though the general trends for all four plots are quite similar, we note that our distributions for late instabilities are slightly better matches to the actual solar system for two reasons. First, the number of outlying Mars analogs which are larger than $\sim .6M_{\oplus}$ is substantially less for the later instability delay times. As discussed previously, because these simulations begin with fewer planetesimals, the lack of disk dispersal and de-excitation via dynamical friction between small bodies makes it difficult for the system to accrete a large Mars over the next ~ 200 Myr of evolution. Next, these systems tend to form more accurate Earth and Venus analogs. Many of the failed early instability delay simulations are clear examples of the instability’s tendency to hinder the formation of Earth and Venus. The larger dispersal of the disk mass profile in these delays

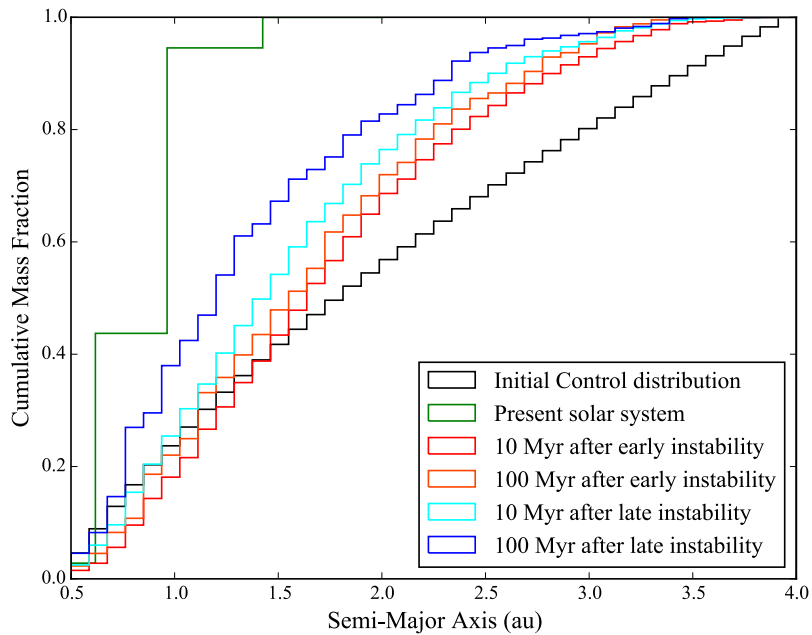


Figure 3.3: Cumulative mass distribution of embryos and planetesimals at the beginning of the control simulations (black line), 10 Myr after the early instability delay times (.01 and 0.1 Myr; red line), 100 Myr after the early instability delay times (orange line), 10 Myr after the late instability delay times (1 and 10 Myr; cyan line) and 100 Myr after the late instability delay times (blue line). The green line represents the current mass distribution of the inner solar system.

consistently deprives the Earth and Venus forming regions of material. In these simulations, we often form systems with small (less than $\sim .6M_{\oplus}$) Venus and Earth analogs, just one total terrestrial planet, or no inner planets at all.

3.4.2 Strengths of an Early Instability

Tables 3.4 and 3.6 show the percentage of systems in each batch that meet our success criteria for the inner solar system. Because the solar system very well could have been formed in a low likelihood scenario, it is important not to place too much weight on meeting specific numerical values and exactly replicating every particular dynamical trait of the actual system. For this reason, we try to keep our success criteria as broad as possible.

We consider our systems roughly successful at meeting our established criteria. Generally, our systems perform better than our control runs in almost all categories. Because the unique dynamical state of the solar system represents just one point in a broad spectrum of possible outcomes, it is unreasonable to expect that our simulations meet every single success criterion exactly, every time. By these standards, our simulations are successful on most accounts. In particular, an instability is very successful at meeting the requirements for the asteroid belt (criterion D) and the formation timescale of Earth (criterion C).

Given the large number of constraints involved in criterion A, our success rates of $\sim 5 - 20\%$ are still very encouraging. For this reason, we also use the broader criterion A1 for the orbital architecture of the inner solar system. This metric considers systems that form planets of the correct mass ratios, but incorrect orbital locations, and those which form no Mars but a proper Earth and Venus pair to be successful. When we look at our rates of success for meeting this criterion when Jupiter and Saturn finish the integration within a period ratio of 2.8 (Table 3.6), we find our later instability delay times are remarkably successful with values closer to $\sim 30\%$. In these successful scenarios, Mars often forms as a stranded embryo. The simulation begins with multiple bodies of order 0.25-2.5 M_{Mars} in the vicinity of Mars' present orbit. When the instability ensues, most of these bodies are

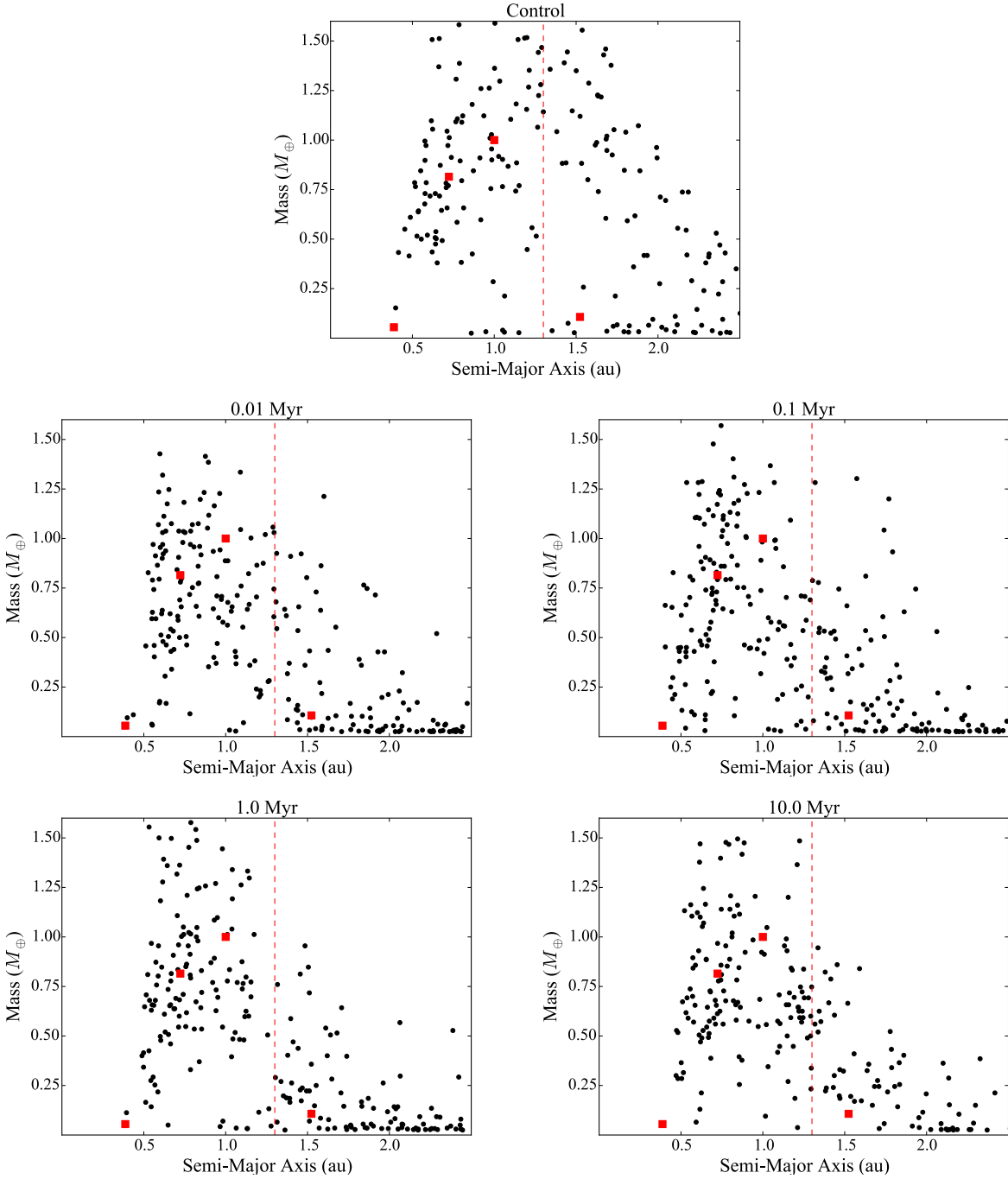


Figure 3.4: Distribution of semi-major axes and masses for all planets formed using $5 M_{\oplus}$ massed planetesimal disks. The red squares denote the actual solar system values for Mercury, Venus, Earth and Mars. The vertical dashed line separates the Earth and Venus analogs (left side of the line) and the Mars analogs (right side). The top panel shows our control runs and each of the 4 lower plots depict a different instability delay time.

ejected. 40% of the time, “Mars” undergoes no further major accretion events with other embryos after the instability simulation begins. [Figure 3.5](#) shows an example of such an evolution scheme. Notice that after the instability ensues the proto-Venus and proto-Earth continue to accrete material while objects in the Mars forming region do not.

The Asteroid Belt

Our simulations are successful at depleting the asteroid belt because of the dynamical excitation provided by the embryos we place in the belt. The embryos pre-excite the asteroid belt during the evolution leading up to the instability. When the instability ensues, excited planetesimals in the belt scatter off the embryos, leading to high mass loss. To test this, we performed a follow-on suite of integrations using our 1 Myr instability control disks, and the Mercury6 hybrid integrator. We place Jupiter and Saturn on orbits corresponding to a period ratio of 1.6, and set an extra ice giant immediately exterior to Saturn. When the ice giant scatters and is ejected, Jupiter and Saturn jump. Next, systems where the post-jump period ratio of Jupiter and Saturn is between 2.1 and 2.4 are selected, and integrated for an additional 10 Myr with a code that mimics smooth migration and eccentricity damping on ~ 3 Myr e-folding timescales using fictitious forces ([Lee & Peale, 2002](#)). To attain final states similar to Jupiter and Saturn, we shut off migration and eccentricity damping when the two gas giants attain a period ratio above 2.45 and eccentricities below 0.06. Through this process, we create a sample of asteroid belts (~ 20) which experience a pre and post-instability evolution broadly similar to the runs from our original simulations that best matched the currently observed orbital architecture of Jupiter and Saturn. By performing 2 sets of runs (embryos and planetesimals and planetesimals only), we are able to test the effects of embryo excitation. Planetesimal only simulations are created by converting all embryos with a > 1.5 au in a given system in to an appropriate number of equal-mass planetesimals with similar semi-major axes, eccentricities and inclinations, and random angular orbital elements. Simulations using embryos and planetesimals lost about twice as much mass beyond 1.5 au

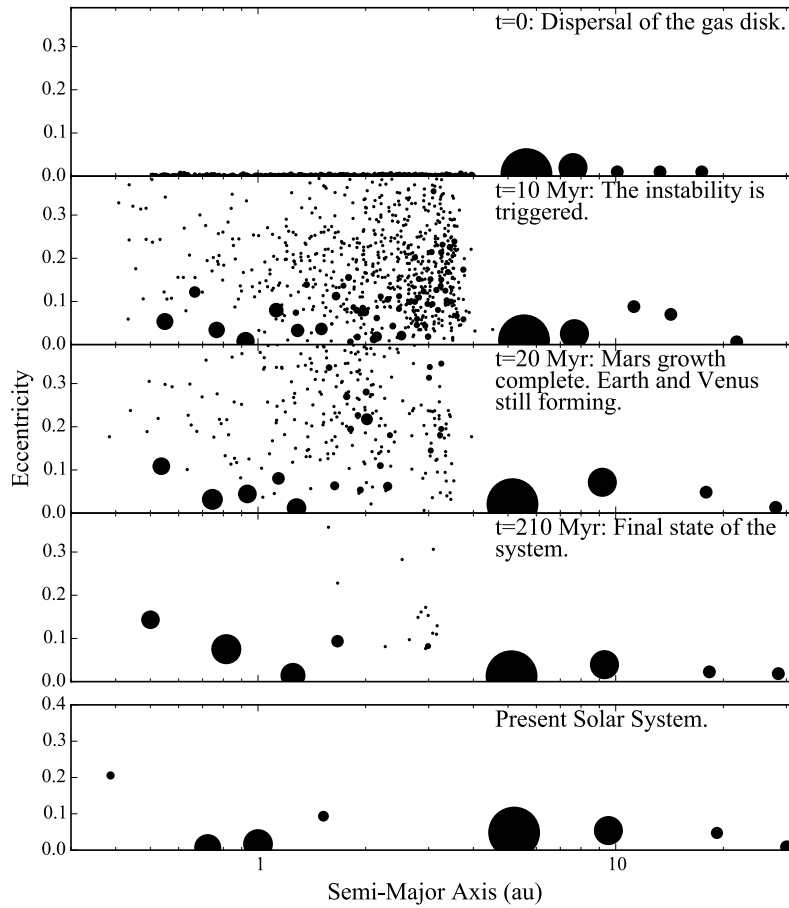


Figure 3.5: Semi-Major Axis/Eccentricity plot depicting the evolution of a successful system in the 5GP/10Myr batch. The size of each point corresponding to the mass of the particle (because Jupiter and Saturn are hundreds of times more massive than the terrestrial planets, we use separate mass scales for the inner and outer planets). The final planet masses are 0.37, 1.0, 0.69 and 0.15 M_{\oplus} respectively.

over just 10 Myr of evolution as the planetesimal only systems. This is consistent with the idea that the dynamical excitement of embryos leads to significantly more mass loss in the asteroid belt.

Our simulations’ ability to replicate the asteroid belt population about the ν_6 resonance is subject to numerical limitations. Our simulations start with 0.0025 and 0.0015 M_\oplus planetesimals, both of which are more massive than the entire present contents of the asteroid belt. Furthermore, most simulations finish with between 10 and 30 bodies in the main belt. Such small numbers makes it difficult to discern subtle dynamical features within our individual simulated asteroid belts. Although statistics can be improved by co-adding many simulations to examine the general effects of giant planet instabilities (Figure 3.6), every instability is unique at some level, and dynamical sculpting processes occurring during some instabilities may not operate in others. When we co-add the asteroids from all of our criterion J satisfying simulations (those which finish with Jupiter and Saturn’s period ratio less than 2.8) and remove objects on planet-crossing orbits, we find a ratio of bodies above to below the ν_6 resonance (between 2.05 and 2.8 au) to be ~ 0.71 . However, when we only consider asteroids between 2.05 and 2.5 au, the ratio is a poorer match (2.24). Though neither number is close to the actual ratio (~ 0.09), the first is quite promising with respect to other numerical modeling attempts. For example, [Deienno et al. \(2016\)](#) imposed a “Grand-Tack” style migration on the asteroid belt and found a ratio of ~ 1.2 . In a similar manner, [Walsh & Morbidelli \(2011\)](#) reported a ratio of ~ 5.2 in a smooth migration scenario.

Due to numerical limitations, further simulations, involving tens of thousands of smaller bodies in the asteroid belt region are required to comprehensively study the detailed effect of an early instability on the asteroid belt. However, an early instability seems to generate an asteroid belt similar to the actual belt in broad strokes. The presence of embryos appears to provide sufficient dynamical excitation to substantially deplete the mass in the region (most simulations deplete more than 95% of belt material in 200 Myr). Though this does fall short of the required depletion of a factor of $\sim 10^4$ ([Petit et al., 2001](#)), our mechanism

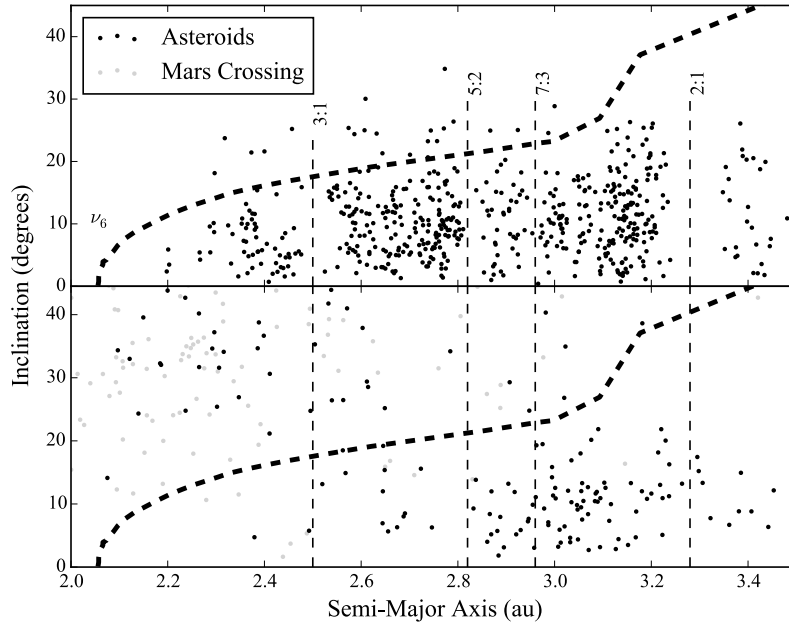


Figure 3.6: The upper plot shows the inclination distribution of the modern asteroid belt (only bright objects with absolute magnitude $H < 9.7$, approximately corresponding to $D > 50$ km, are plotted). The bottom plot combines all planetesimals remaining in the asteroid belt region from all instability simulations that form a Mars analog less massive than 3 times Mars' actual mass, and finish with Jupiter and Saturn's period ratio less than 2.8. Grey points correspond to high-eccentricity asteroids on Mars crossing orbits which will be naturally removed during subsequent evolution up to the solar system's present epoch. The vertical dashed lines represent the locations of the important mean motion resonances with Jupiter. The bold dashed lines indicate the current location of the ν_6 secular resonance.

does produce substantial depletion in the asteroid belt when compared with our control runs. More realistic initial conditions and handling of collisions will be required to more accurately model depletion in the Asteroid Belt in our model. Nevertheless, embryos remaining in the asteroid belt are extremely rare in our instability systems. By using a full instability, rather than a smooth migration scenario, we avoid dragging resonances across the belt, thus broadly preserving its orbital structure.

3.4.3 Weaknesses of an Early Instability

On average, our instability simulations are less successful at meeting the success criteria for the formation timescale of Mars, the WMF of Earth and the AMD of the terrestrial planets. Reproducing the formation timescale of Mars is a difficult constraint for N-body accretion models of terrestrial planetary formation. A successful Mars analog in our simulations need only be composed of 4 embryos. Meanwhile, the real Mars formed from millions of smaller objects that accreted prior to and during the giant impact phase. This difference must be weighed when considering moderate discrepancies between the formation timescales of simulated Mars analogs and the real planet. In fact, $\sim 40\%$ of all our Mars analogs undergo no impacts with other embryos following the instability, and Mars' form on average ~ 39 Myr faster than their Earth counterparts. Additionally, 6 of the 7 Mars analogs in the criterion A1 satisfying [6GP/10 Myr] batch (our most successful simulations), form in under 10 Myr. Because Mars' growth only continued at the $\sim 10\%$ level after $\sim 2-4$ Myr (Dauphas & Pourmand, 2011), our 1 Myr instability delays are the most successful at simultaneously matching the mass distribution of the terrestrial system and the proposed accretion history of Mars. However, the geological accretion history of Mars is inferred relative to CAI formation; the timing relative to gas disk dissipation of which is not fully understood.

Providing a means of water delivery to Earth is not a strict requirement for the success of an embryo accretion model. It should be noted that many ideas for how Earth was populated with water exist, several of which have nothing to do with delivery via bodies from the outer

solar system (Morbidelli et al., 2000, 2012). In fact, water delivering planetesimals may have been scattered on to Earth-crossing orbits during the giant planets’ growth and migration phase (Raymond & Izidoro, 2017a). Despite the small number statistics involved with using only 1000 initial particles in the Kuiper belt, about half of which typically deplete in the initial phase of integration (before the terrestrial disks are imbedded), we do find 12 instances of Earth analogs accreting objects from this region in our simulations. Interestingly, Earth’s noble gases are thought to come primarily from comets, despite the fact that comets are likely a minor source of water (Marty et al., 2016). We find that a late instability delay time (1 and 10 Myr) systematically stretches the feeding zone of Earth analogs further in to the terrestrial disk. This broader feeding zone is basically a result of eccentricity excitation of planetesimals (Levison & Agnor, 2003b). In these cases, mass from the outer disk is able to “leap-frog” its way towards the proto-Earth. In the first phase of evolution (before the instability), forming embryos in the middle part of the disk ($\sim 2.0\text{-}3.0$ au) accrete material from the outermost section of the disk ($\sim 3.0\text{-}4.0$ au). When the instability ensues, these embryos are destabilized, and occasionally scattered inward towards the forming “Earth”.

Our simulations often leave the inner planets with too large of an AMD. Though most runs only exceed the actual AMD of the solar system by a factor of 2-3, some systems occasionally reach AMDs as high as 10 times the value of the current solar system. Many of these outliers are from integrations where particularly violent instabilities leave behind a system of overly excited giant planets. Even when we remove these instances which are not analogous to the actual solar system, our “successful” simulations still tend to possess high AMD values. Often, an overly excited Mars is the source of this orbital excitation (values of $e_{Mars} \sim .1 - .25$ are typical for these systems). The obvious source of this excitation is secular interactions with the excited giant planets. One potential solution to this problem might be accounting for collisional fragmentation. Chambers (2013) showed that angular momentum exchange resulting from hit-and-run collisions noticeably reduces the eccentricity of planets formed in embryo accretion models. Additionally, Jacobson & Morbidelli (2014) showed that

the AMD of systems increases as the total amount of initial mass placed in embryos instead of planetesimals increases, and as individual embryo mass decreases. We observe a similar relationship in overall disk mass loss (§ 3.4.1). Moreover, because of the chaotic nature of the actual solar system, its AMD can evolve by as much as a factor of 2 in either direction over Gyr timescales (Laskar, 1997).

3.4.4 Varied Initial Conditions

Our simulations are broken up into 4 different sets of 25 runs with unique inner disk edge and initial disk mass combinations (Table 3.2). In half of our simulations, we use a disk mass of $3 M_{\oplus}$ rather than a more typical choice of $\sim 5 M_{\oplus}$ (Chambers, 2001; Raymond et al., 2009b). 100% of these systems with lower mass disks fail to meet criterion A for correctly replicating the semi-major axes and masses of the terrestrial planets. Using a lower overall disk mass leads to less dynamical friction available to save bodies from loss after the instability. We find that by far the most likely final configuration for these simulations is a single Venus analog, occasionally accompanied by a Mars analog. However, we note that the percentages of systems that meet the other 6 success criteria (criterion B through G) are roughly similar (within $\sim 5\%$) for systems of either initial disk mass.

We see no noticeable differences between the sets of simulations which truncate the inner planetesimal disk at 0.5 au and those with an inner edge at 0.7 au. Both batches are roughly equally likely (9% and 10% of the time, respectively) to form a Mercury analog (we define this as any planet smaller than $0.2 M_{\oplus}$ interior to an Earth and a Venus analog). For more discussion on the formation of Mercury, see § 3.4.6. Finally, our rates for meeting all success criteria for the inner planets are roughly the same (within $\sim 5\%$), regardless of the selected inner disk edge location.

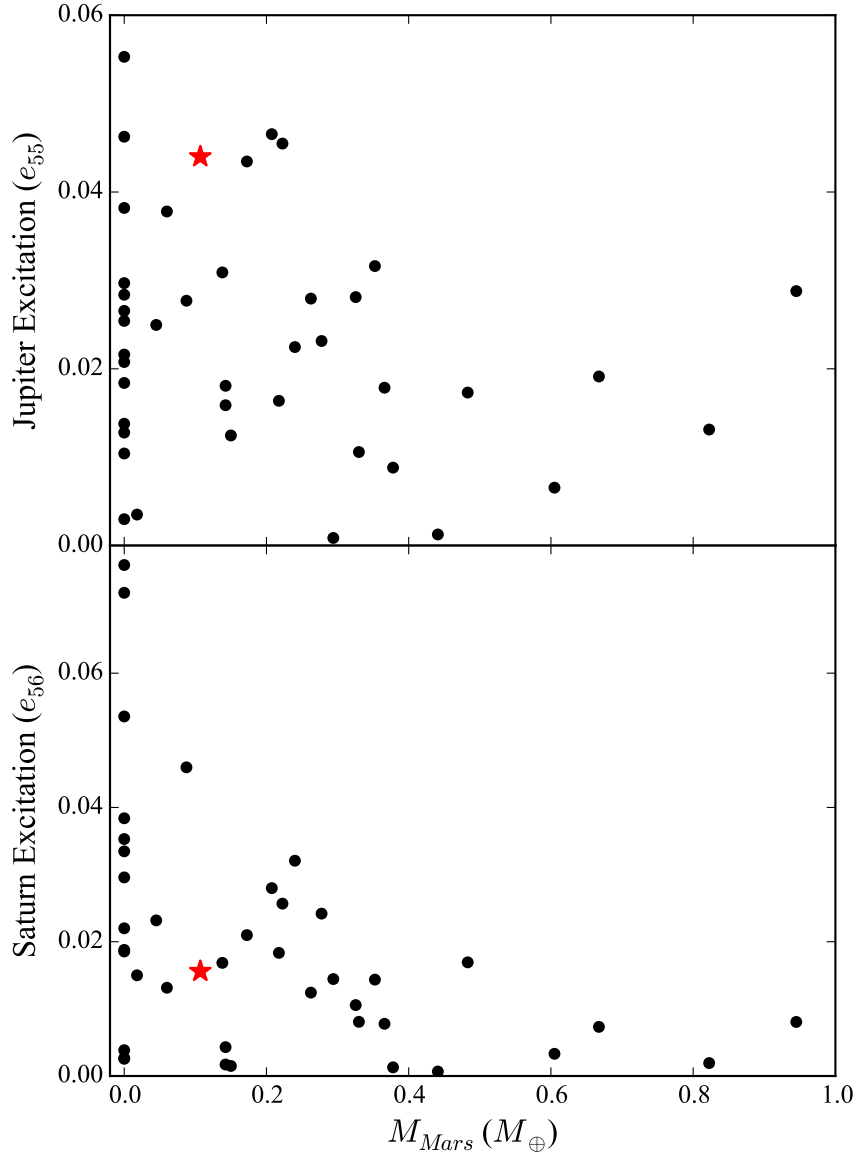


Figure 3.7: Values of the amplitudes of Jupiter’s g_5 mode versus the mass of Mars analogs formed for 10 Myr delayed instability systems where the orbital period ratio of Saturn to Jupiter completing the integration less than 2.8. The red stars correspond with the present solar system values.

3.4.5 Excitation of Jupiter’s g_5 Mode.

The sufficient excitation of Jupiter’s g_5 mode is another important constraint on the evolution of the giant planets. The current amplitude of the mode, $e_{55} = 0.044$, is very important in driving the secular evolution of the solar system (Morbidelli et al., 2009). Additionally, the amplitude of Saturn’s forcing on Jupiter’s eccentricity, $e_{56} = 0.016$, is important for the long term evolution of Mars and the asteroid belt. Overexciting e_{56} might lead to a small Mars and a depleted asteroid belt. However, this scenario is not akin to the actual evolution of the solar system. To evaluate the relationship between the g_5 mode and the mass of Mars, we integrate all systems which finish with Jupiter and Saturn within a period ratio of 2.8 for an additional 10 Myr, and perform a Fourier analysis of the additional evolution (Šidlichovský & Nesvorný, 1996). In Figure 3.7, we plot the values of e_{55} and e_{56} against the masses of Mars analogs produced for these systems in our 10 Myr delayed instabilities. We find that systems with an e_{55} amplitude greater than that of actual solar system never produce a large Mars analog (greater than $0.3 M_{\oplus}$). The average Mars analog mass in systems with e_{55} less than half the solar system value (0.022) is 1.96 times Mars’ mass, compared to 1.03 for systems with $e_{55} > 0.022$. Additionally, we see multiple examples of systems where e_{56} is close to the solar system value, that produce a small Mars. Clearly, the complete excitation of the g_5 mode is linked to reducing the mass of planets in the Mars forming region. Additionally, in Figure 3.8, we plot the normalized AMD of Jupiter and Saturn versus the mass of Mars analogs. It is very apparent that the range of possible values is extensive, with the solar system falling well within the range of our results. Therefore, the actual solar system is consistent with our dynamical evolution model. Furthermore, Jupiter’s excitation also effects Earth and Venus. When we plot the cumulative mass of Earth and Venus against the mass of Mars (Figure 3.9), we find that many of the systems with similar values to the solar system have correspondingly similar values of e_{55} .

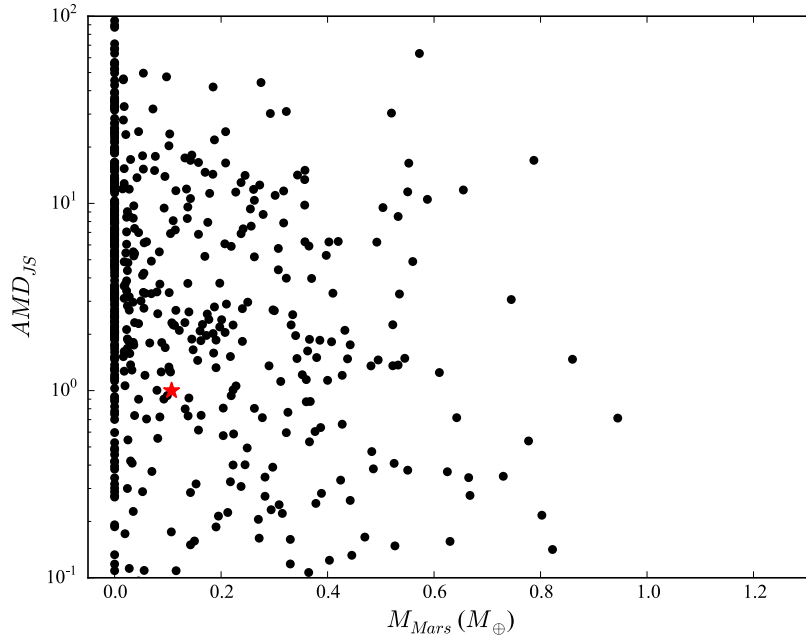


Figure 3.8: The AMD of Jupiter and Saturn (normalized to the actual solar system value) versus the mass of Mars analogs formed for all instability systems. The red star denotes the solar system values.

3.4.6 Impact Velocities

Our simulations use an integration scheme where all collisions are assumed to be perfectly accretionary (Chambers, 1999). This provides a decent approximation of the final outcome of terrestrial planet formation for low relative-velocity collisions between objects with a large mass disparity. However, higher velocity collisions can often be erosive (Genda et al., 2012), particularly when the projectile to target mass ratio is closer to unity. Additionally, depending on the parameters of the impact, glancing blows can lead to the re-accretion of either all, some or none of the original projectile (Asphaug et al., 2006; Asphaug, 2010; Leinhardt & Stewart, 2012). Because of the instability’s tendency to excite small planetesimals on to high-eccentricity orbits, the collisional velocities in our simulations are often quite large (occasionally in excess of 10 times the mutual escape velocity). Because of this, it is very important to consider the effects of collisional fragmentation of bodies when analyzing our results.

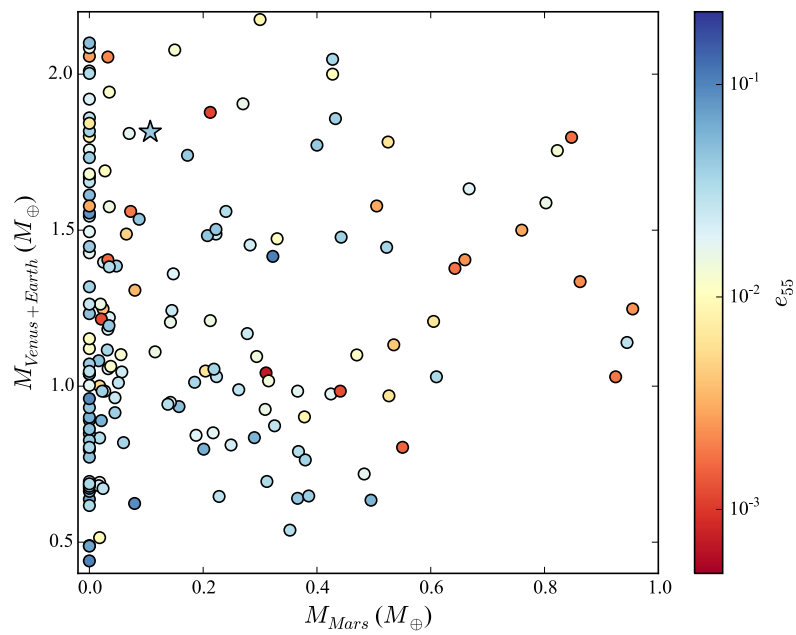


Figure 3.9: Values of the total mass of Earth and Venus analogs versus the mass of Mars analogs formed in instability systems where the value of Jupiter and Saturn's period ratio finished the simulation less than 2.8. The color of each point corresponds to the amplitude of Jupiter's g_5 mode. The blue star denotes actual solar system values.

To check our simulations for erosive collisions, we use a code which determines the collision type from the collision speed and impact angle by following the parameter space of gravity dominated impacts mapped by [Leinhardt & Stewart \(2012\)](#). We find that erosive collisions do occur with the forming planets in our simulations. However, they are infrequent, and comprise less than $\sim 5\%$ of all collisions and less than $\sim 1\%$ by mass. Erosive collisions occur at similar rates for Earth, Venus and Mars analogs, and are almost always planetesimal-on-embryo impacts. We do note, however, that our Mars analogs undergo a significantly higher number of hit and run collisions (36% by mass as opposed to less than 20% for Earth and Venus analogs). This indicates that our Mars analog masses are most likely over-estimated. Additionally, because the effects of hit and run collisions have been shown to reduce the AMD of planets produced ([Chambers, 2013](#)), it is possible that the resulting orbital eccentricities and inclinations of our Mars analogs are similarly over-excited. This is encouraging because the excitation of Mars significantly contributes to our systematically high AMDs.

3.5 Conclusions

In this Chapter, we have presented 800 direct numerical simulations of a giant planet instability occurring in conjunction with the process of terrestrial planet formation. By timing this violent event within the first ~ 100 Myr following the dispersion of the gas disk, the instability scenario no longer requires a mechanism to prevent the destabilization and loss of the fully formed terrestrial planets (such as the “Jumping Jupiter” model). When we scrutinize our fully formed systems against a wide range of success criteria, we note multiple statistical consistencies between our simulated planets and the actual terrestrial system. First, our Mars analogs are more likely to form small and quickly. In fact, 75% of all our instabilities form either no planet in the Mars region whatsoever, or an appropriately sized Mars. Additionally, cases where the instability is delayed 1-10 Myr after the beginning of

the giant impact phase tend to be more successful than earlier timings (<1 Myr). In many of these runs, the instability itself sets the geological formation timescale of Mars. Thus, an early giant planet instability provides a natural explanation for how Mars survived the process of planet formation as a “stranded embryo.”

We find that our simulated asteroid belts are largely depleted of mass when compared with our control set of simulations, and seldom form a planet in the belt region. Furthermore, the broad orbital distribution of the asteroid belt seems to be well matched when we co-add the remaining asteroids from all of our simulations. Because the instability itself is inherently chaotic, each resulting system of giant planets has slightly different orbital characteristics. When we filter out systems where the giant planets orbits most closely resemble those in the actual solar system, we find higher rates of success among the corresponding terrestrial systems.

At first glance, certain geochemical and dynamical constraints somewhat conflict with an instability occurring 1-10 Myr after gas disk dispersal. New isotopic data from comet 67P suggests that $\sim 22\%$ of Earth’s atmospheric noble gases were delivered via cometary impacts after the Earth had fully formed (Marty et al., 2017). Because the giant planet instability is the most likely source of such a cometary onslaught, this seems to suggest that the instability occurred after the conclusion of terrestrial planet formation. However, considerable uncertainty remains in the interpretation of this noble gas signature. Another potential conflict with our result is related to the modern Kuiper belt. The classical Kuiper belt population on high inclination orbits can be explained if Neptune initially migrated in a slow, smooth fashion for at least 10 Myrs after gas disk dispersal before being interrupted by the giant planet instability (Nesvorný, 2015a). Though such a timing matches our longest delay, pushing the instability time later leads to a conflict with constraints on Mars’ accretion history (Dauphas & Pourmand, 2011). However, our understanding of the Kuiper belt’s origins and Mars’ formation timescale are subjects of ongoing study and continually evolving. Given this, we believe this is not enough to rule out the premise of our model, especially

because it is able to replicate so many features of the inner solar system.

The Nice Model explains a number of aspects of the outer solar system. We have shown that, if it occurred within 10 Myr of the dissipation of the gaseous disk, the instability produces inner solar system analogues that match many important observational constraints regarding the formation of Mars and the asteroid belt. In contrast, simulations lacking an instability consistently yield Mars analogs that are too massive, form too slowly, and are surrounded by over-developed asteroid belts. By including a giant planet instability, these same simulations show a dramatic decrease in the mass and formation timescale of Mars, and adequate depletion in the asteroid belt.

3.6 Acknowledgments

This Chapter is reproduced by permission of Elsevier and the American Astronomical Society's Division of Planetary Sciences from the following publication: Clement, M. S., Kaib, N.A., Raymond, S.N. and Walsh, K.J. (September 2018). Mars growth stunted by an early giant planet instability. In: *Icarus* 311: 340-356.

M.S.C. and N.A.K. thank the National Science Foundation for support under award AST-1615975. S.N.R. thanks the Agence Nationale pour la Recherche for support via grant ANR-13-BS05-0 0 03-0 02 (grant MOJO). K.J.W. thanks NASA's SSERVI program (Institute of the Science of Exploration Targets) through institute grant number NNA14AB03A. The majority of computing for this project was performed at the OU Supercomputing Center for Education and Research (OSCER) at the University of Oklahoma (OU). Additional analyses and simulations were done using resources provided by the Open Science Grid ([Pordes et al., 2007](#); [Sfligoi et al., 2009](#)), which is supported by the National Science Foundation award 1148698, and the U.S. Department of Energy's Office of Science. Control simulations were managed on the Nielsen Hall Network using the HTCondor software package: <https://research.cs.wisc.edu/htcondor/>. This research is part of the Blue Waters sustained-

petascale computing project, which is supported by the National Science Foundation (awards OCI-0725070 and ACI-1238993) and the state of Illinois. Blue Waters is a joint effort of the University of Illinois at Urbana-Champaign and its National Center for Supercomputing Applications ([Bode et al., 2013](#); [Kramer et al., 2015](#)).

Chapter 4

The Early Instability Scenario: Terrestrial Planet Formation During the Giant Planet Instability, and the Effect of Collisional Fragmentation

This Chapter is reproduced from [Clement et al. \(2019b\)](#), which appeared in the journal *Icarus*, with only minor typographical and formatting alterations. The abstract has been removed to improve the flow and readability of this thesis.

4.1 Introduction

The “Nice Model” ([Gomes et al., 2005](#); [Tsiganis et al., 2005](#); [Morbidelli et al., 2005](#)) is an evolutionary model for the outer planets that seems to explain many of the solar system’s peculiar traits ([Nesvorný et al., 2007](#); [Levison et al., 2008](#); [Nesvorný et al., 2013](#); [Nesvorný, 2015a,b](#)). Observations of proto-stellar disks indicate that free gas disappears in a just a few Myr ([Haisch et al., 2001](#); [Petit et al., 2001](#); [Mamajek & Hillenbrand, 2008](#); [Halliday, 2008](#); [Pascucci et al., 2009](#)), much faster than the timescales of terrestrial accretion inferred from isotopic dating ([Currie et al., 2009](#); [Kleine et al., 2009](#); [Dauphas & Pourmand, 2011](#)). Because their gaseous envelopes imply formation in the presence of gas, the outer planets must have formed first ([Wetherill, 1996](#); [Chambers & Cassen, 2002](#); [Levison & Agnor, 2003a](#); [Raymond et al., 2004](#)). The combined gravitational torques generated by the star, disk and

other planets have been shown to quickly force the giant planets into a mutual resonant configuration (Masset & Snellgrove, 2001; Morbidelli & Crida, 2007; Nesvorný & Morbidelli, 2012). Such a scenario seems to explain the number of resonant giant exoplanets discovered (eg: Kepler 9, GJ 876 and HR 8799, among others; Holman et al., 2010; Delisle et al., 2015; Trifonov et al., 2017; Boisvert et al., 2018). After the disk phase of evolution, the scattering of small objects by the outer planets causes the resonant chain to break, and moves the giant planets toward their present orbits. Saturn, Uranus and Neptune tend to scatter small bodies from the primordial Kuiper Belt inward, while Jupiter preferentially ejects objects from the system (Fernandez & Ip, 1984; Malhotra, 1993, 1995; Thommes et al., 1999). To conserve angular momentum, the outermost giant planets’ orbits diverge from Jupiter. When this stable resonant chain eventually collapses, a global instability ensues (Gomes et al., 2005). Given that Uranus and Neptune are often ejected in simulations, the current version of the Nice Model invokes the formation of 1-2 additional ice giants in the outer solar system (Nesvorný, 2011; Nesvorný & Morbidelli, 2012).

The precise timing of the instability is dynamically arbitrary. Changing the initial conditions of the primordial Kuiper Belt can delay the event. However, the net result is the same. A late instability (Tsiganis et al., 2005; Gomes et al., 2005; Morbidelli et al., 2005; Levison et al., 2011) would imply a correlation with the late heavy bombardment (LHB, ~ 700 Myr after gas disk dispersal), the existence of which is now in doubt (for a detailed discussion consult Clement et al., 2018; Morbidelli et al., 2018). Moreover, Walsh & Morbidelli (2011) favored a late instability when considering constraints for the dynamical structure of the asteroid belt. On the other hand, an early instability (occurring just a few Myr after the disappearance of the primordial gas disk) is more consistent with Jupiter’s binary trojan population (Nesvorný et al., 2018) and the growing ice giant’s sculpting of the primordial Kuiper Belt (Ribeiro et al., in prep). Most importantly, the survival of the terrestrial planets is a very low probability event in a late Nice Model instability (Brasser et al., 2009, 2013; Agnor & Lin, 2012; Kaib & Chambers, 2016; Roig et al., 2016). In Clement et al. (2018),

henceforward Paper 1, we found that the inner solar system is best reproduced when the instability happens in situ with the process of terrestrial planet formation (roughly 1-10 Myr after the disappearance of the primordial gas disk). This scenario offers the added benefit of significantly limiting the ultimate mass and formation time of Mars.

Early numerical studies of the late stages (giant impact phase) of terrestrial planet formation successfully reproduced the general orbital spacing of the inner planets (Chambers & Wetherill, 1998; Chambers, 2001). However, these simulations fell short in replicating the low masses of Mercury and Mars (5% and 10% that of the Earth, respectively; Wetherill, 1991), leaving behind a low mass asteroid belt (often Mars to Earth-massed planets were formed in the belt region) and reproducing the dynamically cold orbits of the actual terrestrial system (all inner planets but Mercury have $e < 0.1$ and $i < 2^\circ$). O’Brien et al. (2006) and Raymond et al. (2006) showed that accounting for the dynamical friction of small planetesimals helped keep the final planet’s eccentricities and inclinations low. However, under-excited systems similar to the solar system still represent a low-likelihood event in most all studies of terrestrial planet formation. For example, systems in Paper 1 only satisfied this constraint 5-20% of the time, depending on the initial conditions.

Potential solutions to the small Mars problem are numerous within the literature (for recent reviews consult Morbidelli & Raymond, 2016; Raymond et al., 2018). In Paper 1, we provided a thorough discussion of the major competing models, and argued that any complete model for the evolution of the terrestrial planets must reconcile their survivability within the violent Nice Model instability. Here, we summarize 3 leading ideas:

- 1. The “Grand Tack” hypothesis:** Hansen (2009) noted that the low masses of Mercury and Mars could be consistently replicated if the initial terrestrial forming disk is confined to a narrow annulus between $\sim 0.7 - 1.0$ au. The “Grand Tack” hypothesis (Walsh et al., 2011; Walsh & Levison, 2016) provides the physical motivation for these initial conditions by surmising that, during the gas phase of evolution, Jupiter migrated in to, and subsequently back out of the inner solar system. When Jupiter reverses direction (or “tacks”) at the

correct location, the terrestrial disk is truncated at ~ 1.0 au. However, the mechanism for Jupiter’s tack is dependent on the unknown disk structure and gas accretion rates (Raymond & Morbidelli, 2014).

2. An early instability: Raymond et al. (2009b) first recognized that a small Mars could be formed if Jupiter and Saturn were placed in an initial configuration with high eccentricities ($e_J = e_S = 0.1$) and mutual inclination (1.5°). However, since planet-disk interactions damp out the orbits of the growing giant planets (Papaloizou & Larwood, 2000; Tanaka & Ward, 2004), these initial conditions seemed unlikely. Nevertheless, the giant planet’s influence was the crux of many subsequent studies of how Mars’ mass can be limited (eg: resonance sweeping (Thommes et al., 2008; Bromley & Kenyon, 2017) and resonance crossing (Lykawka & Ito, 2013)). In the early instability scenario of Paper 1, the onset of the Nice Model within a few Myr of gas disk dispersion (as opposed to ~ 700 Myr in a late version of the Nice Model; Gomes et al., 2005) effectively set Mars’ geological formation timescale. Since Mars’ accretion is thought to have been mostly complete within 1-10 Myr (Nimmo & Agnor, 2006; Dauphas & Pourmand, 2011), and Earth’s growth continued for ~ 50 -150 Myr (Touboul et al., 2007; Kleine et al., 2009), an early instability provides a natural explanation for the disparity in growth timescales.

3. Low mass asteroid belt: Izidoro et al. (2014) demonstrated that the terrestrial system’s orbits could be generated from a steep initial radial mass distribution. Raymond & Izidoro (2017a) expanded on the model (Izidoro et al., 2015; Raymond & Izidoro, 2017b) by showing that an empty asteroid belt could be populated with volatile-rich material via aerodynamic drag destabilization of planetesimals during Jupiter’s growth phase. Furthermore, these initial conditions, wherein the asteroid belt and Mars-forming region never contained much material in the first place, are largely consistent with modern pebble accretion simulations (Levison et al., 2015a,b; Drążkowska et al., 2016). However, it is still unclear whether such a steep radial distribution of solids is realistic.

Thus the asteroid belt’s low mass is somewhat entangled in the small Mars problem as it

is another piece of the inner solar system that numerical simulations struggle to replicate. As with the small Mars problem, many authors have offered explanations for the asteroid belt’s dynamical state (Petit et al., 2001; O’Brien et al., 2007; Walsh & Morbidelli, 2011; Deienno et al., 2016; Raymond & Izidoro, 2017b,a; Deienno et al., 2018). In a study similar to Paper 1, Deienno et al. (2018) analyzed the effects of an early, “Jumping Jupiter”² style instability on a terrestrial disk composed of 10,000 massless bodies. The authors found good matches to the actual asteroid belt’s structure and composition. Deienno et al. (2018) concluded that the early instability scenario proposed by Paper 1 is viable within the constraints of the asteroid belt, however the total depletion in the main belt is insufficient by about two orders of magnitude (thus the authors favor the low primordial massed asteroid belt model of Izidoro et al., 2015; Raymond & Izidoro, 2017b). The simulations in that paper, however, do not include asteroid self-gravity or the effects of collisional fragmentation. Clement et al. (2019c) investigated the instability’s effect on 3,000, fully self-gravitating asteroids and reported depletions of order 99-99.9% when the giant planets final orbits most closely matched their current configuration. Therefore, a primordially depleted asteroid belt might not be necessary within the early instability framework of Paper 1. The simulations presented in the subsequent sections of our manuscript lack the particle resolution to study the asteroid belt in sufficient detail. In § 4.3.3, however, we comment on the effects of collisional fragmentation in the asteroid belt as compared with the results of Paper 1.

A significant limitation of Paper 1 (and most other numerical studies of terrestrial planet formation) was the treatment of all collisions as perfectly accretionary. Leinhardt & Stewart (2012) and Genda et al. (2012) mapped the various regimes of collisional parameter space, thereby allowing traditional N-body integration packages (Duncan et al., 1998; Chambers, 1999) to be modified to provide an approximation for the effects of fragmentation. Chambers

²A potential solution to the problem of the terrestrial planets orbits being over-excited in simulations of the Nice Model is forcing a rapid jump in the semi-major axes of Jupiter and Saturn (typically achieved by dynamically scattering an Ice Giant on to a highly-eccentric or hyperbolic orbit). Thus Jupiter and Saturn “jump” across their mutual 2:1 MMR, rather than migrate smoothly through it. Through this process, the terrestrial system is less disturbed.

(2013) conducted the first such study, and found the fully evolved systems of planets to be less dynamically excited than those formed using traditional integration schemes due to angular momentum exchange during hit and run collisions. Subsequent authors have used similar codes to study various systems (Dwyer et al., 2015; Bonsor et al., 2015; Carter et al., 2015; Leinhardt et al., 2015; Quintana et al., 2016; Wallace et al., 2017). However, the sample size of such analyses of planet formation in our solar system remains extremely small. In this paper, we repeat the simulations of Paper 1 using a version of the *Mercury6* hybrid integrator that is modified to handle fragmenting collisions (Chambers, 2013). In Paper 1 we posited that an early giant planet instability is potentially compatible with other evolutionary schemes that pre-suppose a prior depleted outer terrestrial disk (the Grand Tack and low mass asteroid belt models). In this paper, we perform an additional suite of simulations where the terrestrial planets form out of a narrow annulus of material (both with and without a Nice Model instability) using the collisional fragmentation scheme. Thus we provide a side-by-side comparison of i) standard initial conditions that assume no prior depletion in the outer disk, ii) standard initial conditions with fragmentation, iii) standard initial conditions with an instability, iv) standard initial conditions with an instability and fragmentation, v) an annulus with fragmentation and vi) an annulus with fragmentation and an instability.

4.2 Methods

4.2.1 Collisional Algorithm

The scheme we utilize for approximating the effects of collisional fragmentation (Chambers, 2013) is limited by the necessity of setting a minimum fragment mass (MFM). Setting too low of a MFM will cause the number of particles in the simulation to rapidly multiply, and make the calculation time unreasonable. Furthermore, collisions producing greater than about 90 fragments can overload the Bulirsch-Stoer portion of *Mercury's* hybrid-symplectic

Name	N_{Pln}	M_{disk} (M_{\oplus})	δr (au)	r_{out} (au)	a_{nep} (au)	Resonance Chain	M_{ice} (M_{\oplus})
5GP	5	35	1.5	30	17.4	3:2,3:2,3:2,3:2	16,16,16
6GP	6	20	1.0	30	20.6	3:2,4:3,3:2,3:2,3:2	8,8,16,16

Table 4.1: Table of giant planet initial resonant configurations from Chapter 3. The columns are: (1) the name of the simulation set, (2) the number of giant planets, (3) the mass of the planetesimal disk exterior to the giant planets, (4) the distance between the outermost ice giant and the planetesimal disks inner edge, (5) the semi-major axis of the outermost ice giant (commonly referred to as Neptune, however not necessarily the planet which completes the simulation at Neptune’s present orbit), (6) the resonant configuration of the giant planets starting with the Jupiter/Saturn resonance, and (7) the masses of the ice giants from inside to outside.

integrator (Wallace et al., 2017). After multiple simulations failed when using MFMs of 0.001 and 0.0025 M_{\oplus} , we found a MFM of 0.0055 M_{\oplus} (around half a lunar mass, or $D \approx 2000$ km assuming $\rho = 3.0 \text{ g/cm}^3$) to be a good choice for 200 Myr simulations of terrestrial evolution. Detailed descriptions of the identical fragmentation scheme can be found in Chambers (2013) and Dwyer et al. (2015). In general, when a collision is detected, the mass of the largest remnant is calculated utilizing relations from Leinhardt & Stewart (2012). Any leftover mass is assigned to a set of equal-massed fragments, each with masses greater than the MFM. The fragments are then ejected in random, uniform directions within the collisional plane at $\sim 5\%$ greater than the two body escape velocity.

4.2.2 Giant Planet Configurations

We described the evolution of our giant planet resonant chains in detail in Chapter 3. Since the parameter space of possible primordial orbits for the outer planets is exhaustive, we use the most successful 5 and 6 planet configurations from Nesvorný & Morbidelli (2012) (Table 4.1). The giant planets are migrated into the appropriate configuration using an additional force designed to approximate gas disk interactions by modifying the equations of motion with forced migration (\dot{a}) and eccentricity damping (\dot{e}) terms (Lee & Peale, 2002; Clement & Kaib, 2017). The resonant chains are then integrated with a 20 day time-step in the presence of 1000 equal-mass primordial Kuiper Belt objects (see Chapter 3) up until

the point when two giant planets first pass within 3 mutual Hill Radii. The terrestrial disks (§ 4.2.3) are then added, and the complete system is integrated through the instability using a 6.0 day time-step.

By its nature, the instability is a chaotic event. Since the parameter space of possible final giant planet configurations is so extensive, outcomes that replicate the actual solar system in broad strokes are quite rare. In fact, only around one third of the best simulation sets in Nesvorný & Morbidelli (2012) finish the integration with the correct number of planets. In Chapter 3, we analyzed all the different outer solar system outcomes, and found that the instability’s tendency to limit the mass and formation time of Mars is largely independent of the particular outcome of the instability. However, we noted that the most successful terrestrial outcomes occurred when the evolution of the giant planets was most akin to that of the solar system in terms of the final period ratio of Jupiter and Saturn, and the excitation of Jupiter’s g_5 mode. For these reasons, we stop simulations if Jupiter and Saturn’s period ratio ever exceeds 2.8, or if an ice giant is not ejected within 5 Myr. In the analysis sections of this manuscript (§ 4.3), we only compare our new fragmentation systems to our Chapter 3 systems with Jupiter and Saturn inside a period ratio of 2.8.

4.2.3 Terrestrial Disks

Standard initial conditions

We follow the same general approach for testing the instability’s effect on terrestrial planet formation as in Chapter 3. We begin by studying the classic model of terrestrial planet formation (Chambers, 2001; O’Brien et al., 2006; Raymond et al., 2006, 2009b). This model, which we refer to as our “standard” set of initial conditions, assumes that the terrestrial planets formed out of a disk of large, Moon-Mars massed planet-forming embryos, and smaller planetesimals, extending between the present location of Mercury and the asteroid belt’s outer edge. Thus, our runs utilizing standard initial conditions assume no prior depletion in the outer terrestrial disk (2.0-4.0 au). Our simulations begin by following the collisional

evolution of 1000 equal-mass planetesimals and 100 equal-mass planet embryos (O’Brien et al., 2006) in the presence of a non-migrating Jupiter and Saturn. Planetesimals only interact gravitationally and undergo collisions with the embryos. Fragments produced in collisions between embryos are treated as fully self-gravitating, while fragments generated in planetesimal-embryo collisions only interact with embryos. Jupiter and Saturn are placed on their pre-instability orbits in a mutual 3:2 mean motion resonance (MMR, $a_j=5.6$ au, $a_s=7.6$ au), a typical outcome of Jupiter and Saturn’s migration during the gas disk phase (Masset & Snellgrove, 2001; Morbidelli & Crida, 2007; Pierens et al., 2014). The initial terrestrial disk mass is set to $5 M_\oplus$, and divided evenly between the embryos and planetesimals. The disk boundaries are at 0.5 and 4.0 au, and the spacing between objects is selected to achieve a surface mass density profile proportional to $r^{-3/2}$. Angular orbital elements are drawn from random, uniform distributions. Eccentricities and inclinations are selected randomly from near circular, Gaussian distributions ($\sigma_e = .02$ and $\sigma_i = .2^\circ$). These initial conditions are selected for their simplicity, and consistency with previous works (Chambers, 2001; Raymond et al., 2006; O’Brien et al., 2006; Raymond et al., 2009b; Kaib & Cowan, 2015). In Chapter 3 we tested different inner disk edges and total disk masses, and found that disks smaller than $5 M_\oplus$ systematically failed to produce Earth and Venus analogs with the correct masses. However, the location of the inner disk edge appeared statistically uncorrelated with any of our success criteria. For these reasons, we do not vary any of these parameters in this work.

We perform 100 simulations as described above using our fragmentation integration scheme (Chambers, 1999, 2013), and a 6 day time-step. We take snapshots of the terrestrial disks at 1.0, 5.0 and 10.0 Myr to input into our giant planet instability simulations (§ 4.2.2). This allows us to test different instability timings with respect to the evolutionary state of the terrestrial disk. In the subsequent text, we refer to these sets collectively as our instability set. The various grouping of simulations testing different instability delay times are referred to as “batches,” and individual simulations are called “runs.” The most successful outcomes of Chapter 3 occurred in the 1.0 and 10.0 Myr simulation batches, hence

our choices of output times. The same systems are also integrated up to 200 Myr without any giant planet evolution, and become our standard initial condition control set (we refer to this set henceforward as the standard set).

Annulus initial conditions

Our annulus set of simulations are set up much the same as the standard initial condition set, with two exceptions. The annulus runs begin with just 400 embryos (planetesimals are not used) distributed between 0.7 to 1.0 au (Hansen, 2009). For this batch, we only take a snapshot at 10 Myr for input into a Nice Model instability due to the massive computational requirements of this project. The annulus runs are also integrated up to 200 Myr without giant planet evolution, and become the annulus control set (referred to henceforward as the annulus set). Otherwise, the integrator, initial giant planet configuration, time-step and orbital element selection method are the same as described above. We summarize the initial conditions used in our various integrations in Table 4.2.

The low mass asteroid belt (Izidoro et al., 2014, 2015; Raymond & Izidoro, 2017b) and Grand Tack (Walsh et al., 2011; Jacobson & Morbidelli, 2014; Rubie et al., 2015; Deienno et al., 2016; Brasser et al., 2016a; Walsh & Levison, 2016) models both assume a truncated terrestrial disk that is largely depleted of material in the primordial asteroid belt and Mars-forming regions (Morbidelli & Raymond, 2016). Our present study is by no means an exhaustive investigation of either the Grand Tack or low mass asteroid belt scenarios. We begin our annulus simulations with overly-simplified initial conditions. Furthermore, our study does not model the inward and outward migration phase of the Grand Tack. Nevertheless, we still present these simulations in § 4.3.5 for three reasons. First, to understand whether accounting for fragmentation is a potential barrier to the success of the annulus setup (also addressed for the Grand Tack in Walsh & Levison, 2016). Second, to ascertain whether the initial conditions are compatible with the early instability framework of Chapter 3 (an open-ended question from that work). And finally, to study the relative accretion timescales

of the planets.

Set	a_{in} (au)	a_{out} (au)	M_{tot} (M_{\oplus})	N_{emb}	N_{pln}	N_{GP}	t_{instb} (Myr)	N_{sim}
standard	0.5	4.0	5.0	1000	100	2	N/A	100
annulus	0.7	1.0	2.0	400	0	2	N/A	100
standard/5GP/1Myr	0.5	4.0	5.0	1000	100	5	1	31
standard/5GP/5Myr	0.5	4.0	5.0	1000	100	5	5	8
standard/5GP/10Myr	0.5	4.0	5.0	1000	100	5	10	21
standard/6GP/1Myr	0.5	4.0	5.0	1000	100	6	1	13
standard/6GP/5Myr	0.5	4.0	5.0	1000	100	6	5	30
standard/6GP/10Myr	0.5	4.0	5.0	1000	100	6	10	40
annulus/5GP/10Myr	0.7	1.0	2.0	400	0	5	10	27
annulus/6GP/10Myr	0.7	1.0	2.0	400	0	6	10	46

Table 4.2: Summary of initial conditions for complete sets of terrestrial planet formation simulations. The columns are (1) the name of the simulation set, (2) the inner edge of the terrestrial forming disk, (3) the disk’s outer edge, (4) the total disk mass, (5) the number of equal-mass embryos used and (6) the number of equal-mass planetesimals used, (7) the number of giant planets, (8) the instability timing in Myr, and (9) the total number of integrations comprising the set (Note that each set begins with 100 calculations, however instability runs where Jupiter and Saturn exceed a period ratio of 2.8 or an ice giant is not ejected within 5 Myr are removed). In the subsequent text, we often refer to the 6 standard/XGP/XMyr (rows 3-8) collectively as our instability sets. It should also be noted that the “standard” set was referred to as the “control” set in Chapter 3.

Code	Criterion	Actual Value	Accepted Value	Justification
A	a_{Mars}	1.52 au	1.3-2.0 au	Inside AB
A,A1	M_{Mars}	$0.107 M_{\oplus}$	$> 0.025, < .3M_{\oplus}$	(Raymond et al., 2009b)
A,A1	M_{Venus}	$0.815 M_{\oplus}$	$> 0.6 M_{\oplus}$	Within $\sim 25\%$
A,A1	M_{Earth}	$1.0 M_{\oplus}$	$> 0.6 M_{\oplus}$	Match Venus
B	τ_{Mars}	1-10 Myr	< 10 Myr	
C	τ_{\oplus}	50-150 Myr	> 50 Myr	
D	M_{AB}	$\sim 0.0004 M_{\oplus}$	No embryos	(Chambers, 2001)
E	ν_6	~ 0.09	< 1.0	
F	WMF_{\oplus}	$\sim 10^{-3}$	$> 10^{-4}$	Order of magnitude
G	AMD	0.0018	< 0.0036	(Raymond et al., 2009b)

Table 4.3: Summary of success criteria for the inner solar system from Chapter 3. The rows are: (1) the semi-major axis of Mars, (2-4) The masses of Mars, Venus and Earth, (5-6) the time for Mars and Earth to accrete 90% of their mass, (7) the final mass of the asteroid belt, (8) the ratio of asteroids above to below the ν_6 secular resonance between 2.05-2.8 au, (8) the water mass fraction of Earth, and (9) the angular momentum deficit (AMD) of the inner solar system.

4.2.4 Success Criteria

We employ the same success criteria for our fully formed terrestrial disks as in Chapter 3 (Table 4.3). Because we remove all systems where the Saturn to Jupiter period ratio is greater than 2.8, or if an ice giant is not ejected within 5 Myr, we do not scrutinize our systems against the Nesvorný & Morbidelli (2012) giant planet success criteria as in Chapter 3. The motivation for the success criteria is described in detail in Chapter 3. Here, we provide a brief synopsis for each criterion we utilize, and any alterations we made from Chapter 3.

The Structure of the Inner Solar System

We use metrics from Chambers (2001) to scrutinize the general orbital structure of the inner solar system. Criteria A and A1 quantify the terrestrial planetary system’s semi-major axis spacing and mass distribution. Any planets formed in the region between 1.3-2.0 au are considered Mars analogs. The inner limit of this region is close to Mars’ actual pericenter (~ 1.38 au) and the outer edge lies at the asteroid belt’s inner limit. Criterion A is satisfied

if the Mars analog is smaller than $0.3 M_{\oplus}$, exterior to Earth and Venus analogs each with masses greater than $0.6 M_{\oplus}$, and the asteroid belt is devoid of objects more massive than $0.3 M_{\oplus}$. Criterion A1 is similar, but it also includes systems that form no Mars, and those that meet the mass distribution requirement but fail the semi-major axis requirements as being successful. We also scrutinize the mass distribution of each system statistically, using a normalized radial mass concentration statistic (RMC in Eq. 4.1; Chambers, 2001). A system of planets dominated by a single, massive planet would yield a steep mass concentration function (the expression in parenthesis) and thus have a high RMC. A system with many smaller planets, and a smoother mass concentration function, would yield a lower RMC. We normalize all of our RMC values to the solar system statistic for Mercury, Venus, Earth and Mars ($RMC_{SS} = 90$).

$$RMC = MAX \left(\frac{\sum_i m_i}{\sum_i m_i [\log_{10}(\frac{a}{a_i})]^2} \right) \quad (4.1)$$

To quantify the orbital excitation of our terrestrial systems, we calculate the angular momentum deficit (AMD, Eq. 2.1; see § 2.2.2) for each planetary system. AMD (Laskar, 1997) computes the degree to which a system of orbits differs from one with circular and co-planar orbits. Because chaotic dynamics can cause the solar system’s AMD to naturally evolve by as much as a factor of two over Gyr integrations (Laskar, 1997; Agnor, 2017), we only require our systems achieve an AMD less than twice the solar system’s modern value of 0.0018 (criterion G). For both our AMD and RMC calculations, we only consider planets (Mercury-massed objects and larger; $m > 0.055 M_{\oplus}$) that are not in the asteroid belt ($a < 2$ au). This allows us to best compare our simulated systems with the actual solar system. It should also be noted that, given our choice of MFM (one tenth that of our planet cut-off mass), fragments are rarely considered in our RMC and AMD calculations.

Relative Formation Timescales

As we discussed in Chapter 3, the disparity between Mars’ inferred rapid formation timescale of just a few million years (Nimmo & Agnor, 2006; Dauphas & Pourmand, 2011; Kruijer et al., 2017) and Earth’s (longer by about a factor of 10; Touboul et al., 2007; Kleine et al., 2009) is an important and defining trait of the inner solar system. However, there is considerable uncertainty in both of these Hf/W dates (Dauphas & Pourmand, 2011). Therefore, we only require our Mars analogs accrete 90% of their final mass within 10 Myr (criterion B), and our Earth’s take at least 50 Myr to do the same (criterion C).

The Asteroid Belt

In Chapter 3 we argued that standard embryo accretion models have insufficient mass and particle resolution to accurately study the asteroid belt. In particular, we model the belt with $0.025 M_{\oplus}$, fully self-gravitating embryos and $0.0025 M_{\oplus}$ planetesimals that only interact gravitationally with the larger objects (each object being tens to hundreds of times more massive than the entire present belt). If perturbations from the giant planets are the dominant sculpting mechanisms in the asteroid belt, then we could expect each individual asteroid to behave as a test particle. Meanwhile, if asteroid belt ”self-stirring” is a more important process, then our super-massive asteroid bodies likely overestimate the level of self-stirring. Furthermore, our choice of initial conditions could also lead to unrealistic fragmentation effects since it requires less energy to break apart a small asteroid than a larger one. These issues are addressed with more detailed simulations in a complimentary study (Clement et al., 2019c). Nevertheless, for completeness, we include the same criteria for the asteroid belt as in Chapter 3 (an asteroid belt completely depleted of planetary embryos, criterion D, and the ratio of asteroids above to below the ν_6 secular resonance between 2.05 and 2.8 au less than 1.0, criterion E).

Earth’s Water Content

Studies and models for the origin of Earth’s water are numerous in the literature. A complete discussion of this topic is far beyond the scope of this Chapter (for robust reviews of various ideas see [Morbidelli et al., 2000, 2012](#); [Marty et al., 2016](#)). As in Chapter 3, we assume a simple bulk distribution ([Eq. 4.2](#)) of water-rich material similar to [Raymond et al. \(2009b\)](#). This distribution assumes that the inner solar system and primordial asteroid belt region was populated with water-rich material from the outer solar system during the gas disk phase ([Raymond & Izidoro, 2017a](#)). Criterion F is satisfied if an Earth analog’s ($m > 0.6 M_{\oplus}$, $0.85 < a < 1.3$ au) water mass fraction (WMF) is boosted to greater than 10^{-4} .

$$WMF = \begin{cases} 10^{-5}, & r < 2au \\ 10^{-3}, & 2au < r < 2.5au \\ 10\%, & r > 2.5au \end{cases} \quad (4.2)$$

4.3 Results and Discussion

We begin by summarizing the percentages of each simulation subset that meet our various success criteria in a modified version of [Table 3.4](#) from Chapter 3 ([Table 4.4](#)). In [Figure 4.1](#), we plot the distribution of planet masses and semi-major axes for each simulation subset as well. In this work we stop all simulations where Jupiter and Saturn’s period ratio exceeds 2.8. Additionally, we only test instability delay times of 1.0, 5.0 and 10.0 Myr (as opposed to Chapter 3 where we investigated 0.01, 0.1, 1.0 and 10.0 Myr). Because of these differences, in the subsequent analysis sections we only compare our current results with the Chapter 3 systems that tested 1.0 and 10.0 Myr instability delay times, and finished with Jupiter and Saturn within a period ratio of 2.8.

Set	A	A1	B	C	D	E	F	G
	a, m_{TP}	m_{TP}	τ_{mars}	τ_{\oplus}	M_{AB}	ν_6	WMF	AMD
std	2 (+2)	2 (+2)	33 (+24)	80 (-5)	2 (0)	0 (-53)	82 (-4)	15 (+7)
ann	58	58	51	27	85	3	N/A	50
std/5GP/1Myr	35 (+9)	35 (+9)	23 (+11)	80 (-15)	70 (+50)	0 (-29)	40 (-25)	12 (-1)
std/6GP/1Myr	33 (+22)	33 (+6)	25 (+13)	100 (+8)	77 (+35)	11 (-32)	66 (-2)	37 (+35)
std/5GP/5Myr	13	13	50	50	100	13	75	25
std/6GP/5Myr	17	24	40	100	27	3	91	17
std/5GP/10Myr	36 (+27)	36 (+18)	28 (+21)	83 (-8)	44 (+28)	4 (-25)	83 (+30)	32 (+7)
std/6GP/10Myr	17 (-2)	17 (-15)	50 (+23)	77 (-9)	47 (+22)	0 (-52)	77 (+0)	29 (+27)
ann/5GP/10Myr	22	22	64	20	94	0	N/A	17
ann/6GP/10Myr	29	32	76	12	97	2	N/A	29

Table 4.4: Summary of percentages of systems which meet the various terrestrial planet success criteria established in Table 4.3. Values in parenthesis indicate the change from the same simulation set in Chapter 3 (where fragmentation was not considered). The subscripts TP and AB indicate the terrestrial planets and asteroid belt respectively.

4.3.1 The Small Mars Problem

Our fragmentation simulations perform better than the systems from Chapter 3 when measured against some of our success criteria, but perform worse when scrutinized against others. As evidenced by criterion A and A1 success rates of $\sim 15\text{-}35\%$ (Table 4.4), an orbital instability still seems to be more efficient at replicating the actual terrestrial system than standard initial conditions without any giant planet evolution. The most obvious difference between the terrestrial systems formed in this work, and those from Chapter 3, is that when fragmentation is included, the simulations produce consistently larger Mars analogs (Figure 4.1). Indeed, when we compare the cumulative distributions of Mars analogs formed across our various simulation sets (Figure 4.2) we find that the addition of the fragmentation algorithm leads to a marked increase in Mars masses for our instability runs. This is particularly the case in our batches testing later instability delay times (5.0 and 10.0 Myr). Though systems in our 1.0 Myr instability delay batches consistently produce the best Mars analogs (Figures 4.1 and 4.2), they are also more likely to destroy Mars all together.

In Chapter 3 we argued that earlier instability delay times (0.01 and 0.1 Myr) are less successful at generating a small Mars. When the instability occurs earlier in the process of terrestrial planet formation, a greater fraction of the total disk mass is distributed in a sea of small planetesimals. The increased dynamical friction between the planetesimals and growing embryos that remain after the instability truncates the disk has a net spreading effect. While the instability does remove mass from the Mars-forming region, the area is essentially repopulated with material as the mass distribution profile flattens via dynamical friction and scattering events. Furthermore, the increased dynamical friction in the vicinity of the growing Mars tends to dampen orbits in the area, and prevents the unstable giant planets from exciting material on to orbits where it is lost from the system. These combined effects tend to yield over-massed Mars and under-massed Earth and Venus analogs.

In this study, we find that the fragmentation process has much the same effect as an overly-early instability. The total particle number in the disk stays consistently higher

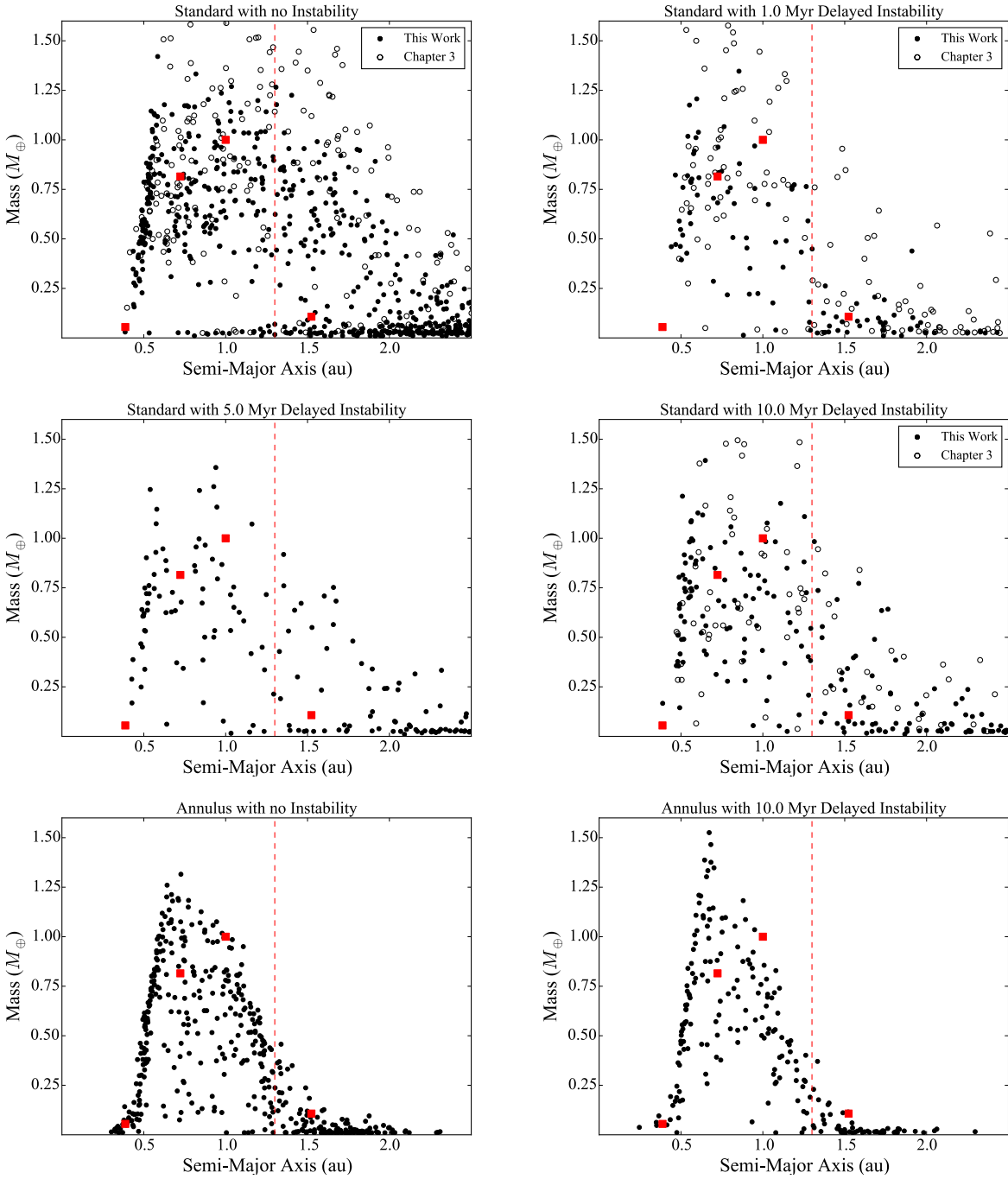


Figure 4.1: Distribution of semi-major axes and masses for all planets formed in all simulation sets. The red squares denote the actual solar system values for Mercury, Venus, Earth and Mars. The vertical dashed line separates the Earth and Venus analogs (left side of the line) and the Mars analogs (right side). Planets from Chapter 3 simulations that do not include collisional fragmentation (control (standard) sets, 1.0 Myr and 10.0 Myr instability delays) are denoted with open circles.

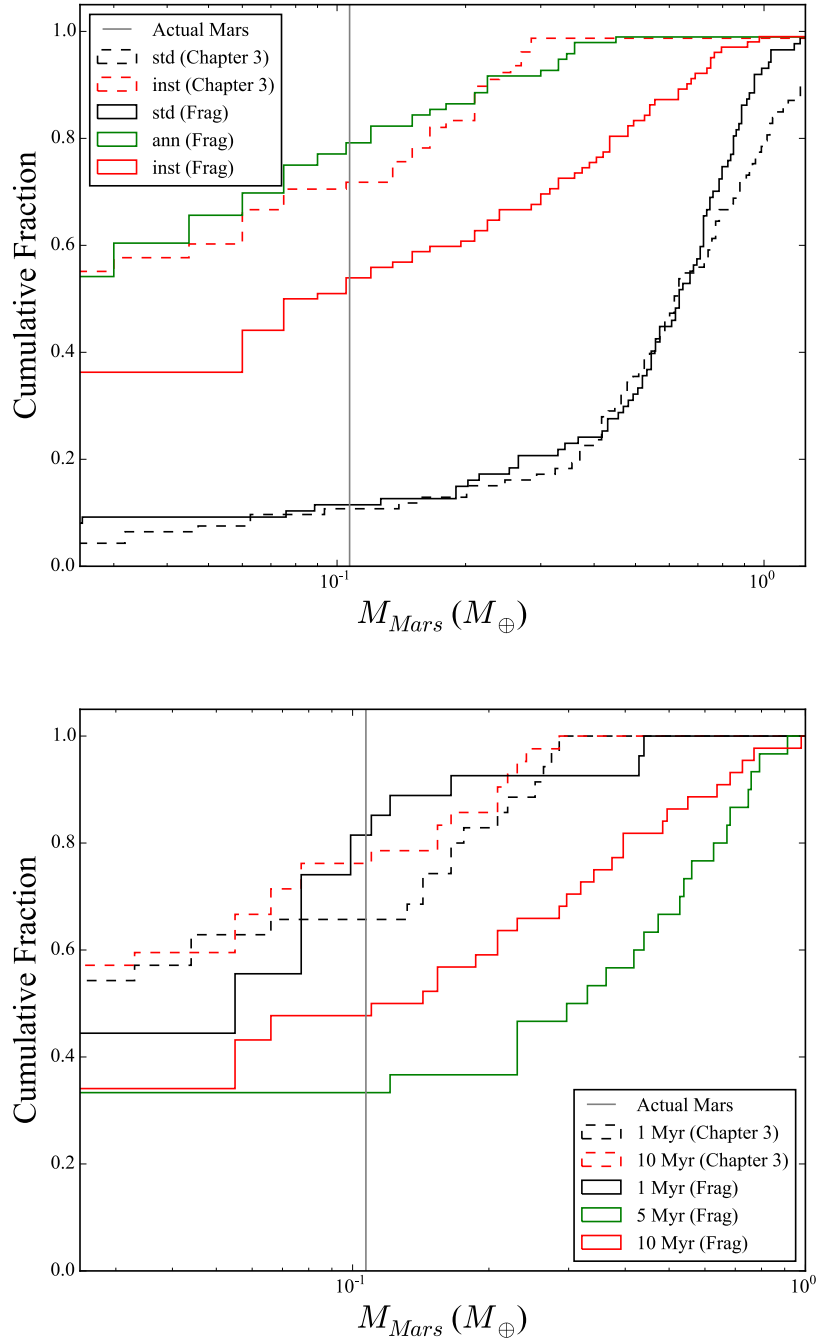


Figure 4.2: The top panel depicts the cumulative distribution of Mars analog masses formed in our various fragmentation simulation sets (solid lines) compared with our results from Chapter 3 (dashed lines). The bottom panel depicts the same data for the various instability delay times tested in this work (solid lines), and in Chapter 3 (dashed lines). The grey vertical lines corresponds to Mars actual mass. Note that some systems may form multiple planets in this region, but here we only plot the most massive planet. Systems that do not form a Mars analog via embryo accretion are plotted as having zero mass.

for longer in the fragmentation simulations because of particle addition via fragmenting collisions and accounting for hit-and-run collisions (which would be treated as mergers by conventional integrators). Though objects that hit-and-run typically go on to merge later in the simulation, the effect is still significant. In fact, hit-and-runs account for $\sim 30\%$ of all collision events in our different standard simulation sets, and $\sim 40\%$ in the various annulus runs. The net effect is greater dynamical friction in the new fragmentation simulations than in Chapter 3. To demonstrate this, the upper panel of [Figure 4.3](#) plots an exponential fit of the average particle number for all instability simulations in this Chapter versus the corresponding set of simulations from Chapter 3 (note, in this plot $t=0$ corresponds to the instability time). In the bottom two panels, we plot the average eccentricity and inclination of all eventual Earth and Venus analogs (defined in this study as fully formed planets with $a < 1.3$ and $m > 0.6 M_{\oplus}$; see [§ 4.2.4](#)) at each simulation data output point. Since embryo orbits are constantly being damped in the disk, it is more difficult for the excited giant planets to remove material from the Mars-forming region than in Chapter 3.

A significant percentage ($\sim 35\%$) of our instability systems form no Mars analog; instead leaving behind a handful of planetesimals or collisional fragments in the region with masses of order 2-5% the actual mass of Mars. Though $\sim 30\%$ of the remaining systems that do form Mars analogs via embryo accretion form planets less massive than Mars (over half are within our success criterion mass of $0.3 M_{\oplus}$), the instability’s tendency to totally inhibit Mars’ formation is a potential weakness of the early instability scenario. We note that this effect is most pronounced in our 1.0 Myr instability delay set. $\sim 47\%$ of these systems fail to grow a Mars analog via embryo accretion. Because the average embryo mass is smaller, collisional grinding in the region is more efficient. The average impact velocity (in terms of the mutual, two body escape velocity) for fragmenting collisions is 12% higher in the 1.0 Myr batch than in the 5.0 and 10.0 Myr batches. Thus more excited fragments are produced and growth is inhibited.

In general, accounting for collisional fragmentation tends to result in worse Mars analog

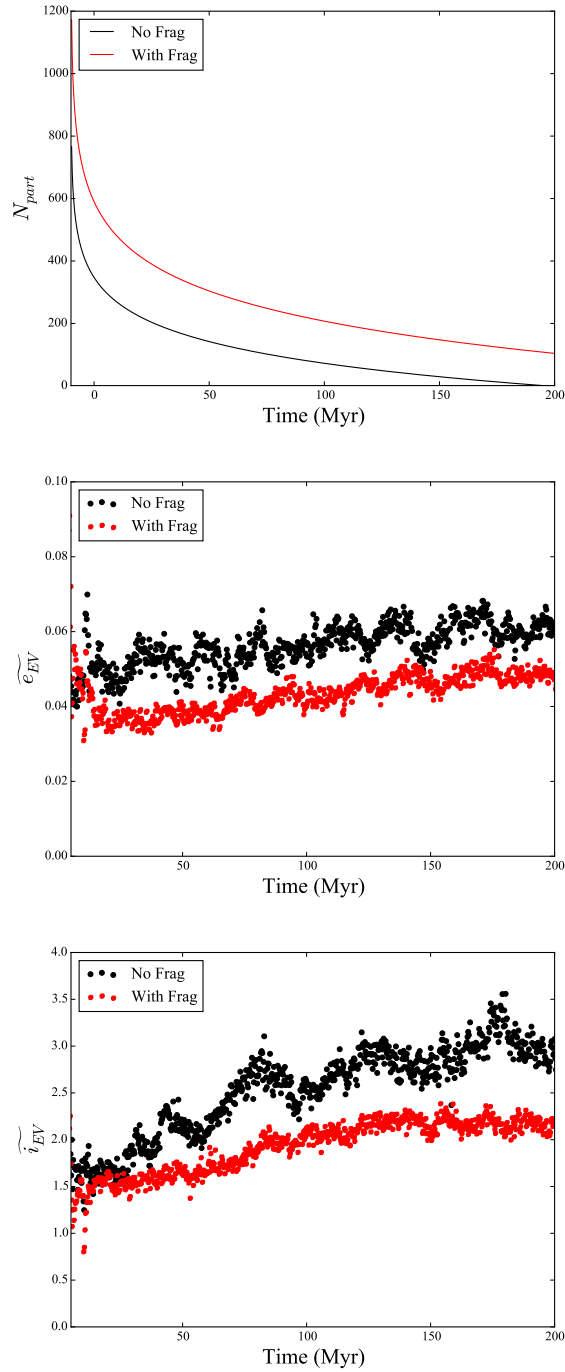


Figure 4.3: Comparison of disk properties in our instability simulations that include fragmentation (this work) and those performed using a conventional integration scheme (Chapter 3). The red and black lines in the upper panel plot an exponential fit of the average total particle number in the terrestrial forming disk with respect to time. The red and black points denote mean eccentricities (middle panel) and inclinations (bottom panel) for growing Earth and Venus analogs.

masses, and more realistic terrestrial eccentricities and inclinations. The Mars analogs in our fragmentation runs are consistently larger than those formed in Chapter 3. However, they are still dramatically smaller than those in our standard runs without an instability, and well within our established criteria for success (§ 4.2.4). Additionally, as we showed in Chapter 3, the majority of our systems with larger Mars analogs experience instabilities that fail to sufficiently excite Jupiter’s eccentricity. In many instances, including the effects of collisional fragmentation results in producing fully evolved systems that are better matches to the actual solar system. In Figure 4.4, we plot an example of the evolution of such a successful system where the final orbits and masses of both the inner and outer planets are most akin to the present solar system. Though Saturn and Uranus are over-excited, this particular system is highly successful at matching the low orbital eccentricities of the modern terrestrial system. We discuss this effect in greater detail in § 4.3.4.

4.3.2 Mars’ Formation Timescale

In Chapter 3, we argued that an early instability provides a natural explanation for the disparity between the inferred geological accretion timescales of Earth and Mars. Since the perturbative effect of the excited giant planet orbits (particularly Jupiter and Saturn) is most pronounced in the Mars-forming region and the asteroid belt, Mars’ accretion is essentially “shut off” by the instability. In that work, we noted that $\sim 40\%$ of Mars analogs underwent no impacts with embryos following the instability time. In this study, we find that effect to be more pronounced due to the integrator’s ability to account for hit-and-run collisions. Depending on the relative velocities and masses involved in such collisions, either all, some or none of the projectile material can be accreted (or re-accreted) over the course of the simulation. Some objects undergo tens of repeated hit-and-run collisions with one another. Through this process, it is possible to have a net erosive effect on the larger body.

Since the parameter space of collisional scenarios is quite complex (number of repeated hit and run collisions, number of initial bodies involved, number of fragments produced,

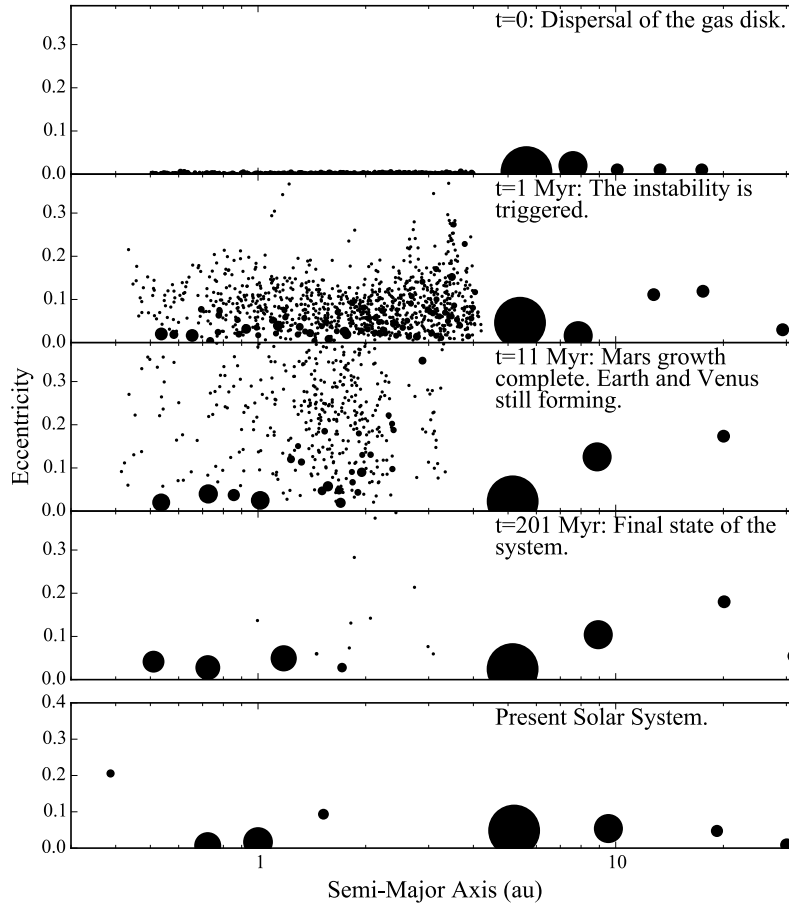


Figure 4.4: Semi-Major Axis/Eccentricity plot depicting the evolution of a successful system in the standard/5GP/1Myr batch. The size of each point corresponds to the mass of the particle (because Jupiter and Saturn are hundreds of times more massive than the terrestrial planets, we use separate mass scales for the inner and outer planets). The final terrestrial planet masses are 0.52, 0.68, 0.76 and 0.08 M_{\oplus} respectively.

number of fragments involved in subsequent interactions, etc), it is difficult to encapsulate this statistically. Nevertheless, hit-and-run collisions are extremely common collisional outcomes in our simulations ($\sim 40\%$ for all collisional interactions in the annulus sets, and $\sim 30\%$ in the standard sets). The result is that, for our fragmentation instability systems, $\sim 60\%$ of Mars analogs undergo no complete accretion events with other embryos following the instability time. For this reason, our fragmentation runs have much higher rates of satisfying success criterion B (the formation timescale of Mars) than in Chapter 3 (see [Table 4.4](#)). Furthermore, Mars analogs in this study accrete at least 90% of their mass an average of 56 Myr faster than Earth analogs (as compared to 39 Myr in Chapter 3 systems).

4.3.3 Collisional Evolution of the Asteroid Belt

As we discuss in [§ 4.2.4](#), it is difficult to study the detailed structure of the asteroid belt using $0.025 M_{\oplus}$ embryos and $0.0025 M_{\oplus}$ planetesimals. Even our minimum fragment mass of $\sim 0.0055 M_{\oplus}$ is 37 times that of the largest asteroid in the belt, Ceres (see discussion in [§ 4.2.4](#)). In spite of our coarse asteroid belt resolution, two general trends are obvious. First, our fragmentation systems have consistently higher rates of meeting success criterion D (leaving behind no embryos in the asteroid belt) than in Chapter 3. Second, our new simulations have lower rates for satisfying criterion E (ratio of main belt asteroids with $a < 2.8$ au above to those below the ν_6 secular resonance). We find that this is because collisional fragmentation tends to prevent asteroids from growing larger and accreting in to planets after they are excited by the instability; often times completely shattering them in to many smaller fragments. Because our fragmentation simulations' embryos stay smaller for longer, they are more easily shattered and destroyed completely in fragmenting collisions. The main belt's population of relatively young collisional families suggests that its structure has evolved significantly since the epoch of planet formation ([Bottke et al., 2006a](#); [Walsh et al., 2013](#); [Bottke et al., 2015](#); [Dermott et al., 2018](#)). However, it is extremely difficult to reconstruct the primordial size distribution from the current observed population ([Bottke et al., 2005b,a](#);

Delbo' et al., 2017). Yet empirical evidence suggests that collisional fragmentation is a dominant process in sculpting the belt's structure (Dermott et al. (2018) argued that 85% of all inner main belt asteroids originate from just 5 families). Since traditional N-body routines used to study planetary dynamics treat all collisions as perfectly accretionary (Duncan et al., 1998; Chambers, 1999), studying these processes numerically has been difficult until recently (Chambers, 2013; Walsh & Levison, 2016).

Collisions of any kind, including those of the fragmenting variety, are less frequent in the asteroid belt than in the inner solar system due to the lower surface density of material, longer accretion timescales, and higher degree of orbital excitation. However, when collisions do occur, it is easier for the ejected fragments to survive in the asteroid belt without being re-accreted. This is because our integrators fragment ejection velocity (set to $\sim 5\%$ greater than the mutual escape velocity in this study) represents a higher percentage of the mean orbital velocity in the region. Therefore, it is easier for fragments in the asteroid belt to be ejected on to orbits where they interact less frequently with the original target embryo. Indeed, over 11% of all surviving asteroids in our instability systems are collisional fragments. Additionally, the inclusion of collisional fragmentation further lengthens the accretion timescale in the asteroid belt. This makes it more difficult for embryos in the asteroid belt to grow in to larger, planet-massed objects; resulting in higher success rates for criterion D.

The small number statistics involved in analyzing each asteroid belt (most contain less than about 30 asteroids) individually can make our calculated ν_6 ratios somewhat uncertain. However, we note that over half of the surviving asteroid belt collisional fragments in our instability simulations are on orbits above the ν_6 resonance. Given the highly excited fragment ejection orbits that are possible in the asteroid belt, this seems to make sense. However, the vast majority of these asteroids are also on highly eccentric, Mars-crossing orbits. If we remove fragments on Mars-crossing orbits, only 8% of the remaining fragment asteroids are above the ν_6 resonance. This is in good agreement with the actual asteroid belt's inclination structure, where the ratio of objects above to those below the ν_6 secular resonance is 0.08.

Because collisions occur more frequently at lower inclinations and eccentricities, those asteroids are more likely to be broken up and populate the low inclination parameter space with fragments. In contrast, over half of all primordial asteroids (embryos and planetesimals) finish the integration above the ν_6 resonance.

Though future simulations similar to those in [Deienno et al. \(2018\)](#) and [Clement et al. \(2019c\)](#) are required to validate the effect of a full early instability on the asteroid belt, our fragmentation simulated asteroid belts are encouraging for three reasons. First, the additional dynamical friction provided by collisional fragments does not have an appreciable effect on the overall depletion in the Asteroid Belt. Our new asteroid belts consistently deplete the region at the 90-99% level. Second, fragmenting and hit-and-run collisions significantly reduce the rate of planet formation in the asteroid belt. Finally, non Mars-crossing collisional fragments tend to preferentially populate the inclination parameter space below the ν_6 secular resonance.

4.3.4 AMDs and RMCs

When we scrutinize the systems formed using our fragmentation code, we observe the same general trend of lower final system AMDs as in [Chambers \(2013\)](#). Including fragmentation in our calculation results in a substantial drop in the AMDs of the fully formed terrestrial systems (for a complete discussion consult [Chambers, 2013](#)). In [Figure 4.5](#) (top panel) we plot the cumulative distribution of AMDs for our various simulation sets (standard, annulus and instability) compared with the standard and instability sets from Chapter 3. Though the majority of all the simulation sets besides the annulus runs still possess AMDs larger than the current solar system value, the solar system falls closer to the heart of our new fragmentation AMD distributions. In Chapter 3, fewer than 10% of our instability systems had AMDs less than that of the modern solar system. In contrast, over 25% of the instability systems from our present study have AMDs less than the solar system value. Since the solar system’s terrestrial architecture is well within the spectrum of outcomes that we observe, we

argue that accounting for collisional fragmentation is a compelling solution to the terrestrial excitation problem. Furthermore, given studies that have shown terrestrial AMDs to evolve by a factor of two in either direction over Gyr timescales (Laskar, 1997; Agnor, 2017), it may not be necessary for the system AMD to be precisely matched after 200 Myr of planet formation.

In addition to significantly de-exciting the orbits of the fully formed terrestrial planets, accounting for collisional fragmentation also tends to yield systems with better RMCs. We plot the cumulative distribution of RMCs for our different simulation sets (and Chapter 3 systems) in the bottom panel [Figure 4.5](#). The runs without a Nice Model instability (standard set) from both Chapter 3 and our present study consistently yield low RMC values due to the abundance of over-massed Mars analogs and large planets in the asteroid belt. Our annulus simulations also consistently possess low RMCs because their final architectures often consist of several tightly packed, under-massed planets. In contrast, more widely spaced systems of larger planets are more common in the standard sets. These differences reflect the differences in initial mass distribution between the two sets.

In general, our instability sets consistently yield the best RMC values. Though the instability sets both with and without fragmentation have similar fractions of systems with RMCs greater than and less than that of the solar system, the average fragmentation system value is closer to the solar system than in Chapter 3 (0.73 as opposed to 0.62). However, many of the fragmentation instability simulation RMCs are lower due to slightly larger Mars analogs ([§ 4.3.1](#)).

In addition to orbits being damped via angular momentum exchange during hit-and-run collisions, dynamical friction between fragments generated in collisions also plays a role in improving system AMDs and RMCs (see discussion in [§ 4.3.1](#) and [Figure 4.3](#)). Though this process tends to result in larger Mars analogs on average, our sample of fully formed systems contains multiple runs that simultaneously meet our constraints for terrestrial system mass distribution and AMD (criterion A and G). In particular, systems with more realistic

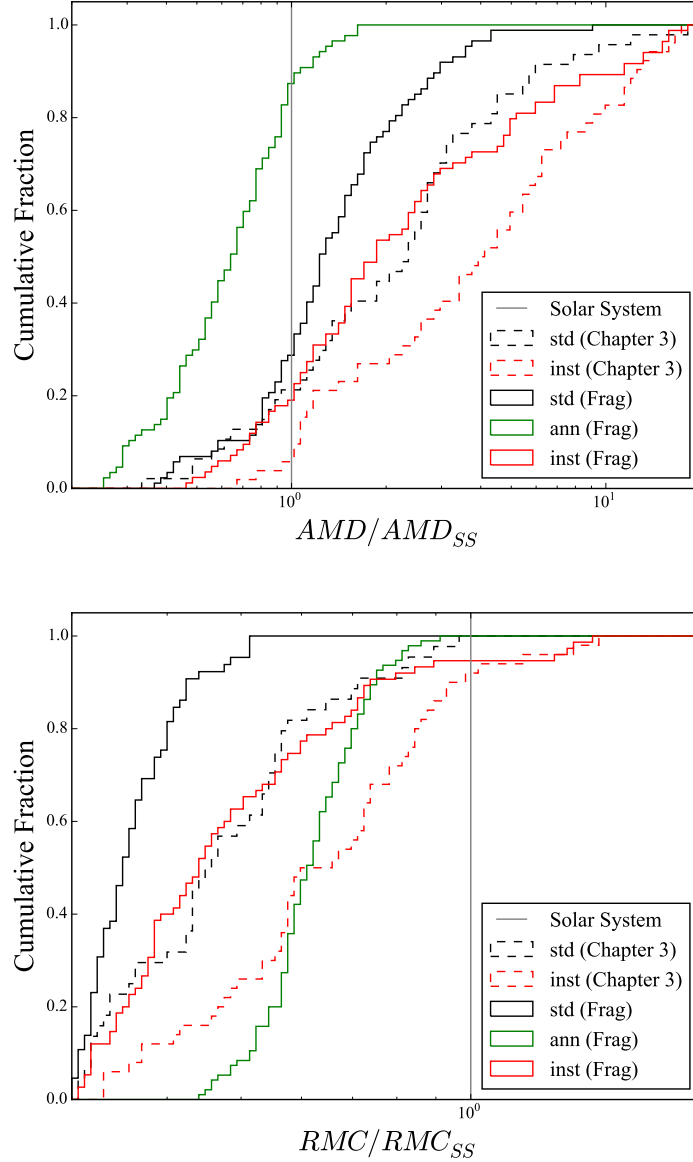


Figure 4.5: Cumulative distribution of normalized AMDs (top panel) and RMCs (bottom panel) for the terrestrial systems formed in our various fragmentation simulation sets (solid lines) compared with our results from Chapter 3 (dashed lines). The grey vertical line corresponds to the solar system value (1 by normalization). Each statistic is calculated utilizing all terrestrial objects that complete the simulation with $a < 2.0$ au and $m > 0.055 M_{\oplus}$, and normalized to the modern solar system value.

Earth/Venus spacings ($\Delta a_{EV,SS} = 0.28$ au) are able to survive 200 Myr of planet formation without combining into a super-Earth. Indeed, the median semi-major axis spacing between Earth and Venus analogs is 10% less in our instability fragmentation simulations than in Chapter 3. This is also true for the standard set, where the fragmentation simulations' Δa_{EV} is 11% less than in Chapter 3 systems. Thus, accounting for collisional fragmentation leads to forming systems that are better matches to the actual terrestrial system in terms of the Earth/Venus spacing, and total AMD.

4.3.5 Annulus Initial Conditions

Since the annulus simulation set consistently outperforms our other sets in many of our analyses (specifically the masses of Mars analogs, the AMD of the terrestrial system, and our total inner solar system structure success criterion A; see Figures 4.1, 4.2 and 4.5), the answer to the question of fragmentation's effect on the setup is fairly straightforward. Our simulations indicate that collisional fragmentation is not a significant impediment to the success of the low mass asteroid belt or Grand Tack models; both of which assume a truncated terrestrial disk similar to our annulus initial conditions. In fact, collisional fragmentation could provide a mechanism for populating a primordially empty asteroid belt (Izidoro et al., 2015) with silicate-rich material from the inner solar system. Indeed, 48% of all final surviving asteroid belt objects in our annulus simulation set are implanted fragments (though $\sim 90\%$ of them are on highly eccentric, Mars crossing orbits).

In Chapter 3 we showed that the Nice Model instability is efficient at disturbing and depleting the terrestrial disk mass in the Mars-forming region and beyond ($a > 1.3$ au). Since our annulus simulation set begins with all the terrestrial forming mass concentrated in a narrow annulus with $0.7 < a < 1.0$ au, we do not expect the instability to have a substantial effect on the planet formation process in these simulations. Indeed, the annulus/XGP/10Myr simulations have similar success rates for criteria A and A1 (the bulk architecture of the inner solar system) as the annulus simulations (which do not include any giant planet evolution).

The instability set is, however, less successful at satisfying the terrestrial AMD requirement (criterion G). This is expected given the tendency for the terrestrial planets to be excited by the evolving giant planet orbits in simulations of the Nice Model (Brasser et al., 2009; Agnor & Lin, 2012; Brasser et al., 2013; Kaib & Chambers, 2016). Furthermore, since the annulus set begins with a larger number of embryos on Hill-crossing orbits, they evolve much quicker (see discussion below), and are at a more advanced stage of evolution when the instability ensues. Therefore, the effect of fragmentation and hit-and-run collisions on AMDs (§ 4.3.4) is less drastic in the annulus instability set.

Overall, the results of the annulus/5GP/10Myr and annulus/6GP/10Myr simulations do not differ substantially from the annulus set. These sets frequently produce systems that broadly match the observed characteristics of the real inner solar system. An example of a successful simulation is plotted in Figure 4.6. These results should be taken in the appropriate context given the over-simplification of our annulus initial conditions. The important conclusion is that timing the orbital instability in conjunction with terrestrial planet formation (regardless of the terrestrial disk initial conditions or prior evolutionary scheme) is a viable solution to the problem of terrestrial system disruption in a late instability scenario (particularly the high rates of collisions and ejections).

Finally, we note that the Earth analogs ($m > 0.6 M_{\oplus}$, $0.85 < a < 1.3$ au) in all of our annulus simulation sets have much lower rates of satisfying criterion C (geological formation timescale of Earth; only 27% of annulus systems). Mars analogs in the annulus set form an average of just 11 Myr faster than their counterpart Earth analogs (as compared to 56 Myr in our instability sets). Given the higher initial surface density, faster accretion timescales are expected in this set. Indeed, 3 of our annulus Earth analogs accrete 90% of their mass in less than 20 Myr. To test whether this is a consequence of our use of 400 self-gravitating embryos, and no planetesimals (see also Jacobson & Morbidelli, 2014), we perform an additional batch of 25 simulations that include planetesimals. The setup for these integration is identical to the annulus set’s initial conditions, with the exception of the disk mass being divided in to 1

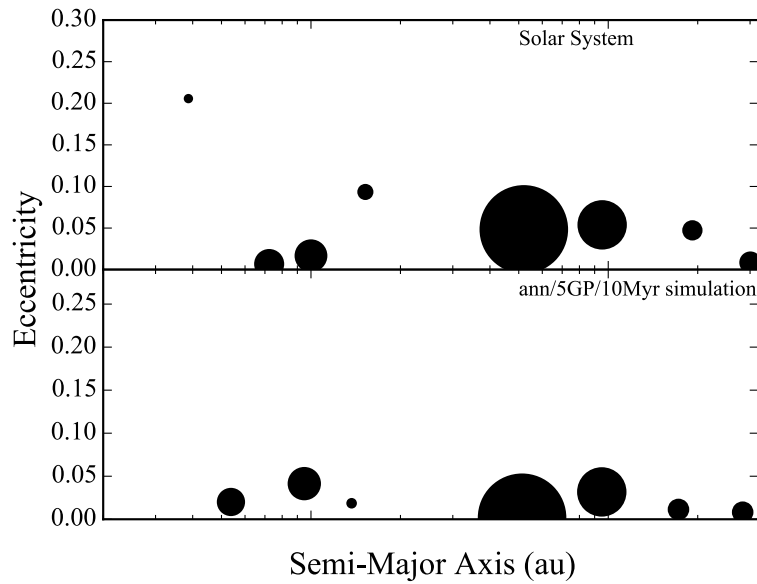


Figure 4.6: Semi-Major Axis/Eccentricity plot depicting a successful system in the annulus/5GP/10Myr batch (bottom panel), compared with the actual solar system (top panel). The size of each point corresponds to the mass of the particle (because Jupiter and Saturn are hundreds of times more massive than the terrestrial planets, we use separate mass scales for the inner and outer planets). The final terrestrial planet masses are 0.73, 1.04 and 0.076 M_{\oplus} respectively.

M_{\oplus} of 50 equal-mass embryos and 1 M_{\oplus} of 500 equal-mass planetesimals. Indeed, the lack of a bi-modal initial disk mass distribution seems to be the cause of the rapid growth of Earth analogs in our annulus set. 83% of Earth analogs in our new, embryo/planetesimal annulus set meet success criterion C. Furthermore, Earth analogs take 36.2 Myr longer to form than corresponding Mars analogs in this new set.

4.4 Future Work

We have shown that the early instability scenario (Clement et al., 2018) and the various annulus models (Grand Tack and low mass asteroid belt; Walsh et al., 2011; Raymond & Izidoro, 2017b) are all viable when scrutinized against multiple standard success criteria (Table 4.3). In the subsequent sections, we offer a brief synopsis of how future studies can use different constraints and higher resolution simulations to accurately distinguish between models.

4.4.1 Late Terrestrial Bombardment

The robust set of samples returned by the Apollo missions yielded ages for several large impact basins between ~ 4.3 and 3.7 Gyr (Heiken et al., 1974; Fritz et al., 2014; Zellner, 2017). Furthermore, the low maturity index of regolith overlying orange ash at Shorty Crater has been interpreted to imply that the regolith could not have existed in the presence of a significant flux of micro-meteor impacts (Heiken et al., 1974; Morris, 1978; Schmitt, 2014). Since these ash samples returned ages around 3.5 Gyr, the micro-meteor flux on the Moon must have been essentially zero when they were formed. The ages of impact pulverized lava flow returned in lunar core sample tubes is also consistent with the bombardment being totally complete about 3.5 Gyr ago (Schmitt, 2014). Thus, regardless of the early impact distribution (smooth decline or LHB), the majority of the larger basins must form before ~ 3.7 Gyr ago, and the inner solar system must be essentially clear of debris before ~ 3.5

Gyr ago (Fritz et al., 2014; Zellner, 2017). However, it should be noted that the topic of the Moon’s geological history is extremely complex, with many competing models and contradicting pieces of data. In fact, evidence exists that the micro-meteor flux has been variable throughout the last 3.5 Gyr (Johnson et al., 2016), and has been relatively high for about the last 75 Myr (Schmitt & Petro, 2017). Nesvorný et al. (2010) showed that the majority of this modern flux is fueled from Jupiter family comets. It is thus difficult to correlate ancient micro-meteor activity with debris clearing in the inner solar system. As for the formation of the larger basins, collisional grinding has been shown to quickly break up large enough projectiles (Bottke et al., 2007).

4.4.2 Extended Simulations

To compare our simulations with the record of lunar samples, we must express time relative to CAI formation (calcium aluminum-rich inclusion; approximately time zero in our simulations as discussed in Chapter 3). Thus the 3.7 Gyr basin ages corresponds with ~ 800 Myr after CAI, and the 3.5 Gyr zeroing of the micro-meteor flux converts to ~ 1 Gyr after CAI. This provides an interesting constraint for our terrestrial evolution simulations. Indeed, our fragmentation simulations typically finish with a population of small, unstable debris in the inner solar system after 200 Myr of integration (Chambers, 2013, noted a similar lengthening of complete accretion timescales in the inner solar system). The instability simulations in Chapter 3 had an average of 1.1 additional objects smaller than Mercury in the inner solar system ($a < 2.0$ au), as compared to 2.9 in our new fragmentation simulations. This gives average leftover masses consistent with the $\sim 0.05 M_{\oplus}$ necessary to produce the highly siderophile element (HSE) signature in the Earth’s mantle (Raymond et al., 2013, see also Brassier et al. (2016b)).

To investigate the late bombardment in these systems, we randomly select 32 systems with higher than the median number of debris particles from each of our most successful simulation sets (our standard instability set and our annulus set without giant planet evo-

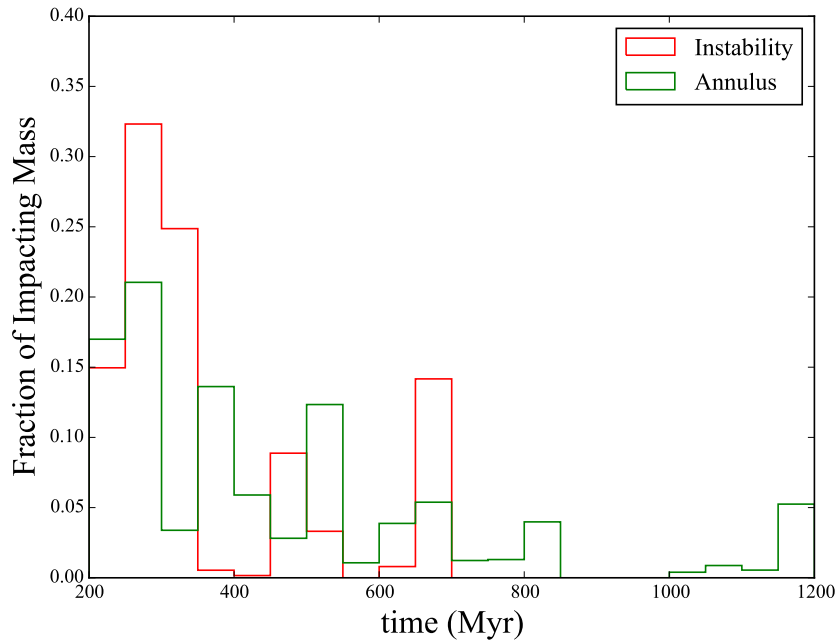


Figure 4.7: Relative late impact rates with respect to time on Venus, Earth and Mars analogs in our 1 Gyr extended annulus and instability integrations.

lution), and integrate them for an additional 1 Gyr. These extended simulations utilize the same integrator and time-step as the original terrestrial planet formation runs. To limit the computational cost of these integrations, we remove all ice giants, Kuiper Belt objects, and asteroids with perihelion greater than 2.0 au. Objects with masses less than $0.055 M_{\oplus}$ do not interact gravitationally with one another. In Figure 4.7, we plot the relative late mass delivery rate on all Venus, Earth and Mars analogs for each simulation set.

4.4.3 Late Impacts

The particles in our simulations are too massive to adequately study the process of late terrestrial bombardment. The lower range of our debris particles' mass distribution (ranging from $\sim 5\%$ the mass of the Moon to several lunar masses) is two orders of magnitude larger than that of the objects that formed the lunar basins. The mass of the impactor that formed the Imbrium basin, for example, is estimated to have been just $\sim 0.03\%$ that of the

Moon (Schultz & Crawford, 2016). However, the clearing rates of our instability set (no late impacts after 700 Myr) is noticeably different than the annulus set (the distributions were determined to be significantly different via a Kolmogorov-Smirnov test yielding a p-value of 2.23×10^{-5}). This is because the debris particles in the annulus set are not as dynamically excited ($\bar{e}_{ann} = 0.24$, $\bar{i}_{ann} = 10.7^\circ$) as the instability set's debris ($\bar{e}_{instb} = 0.31$, $\bar{i}_{instb} = 21.3^\circ$). Thus the debris objects in the annulus set are more likely to be on less eccentric, quasi-stable orbits that can survive for nearly 1 Gyr without experiencing an instability. Indeed, our extended instability simulations lose 36 times as many objects via mergers with the Sun than in the annulus simulations (part of this is due to the giant planets' orbits not being as excited in the annulus set as in the instability set).

4.4.4 HSE Constraints

We can also scrutinize our extended simulation set against constraints for the late veneer and Earth's HSE inventory (Raymond et al., 2013; Jacobson et al., 2014; Morbidelli et al., 2018). Earth analogs ($m > 0.6 M_\oplus$, $0.85 < a < 1.3$ au) in our instability set accrete an average of $0.006 M_\oplus$ in chondritic (non-fragment) material after the last giant impact as opposed to $0.009 M_\oplus$ in our annulus set. Given the low particle resolution, both of these values are roughly consistent with the 0.003 - $0.007 M_\oplus$ required to match the modern HSE concentration (Walker, 2009). However, our instability set Earth analogs accrete two full orders of magnitude more silicate-rich fragment material than the annulus set (0.02 vs $0.0003 M_\oplus$). Given the small number of simulations and impacts, it is difficult to draw significant conclusions from these values. Nevertheless, comparing late accretion histories in high-resolution N-body simulations including fragmentation could be a promising means of differentiating between formation models in the future.

4.5 Conclusions

In this Chapter, we presented the largest ever sample of simulations of terrestrial planet formation in the solar system using an integrator that considers the effects of collisional fragmentation. In particular, we performed a detailed reinvestigation of the early instability scenario proposed in [Clement et al. \(2018\)](#) (Chapter 3). Our new simulations of terrestrial planet formation occurring in conjunction with the Nice Model instability consistently outperformed those with no giant planet evolution when measured against a wide range of success criteria.

Including the effects of collisional fragmentation yielded systems of terrestrial planets with more realistic radial mass distribution profiles (particularly the Earth/Venus spacing), on orbits that were better matches to the solar system in terms of their lower eccentricities and inclinations. While dynamical friction from the additional collision-generated fragments and angular momentum transfer in hit-and-run collisions tends to damp the orbits of the growing planets, these processes also occasionally inhibit mass-loss in the Mars region during the instability. As a result, the Mars analogs in our fragmentation simulations of the early instability scenario are somewhat larger than those reported in Chapter 3. This problem is lessened somewhat by moving the instability earlier (~ 1.0 Myr after gas dissipation), but such a timing also boosts the probability of entirely preventing Mars' formation. Still, many of our new instability systems form planets in the Mars region smaller than Mars.

Because hit-and-run collisions prevent the late growth of Mars analogs, and the constant resupply of fragments lengthens the accretion timescales of Earth analogs, our fragmentation simulations provide better matches to the inferred geological growth histories of the two planets ([Kleine et al., 2009](#); [Dauphas & Pourmand, 2011](#)) than in Chapter 3. Finally, we find that collisional fragmentation and hit-and-run collisions play a dominant role in preventing planet formation in the primordial asteroid belt.

The early instability scenario's explanation for Mars' small mass has the advantage of simplicity, while still relying on the giant planets' influence to help solve the small Mars

problem. The model is consistent with the diminishing evidence for a LHB (Zellner, 2017; Morbidelli et al., 2018), does not involve a dynamically fine tuned delayed instability and, most importantly, saves the terrestrial planets. Certain geochemical and dynamical constraints including isotopic data from comet 67P (Marty et al., 2017) and constraints on forming the cold classical Kuiper Belt (Nesvorný, 2015a) are somewhat at odds with our preferred instability timing of ~ 1.0 Myr after gas disk dispersal (see full discussion in Chapter 3). However, we argue that our model’s ability to preserve the terrestrial system during the giant planet instability is more important than simultaneously reconciling all timing constraints; each of which have their own uncertainties and model dependencies.

Despite the advantages of the early instability model, the processes involved in terrestrial planet formation are highly chaotic and stochastic. Since observational constraints are limited, it is difficult to rule out one formation model in favor of another. Furthermore, the various explanations for Mars’ small mass (eg: early instability, low-mass asteroid belt, pebble accretion, Grand Tack hypothesis, etc.) could have actually sculpted Mars’ early evolution in tandem with one another. To address this, we performed an additional set of simplified simulations to study the compatibility of the early instability scenario with the truncated disk initial conditions supposed by the Grand Tack and low mass asteroid belt models (a narrow annulus of terrestrial forming material between ~ 0.7 and 1.0 au; Hansen, 2009). These simulations indicated that the annulus setup is compatible with an early giant planet instability. Additionally, collisional fragmentation does not seem to be a barrier to the success of the initial conditions.

Future work on these topics is required to clarify the advantages and disadvantages of the various proposed terrestrial evolutionary schemes. In particular, fragmentation-style simulations like those presented in this Chapter should be analyzed in more detail to see if the cratering record of the Moon is consistent with the tail end of terrestrial planet formation. This next step might provide a concrete test with which to differentiate between models.

4.6 Acknowledgments

This Chapter is reproduced by permission of Elsevier and the American Astronomical Society's Division of Planetary Sciences from the following publication: Clement, M. S., Kaib, N.A., Raymond, S.N., Chambers, J.E. and Walsh, K.J. (March 2019). The early instability scenario: terrestrial planet formation during the giant planet instability, and the effect of collisional fragmentation. In: *Icarus* 321: 778-790.

This material is based upon research supported by the Chateaubriand Fellowship of the Office for Science and Technology of the Embassy of France in the United States. M.S.C. and N.A.K. thank the National Science Foundation for support under award AST-1615975. S.N.R. thanks the Agence Nationale pour la Recherche for support via grant ANR-13-BS05-0003-002 (grant MOJO) and acknowledges NASA Astrobiology Institutes Virtual Planetary Laboratory Lead Team, funded via the NASA Astrobiology Institute under solicitation NNH12ZDA002C and cooperative agreement no. NNA13AA93A. This research is part of the Blue Waters sustained-petascale computing project, which is supported by the National Science Foundation (awards OCI-0725070 and ACI-1238993) and the state of Illinois. Blue Waters is a joint effort of the University of Illinois at Urbana-Champaign and its National Center for Supercomputing Applications (Bode et al., 2013; Kramer et al., 2015). Further computing for this project was performed at the OU Supercomputing Center for Education and Research (OSCER) at the University of Oklahoma (OU). Additional analysis and simulations were done using resources provided by the Open Science Grid (Pordes et al., 2007; Sfligoi et al., 2009), which is supported by the National Science Foundation award 1148698, and the U.S. Department of Energy's Office of Science. Several sets of simulations were managed on the Nielsen Hall Network using the HTCondor software package: <https://research.cs.wisc.edu/htcondor/>.

Chapter 5

Dynamical Constraints on Mercury’s Collisional Origin

This Chapter is reproduced from [Clement et al. \(2019a\)](#), which appeared in the *Astronomical Journal*, with only minor typographical and formatting alterations. The abstract has been removed to improve the flow and readability of this thesis.

5.1 Introduction

The late stages of terrestrial accretion (giant impact phase) have been studied numerically ([Duncan et al., 1998](#); [Chambers, 1999](#)) by numerous authors. By assuming a surface density of solids roughly commensurate with the minimum mass solar nebula ([Weidenschilling, 1977](#)), numerical integrators produce appropriately massed Earth and Venus analogues (at the proper orbital locations) with great frequency regardless of whether other parameters are varied ([Chambers, 2001](#); [O’Brien et al., 2006](#); [Raymond et al., 2006, 2009b](#); [Hansen, 2009](#); [Clement et al., 2018](#)). However, replicating the small mass of Mars ($\sim 10\%$ that of the Earth) requires modification to the classic initial conditions ([Wetherill, 1991](#)); the exact mechanism for which is a topic of continued debate ([Thommes et al., 2008](#); [Walsh et al., 2011](#); [Izidoro et al., 2014](#); [Fischer & Ciesla, 2014](#); [Drażkowska et al., 2016](#); [Raymond & Izidoro, 2017b](#); [Clement et al., 2018](#)). Notably, [Raymond et al. \(2009b\)](#) demonstrated that a configuration of Jupiter and Saturn with a mutual inclination of 1.5° and $e_J = e_S = 0.1$ (extra eccentric Jupiter and Saturn, EEJS) consistently produced a small Mars. However,

these initial conditions appeared unlikely since interactions between the primordial gas disk and the growing gas planets are thought to result in a system of fully formed giant planets on near circular orbits (Papaloizou & Larwood, 2000; Tanaka & Ward, 2004; Cresswell et al., 2007). In a similar manner, the giant planets can influence Mars’ formation via resonance sweeping (the so-called “dynamical shakeup;” Thommes et al., 2008; Bromley & Kenyon, 2017) or mean motion resonance (MMR) crossing (Lykawka & Ito, 2013). It has also been proposed that the Mars forming region and primordial asteroid belt were largely empty, and subsequently implanted with material from the outer solar system during Jupiter’s growth phase (Izidoro et al., 2015; Raymond & Izidoro, 2017b,a). An alternative idea, the “Grand Tack” hypothesis (Walsh et al., 2011; Walsh & Levison, 2016), suggests that the still-forming Jupiter and Saturn migrated in to the inner solar system during the gas disk phase of evolution, and subsequently back out. By truncating the primordial disk of planetesimals at ~ 1 au, the terrestrial planets form out of a narrow annulus, and Mars’ final mass is greatly limited (Hansen, 2009). Finally, a giant planet orbital instability (the so-called “Nice Model;” Gomes et al., 2005; Tsiganis et al., 2005; Morbidelli et al., 2005) timed in conjunction with the late stages of terrestrial planet formation can also result in a small Mars (Clement et al., 2018; Clement et al., 2019b,c). Interestingly, the Nice Model instability might also explain Mercury’s uniquely excited orbit (Roig et al., 2016).

Despite these significant advances, fully understanding the formation of Mercury (which is only $\sim 5\%$ the mass of Earth) remains a mystery to dynamicists. Most previous studies of terrestrial planet formation find that Mercury analogues form in only 5-10% of simulated systems (Chambers, 2001; Raymond et al., 2009b; Clement et al., 2018). While terrestrial planet formation simulations occasionally produce planets near Mercury’s location, its other physical characteristics seem to suggest it also had a unique accretion history. In particular, it has an unusually large iron-rich core ($\sim 70\text{-}80\%$ of its entire mass; Siegfried & Solomon, 1974; Hauck et al., 2013; Nittler et al., 2017; Margot et al., 2018) and depleted volatile inventory (however the MESSENGER mission detected abundances of moderately volatile

elements similar to that of the other terrestrial planets). These features have generally been interpreted as the consequences of an energetic, fragmenting collision during its formation (Benz et al., 1988; Asphaug, 2010; Asphaug & Reufer, 2014), though other explanations have also been proposed.

Models of terrestrial planet formation in the solar system require truncation of the inner disk at ~ 0.5 au in order to replicate the modern mass distribution and orbital excitation profile of the inner planets. However, the number of known multi-planet systems of terrestrial exoplanets with semi-major axes less than Mercury’s (eg: Kepler-102, Kepler-11, Kepler-85 and TRAPPIST-1; Lissauer et al., 2013, 2014; Gillon et al., 2017) seem to imply that this is not always the case. In fact, Mulders et al. (2018) argued that as many as $\sim 90\%$ of Main Sequence stars possess close-in Super-Earths. Volk & Gladman (2015) proposed that the young solar system may have contained a similar population of tightly packed planets. In this scenario, some time in the solar system’s early history these planets underwent a cataclysmic instability that left behind Mercury as the lone survivor. However, the simulations of Volk & Gladman (2015) demonstrated quasi-stability in known systems of exoplanets and did not include realistic collisions (see further discussion in Wallace et al., 2017). Furthermore, the systems studied in that work were not necessarily analogous to the young solar system since they did not include the other planets. In an alternative scheme, the lack of planets interior to Mercury might be explained by planetesimal shepherding during Jupiter’s outward migration phase (Raymond et al., 2016). Another idea is that Jupiter’s inward migration in the Grand Tack model could have cleared out the Mercury forming region via resonant excitation of small planetesimals (Batygin & Laughlin, 2015), though this scenario directly conflicts with the results of accretion models (Kenyon & Bromley, 2009; Raymond et al., 2016).

Nevertheless, Mercury’s iron-rich composition makes the collisional hypothesis a compelling one. However, most modern integration schemes (Duncan et al., 1998; Chambers, 1999; Grimm & Stadel, 2014) used for modeling the giant impact phase of terrestrial acce-

tion treat all collisions as perfectly accretionary. Thus, if Mercury truly originated from a large, energetic collision during the tail-end of planet formation, it makes sense that N-body simulations consistently fail to produce accurate Mercury analogs. For recent reviews on the topics of Mercury’s formation and composition consult [Ebel & Stewart \(2017\)](#), [Nittler et al. \(2017\)](#) and [Margot et al. \(2018\)](#).

While the literature concerning the collisional origin of the moon is extensive ([Hartmann & Davis, 1975](#); [Ćuk & Stewart, 2012](#); [Canup, 2012](#); [Herwartz et al., 2014](#); [Mastrobuono-Battisti et al., 2015](#); [Kaib & Cowan, 2015](#); [Quarles & Lissauer, 2015](#); [Rufu et al., 2017](#); [Citron et al., 2018](#)), the topic of Mercury’s collisional origin is not as well explored. Nevertheless, two different collisional scenarios ([Sarid et al., 2014](#); [Ebel & Stewart, 2017](#)) have been proposed to explain Mercury’s high core mass fraction (CMF) and low concentration of volatiles. The first scheme involves the erosion of an originally larger planet by repeated hit-and-run collisions ([Asphaug et al., 2006](#); [Svetsov, 2011](#); [Chau et al., 2018](#)). However, hydrodynamical simulations indicate that the disrupted volatiles would eventually be re-accreted, and the resulting planet would not be as volatile poor as Mercury ([Marchi et al., 2014](#)). The second scenario concerns a fragmenting collision between two large protoplanets ([Benz et al., 2007](#); [Asphaug, 2010](#); [Asphaug & Reufer, 2014](#); [Chau et al., 2018](#)). While the logical target for a Mercury-forming impact would be the proto-Venus, the lack of an internally generated magnetic dynamo might be evidence that primordial stratification still exists within the Venus’ core. This may imply that the planet was never disrupted by such a large impact ([Jacobson et al., 2017](#)).

While the specific collisional parameters required in either Mercury-forming scenario have been evaluated before ([Asphaug et al., 2006](#); [Svetsov, 2011](#); [Asphaug & Reufer, 2014](#); [Chau et al., 2018](#)), the full picture of the event within the greater context of terrestrial planet formation as a whole is not as well understood. Since the various regimes of collisional parameter space have been mapped by [Leinhardt & Stewart \(2012\)](#) and [Genda et al. \(2012\)](#), traditional N-body integrators used for investigating the dynamics of terrestrial planet for-

mation can be modified to include the effects of collisional fragmentation. [Chambers \(2013\)](#) performed the first such simulations, and found several examples of the fragmentation processes producing planets with CMFs similar to Mercury. [Dwyer et al. \(2015\)](#) performed an in-depth analysis of the bulk chemical content of the planets formed in these same simulations, and noted that it was difficult to form Mercury-like planets with low silicate mass fractions. However, the small sample size of just 8 integrations makes it difficult to draw any statistical conclusions from these simulations. Additional authors have used similar N-body codes to study planetary dynamics ([Bonsor et al., 2015](#); [Carter et al., 2015](#); [Leinhardt et al., 2015](#); [Quintana et al., 2016](#); [Wallace et al., 2017](#)). However, no dedicated study of the dynamical barriers involved in forming Mercury via repeated hit-and-run collisions or a single giant impact has been performed. It should also be noted that [Lykawka & Ito \(2017\)](#) investigated the possibility of Mercury forming naturally in the inner region (between 0.2 and 0.5 au) of the terrestrial disk, and found that the final Mercury analogs were typically over-massed and under-excited. In this paper, we systematically investigate Mercury’s collisional origin using the modified version of the *Mercury6* hybrid integrator ([Chambers, 1999](#)) described in [Chambers \(2013\)](#). Our analysis is divided into three segments. First, we investigate the frequency of planets with Mercury-like compositions formed in a large sample of 360 full simulations of terrestrial planet formation. Next, we analyze the architectures of these systems of terrestrial planets, and specifically look for Mercury-like planets on Mercury-like orbits. In the final section of this manuscript, we comment on the dynamical barriers involved in the scenario where Mercury forms via a single giant impact.

5.2 Methods

We investigate three suites of simulations designed to replicate the early instability scenario ([Clement et al., 2018](#); [Clement et al., 2019b,c](#)), the Grand Tack and low mass asteroid belt hypotheses ([Walsh et al., 2011](#); [Raymond & Izidoro, 2017b](#)), and a control set using classic

initial conditions (Chambers, 2001, 2013). For a complete discussion and full presentation of these simulations, consult Clement et al. (2019b).

Our work utilizes the same modified version of the *Mercury6* hybrid integrator (Chambers, 1999) described in Chambers (2013) and Dwyer et al. (2015). The collisional fragmentation algorithm functions by first calculating the largest remnant utilizing relations from Leinhardt & Stewart (2012). The leftover mass is divided into an appropriate number of equal-massed fragments, with masses greater than the minimum fragment mass (MFM). Our simulations use a 6 day time-step and set the MFM to $\sim 10\%$ the mass of Mercury. Because collisions producing 90 fragments can cause the Bulirsch-Stoer portion of *Mercury's* hybrid-symplectic integrator to be bogged down, we find a MFM of $0.0055 M_{\oplus}$ to be the limit of our resolution (for a more in depth discussion of this see Wallace et al., 2017). Objects are considered to be merged with the Sun at 0.1 au, and removed via ejection at 100 au. Because of the hybrid symplectic scheme's inability to accurately integrate through low pericenter passages (Chambers, 1999), removing objects that pass within ~ 0.1 au of the Sun is common practice in similar numerical studies (Chambers, 2001, 2013).

5.2.1 Control Simulations

For our primordial control disks, we choose the simplest set of initial conditions consistent with those chosen by many previous authors (Chambers, 2001; Raymond et al., 2006; O'Brien et al., 2006; Chambers, 2013; Kaib & Chambers, 2016; Clement et al., 2018). We first begin 100 integrations of a $5 M_{\oplus}$ terrestrial forming disk of bodies distributed between 0.5 and 4.0 au. As in Clement et al. (2018), half the disk mass is placed in 100 equal-mass embryos, and the other half in 1,000 equal-mass planetesimals. While the planetesimals do not interact gravitationally or collide with one another, they can experience fragmenting collisions if they collide with one of the embryos. When this is the case, the resulting fragments are also treated as planetesimals (fragments from embryo-embryo collisions are considered fully self-gravitating). The radial spacing within the disk is selected to achieve a surface density profile

proportional to $r^{-3/2}$ (Birnstiel et al., 2012). Angular orbital elements are drawn randomly, and eccentricities and inclinations are selected from near circular Gaussian distributions ($\sigma_e = .02$ and $\sigma_i = .2^\circ$). Thus all initial eccentricities and inclinations are below 0.001 and 1° , respectively. Since the outer planets are thought to form first (Haisch et al., 2001; Halliday, 2008; Kleine et al., 2009), we include Jupiter and Saturn in a 3:2 MMR ($a_J = 5.6$ au, $a_S = 7.6$ au) in these integrations (Wetherill, 1996; Chambers & Cassen, 2002; Levison & Agnor, 2003a; Raymond et al., 2004; Clement et al., 2018). These simulations are evolved for 200 Myr, and become our control set.

5.2.2 Instability Scenario

To test the effects of a Nice Model style instability (Gomes et al., 2005; Tsiganis et al., 2005; Morbidelli et al., 2005), we take snapshots of our control disks at 1,5 and 10 Myr, and input them in to unstable giant planet configurations (Nesvorný, 2011; Clement et al., 2018). Because ice giants are routinely excited to the point of ejection in simulations of the classical Nice Model (Gomes et al., 2005), the current version includes one or two additional primordial ice giants (Nesvorný & Morbidelli, 2012). As in Clement et al. (2018), we perform one set of integrations using a 5 giant planet configuration, and a second with a 6 giant planet configuration. These simulations are evolved for an additional 200 Myr using the same integrator and time-step described above. To ensure we only sample systems where the evolution of the giant planets is most akin to the actual solar system, simulations that fail to eject an ice giant within 5 Myr, and those where Jupiter and Saturn’s period ratio exceeds 2.8 (the present ratio is 2.49) are deleted. Through this process, our initial sample of 600 instability simulations is reduced to 160.

There are advantages and disadvantages to both a 5 and 6 giant planet instability. For instance, a 6 planet setup excites Jupiter’s eccentricity in two stages (with each primordial ice giant ejection). This evolutionary scheme can potentially prevent Jupiter’s eccentricity from being damped to below its modern value via secular friction (Nesvorný & Morbidelli,

Set	a_{in} (au)	a_{out} (au)	M_{tot} (M_{\oplus})	N_{emb}	N_{pln}
Control	0.5	4.0	5.0	100	1000
Instability	0.5	4.0	5.0	100	1000
Annulus	0.7	1.0	2.0	400	0

Table 5.1: Summary of initial conditions for complete sets of terrestrial planet formation simulations. The columns are (1) the name of the simulation set, (2) the inner edge of the terrestrial forming disk, (3) the disk’s outer edge, (4) the total disk mass, (5) the number of equal-mass embryos used, and (6) the number of equal-mass planetesimals used.

2012). Since the precise nature of the solar system’s instability is unconstrained, we study both types of giant planet configurations (for a complete discussion of this methodology consult Clement et al., 2018; Clement et al., 2019b). Other previous works test the effects of the Nice Model by performing a large number of instability simulations, selecting the run with the best final giant planet architecture, and then “replaying” the chosen instability in the presence of the objects of interest to the study (eg: the terrestrial planets, asteroid belt, etc; Brasil et al., 2016; Roig et al., 2016; Deienno et al., 2017). However, given the unconstrained, chaotic nature of the giant planets’ particular evolution within the instability, we choose to perform many simulations, and then select a sample of the best final Jupiter-Saturn configurations (Kaib & Chambers, 2016; Clement et al., 2018).

5.2.3 Annulus Scenario

To roughly replicate the initial conditions supposed by the Grand Tack (Walsh et al., 2011) and low mass asteroid belt (Raymond & Izidoro, 2017b) models, we lay down 400 equal-mass planet embryos in a narrow annulus between 0.7 and 1.0 au (Hansen, 2009). Planetesimals are not used in these 100 simulations, and thus each object interacts gravitationally with every other object in the run), and the total disk mass is set to $2.0 M_{\oplus}$. The integrator, time-step and method of selecting orbital elements are the same as described above. Including the additional 100 control simulations and 160 instability runs, our total sample of fully accreted systems of terrestrial planets is 360. A summary of our three sets of terrestrial planet formation simulations is provided in Table 5.1.

5.2.4 Analysis Metrics

Core Mass Fraction Calculation

In order to filter out Mercury-like objects with a high CMFs (Siegfried & Solomon, 1974; Hauck et al., 2013), we calculate the mass of each object’s iron core using the same method described by Chambers (2013). We first assume that each body is fully differentiated, with 30% of its mass concentrated in the core, and the other 70% representing its silicate-rich mantle material. In fully accretionary collisions, the new object’s core mass is equal to the sum of the impactor and target bodies’ core masses. In a fragmenting collision, the fragments come from the mantle material. If the mantle is depleted, the remaining fragments come from the core material. If the fragmenting collision is of the hit-and-run type, the fragments first come from the mantle of the projectile, and then from its core. In the subsequent text, we refer to an object with $CMF > 0.5$ as a “high CMF” object.

Terrestrial Angular Momentum Deficit

To compare the orbital excitation of our systems to the solar system quantitatively, we calculate the normalized angular momentum deficit (AMD, Eq. 2.1; see § 2.2.2) for all of our integrated systems (Laskar, 1997). AMD quantifies the deviation of the orbits in a system from perfectly co-planar, circular orbits. While the terrestrial planets’ AMD can evolve marginally over Gyr timescales (Laskar, 1997; Agnor, 2017), a simulated system finishing with an AMD greater than twice the modern value of AMD_{MVEM} is considered a poor solar system analog by most authors (Raymond et al., 2009b; Clement et al., 2018).

Mercury-Venus dynamical spacing

In general, a successful Mercury analog must undergo a series of CMF-reducing collisions during the planet-formation epoch, and then finish on an orbit that is stable for ~ 4 Gyr. Because late ($t > 200$ Myr) instabilities are common results of terrestrial planet formation

models (Clement & Kaib, 2017), we are particularly interested in Mercury-like planets sufficiently dynamically separated from Venus-like planets (eg: not on crossing orbits). For this reason, we compare the difference in the perihelion of Venus analogs and the aphelion of Mercury analogs, as well as the planets’ relative period ratios, to solar system values throughout our study. However, forming Mercury on an orbit well separated from Venus does not necessarily imply that the same is true for Venus and Earth, or Earth and Mars. For that reason we also employ metrics from Clement et al. (2018) and Clement et al. (2019b) to quantify the entire inner solar system’s structure. To satisfy this criterion (criterion A), a terrestrial system must contain 4 planets meeting the following requirements: $M_{Merc} < 0.2 M_{\oplus}$; $M_{Ven,Ear} > 0.6 M_{\oplus}$; $M_{Mars} < 0.3 M_{\oplus}$; $a_{Merc} < 0.5$ au; 0.5 au $< a_{Ven,Ear} < 1.3$ au; and 1.3 au $< a_{Mars} < 2.0$ au. Given the stochastic nature of the planet formation process, it is unreasonable to expect our systems simultaneously match a large number of highly specific constraints (Nesvorný & Morbidelli, 2012; Clement et al., 2018). Therefore, we maintain broad success criteria, and avoid multiplying metrics.

5.3 Results and Discussion

5.3.1 High CMF Objects

The integrator’s fragmentation routine ejects equal massed fragments in uniform directions along the collisional plane. When an impact with sufficient energy to erode core material occurs, it is realistic to assume that the resulting fragments will not be made of equally mixed fractions of core and mantle material. More likely, many fragments will be made entirely of mantle elements, and a few will come mostly from the core (Chambers, 2013). Our method of assigning mantle material to the first fragments produced is plausible for embryos that have their CMFs boosted as the result of repeated hit-and-run collisions. However, when a particularly energetic collision creates many fragments, and fully erodes the entire mantle inventory, we must randomly assign particular fragments as originating

from the core. In [Figure 5.1](#), we plot all objects larger than $0.01 M_{\oplus}$ from all of our different batches of terrestrial planet formation simulations with CMFs greater than 0.5. While the annulus simulations produce the best Mercury analogs, the instability simulations prove most efficient at producing very large objects with high CMFs (several of which are nearly the mass of the Earth). Since the average impact velocities are higher in the annulus set due to the higher initial surface density and lower embryo masses ($v_{imp}/v_{esc} = 2.51$ for fragmenting collisions as compared to 2.14 and 2.26 for the control and instability sets, respectively), the fragmentation process is more likely to grind high CMF objects down in to many, smaller particles. This is also evidenced by the larger percentage of hit and run collisions (42% of all collisions) in the annulus set versus the other sets (22% for control and 29% for instability). Indeed, our fully formed annulus simulations contain approximately twice as many objects with masses less than Mercury and perihelia less than 2.0 au than our other simulation sets. Thus, our results imply that the higher initial surface density of the annulus set makes it difficult for those systems to produce high massed, high CMF objects via the multiple hit-and-run process. Similarly, the instability batch is less efficient at producing lower massed, high CMF objects.

The majority of the larger objects in [Figure 5.1](#) are embryos with CMFs boosted as a result of repeated hit-and-run collisions. Smaller collisional fragments with masses closer to the MFM are more common, but also more likely to be on unstable orbits. The reason for this is that our sample is biased towards objects that are produced near the end of our integration. Many high CMF objects are produced throughout the duration of the simulation that eventually merge with one of the growing terrestrial planets, or are lost from the system via ejection or merger with the Sun. As the terrestrial planets grow larger over the course of the simulation, the MFM is smaller relative to the the total mass involved in fragmenting collisions, and more fragments are produced. Because of this, and the fact that we randomly assign mantle and core material to fragments, we are also interested in the high CMF objects that were produced, but eventually lost (but may have survived if assigned to a different

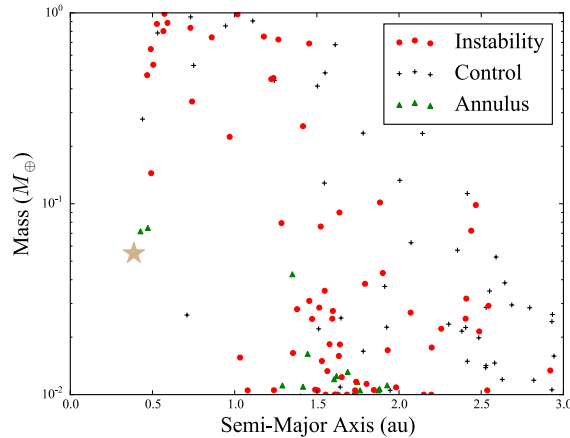


Figure 5.1: Distribution of all objects with masses greater than $0.01 M_{\oplus}$ and CMFs greater than 0.5 surviving 200 Myr of terrestrial planet formation. The colors black, red and green correspond to the control, instability and annulus simulations respectively. The yellow star plots the actual planet Mercury.

fragment). We note that the early instability scenario (Clement et al., 2018; Clement et al., 2019b,c) produces the most objects with boosted CMFs per simulation. This is the result of the orbital excitation induced in the inner solar system by the chaotic perturbations from the unstable giant planets. Indeed, fragmenting collisions account for $\sim 11\%$ of all collisions in the instability runs.

Nevertheless, high CMF objects are a common type of object produced in our planet formation simulations, regardless of the initial conditions. We note many examples of such bodies surviving the planet formation process on stable orbits. 90% of all our simulations finish with at least one high CMF object. However, some of these bodies that finish in the asteroid belt and Mars region are more representative of small debris, leftover from the terrestrial formation process that will be eventually cleared in the subsequent 4.5 Gyr of evolution (see Chambers, 2013; Clement et al., 2019b, for a further discussion of the longer accretion timescales in fragmentation simulations).

5.3.2 Prevalence of Mercury Analogs

The CMF results presented in the previous section should be taken in context with the fact that Mercury analogs (regardless of CMF) are still rare in all of our simulations. We define a Mercury analog as any planet with $m < 0.2 M_{\oplus}$ and $a < 0.5$ au. Our most successful simulation set at meeting this metric is the annulus set (16%). However, only two of those Mercury analogs have CMFs greater than 0.5. Both the instability scenario and control runs meet this metric less than 2% of the time. Furthermore, only one of our criterion A (Clement et al., 2018) satisfying simulations yields a high CMF Mercury analog.

In the actual solar system the difference between Mercury’s aphelion and Venus’ perihelion is ~ 0.25 au. Figure 5.2 plots the cumulative distribution of $q_{Venus} - Q_{Mercury}$ for all systems that form a Mercury-Venus pair (planet with $a < 0.5$ au and $m < 0.2 M_{\oplus}$, interior to a larger body with $a < 1.3$ au and $m > 0.6 M_{\oplus}$). It is clear that systems with Mercury-Venus spacings similar to the solar system are almost non-existent in all 3 of our simulation sets. This is largely due to our chosen initial conditions (specifically the location of the inner terrestrial disk’s edge). Truncating the primordial terrestrial disk at 0.5 or 0.7 au is often justified in the literature as a means of preventing Earth or Super-Earth massed planets from growing near Mercury’s orbit (Chambers, 2001; Raymond et al., 2009b). These authors also cite Mercury’s hypothetical collisional origin (Benz et al., 1988) as a rationale for neglecting the planet in N-body studies of planet formation in the solar system (Raymond et al., 2009b). Our work indicates that such assumptions are precarious from a dynamical standpoint. Even in our most successful simulation set (annulus), where 16% of systems form small ($m < 0.2 M_{\oplus}$) planets interior to 0.5 au, only 2 such systems meet criterion A, and no system finishes with $P_{Venus}/P_{Mercury}$ within 20% of the solar system value.

In Figure 5.3, we plot examples of final inner solar system architectures where a high CMF object finishes on a Mercury-like orbit. While none of these systems match all aspects of the actual solar system, they demonstrate that the fragmentation process within the larger context of terrestrial planet formation is a viable explanation for Mercury’s peculiar

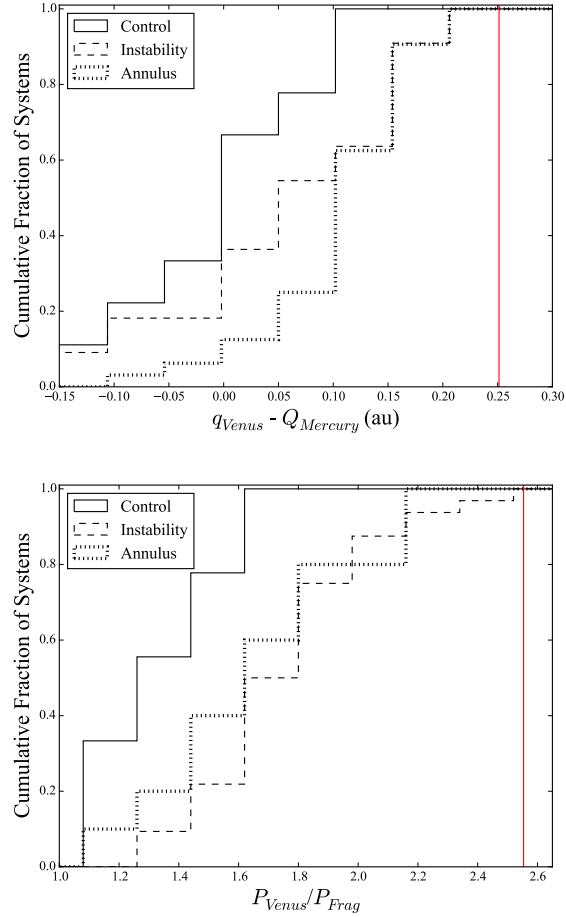


Figure 5.2: Cumulative distribution of the difference between the perihelion of Venus analogs and aphelion of Mercury analogs (top panel), and relative period ratios (bottom panel), produced in our complete simulations of terrestrial planet formation. The figure only depicts systems that finish with a planet (Mercury) with $a < 0.5$ au and $m < 0.2 M_{\oplus}$, interior to a larger body (Venus) with $a < 1.3$ au and $m > 0.6 M_{\oplus}$. The red vertical lines corresponds to the solar system values for Mercury and Venus. The different line styles denote our different simulation sets.

composition. In particular, the system denoted “Annulus 2” provides an excellent match to the real masses and CMFs of Mercury, Venus, Earth and Mars. As is true in the vast majority of our simulations, however, the semi-major axis spacing of the inner planets in this system is incorrect. We also provide plots of the giant planets’ evolution within the Nice Model for [Figure 5.3](#)’s two Instability simulations in [Figure 5.4](#). Though neither final giant planet configuration perfectly matches the solar system, both Jupiter-Saturn systems finish in a state mostly analogous to the real one. Because the terrestrial disk is less affected by the particular dynamics of the ice giants ([Clement et al., 2018](#)), we consider both of these outcomes adequate for our analysis.

5.3.3 Dynamical Barriers to the Single Impact Scenario

Our terrestrial accretion simulations rely on the stochasticity of the planet formation process to generate high CMF planets similar to Mercury. Such planets have their mantle inventories depleted via complex and unique sequences of fragmenting collisions, erosive hit-and-run impacts, and accretion events with objects also altered in CMF. Taking in to account the chaotic nature of planet formation, and the fact that $\sim 90\%$ of our simulations finish with a high CMF terrestrial planet, it seems reasonable to argue that this process might explain Mercury. However, similar to the results of previous studies ([Chambers, 2001](#); [Raymond et al., 2009b](#); [Clement et al., 2018](#)), our simulations consistently fail to generate Mercury-massed planets sufficiently dynamically separated from Venus-like planets. In this final section, we perform an additional suite of simplified simulations to study whether a single giant impact, occurring at the end of the planet formation epoch, might explain Mercury’s offset from Venus.

Our simulations focus on the preferred single energetic impact scenario from [Asphaug & Reufer \(2014\)](#), where a $0.25 M_{\oplus}$ object strikes a $0.85 M_{\oplus}$ target. [Chau et al. \(2018\)](#) also agreed with this most promising scheme in a similar study that considered multiple initial target and projectile masses and several different collisional scenarios. At the beginning of

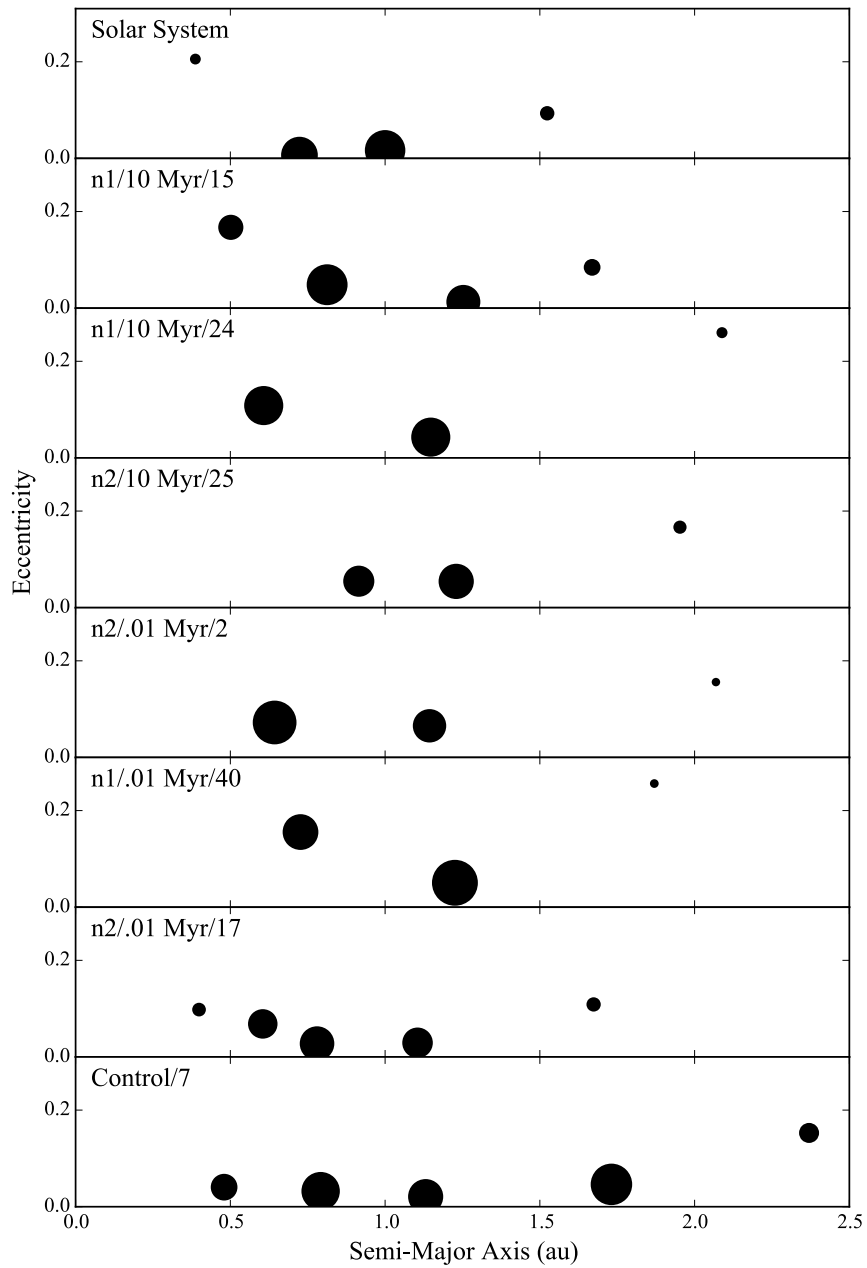


Figure 5.3: Semi-Major Axis/Eccentricity plot of selected successful simulations. The size of each point is proportional to the mass of the planet. The color of each point indicates the planet's CMF. The top 6 panels show examples from each of our 3 simulation sets (Control, Annulus and Instability). The bottom panel shows the actual solar system.

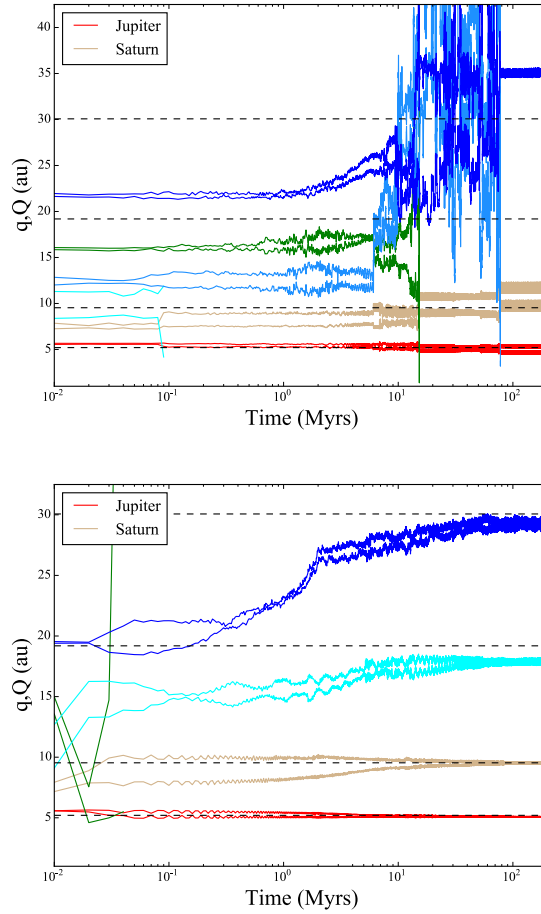


Figure 5.4: Giant planet instability evolutionary schemes for the two instability systems from Figure 5.3. The perihelia and aphelia are plotted for each outer planet in the simulation. The horizontal dashed lines correspond to the modern semi-major axes of Jupiter, Saturn, Uranus and Neptune. The top panel corresponds to “Instability 1” and the bottom panel plots “Instability 2.”

such a scenario, we assume that the potential targets are nearly formed versions of Venus, Earth ($M_{Earth} = M_{Venus} = 0.85 M_{\oplus}$), and Mars on their modern orbits, while the projectile occupies an unstable orbit. To determine suitable unstable locations to place the projectile, we first use the WHFAST integrator (Rein & Tamayo, 2015) in the REBOUND simulation package (Rein & Liu, 2012) to investigate the object’s stability in a/e space. To account for the effects of general relativity, we utilize the additional forces provided in the expanded REBOUNDx library (Tamayo et al., 2016). We probe all regions of a/e phase space ($0.1 < a < 2.0$ au) with 50 Myr integrations. It should be noted that 50 Myr may not be long enough to detect unstable regions because secular resonance overlaps can take Gyr timescale to develop (Lithwick & Wu, 2011). In the interest of minimizing computational time, we chose 50 Myr for a first-order approximation of the parameter space.

After mapping this parameter space, we designate 4 different zones in which to place a potential Mercury-forming projectile. These are listed in Table 5.2. We then perform a large suite of 1 Gyr simulations of these scenarios using a 5 day time-step. Each integration includes the effects of general relativity, and sets the MFM to $0.025 M_{\oplus}$. In the first 3 scenarios, we vary the speed at which the fragments are ejected in random directions within the collisional plane (5, 10 and 20% greater than the mutual escape velocity). In Scenario 4, we evaluate the high inclination parameter space proposed in Jackson et al. (2018).

Regardless of the parameters varied, accurate Mercury analogs are exceedingly rare in this suite of single giant impact simulations. In the following subsections, we briefly discuss the scenario’s major shortcomings.

Dynamical Offset from Venus

A common outcome of fragmenting collisions (particularly those of the hit-and-run variety) is the re-accretion of ejected fragments (Chambers, 2013). This is particularly the case when the velocity vectors of the projectile and target objects are near parallel. In this scenario the fragments are ejected along a plane nearly parallel to the orbit of the target particle;

and are still on orbits where they heavily interact with this remnant. Because the fragments have lower masses than the original projectile object, the subsequent collisions are much more likely to be totally accretionary (Leinhardt & Stewart, 2012). We attempt to replicate Mercury and Venus’ modern orbital offset by boosting the velocity of escaping fragments. We find that this only slightly limits the probability of fragment re-accretion. In such a scenario, the initial two velocity vectors are far from parallel, and the fragments are often ejected on to highly excited orbits. Over the subsequent billion years of evolution, these bodies can be further excited by chaotic interactions with the other planets (Laskar, 1997; Laskar & Gastineau, 2009; Clement & Kaib, 2017) to the point where they are either ejected from the system or collide with the Sun. In general, increasing the fragment ejection velocity leads to a far lower chance of immediate re-accretion by the target body. However, this difference becomes statistically insignificant when the integration is extended to 1 Gyr because of the longer timescales of re-accretion for high velocity fragments. Additionally, increasing the ejection speed leads to about a factor of two increase in the chance of loss due to collision with the Sun or ejection from the system. Figure 5.5 plots the Mercury-Venus dynamical offset for all fragments that finish the 1 Gyr integration Sun-ward of Venus in the same manner as Figure 5.2. Interestingly, though the subsets that fix the fragment ejection velocity at 20% greater than the mutual escape velocity provide the best matches to the actual solar system, the total sample of such objects (2) is a full order of magnitude smaller than that of the other subsets. Since all three subsets include roughly an equal number of simulations, we suspect this is due to the fact that subset c (Table 5.2, column 5) simulations are twice as likely to lose fragments via merger with the Sun than are subsets a or b. Thus ejecting a fragment with sufficient energy to subsequently scatter off and dynamically separate from the initial target particle also implies a greater chance of losing the fragment by other means.

Scenario	a_o (au)	e_o	i_o ($^\circ$)	v_{frag}/v_{esc}	N_{sim}	N_{frag}
1	0.43-0.45	0.25-0.5	0-1	(a)1.05,(b)1.1,(c)1.2	5472	235
2	0.85-0.87	0.25-0.5	0-1	(a)1.05,(b)1.1,(c)1.2	3286	1956
3	0.34-0.36	0.25-0.5	0-1	(a)1.05,(b)1.1,(c)1.2	9840	62
4	0.43-0.45	0.6-0.75	30-40	(a)1.05	569	113

Table 5.2: Summary of initial conditions for simulations to produce Mercury as suggested by [Asphaug & Reufer \(2014\)](#). The columns are (1) the scenario number, (2-4) the semi-major axis, eccentricity and inclination ranges from which the projectiles orbit is selected, (5) the fragment ejection velocity with respect to the mutual two-body escape velocity (6) the total number of integrations performed, and (7) the total number of integrations where fragmenting collisions occurred.

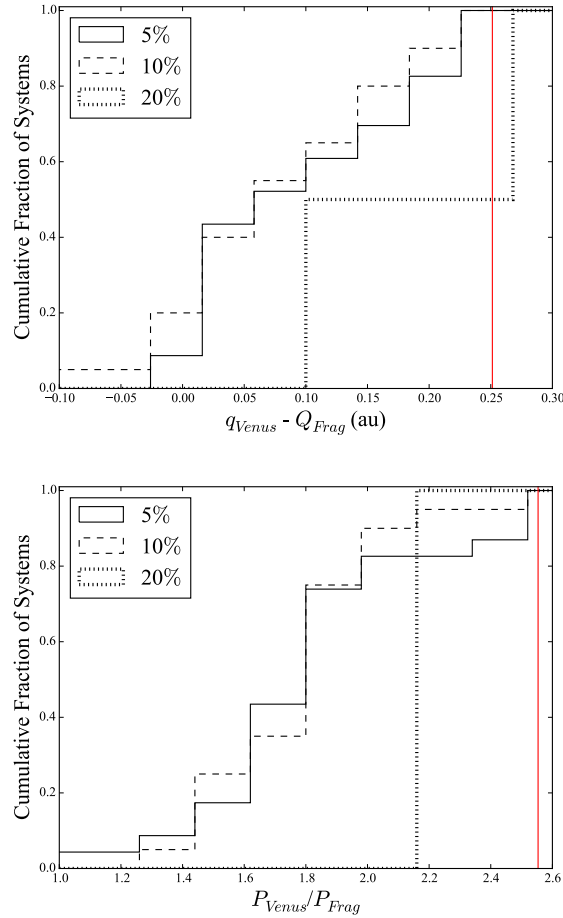


Figure 5.5: Cumulative distribution of the difference between the perihelion of Venus and aphelion of fragments (top panel), and relative period ratios (bottom panel), in all simulation batches after 1 Gyr of evolution. The red vertical lines correspond to the solar system values for Mercury and Venus. The different line styles denote the fragment ejection speed (percentage greater than the mutual escape speed; denoted as subsets a, b and c in [Table 5.2](#), column 5).

Terrestrial AMD

Nearly all modern simulations of planet formation in the inner solar system struggle to replicate the extremely low eccentricities and inclinations of the solar system’s four terrestrial planets. In fact, when integrated over Gyr timescales, the orbits of all the planets except Mercury usually stay remarkably low (Quinn et al., 1991; Laskar & Gastineau, 2009). For the formation of Mercury by energetic collision model to be viable, the resulting terrestrial system must be appropriately dynamically cold. In Figure 5.6, we plot the cumulative distribution of AMDs across all four of our scenarios. This final distribution of AMDs should be taken in context with the fact that our simulation set-ups are quite idealized. If the Mercury-forming impact occurred during the later stages of planet formation, a population of small bodies would have still existed to damp out the excited orbits of the young planets via dynamical friction. Nevertheless, our results indicate that it is unlikely for a system to undergo such a violent dynamical process and finish in a state similar to the solar system. The fact that the solar system’s AMD is outside the range of the values for scenarios 3 and 4 (Table 5.2) does speak against these initial projectile orbits. In particular, no scenario 4 systems finish the 1 Gyr evolution with an AMD within a factor of two of the solar system.

Jackson et al. (2018) prefer the multiple hit-and-run setup of Asphaug & Reufer (2014) from a probabilistic perspective, however the majority of their favored pre-impact orbits have extremely high inclinations ($\sim 20\text{-}60^\circ$). In the actual solar system, the orbits of all the terrestrial planets except Mercury ($e=0.20$, $i=6.3^\circ$) are nearly circular and co-planar (all three have inclinations less than 2.5° , Venus and Earth have eccentricities less than 0.02). For this reason, many studies of early solar system giant impacts only consider co-planar projectiles (Quarles & Lissauer, 2015; Kaib & Cowan, 2015). In order for a high-inclination impactor scenario to be viable, some mechanism is needed to dissipate the non-perpendicular components of angular momentum delivered by a several-Mars-massed projectile in order to keep the final orbits in the inner solar system dynamically cold. As a point of reference, only 5 of the terrestrial objects ($a < 2.0$ au, $m > 0.1 M_\oplus$) in our 360 complete planet formation

simulations attain inclinations larger than 20° (the highest being 34°). This indicates that it is unlikely that the hypothetical Mercury forming impactor could have originated on a highly excited, non-coplanar orbit.

Less than 1% of simulations in our best subset (scenario 1; [Table 5.2](#)), finish with four terrestrial planets, a system AMD less than twice AMD_{MVEM} , and $q_{Venus} - Q_{Frag}$ within $\sim 20\%$ of the solar system value. An example of a successful system’s evolution is plotted in [Figure 5.7](#). Initially, the projectile is interacting heavily with the proto-Venus, quickly exciting both objects. Through repeated close encounters, Venus’ eccentricity is excited to ~ 0.10 , and it continues to oscillate between ~ 0.01 and 0.20 over the next 125 Myr. Since Venus’ excited orbit continually brings it in close proximity to Earth, its eccentricity excitation quickly bleeds to Earth via stochastic diffusion. Eventually, the projectile smashes into the proto-Venus at a velocity of 1.93 times the mutual escape velocity. This collision ejects five fragments, each with a mass of $\sim 0.032 M_\oplus$. 4 Myr later, Venus absorbs one of the initial fragments. Two of the fragments are quickly scattered on to orbits where they heavily interact with Earth, and the other two undergo a series of hit-and-run collisions with one another and Venus. Through this process, four additional fragments are produced. Over the next 10 million years, Earth excites the eccentricity of the outer two fragments, placing them on orbits where they eventually merge with Venus. At 157 Myr, there are just 2 remaining fragments in the system, both interior to Venus’ orbit. These two bodies undergo a series of three hit-and-run collisions before they finally merge at 187 Myr. During this sequence of repeated hit-and-run collisions with other fragments, the final “Mercury” analog dissipates angular momentum and finishes on an orbit that is sufficiently dynamically separated from Venus.

Thus we cannot rule out the [Asphaug & Reufer \(2014\)](#) giant impact scenario as dynamically incompatible with Mercury’s current orbit. However, our simplified simulations indicate that it represents a rare and unlikely pathway for Mercury’s formation.

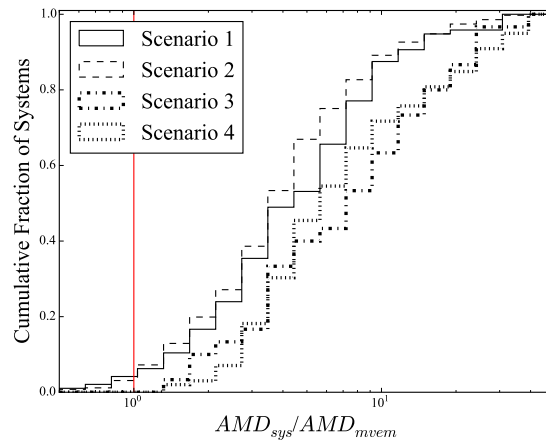


Figure 5.6: Cumulative distribution of system AMDs after 1 Gyr of evolution, normalized to the solar system value for Mercury, Venus, Earth and Mars. The different line styles represent the different initial projectile orbital parameter space tested (Table 5.2). The red vertical line corresponds to the solar system value.

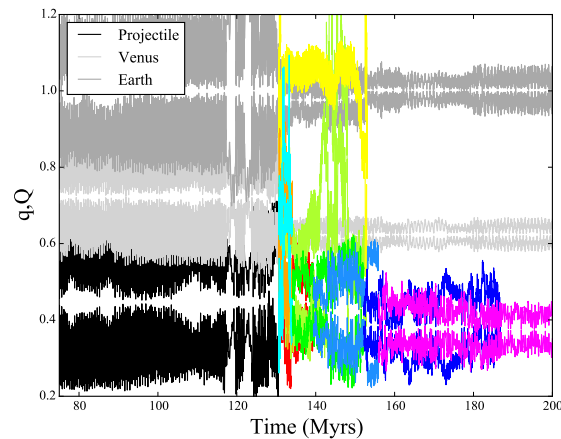


Figure 5.7: Example evolution of a successful simulation in the scenario 1b set (Table 5.2, column 5). The perihelia and aphelia are plotted for each body in the simulation. After the projectile (color coded black) smashes into the proto-Venus at 131 Myr, five fragments are ejected. Four more fragments are formed over the next 25 Myr in four different collisions between the original fragments. Each fragment is coded a different non-greyscale color.

5.4 Conclusions

In this paper we presented a dynamical analysis of the various avenues proposed for Mercury’s formation utilizing an N-body code that includes the effects of collisional fragmentation. A major limitation of our work is that the integrator must cap the total number of fragments by setting a MFM in order to maintain a reasonable number of bodies in the calculation.

In the first part of our study, we utilized the largest sample of complete simulations of terrestrial planet formation that include the effects of collisional fragmentation to search for objects with high CMFs boosted by repeated hit-and-run collisions. While the very large majority of the planets we produce differ from Mercury in terms of their orbits, masses and CMFs, this sample also provides numerous objects with compositions similar to Mercury. 90% of all our complete simulations of terrestrial planet formation finish with a high CMF object ($\text{CMF} > 0.5$). We find that our annulus and instability sets produce the most high CMF objects. Our instability simulations are most efficient at generating the largest high CMF objects, and the annulus runs yielded better matches to the terrestrial system as a whole. Depending on the particular initial conditions of a simulation, we find that planets with similar masses and orbits to Mercury from 1-15% of the time. However, only one of our 360 simulations generated a Mercury analog with the proper mass, orbit and CMF within a larger terrestrial architecture that matches the real one.

Additionally, we performed a large suite of simulations designed to replicate the collisional scenario of [Asphaug & Reufer \(2014\)](#). Our results indicate that such a violent collision occurring late in the giant impact phase represents a very low-likelihood scenario for Mercury’s origin. In particular, replicating the present dynamical separation between Mercury and Venus proves challenging. Increasing the velocity of escaping fragments to $\sim 20\%$ greater than the mutual escape velocity can help in attaining this separation, but only to a minor degree. We also conclude that highly excited, non-co-planar initial projectile orbits similar to those proposed in [Jackson et al. \(2018\)](#) are unlikely. In particular, the final systems of planets in this scenario systematically fail to match the solar system’s low AMD. Despite all

the efforts made, forming Mercury continues to be a major challenge for terrestrial planet formation models.

Acknowledgments

This Chapter is reproduced by permission of the American Astronomical Society from the following publication: Clement, M. S., Kaib, N.A., and Chambers, J.E. (2019, in press). Dynamical Constraints on Mercury’s Collisional Origin. In: *AJ*.

We thank Sean Raymond and Rogerio Deienno for insightful comments and suggestions that greatly enhanced the quality of this manuscript. This material is based upon research supported by the Chateaubriand Fellowship of the Office for Science and Technology of the Embassy of France in the United States. M.S.C. and N.A.K. thank the National Science Foundation for support under award AST-1615975. This research is part of the Blue Waters sustained-petascale computing project, which is supported by the National Science Foundation (awards OCI-0725070 and ACI-1238993) and the state of Illinois. Blue Waters is a joint effort of the University of Illinois at Urbana-Champaign and its National Center for Supercomputing Applications (Bode et al., 2013; Kramer et al., 2015). Further computing for this project was performed at the OU Supercomputing Center for Education and Research (OSCER) at the University of Oklahoma (OU). Additional analysis and simulations were done using resources provided by the Open Science Grid (Pordes et al., 2007; Sfiligoi et al., 2009), which is supported by the National Science Foundation award 1148698, and the U.S. Department of Energy’s Office of Science. Several sets of simulations were managed on the Nielsen Hall Network using the HTCondor software package: <https://research.cs.wisc.edu/htcondor/>.

Chapter 6

Excitation and Depletion of the Asteroid Belt in the Early Instability Scenario

This Chapter is reproduced from [Clement et al. \(2019c\)](#), which appeared in the *Astronomical Journal*, with only minor typographical and formatting alterations. The abstract has been removed to improve the flow and readability of this thesis.

6.1 Introduction

The modern asteroid belt's (AB) structure starkly contrasts that of the terrestrial and giant planet systems in that it contains less than $\sim 5 \times 10^{-4} M_{\oplus}$ of material on dynamically excited (large eccentricities and inclinations) orbits ([DeMeo & Carry, 2013](#); [Kuchynka & Folkner, 2013](#)). Though hundreds of thousands of constituents have been observed, around half of the main belt's (MB) mass is concentrated in just 4 asteroids (in order of descending mass: Ceres, Vesta, Pallas, Hygiea). Furthermore, the composition of the belt is far from homogeneous. The inner MB is primarily composed of silicate-rich, moderate albedo S-types, while the belt's outer regions are dominated by carbonaceous, low albedo C-types ([Chapman et al., 1975](#); [Gradie & Tedesco, 1982](#); [Gradie et al., 1989](#); [Bus & Binzel, 2002](#); [DeMeo & Carry, 2013](#)). However, these two populations overlap substantially, and C-types account for around two thirds of all large ($D > 50$ km), bright ($H < 9.7$) asteroids ([Campins](#)

et al., 2018).

While the present-day asteroid belt is well-constrained, the primordial belt is not. In particular, there is a huge disparity in the assumed total mass in the early belt. The primordial AB's total mass as inferred from disk models (Hayashi, 1981; Bitsch et al., 2015) was around $\sim 1\text{-}5 M_{\oplus}$. However, what counts from a dynamical point of view is the asteroidal mass in planetesimals and planetary embryos. Simulations of planetesimal formation in evolving disks have found a range of outcomes (eg: Carrera et al., 2017; Drazkowska & Dullemond, 2018), including the possibility of forming a ring of planetesimals around ~ 1 AU, but none in the AB (Drazkowska et al., 2016). The low-mass AB model (Izidoro et al., 2015; Raymond & Izidoro, 2017b) discussed below makes the assumption that very few planetesimals originated in the belt.

Because the primordial mass distribution is not well characterized, studying the long-term evolution of the MB can be challenging (Bottke et al., 2015). Meteorites believed to originate from Vesta indicate that it differentiated and formed a crust just a few Myr (Shukolyukov & Lugmair, 2002) after calcium aluminum-rich inclusion (CAI formation; the oldest samples known in the solar system). Thus the most massive asteroids grew to their present size when the solar system was in its infancy, and have not grown substantially larger since. This is primarily the result of the belt's high degree of dynamical excitation greatly lengthening accretion timescales.

Over Gyr timescales, collisional grinding and fragmentation tend to push the belt's size distribution towards smaller diameters (Bottke et al., 2005a). This seems consistent with the large number of known collisional families, particularly in the inner MB (Bottke et al., 2006a; Walsh et al., 2013). In fact, Dermott et al. (2018) argued that nearly all asteroids in the inner MB are members of collisional families. Using constraints for the formation of Vesta's two enormous craters (the 505 km Rheasilvia crater on the south pole and the underlying 395 km Veneneia crater; Schenk et al., 2012), Bottke et al. (2005b) calculated the probability that these impacts occurred during the complete collisional evolution of the MB.

If the two basins were formed in the last ~ 2 Gyr, the probability of both events happening given the current MB size distribution would be $\sim 1\%$ (Bottke et al., 2015). The lack of other such basins on Vesta would therefore imply that the belt has always had a low mass. Thus, from a probabilistic standpoint, it seems unlikely that the AB has lost a substantial amount of mass over the last several Gyr. However, this implication would not hold if Vesta was implanted into the belt from a different region of the solar system (Bottke et al., 2006b; Mastrobuono-Battisti & Perets, 2017; Raymond & Izidoro, 2017a).

Mean Motion (MMR) and secular resonances are the dominant mass loss mechanisms in the modern AB. MMRs occur when an asteroid’s orbital period is in integer ratio with that of another body; in this case Jupiter. Secular resonances are the result of an object’s longitude of perihelion (ϖ) or longitude of ascending node ($\dot{\Omega}$) precession frequency equalling one of the solar system’s dominant eigenfrequencies. Since the ν_5 and ν_6 secular resonances overlie several dominant MMRs with Jupiter (4:1, 3:1, 5:2, 7:3, 2:1), asteroids in these regions are quickly excited on to planet crossing orbits (Morbidelli et al., 1995). In addition to depleting the MB, these processes also form the Kirkwood gaps in the belt’s orbital distribution (Petit et al., 2001; O’Brien et al., 2007; Deienno et al., 2016). In spite of these loss mechanisms, Minton & Malhotra (2010) concluded that the MB has lost only 50% of large asteroids since attaining it’s current dynamical state. However, the simulations of Minton & Malhotra (2010) only modeled large asteroids as test particles. This means that around two to three orders of magnitude worth of AB depletion must be accounted for before the end of the planet formation epoch (for recent summaries on the evolution of the AB consult Bottke et al., 2015; Morbidelli et al., 2015).

Most models for terrestrial planet formation account for depletion at the 99-99.9% level with some combination of the following mechanisms: primordial depletion, giant planet influence and embryo excitation. In the classical model of terrestrial planet formation, a population of ~ 100 Moon to Mars massed planet-forming embryos extend throughout the inner terrestrial disk and MB region (Wetherill, 1992; Chambers & Wetherill, 1998; Chambers,

2001; Chambers & Wetherill, 2001; Chambers, 2007; Raymond et al., 2009b). The orbital excitation provided by a population of embryos can result in substantial mass loss (Petit et al., 2001; O’Brien et al., 2007). However, these standard initial conditions fail in that they systematically produce over-massed Mars analogs and Mars to Earth massed planets in the AB (Chambers, 2001; Raymond et al., 2009b; Morbidelli et al., 2012). Furthermore, given the strong radial dependence of embryo growth (eg: Kokubo & Ida, 1996, 1998, 2000), it is possible that large embryos never existed in the young belt. Thus the most compelling solutions to the so-called “small Mars problem” are those that also deplete the primordial MB and sufficiently mix the radial distribution of S and C-types. Here, we summarize the various classes of models (see Raymond et al., 2018, for a review of the models’ assumptions).

1. Low-mass asteroid belt model: Izidoro et al. (2014) showed that the inner solar system could be consistently replicated if built from a steep initial radial mass distribution. These initial conditions, wherein the primordial Mars-forming and AB regions never contained a substantial amount of mass (Izidoro et al., 2015), are largely consistent with modern pebble accretion simulations of embryo and planetesimal formation (Levison et al., 2015b; Drażkowska et al., 2016). Raymond & Izidoro (2017a) provided the explanation for the MB’s compositional dichotomy by suggesting that planetesimals near the growing giant planets could be destabilized via aerodynamic drag and scattered into the empty primordial belt. Thus the MB’s current population of C-types originated in the outer solar system prior to being implanted throughout the AB. The major weakness of the low-mass AB model lies in the initial conditions, and whether such a steep initial mass distribution profile is realistic.

2. The “Grand Tack” hypothesis: By assuming that the terrestrial planets formed out of a narrow annulus of material extending from ~ 0.7 -1.0 au, Hansen (2009) consistently replicated the terrestrial planets’ mass distribution, in particular the large mass ratios between neighboring planets (Mercury/Venus and Mars/Earth). Walsh et al. (2011) provided a dynamical mechanism for these initial conditions by proposing that, during the solar system’s gas disk phase, Jupiter and Saturn migrated in and out of the inner solar system

(Masset & Snellgrove, 2001; Morbidelli & Crida, 2007; Pierens et al., 2014). Jupiter’s presence serves to shepherd primordial MB objects on to orbits where they are scattered out of the region. Thus, the MB was already substantially depleted during the gas disk phase. Furthermore, Deienno et al. (2016) investigated the effects of the Nice Model (an orbital instability among the giant planets; the leading evolutionary model for the outer solar system, Gomes et al., 2005; Tsiganis et al., 2005; Morbidelli et al., 2005) on the post “Grand Tack” MB distribution and found that the final orbital structure was largely consistent with the current AB. However, the high inclination orbital parameter space of the post-instability belt in that work was over-populated. While the Grand Tack scenario succeeds at explaining the radial mixing of C and S-types, the outward migration mechanism is highly dependent on the supposed disk structure and gas accretion rates (D’Angelo & Marzari, 2012; Raymond & Morbidelli, 2014; Pierens et al., 2014).

3. An early instability: The classical Nice Model (Gomes et al., 2005; Tsiganis et al., 2005; Morbidelli et al., 2005) was originally timed in conjunction with the Late Heavy Bombardment (LHB); an inferred delayed spike in the lunar cratering record around ~ 400 Myr after the planets formed. Recent evidence (Boehnke & Harrison, 2016; Zellner, 2017; Morbidelli et al., 2018; Nesvorný et al., 2018) has called the LHB’s existence in to doubt. Since the instability need not be tied to a specific time, moving its occurrence earlier might prevent the disruption of the fully formed terrestrial planets. Indeed, planet ejections and collisions are common in simulations of a delayed Nice Model instability (Brasser et al., 2009; Agnor & Lin, 2012; Brasser et al., 2013; Kaib & Chambers, 2016). Clement et al. (2018) showed that timing the instability ~ 1 -10 Myr after gas disk dispersal substantially limits the mass and formation time of Mars. This provides a natural explanation for the differences in the inferred geological formation times of Earth (Kleine et al., 2009) and Mars (Dauphas & Pourmand, 2011). While the co-added simulations of Clement et al. (2018) matched the broad orbital structure of the MB, and depleted the region at greater than the $\sim 95\%$ level, they began with unrealistic populations of large embryos and planetesimals (with the smallest

simulation particles being more than an order of magnitude larger than the entire current AB mass). In a study similar to this one, [Deienno et al. \(2018\)](#) studied the effect of an early “Jumping Jupiter” style instability on a primordial terrestrial disk constructed of 10,000 massless test particles. The final MB orbital distribution of [Deienno et al. \(2018\)](#) was a good match to the real one, and the authors argued that their inferred net depletion of $\sim 90\%$ would be consistent with the low-mass AB framework of [Izidoro et al. \(2015\)](#) and [Raymond & Izidoro \(2017b\)](#). However, the [Deienno et al. \(2018\)](#) simulations only considered the “Jumping Jupiter” style instability ([Brasser et al., 2009](#); [Nesvorný et al., 2013](#)). Additionally, the integrations utilized massless test particles, and rely on a primordial low mass AB to match the current low mass of the MB.

Here, we expand on the early instability framework of [Clement et al. \(2018\)](#) with detailed simulations of the scenario’s consequences in the AB. Our work differs from [Deienno et al. \(2018\)](#) in that we model the MB with fully self-gravitating bodies and include control cases with test particles. Additionally, we assume a primordial AB mass ($\sim 2 M_{\oplus}$) consistent with the value derived from disk models. Since each simulated instability is highly chaotic, and therefore inherently unique, our study investigates a range of instabilities. By placing the specific dynamical state of the solar system’s giant planets on our spectrum of simulated instabilities, our study seeks to infer the approximate range of MB depletion possible in an early Nice Model instability. Thus, while [Deienno et al. \(2018\)](#) analyzed one particular instability with an outcome very similar to the modern solar system, our work scrutinizes a range of instabilities (none of which are perfect matches to the solar system) and looks for trends.

6.2 Methods

We begin by selecting 8 simulations from [Clement et al. \(2018\)](#) that best replicated both the inner and outer solar system structure in accordance with the success criteria from

that work. Using the naming conventions of Chapter 3, these simulations are 5GP/1Myr/6, 6GP/10Myr/14, 6GP/10Myr/44, 6GP/1Myr/40, 5GP/10Myr/15, 5GP/1Myr/46, 5GP/10Myr/29 and 6GP/10Myr/25 (number of additional primordial ice giants/instability delay time/run number; henceforward referred to as runs 1-8, respectively). We commence our study with each of these systems evolved up to the instability time. In [Clement et al. \(2018\)](#), instability simulations were created by first separately evolving, and then combining two independent sets of integrations. The first was a set of giant planet resonant configurations ([Lee & Peale, 2002](#)) interacting with an external disk of primordial Kuiper Belt objects ([Nesvorný & Morbidelli, 2012](#); [Deienno et al., 2017](#)) up until the instability time. The second followed the evolution of a $5 M_{\oplus}$ terrestrial forming disk of 100 embryos and 1000 planetesimals in the presence of a static Jupiter and Saturn (locked in a 3:2 MMR). Snapshots of the terrestrial disks at various phases of evolution (1.0 or 10.0 Myr for the systems concerned in this Chapter) were then added to the giant planet simulations and integrated through the Nice Model instability for an additional 200 Myr. It is at this combination time that we select the initial conditions for the simulations of this Chapter.

Accurately modeling the asteroid belt with numerical integrators ([Duncan et al., 1998](#); [Chambers, 1999](#); [Rein & Tamayo, 2015](#)) is difficult because of the vast disparity between the sizes of modern asteroids and the belt’s extrapolated primordial mass. Simulating the primordial belt using Ceres sized particles would require close to 10,000 objects; exceeding the capabilities of the conventional integrators used to study terrestrial planet formation. Doing so using particles the size of Hygiea would involve over 100,000 individual primordial objects. Thus, most authors are forced to model the detailed structure of the MB with massless test particles, or approximate its early state with unrealistically massive planet embryos and planetesimals. Improving simulation resolution with test particles can be a useful tool for studying complex orbital dynamics in models where the MB is already heavily depleted in the gas disk phase due to the giant planet’s influence ([Walsh et al., 2011](#); [Izidoro et al., 2015](#); [Raymond & Izidoro, 2017a,b](#)). In this low surface density limit, the AB can be

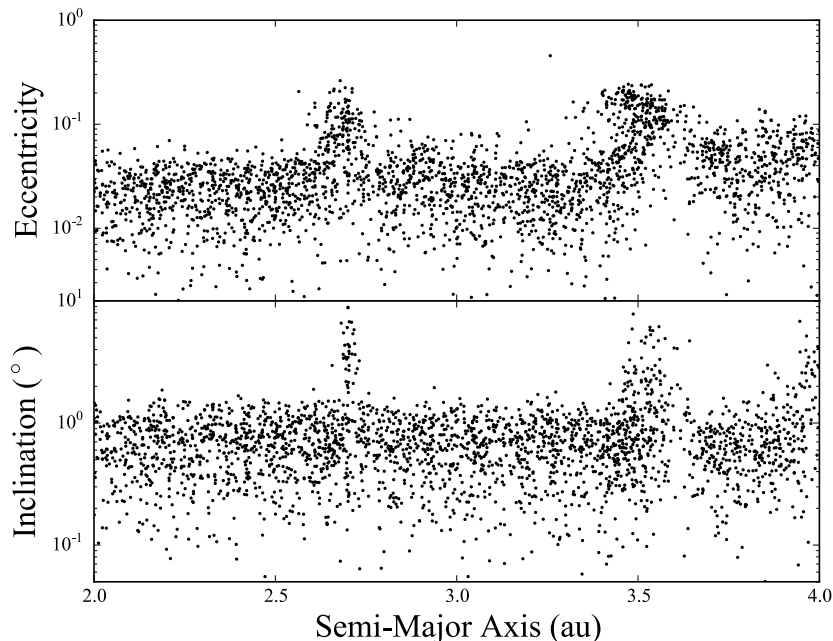


Figure 6.1: Pre-instability, self-stirred eccentricity (top panel) and inclination (bottom panel) distribution of our simulated AB after 1 Myr of evolution in the presence of a static Jupiter and Saturn.

well characterized with test particles. However, the early instability scenario as described in [Clement et al. \(2018\)](#) assumes no prior depletion in the AB at the start of the giant impact phase. Because of this higher AB surface density, characterizing the levels of depletion in a fully self-gravitating AB with somewhat realistic mass resolution is an important step in validating the viability of the early instability scenario.

To study the evolution of the MB in sufficient detail, we select the GENGA (Gravitational Encounters with GPU (Graphics Processing Unit) Acceleration) simulation package ([Grimm & Stadel, 2014](#)). GENGA is based on the Mercury hybrid integrator ([Chambers, 1999](#)) and runs on Nvidia GPUs. For each system, we remove all terrestrial-forming objects in the AB region ($a > 2.0$ au) and replace them with 3000 primordial asteroids, each four times the current mass of Ceres. Thus the total MB mass is $\sim 1.8 M_{\oplus}$. Our selection of total initial mass is derived from the average pre-instability mass of the $a > 2.0$ au region in runs 1-8.

To create our 3000 particle ABs, we assume a surface density profile proportional to $r^{-3/2}$

Name	Runs	0.0006 M_{\oplus} asteroids	0.055 M_{\oplus} embryos
Interact	1-8	3000 self-gravitating	0
Test Particle	1a-8a	3000 test particles	0
Embryo	1b,2b	3000 self-gravitating	4

Table 6.1: Summary of our three different simulation batches. The columns are as follows; (1) the name of the set of simulations, (2) the numbering scheme for the set’s runs, (3) the number of 0.006 M_{\oplus} asteroids, and (4) the number of 0.055 M_{\oplus} embryos.

([Birnstiel et al., 2012](#)). Eccentricities and inclinations are drawn from near-circular and coplanar, Gaussian distributions ($\sigma_e = .02$ and $\sigma_i = .2^\circ$). The remaining orbital elements are selected randomly from uniform distributions. Next, we integrate our model AB in the presence of a static Jupiter and Saturn in a 3:2 MMR ($a_j=5.6$ au, $a_s=7.6$ au) for 1.0 Myr using a 50 day time-step. 305 accretion events occur during this initial phase of evolution, with the largest object growing to five times its initial size. These lengthy accretion times are roughly consistent with the results of semi-analytical studies of runaway growth and embryo accretion ([Kokubo & Ida, 1996, 1998](#)). However, we do note that such oversimplified initial conditions might influence our results. Indeed, constructing the primordial belt strictly out of large bodies might overestimate the effects of planetesimal scattering and dynamical spreading in the disk. Furthermore, our simulations are not designed to simulate fragmenting and hit-and-run collisions. Because we are studying MB dynamics in the high surface density limit, not accounting for the dynamical damping effects of such collisions ([Chambers, 2013](#)) might artificially increase the orbital excitation in our fully evolved systems.

The eccentricity and inclination structure of our self-stirred initial MB is plotted in [Figure 6.1](#). We perform 18 separate, 200 Myr integrations ([Table 6.1](#)) of this AB imbedded within our respective Nice Model instability simulations using a 6 day time-step as follows (note that each individual simulation contains over 4000 objects including the forming inner terrestrial disk, 3000 asteroids, unstable giant planets, and primordial Kuiper Belt):

- 1) 8 systems (runs 1-8) are integrated with all simulation objects treated as fully self-gravitating.
- 2) The same 8 systems (now denoted runs 1a-8a) are integrated with the asteroids treated

as test particles, and all other objects as fully self-gravitating. Simulations presented in [Levison et al. \(2011\)](#) indicated that disk self gravity is important in driving the evolution of the young Kuiper Belt. By performing two sets of simulations both with and without asteroid self-gravity, we are able to test whether accounting for self-gravity affects the overall depletion or orbital structure in the MB.

3) For systems 1 and 2, we perform an additional batch of integrations (runs 1b and 2b) where we embed 4 Mercury massed planet embryos within the MB. This allows us to probe whether embedded embryos are necessary for the success of the early instability scenario ([Clement et al., 2018](#), found that much of the depletion in the scenario was due to embryo excitation).

6.3 Results and Discussion

Traditionally, the success criteria considered by dynamical studies of the AB's early evolution fall in to three general categories: depletion, radial mixing of C and S-types, and orbital structure (specifically producing a dynamically excited MB without overpopulating the high inclination parameter space above the ν_6 secular resonance). In the subsequent three sections, we address each of these constraints individually.

6.3.1 Depletion

Since each instability is inherently unique, it is important to place the solar system outcome on the spectrum of instabilities our systems experience (and corresponding levels of depletion). It is important to note here that none of our final giant planet configurations simultaneously replicate all the important qualities of the modern outer solar system (eg: success criteria A-D in [Nesvorný & Morbidelli \(2012\)](#) and E in [Deienno et al. \(2017\)](#)). Of our 18 simulations, only 7 finish with the correct number of giant planets. One simulation finished with 5 giant planets, and the instability of another (run 4a) was so violent that

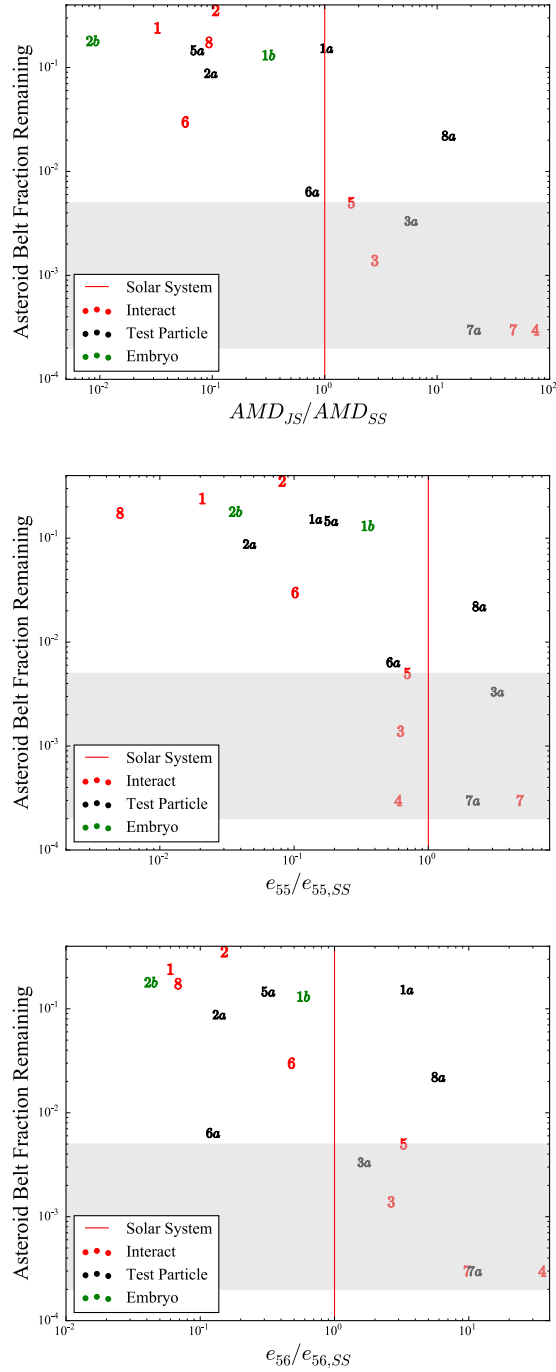


Figure 6.2: Dependence of AB depletion on the AMD of Jupiter and Saturn (top panel), the excitation of Jupiter’s g_5 mode (e_{55} , middle panel) and Saturn’s forced eccentricity (e_{56} , bottom panel). Runs 1-8 (fully self gravitating AB) are plotted in red. Runs 1a-8a (test particle AB) are plotted with black. Runs 1b and 2b (embedded planet embryos) are plotted in green. The red line denotes the solar system value for each statistic and the grey region denotes the area within a factor of 5 of a 10^{-3} depletion factor. Note, run 4a is not plotted since Saturn was ejected.

Saturn was ejected. However, as shown directly in [Deienno et al. \(2018\)](#), the perturbative effects of the ice giants on the MB are relatively weak compared to that of Jupiter and Saturn ([Morbidelli et al., 2009](#)). Therefore, systems with significantly different ice giant evolutionary schemes might still be good analogs to the solar system if their Jupiter/Saturn systems are similar. The ratio of Saturn’s orbital period to that of Jupiter is ~ 2.48 , and 8 of our systems have period ratios between 1.95-2.65 (note, $N_{GP} = 4$ and $P_S/P_J < 2.8$ are success criteria A and D in [Nesvorný & Morbidelli \(2012\)](#) and [Deienno et al. \(2017\)](#), respectively).

To compare the final orbital structure of our various Jupiter/Saturn systems with the solar system (besides run 4a that lost Saturn), we begin by calculating the normalized Angular Momentum Deficit (AMD, [Eq. 2.1](#); see [§ 2.2.2](#)) for each system ([Laskar, 1997](#)). AMD quantifies the degree to which a system of orbits differs from that of a co-planar, circular system. Thus a simulation that finishes with an AMD_{JS} close to that of the modern solar system would possess a Jupiter/Saturn pair with combined dynamical excitation similar to the actual planets. We plot the relationship between AB depletion and AMD_{JS} in the top panel of [Figure 6.2](#). There is significant scatter in the data because the instability is a highly chaotic event. However, the overall trend is very clear. Systems that finish with a more dynamically excited Jupiter/Saturn pair also experience greater depletion in the AB. Given these results, the systems that best match the solar system’s value for AMD_{JS} experience one to three orders of magnitude worth of depletion in the AB.

However, many of our systems with values of AMD_{JS} similar to that of the actual solar system are poor analogs for other reasons. In particular, the secular architecture of the solar system is dominated by the highly excited g_5 mode (success criteria C in [Nesvorný & Morbidelli, 2012](#)). For a complete discussion of the solar system’s secular structure consult [Brasser et al. \(2009\)](#) and [Morbidelli et al. \(2009\)](#). To compare the secular landscapes of our simulated systems with the solar system we calculate e_{55} (the amplitude of the Jupiter’s g_5 eigenmode; $e_{55,SS} = 0.044$) and e_{56} (the amplitude of Saturn’s forcing on Jupiter’s eccentricity; $e_{56} = 0.016$) for each integration via Fourier analysis ([Šidlichovský & Nesvorný, 1996](#)). The

bottom two panels of [Figure 6.2](#) show the dependence of AB depletion on the values of e_{55} and e_{56} . Again, in spite of significant data scatter and small number statistics, both plots show the same general trend of increased secular amplitudes correlating with larger AB depletion fractions. The relationship between e_{55} and AB depletion is perhaps the clearest of the three panels in [Figure 6.2](#). Multiple previous studies have concluded that the sufficient excitation of e_{55} is supremely important in driving the secular evolution of the solar system ([Morbidegli et al., 2009](#); [Nesvorný & Morbidelli, 2012](#); [Clement et al., 2018](#)). Therefore, it is promising that all but one of the systems in our study that sufficiently excite e_{55} to within a factor of two of its present value experience at least two orders of magnitude worth of depletion in the AB. This depletion, which is related to orbital excitation, is thus largely driven by e_{55} transmitting excitation to the MB via large forced vectors during the instability phase. Our results therefore indicate that the early instability scenario should be able to account for AB depletion at the 99-99.9% level. As an example, run 3 finishes with $N_{GP} = 4$, $P_S/P_J = 2.3$, $AMD_{JS} = 2.7 \times AMD_{JS,SS}$, $e_{55} = 0.62 \times e_{55,SS}$ and 0.13% of AB objects remaining. Furthermore, achieving this level of AB depletion and successfully forming the inner solar system are not mutually exclusive traits in our simulations. To illustrate this, [Figure 6.3](#) plots the final planets from run 2a, compared with the current solar system. The stochastic nature of planet formation makes it impossible to select a perfect solar system analog out of just 18 simulations. In run 2a the eccentricities of Earth and Venus are too large, the first three outer planets are under-excited, Mercury is over-massed, Neptune’s semi-major axis is incorrect, and an extra Mars analog forms near the inner edge of the AB. However, we still plot this result to demonstrate how the run depletes 91.2% of the AB’s mass without totally inhibiting the formation of the terrestrial planets.

It is also important to point how challenging it is for N-body simulations of the Nice Model instability to simultaneously replicate all facets of the outer solar system ([Nesvorný & Morbidelli, 2012](#); [Gomes et al., 2018](#); [Deienno et al., 2017](#)). In particular, few simulations are able to sufficiently excite AMD_{JS} and e_{55} while keeping P_S/P_J low. [Nesvorný & Morbidelli](#)

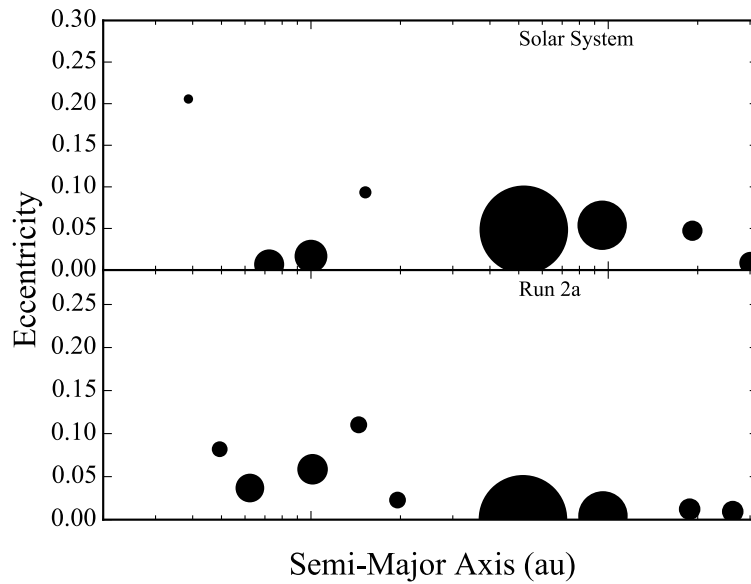


Figure 6.3: Semi-Major Axis/Eccentricity plot depicting the final planets from run 2a (bottom panel), compared with the actual solar system (top panel). The size of each point corresponds to the mass of the particle (because Jupiter and Saturn are hundreds of times more massive than the terrestrial planets, we use separate mass scales for the inner and outer planets). The final terrestrial planet masses are 0.20, 0.75, 0.86, 0.23 and 0.23 M_{\oplus} respectively.

(2012) performed over 5,000 instability simulations using a variety of different giant planet configurations and only 5% of the most successful batch simultaneously met constraints for e_{55} and P_S/P_J (success criterion C and D in that work). Within our sample of 18 instabilities, only one (run 3) successfully excites the orbits of Jupiter and Saturn while maintaining $P_S/P_J < 2.8$. Though it is encouraging that this run depletes the MB at close to the 99.9% level, our results should still be taken in context with the fact that all our other runs that experience three orders of magnitude worth of MB depletion (Table 6.2) finish with $P_S/P_J > 2.8$.

Though the differences in depletion trends between our fully self-gravitating and test particle ABs are not statistically significant, the null result is still important. Nearly all dynamical studies of early depletion in the AB only consider test particles (O’Brien et al., 2007; Deienno et al., 2016; Izidoro et al., 2016; Deienno et al., 2018). As discussed in the § 6.2, test particles provide a good approximation in the low surface density limit. However, since we assume no prior depletion in the AB, including the effects of asteroid self-gravity could be important when studying the total early depletion.

6.3.2 Radial Mixing

It is inherently difficult for N-body studies of terrestrial planet formation to explain the compositional dichotomy between S and C-types because there is no consensus as to where each type originated from in the disk. However, nucleosynthetic differences between ordinary and carbonaceous chondrite groups (Burkhardt et al., 2011) indicate that they formed at different radial distances (Kruijer et al., 2017). Early studies of planet formation in the inner solar system assumed that the different populations exist today because of a primordial division (commonly referred to as a “snow line”) in the material (Wetherill, 1992; Chambers & Wetherill, 1998). Grimm & McSween (1993) proposed that S-types formed inside ~ 2.7 au because of the higher probability of capturing energy from radionuclides (eg: ^{26}Al). In the same manner, C-types formed exterior to ~ 2.7 au where ^{26}Al is extinct. However, whether

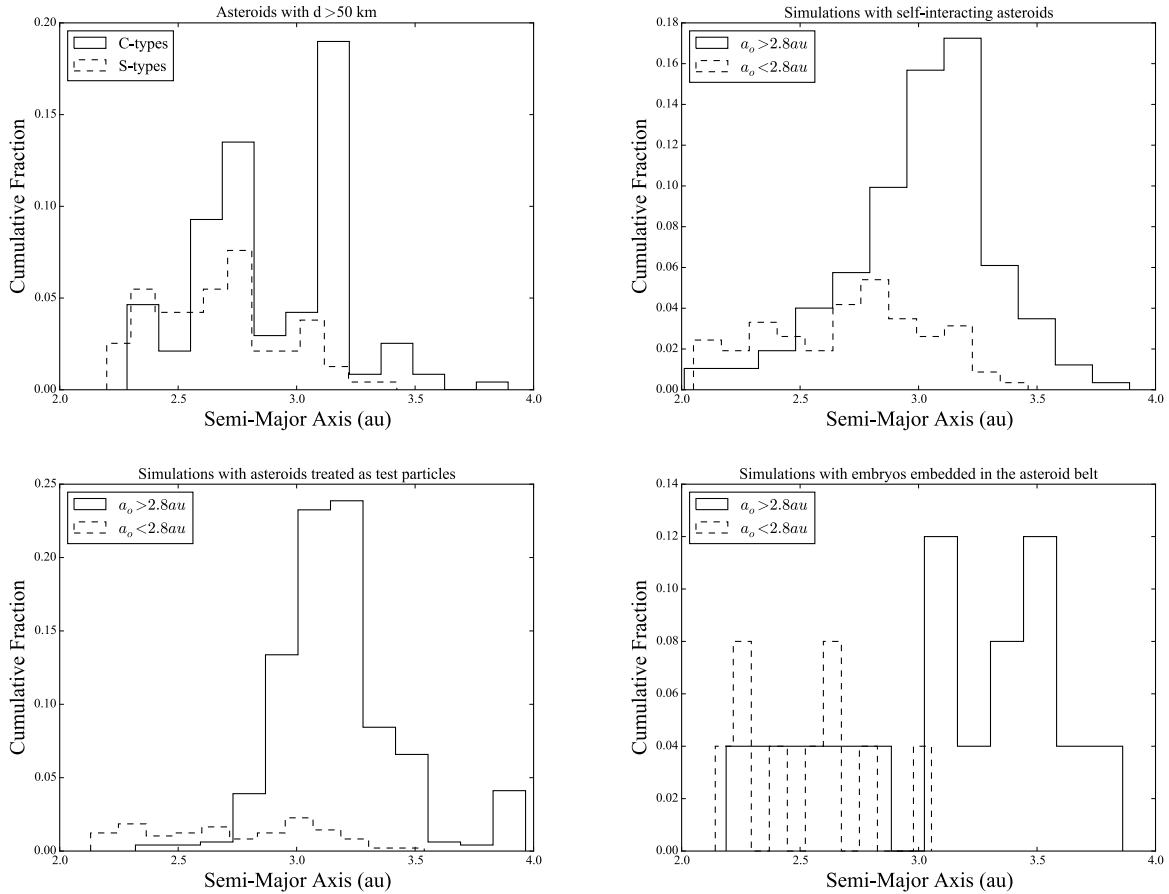


Figure 6.4: Radial mixing of silicate rich (S-type; dashed line) and carbonaceous (C-type; solid line) bodies in the actual AB (top left panel; all known asteroids with spectral classifications and $D > 50$ km) and our various simulation sets. The different curves in the other three plots (Interact, Test Particle and Embryos) compare the final distributions of all asteroids that began the integration with $a < 2.8$ au (dashed lines) to those that started with $a > 2.8$ au (solid lines). Only asteroids not on planet crossing orbits are considered.

ice exists at a snow line depends on the drift of small particles (Ciesla & Cuzzi, 2006). Studies of disk dynamics seem to indicate that snow lines tend to migrate inward (Lecar et al., 2006; Kennedy & Kenyon, 2008; Martin & Livio, 2012). Further complicating the problem, this migration can be blocked by the growing massive planets (Lambrechts et al., 2014), and thus the condensation temperature at any given point in the disk may not be correlated with the presence of volatiles (Morbidelli et al., 2016). Alternatively, Raymond & Izidoro (2017a) proposed that the AB could have already been populated with material from the outer disk (~ 5 -20 au) via scattering events during the giant planet growth phase.

We adopt a simple model to test how the giant planet instability mixes material from different radial origins in the AB. We assume that our simulations begin with the outer AB ($a > 2.8$ au) highly populated with C-types, and the inner MB dominated by S-types. In [Figure 6.4](#) we plot the final distributions of asteroids originating from inside and outside 2.8 au for our three simulation sets. Though this figure is biased towards simulations with less depletion, our fully interacting runs provide the best match to the current two distributions. The majority of the total belt material is in the form of C-types, and the interior population of S-types is significantly mixed with the outer C-types. Specifically, 67% of all remaining asteroids in these runs are considered C-types (originate outside 2.8 au), as compared to 60% of all modern asteroids with $D > 50$ km. 43% of those same asteroids that reside in the inner MB ($a < 2.8$ au) are C-types (compared with 49% in the solar system). Furthermore, our runs with more violent instabilities (and large depletion fractions) where P_S/P_J finished greater than 2.8 display a similar mixing trend. In these runs 76% of all surviving asteroids are C-types. Thus our mixing results are loosely consistent across the range of our instabilities. Though this trend is similar for all 3 simulation sets, the test particle runs over-deplete both the inner MB and total S-type inventory. Contrarily, the Embryo runs scatter a significant number of C-types inward, but fail to scatter the primordial S-types outward.

In general, the test particle only runs (1a-8a) over-deplete the inner MB of S-types because there is no dynamical friction present to save material with $a < 2.5$ au from loss when the ν_{16} and ν_6 secular resonances sweep through the belt. Indeed, our test particle simulations lose an average of 29% more mass in the inner MB ($2.0 < a < 2.5$ au) in the 100 Kyr after the first ice giant ejection than in our other simulations. This is consistent with other studies of resonant sweeping in the AB ([Walsh & Morbidelli, 2011](#)). However, it is also possible that this is the result of small number statistics and the limited number of simulations used in our study. When disk self-gravity is included (runs 1-8), the overall distribution is a much better match to that of the actual solar system.

Though the populations of S and C-types in runs 1b and 2b are not as well mixed as

those in runs 1-8, the small number statistics make it difficult to say whether the difference is significant. Indeed, runs 1b and 2b both experience uncharacteristically weak instabilities when compared with our other runs (see [Figure 6.2](#)). Both only excite e_{55} to less than half the modern value, and finish with an AMD_{JS} less than a third that of $AMD_{JS,SS}$. Since the giant planets' resonant perturbations were less strong in these simulations, it makes sense that the final MB populations are less mixed than those of the other simulation sets.

Nevertheless, the radial mixing results of our interaction set are encouraging and in decent agreement with the modern solar system's distribution (though this assumes perfect zoning at the beginning of our runs, and is biased towards runs with less depletion). Furthermore, since the Kirkwood gaps have yet to fully shape the radial structure of the MB at $t=200$ Myr, we need not expect the shapes (in particular the inter-gap peaks) of the distributions to match exactly ([Morbidelli et al., 1995](#); [Petit et al., 2001](#); [O'Brien et al., 2007](#); [Deienno et al., 2016, 2018](#)).

6.3.3 Orbital Structure

Most studies of the MB's detailed structure attempt to match a simulated belt's a/e and a/i distributions with that of the actual MB. The actual MB orbital distribution is well characterized in a/e space by a uniform distribution of excited orbits that inhabit the entire allowed parameter space (that is to say all excited orbits that are not planet crossing). However, the present day MB's a/i distribution is peculiar in that it is largely devoid of high inclination asteroids above the ν_6 secular resonance. The inability to match the ratio of simulated asteroids in the inner MB above to below this resonance with that of the solar system (often cited as ~ 0.08 ; calculated by taking the 100 biggest asteroids with $a < 2.8$ au) is a common pitfall of many studies of MB dynamics ([Walsh & Morbidelli, 2011](#); [Deienno et al., 2016](#)). However, the MB's radial mass distribution profile is far from uniform because half of its mass is concentrated in just 4 asteroids. From the standpoint of mass distribution, the MB's structure seems to be better characterized by just a handful of massive bodies

Run	AMD_{JS}	P_S/P_J	$M_{AB,f}/M_{AB,i}$	ν_6 ratio
1	0.048	2.35	0.23	0.31
2	0.097	1.93	0.34	2.31
3	2.33	2.77	0.0014	inf
4	74.3	21.5	0	N/A
5	1.72	3.94	0.005	inf
6	0.057	2.08	0.030	4.25
7	47.7	17.9	0	N/A
8	0.093	3.94	0.17	0.50
1a	1.03	5.16	0.15	0.60
2a	0.096	2.53	0.088	2.00
3a	5.84	4.12	0.0033	3.00
4a	N/A	N/A	0.036	0.91
5a	0.074	2.41	0.14	1.45
6a	0.78	4.37	0.0064	0.67
7a	21.29	6.19	0	N/A
8a	12.7	8.02	0.022	1.67
1b	0.31	2.70	0.13	1.00
2b	0.0086	2.23	0.18	inf

Table 6.2: Table of results for our 18 runs. The columns are as follows: (1) the run number, (2) the AMD of the Jupiter/Saturn system, (3) Jupiter and Saturn period ratio, (4) the run’s AB depletion fraction, and (5) the ratio of asteroids above to below the ν_6 resonance. Only asteroids not on planet crossing orbits are considered.

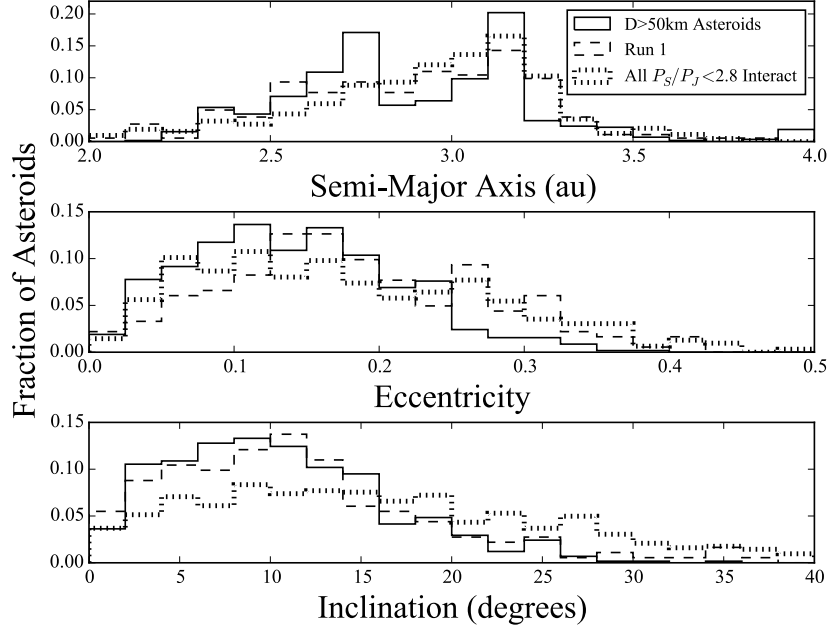


Figure 6.5: Histograms of semi-major axis (top panel), eccentricity (middle panel), and inclination (bottom panel) distributions for the modern asteroid belt (solid lines; $H < 9.7$, $D > 50$ km), run 1 (dashed lines) and all interaction systems with $P_S/P_J < 2.8$ (dot-dashed lines). Only asteroids not on planet crossing orbits are considered.

embedded in a sea of objects several orders of magnitude smaller (many of which are likely the products of collisional grinding; Bottke et al., 2005b, 2015; Dermott et al., 2018). Indeed, the ν_6 ratio calculated for all known asteroids with $a < 2.8$ au with respect to number of asteroids (0.04), is a significantly smaller than when it is calculated with respect to mass (0.14). The reason for this is that the third largest asteroid, Pallas, has an inclination above the ν_6 resonance (33°).

In the sense that the AB’s structure is dominated by a small number of asteroids, the third largest of which is above the ν_6 resonance, our simulations are largely successful. Since our initial asteroids have masses within an order of magnitude or so of the actual larger asteroids in the MB, it is encouraging that the majority of our simulations deplete the MB down to just a few of such objects. Furthermore, the MB structure is also dominated by multiple large collisional families that formed after the epoch of terrestrial planet formation

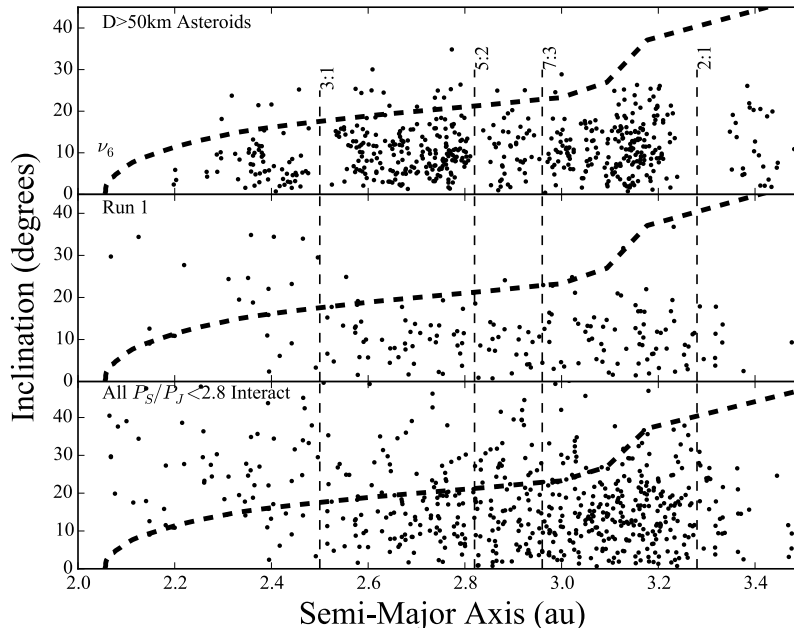


Figure 6.6: Semi-major axis/inclination plot for the modern asteroid belt (top panel; $H < 9.7$, $D > 50$ km), run 1, and all interaction systems with $P_S/P_J < 2.8$. Only asteroids not on planet crossing orbits are considered. The vertical dashed lines represent the locations of the important mean motion resonances with Jupiter. The bold dashed lines indicate the current location of the ν_6 secular resonance.

(Bottke et al., 2015; Dermott et al., 2018). Thus it is supremely difficult to correlate the current belt’s orbital and size distributions with those at $t=200$ Myr (Bottke et al., 2005b).

Nevertheless, our simulated belt’s eccentricity and inclination distributions are fairly similar to the real distribution. In Figures 6.5, 6.6 and 6.7, we compare the orbital distributions for all bright ($H < 9.7$) asteroids larger than 50 km with our results from run 1, and all of our interaction runs where Jupiter and Saturn’s period ratio finished below 2.8. We select run 1 in this figure because it finished with the most MB objects of any interaction run with $P_S/P_J < 2.8$ and $N_{GP} = 4$. Thus we provide an example of a single successful distribution without co-adding results. However, this plot should be taken in context with the fact that run 1 finishes with a low $AMD_{JS,SS}$, and significantly under-excited e_{55} and e_{56} amplitudes. Furthermore, the co-added plot is biased toward similar simulations with lower depletion.

In keeping with previous works, our simulations consistently struggle to replicate the

modern AB’s structure about the ν_6 secular resonance. [Walsh & Morbidelli \(2011\)](#) reported a ratio of ~ 5.2 in a smooth migration scenario. [Deienno et al. \(2016\)](#) evaluated a post-Grand Tack version of the late Nice Model and determined a ratio ~ 1.2 (0.10 when removing post-Grand Tack asteroids with $i > 20^\circ$). Studies of an early instability have shown promise in replicating some aspects of the belt’s structure, but still fall short when it comes to the ν_6 ratio. [Clement et al. \(2018\)](#) co-added the remaining asteroids from successful simulations ($P_S/P_J < 2.8$) and found the ratio to be ~ 0.73 , but the value was much worse when only considering the inner MB asteroids with $a < 2.5$ au (~ 2.2). In a similar study, [Deienno et al. \(2018\)](#) considered a “Jumping Jupiter” style instability and found the ratio to be ~ 1.3 (0.07 when removing post-instability asteroids with $i > 20^\circ$). In general, our simulations ([Table 6.2](#)) finish with ratios of similar order to those found in previous early instability studies. Our best ratio occurred in run 1 (0.31). Because the sculpting mechanisms in each instability are unique, it is difficult to extrapolate a correlation between depletion and the final ν_6 ratio.

Two of our runs finished with the entire inner MB population’s inclinations above the ν_6 resonance. This occurs when the location of the ν_6 resonance drags more smoothly through the inner MB. Instabilities where the migration of the giant planet’s orbits and respective resonances is more chaotic are less likely to excite the entire region uniformly, and finish with better ratios. This is also the case in the nominal “Jumping Jupiter” style instability ([Brasser et al., 2009](#); [Nesvorný et al., 2013](#); [Deienno et al., 2018](#)). In either scenario, the location of the resonance does not spend a significant amount of time in any one location during the planetary instability.

In spite of several moderately successful runs (eg: runs 1, 8, 1a, 4a and 6a) that finish with ν_6 ratios less than unity, reproducing the inner MB’s a/i structure is still an outstanding problem for the early instability model. However, the MB’s orbital distribution has evolved as the result of family-forming events over the past ~ 4 Gyr ([Bottke et al., 2015](#)). In fact, [Dermott et al. \(2018\)](#) estimated that $\sim 85\%$ of inner MB asteroids originated from one of

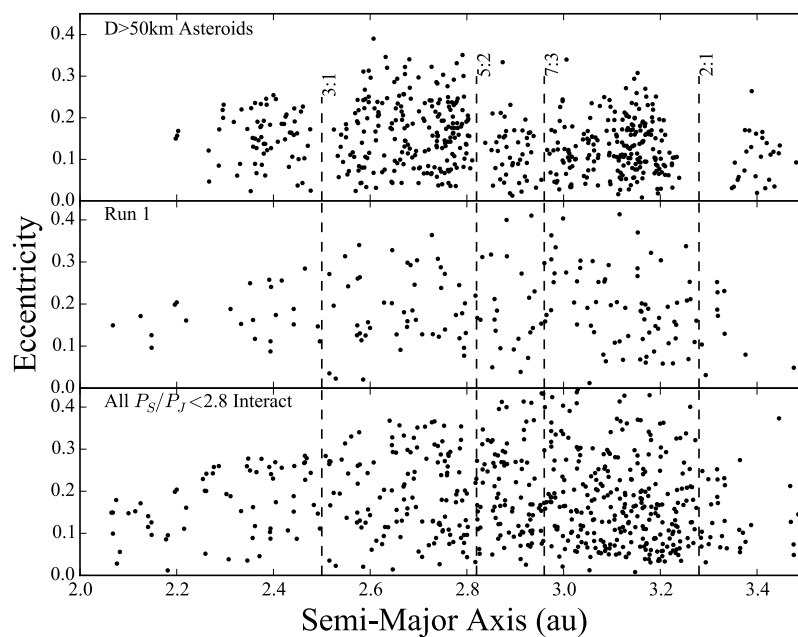


Figure 6.7: Semi-major axis/eccentricity plot for the modern asteroid belt (top panel; $H < 9.7$, $D > 50$ km), run 1, and all interaction systems with $P_S/P_J < 2.8$. Only asteroids not on planet crossing orbits are considered. The vertical dashed lines represent the locations of the important mean motion resonances with Jupiter.

just five original collisional families (Flora, Vesta, Nysa, Polana and Eulalia). Thus, it is possible that the primordial AB contained very few objects. If Pallas was one of this primordial population of a few, “large” asteroids, and its high inclination (above the ν_6 resonance) is primordial, our results may not be particularly problematic. Indeed, planet formation simulations that include collisional fragmentation (Clement et al., 2019b) indicate that collisional fragments tend to preferentially populate the inclination parameter space below the ν_6 secular resonance. Thus, future work on the topic must utilize similar GPU accelerated integration schemes to study how collisional fragmentation shapes the young asteroid belt. If it turns out that the fragmentation process dramatically alters the primordial belt’s size distribution, it is possible that the dynamical friction generated by a diverse population of fragments could save material from loss during the instability. If that were the case, the depletion values discussed in § 6.3.1 might be overestimated.

6.3.4 Seeded Embryos

We implanted 4 Mercury massed embryos in the primordial MB in two of our simulations (runs 1b and 2b). As discussed in the introduction, early dynamical studies of terrestrial planet formation often argued that primordial Moon to Mars massed planet embryos might explain the AB’s substantial early mass loss (Wetherill, 1992; Chambers & Wetherill, 2001; Chambers, 2001; Petit et al., 2001). To prevent additional semi-major axis gaps in the belt’s structure from being fossilized, embryos larger than Mercury could not have survived the planet formation process (Chambers, 2007; Raymond et al., 2009b; O’Brien & Sykes, 2011). Thus the problem with the depletion via primordial embryos model is two-fold. First, recent studies of pebble accretion during the gas disk phase indicate that large embryos may not have formed so far out in the terrestrial disk (Levison et al., 2015b). Second, studies that include large embryos throughout the entire MB region often fail to destabilize all of them within the ~ 200 Myr of terrestrial planet formation (Chambers, 2001; Raymond et al., 2009b). Indeed only 54% of the best set of the early instability simulations in Clement et al.

(2018) deplete all primordial embryos from the AB.

Our simulations that began with four, Mercury-massed planet embryos in the MB provide poor matches to the current solar system for several reasons. Both simulations finish with a $\sim 0.25 M_{\oplus}$ planet in the MB on a stable orbit. In contrast, only one of our other 16 systems finishes with an object larger than Mercury in the MB region. In those runs, accretion began slowly in the belt during the initial 1 Myr of integration that did not include any giant planet evolution (Kokubo & Ida, 1996, see discussion in § 6.2). This growth was then aborted when the Nice Model instability ensued (Clement et al., 2018). While the instabilities in both runs were relatively weak in terms of the excitation of the giant planets (AMD_{JS} , e_{55} and e_{56}), neither system experienced substantially more depletion than did other runs with similar giant planet outcomes (Figure 6.2). Thus, our results indicate that excitation from the giant planets, rather than from embedded embryos, is the dominant depletion mechanism in the early instability scenario (Clement et al., 2018). Though our current study’s sample of just 2 embryo systems is small, our other successful simulations consistently depleted a substantial percentage of AB material (~ 99 - 99.9%). Therefore, embedding embryos in the primordial MB population is not necessary within the context of the early instability scenario to deplete the MB by ~ 3 orders of magnitude.

6.3.5 The formation of Veneneia

As the instability excites asteroids on to orbits where they are ejected from the solar system, many continue to cross the MB region for some time before being lost completely. In our fully self-interacting runs, these excited objects can still undergo collisions with stable MB asteroids. When we evaluate the accretion histories of asteroids in our 4 interaction runs that finished with $P_S/P_J < 2.8$, we find that the results are highly dependent on the instability’s strength. Runs 1 and 2 each experienced weaker instabilities, and finished with more asteroids, and low values of AMD_{JS} , e_{55} and e_{56} . Asteroids in these instabilities undergo an average of ~ 0.7 collisions over the 200 Myr simulation duration. On the other hand, runs 3

and 6 experienced more violent instabilities. In those runs, surviving asteroids experienced no accretion events. Since our simulations only model larger asteroids (similar to Ceres and Vesta), we can loosely correlate the accretion histories of our simulated MB particles to that of Vesta. Because the projectiles that formed the Rheasilvia and Veneneia craters are estimated to have had diameters between $\sim 60\text{-}70$ km (Jutzi et al., 2013), we can use the AB’s modern size distribution to extrapolate how likely such collisions would be in our models. The present day belt contains 86 such asteroids. Therefore, we can conclude that Rheasilvia and Veneneia-forming events would have been too common in runs 1 and 2. Unfortunately, such a calculation is beyond the resolution of our simulations in runs 3 and 6. These results, however, are highly biased by the stochastic nature of the instability and the small number of simulations presented in our study.

6.4 Conclusions

In this Chapter we presented 18 N-body simulations of the effect of an early Nice Model instability (Tsiganis et al., 2005; Clement et al., 2018) on a 3000 particle AB. In 10 of our simulations, the entire AB is modeled as fully self-gravitating. Our simulations show that the early instability scenario can deplete a $\sim 2 M_{\oplus}$ primordial AB (commensurate with the minimum mass solar nebula; Weidenschilling, 1977) at the $\sim 99\text{-}99.9\%$ level. The level of depletion experienced by a particular system is related to the unique evolution of the giant planets within the chaotic orbital instability. Since each instability is unique, and it is impossible to know the exact evolution of the giant planets in the young solar system’s own instability, our work establishes a spectrum outcomes on which we place the solar system. In particular, depletion increases with higher values of AMD_{JS} and e_{55} (the amplitude of Jupiter’s g_5 eigenmode). Systems that finish with values of AMD_{JS} and e_{55} similar to those of the present solar system tend to deplete the AB by two to three orders of magnitude.

Assuming the outer primordial AB was populated with volatile rich C-type asteroids

(either because of a primordial “snow-line” or via scattering during the giant planet growth phase as described in [Raymond & Izidoro, 2017a](#)), our fully self-gravitating simulations are very successful at reproducing the observed distribution of S and C-types. Contrarily, radial mixing is not as strong in our simulations that only consider asteroids as test particles. Furthermore, these test particle only simulations typically over-erode the inner MB region ($2.0 < a < 2.5$ au). Dynamical friction between asteroids helps to de-excite orbits in the region, and prevent this erosion in our fully self-interacting systems.

In general, our systems adequately replicate the eccentricity and inclination distributions of the modern AB. However, consistent with various previous studies ([Walsh & Morbidelli, 2011](#); [Deienno et al., 2016](#); [Clement et al., 2018](#); [Deienno et al., 2018](#)), our simulations often fail to replicate the AB’s population about the ν_6 secular resonance. However, the MB size distribution has evolved significantly since the epoch of terrestrial planet formation ([Bottke et al., 2005b](#)), and its orbital distribution has likely been altered via the formation of collisional families ([Dermott et al., 2018](#)). Since the MB’s mass profile is dominated by just a few asteroids, one of which (Pallas) is on a highly inclined orbit above the ν_6 resonance, our systems still broadly replicate the distribution of the most massive asteroids.

Our results should be taken in the appropriate context given the sensitivity of the AB’s depletion and final structure to the particular dynamics of the giant planet instability. It is impossible to know the exact evolutionary path followed by the giant planets during the Nice Model instability. Furthermore, none of our final giant planet systems are exact matches to the modern solar system. Therefore, our study can only correlate specific dynamical qualities of the present solar system with those of our simulations. Nevertheless, our fully self-gravitating ABs are largely successful at replicating the modern belt for several reasons. These include a number of systems with low ratios of asteroids above to below the ν_6 resonance, accurate radial distributions of S and C-types, and relatively high levels of MB depletion.

While our work demonstrates that GPU accelerated N-body simulations offer an unprece-

dened opportunity to explore higher-N systems, each of our simulations still requires large amounts of computing resources. Specifically, each simulation in this Chapter required the same number of node hours to complete as 32 conventional (CPU only) integrations of terrestrial planet formation using standard initial conditions (Chambers, 2001; Clement et al., 2018). In spite of generating a suite of simulated asteroid belts sculpted by giant planet instabilities, the stochasticity of instabilities and the small number of surviving asteroids prevents us from developing detailed predictions of asteroid belt structure as a function of instability characteristics. Doing so will likely require still more extensive sets of instability simulations.

6.5 Acknowledgments

This Chapter is reproduced by permission of the American Astronomical Society from the following publication: Clement, M. S., Raymond, S.N., and Kaib, N.A. (April 2019). Excitation and Depletion of the Asteroid Belt in the Early Instability Scenario. In: *AJ* 157: 38.

This material is based upon research supported by the Chateaubriand Fellowship of the Office for Science and Technology of the Embassy of France in the United States. We thank Rogerio Deienno and Bill Bottke for thoughtful comments and insight. M.S.C. and N.A.K. thank the National Science Foundation for support under award AST-1615975. S.N.R. thanks the Agence Nationale pour la Recherche for support via grant ANR-13-BS05-0003-002 (grant MOJO) and acknowledges NASA Astrobiology Institutes Virtual Planetary Laboratory Lead Team, funded via the NASA Astrobiology Institute under solicitation NNH12ZDA002C and cooperative agreement no. NNA13AA93A. This research is part of the Blue Waters sustained-petascale computing project, which is supported by the National Science Foundation (awards OCI-0725070 and ACI-1238993) and the state of Illinois. Blue Waters is a joint effort of the University of Illinois at Urbana-Champaign and its National

Center for Supercomputing Applications ([Bode et al., 2013](#); [Kramer et al., 2015](#)).

Chapter 7

Conclusions

In this thesis I presented several sets of numerical simulations that modeled terrestrial planet formation and evolution in our solar system. Through this work, we developed the first theoretical model for the solar system's evolution that simultaneously explains both the terrestrial and giant planet systems. Motivated by multiple recent studies that argue against the occurrence of a LHB (Kaib & Chambers, 2016; Zellner, 2017; Morbidelli et al., 2018; Nesvorný et al., 2018; Quarles & Kaib, 2019), we expanded the Nice Model evolutionary scheme for the outer solar system to include the terrestrial system as well. By timing the instability in situ with the process of terrestrial planet formation ($\sim 1-10$ Myr after gas disk dispersal), we showed that an early Nice Model instability also resolves several longstanding problems with the classic model of terrestrial planet formation.

In Chapter 2 (Clement & Kaib, 2017) we probed the sources of chaos in terrestrial planet systems grown via embryo accretion models. We showed that chaos is prevalent in around half of our 145 systems. Perturbations from Jupiter and Saturn appeared to drive the majority of this chaos. The unique makeup of each terrestrial system was also found to be a reliable indicator of the presence of chaos. Specifically, systems with less than 4 inner planets, and those with a center of mass highly concentrated between $\sim 0.8-1.2$ au were less susceptible to chaos. Furthermore, we showed that late (>200 Myr) instabilities are a common outcome of the planet formation process as we presently understand it. Thus our

solar system’s marginally stable, chaotic state (largely driven by perturbations from Jupiter) is consistent with the results of our planet formation models.

In Chapter 3 (Clement et al., 2018) we developed the framework for the early instability scenario. We presented 800 numerical simulations of a Nice Model instability taking place in conjunction with the epoch of terrestrial planet formation. By systematically testing different instability timings, we demonstrated that an instability occurring ~ 1 -10 Myr after the disappearance of the Sun’s primordial gas disk aborts Mars’ formation, while leaving the growth of Earth and Venus uninhibited. Our preferred instability timing also has the advantage of naturally explaining the disparity between Earth (Touboul et al., 2007; Halliday, 2008; Kleine et al., 2009) and Mars’ (Nimmo & Agnor, 2006; Dauphas & Pourmand, 2011) geological accretion timescales. We also scrutinized the giant planet outcomes from our various simulations, and noted that the terrestrial system is best replicated when the outer solar system most closely matches its modern configuration. While a Nice Model instability delayed by ~ 600 Myr is very likely to destabilize the fully formed inner planets, our work shows that multiple longstanding problems with terrestrial planet formation models can be resolved if the instability takes place 1-10 Myr after the nebular gas disappears.

In Chapter 4 (Clement et al., 2019b) we explored the early instability scenario in further depth with a numerical integration scheme (Chambers, 2013) that accounts for collisional fragmentation. Our new batch of simulated terrestrial systems consistently yielded better solar system analogs than our original runs that did not include a fragmentation scheme. Because of increased dynamical friction from collisional fragments, and hit-and-run collisions that dissipate angular momentum, the differences between our two sets’ terrestrial AMDs and RMCs was most pronounced. The Earth and Venus analogs in our new simulations proved to be excellent matches to the real planets in terms of their eccentricities, inclinations and mutual orbital spacings. While accounting for collisional fragmentation often yielded larger Mars analogs, it also tended to lengthen the growth timescales of Earth, and shorten those for Mars. Thus, the observed formation timescale disparity between Earth and Mars is better

matched when fragmentation processes are included, but the Earth-Mars mass disparity is more difficult to reproduce. Our simulations that employed a 1 Myr instability time often produced low-mass Mars analogs, but also frequently prevented Mars' accretion entirely. This provides further constraints on the specific instability timing required to resolve the small Mars problem.

In Chapter 5 (Clement et al., 2019a) we continued to investigate the Clement et al. (2019b) simulation set (Chapter 4), and presented new simulations designed to investigate Mercury's collisional origin. We found that simultaneously replicating Mercury's current orbit and the terrestrial system's AMD is an extremely low probability event when modeling Mercury's origin via a collision between an unstable proto-planet and a proto-Earth or proto-Venus. While boosting the speed of escaping fragments helped produce better matches to the modern dynamical spacing between Mercury and Venus, it came with the added disadvantage of increasing the likelihood of over-exciting the fragment (Mercury) to the point where it was lost from the system. We concluded that it is highly improbable that Mercury formed as the result of a single giant impact with the proto-Venus (Asphaug & Reufer, 2014). However, our suite of terrestrial systems provided numerous examples of Mercury-like planets with high CMFs. While numerical simulations of terrestrial planet formation still struggle to routinely generate planets with masses and semi-major axes analogous to Mercury's, we postulated that Mercury's true origin is likely buried deep within the stochastic, chaotic process of planet formation.

In Chapter 6 (Clement et al., 2019c) we found that a primordially massive belt (consistent with the masses inferred from disk models; Weidenschilling, 1977; Hayashi, 1981; Bitsch et al., 2015) can be depleted at the 99-99.9% level by an early Nice Model instability, and provide a good match to the modern solar system. Furthermore, we observed higher depletion values in simulations where the giant planets' final orbital configuration most closely matched their actual structure. We also showed that the instability provides an efficient mechanism to radially mix the populations of asteroids in the belt. Furthermore, our simulations final a/e

and a/i distributions were in broad agreement with the distribution of mass in the actual belt. While our simulations struggle to replicate the inner main belt's population about the ν_6 secular resonance, the final ratios in several of our runs provide a marked improvement over those from previous studies (Walsh & Morbidelli, 2011; Deienno et al., 2016; Clement et al., 2018; Deienno et al., 2018).

Future investigations into terrestrial planet formation in the solar system must seek out constraints and tests to distinguish between the major classes of proposed models (specifically those supposing a truncated initial disk and those relying on the influence of the fully formed giant planets). We discussed how detailed investigations into planetesimal formation in the gas disk phase, the long term evolution of the asteroid belt, and the epoch of late terrestrial bombardment and late veneer formation are all promising avenues for such projects. These future studies must continue to attain higher particle resolution and develop more accurate models of the accretion process through advancements in algorithm efficiency and the handling of collisions, analogous to the advances employed in this thesis.

Bibliography

- Agnor, C. B. 2017, in AAS/Division of Dynamical Astronomy Meeting, Vol. 48, AAS/Division of Dynamical Astronomy Meeting, 102.04
- Agnor, C. B., & Lin, D. N. C. 2012, *ApJ* , 745, 143
- Àngel Jorba. 2012, UNESCO Encyclopedia of Life Support Systems, Vol. 6.119.55 Celestial Mechanics
- Asphaug, E. 2010, *Chemie der Erde / Geochemistry*, 70, 199
- Asphaug, E., Agnor, C. B., & Williams, Q. 2006, *Nature* , 439, 155
- Asphaug, E., & Reufer, A. 2014, *Nature Geoscience*, 7, 564
- Badro, J. 2014, *Annual Review of Earth and Planetary Sciences*, 42, 231
- Barr, A. C., & Canup, R. M. 2010, *Nature Geoscience*, 3, 164
- Baruteau, C., Crida, A., Paardekooper, S.-J., et al. 2014, *Protostars and Planets VI*, 667
- Batygin, K., & Brown, M. E. 2010a, *ApJ* , 716, 1323
- . 2010b, *ApJ* , 716, 1323
- Batygin, K., Brown, M. E., & Betts, H. 2012, *ApJL* , 744, L3
- Batygin, K., & Laughlin, G. 2015, *Proceedings of the National Academy of Science*, 112, 4214
- Beaugé, C., & Nesvorný, D. 2012, *ApJ* , 751, 119
- Benz, W., Anic, A., Horner, J., & Whitby, J. A. 2007, *Space and Science Reviews* , 132, 189
- Benz, W., Slattery, W. L., & Cameron, A. G. W. 1988, *Icarus*, 74, 516
- Birnstiel, T., Klahr, H., & Ercolano, B. 2012, *A&A* , 539, A148
- Bitsch, B., Johansen, A., Lambrechts, M., & Morbidelli, A. 2015, *A&A* , 575, A28
- Bode, B., Butler, M., Dunning, T., et al. 2013, in *Contemporary High Performance Computing*, Chapman & Hall/CRC Computational Science (Chapman and Hall/CRC), 339–366

- Boehnke, P., & Harrison, T. M. 2016, *Proceedings of the National Academy of Science*, 113, 10802
- Boisvert, J. H., Nelson, B. E., & Steffen, J. H. 2018, *MNRAS* , 480, 2846
- Bonsor, A., Leinhardt, Z. M., Carter, P. J., et al. 2015, *Icarus*, 247, 291
- Bottke, W. F., Brož, M., O'Brien, D. P., et al. 2015, *The Collisional Evolution of the Main Asteroid Belt*, ed. P. Michel, F. E. DeMeo, & W. F. Bottke, 701–724
- Bottke, W. F., Durda, D. D., Nesvorný, D., et al. 2005b, *Icarus*, 175, 111
- . 2005a, *Icarus*, 179, 63
- . 2006a, *Icarus*, 183, 235
- Bottke, W. F., Levison, H. F., Nesvorný, D., & Dones, L. 2007, *Icarus*, 190, 203
- Bottke, W. F., Nesvorný, D., Grimm, R. E., Morbidelli, A., & O'Brien, D. P. 2006b, *Nature* , 439, 821
- Bottke, W. F., Walker, R. J., Day, J. M. D., Nesvorný, D., & Elkins-Tanton, L. 2010, *Science*, 330, 1527
- Brasil, P. I. O., Roig, F., Nesvorný, D., et al. 2016, *Icarus*, 266, 142
- Brasser, R., Matsumura, S., Ida, S., Mojzsis, S. J., & Werner, S. C. 2016a, *ApJ* , 821, 75
- Brasser, R., Mojzsis, S. J., Werner, S. C., Matsumura, S., & Ida, S. 2016b, *Earth and Planetary Science Letters*, 455, 85
- Brasser, R., Morbidelli, A., Gomes, R., Tsiganis, K., & Levison, H. F. 2009, *A&A* , 507, 1053
- Brasser, R., Walsh, K. J., & Nesvorný, D. 2013, *MNRAS* , 433, 3417
- Bromley, B. C., & Kenyon, S. J. 2017, *AJ* , 153, 216
- Burkhardt, C., Kleine, T., Oberli, F., et al. 2011, *Earth and Planetary Science Letters*, 312, 390
- Bus, S. J., & Binzel, R. P. 2002, *Icarus*, 158, 146
- Campins, H., de Leon, J., Licandro, J., et al. 2018, *ArXiv e-prints*, arXiv:1809.01148
- Canup, R. M. 2012, *Science*, 338, 1052
- Carrera, D., Gorti, U., Johansen, A., & Davies, M. B. 2017, *ApJ* , 839, 16
- Carter, P. J., Leinhardt, Z. M., Elliott, T., Walter, M. J., & Stewart, S. T. 2015, *ApJ* , 813, 72

- Chambers, J. E. 1999, *MNRAS* , 304, 793
- . 2001, *Icarus*, 152, 205
- . 2007, *Icarus*, 189, 386
- . 2013, *Icarus*, 224, 43
- Chambers, J. E., & Cassen, P. 2002, *Meteoritics and Planetary Science*, 37, 1523
- Chambers, J. E., & Wetherill, G. W. 1998, *Icarus*, 136, 304
- . 2001, *Meteoritics and Planetary Science*, 36, 381
- Chapman, C. R., Cohen, B. A., & Grinspoon, D. H. 2007, *Icarus*, 189, 233
- Chapman, C. R., Morrison, D., & Zellner, B. 1975, *Icarus*, 25, 104
- Chatterjee, S., Ford, E. B., Matsumura, S., & Rasio, F. A. 2008, *ApJ* , 686, 580
- Chau, A., Reinhardt, C., Helled, R., & Stadel, J. 2018, *ApJ* , 865, 35
- Ciesla, F. J., & Cuzzi, J. N. 2006, *Icarus*, 181, 178
- Cincotta, P. M., Giordano, C. M., & Simó, C. 2003, *Physica D Nonlinear Phenomena*, 182, 151
- Citron, R. I., Perets, H. B., & Aharonson, O. 2018, *ApJ* , 862, 5
- Clement, M. S., & Kaib, N. A. 2017, *Icarus*, 288, 88
- Clement, M. S., Kaib, N. A., & Chambers, J. E. 2019a, arXiv e-prints, arXiv:1904.02173
- Clement, M. S., Kaib, N. A., Raymond, S. N., Chambers, J. E., & Walsh, K. J. 2019b, *Icarus*, 321, 778
- Clement, M. S., Kaib, N. A., Raymond, S. N., & Walsh, K. J. 2018, *Icarus*,
- Clement, M. S., Raymond, S. N., & Kaib, N. A. 2019c, *AJ* , 157, 38
- Cresswell, P., Dirksen, G., Kley, W., & Nelson, R. P. 2007, *A&A* , 473, 329
- Ćuk, M., & Stewart, S. T. 2012, *Science*, 338, 1047
- Currie, T., Lada, C. J., Plavchan, P., et al. 2009, *ApJ* , 698, 1
- D'Angelo, G., & Marzari, F. 2012, *ApJ* , 757, 50
- Dauphas, N., & Pourmand, A. 2011, *Nature* , 473, 489
- Day, J. M. D., Pearson, D. G., & Taylor, L. A. 2007, *Science*, 315, 217
- Deck, K. M., Payne, M., & Holman, M. J. 2013, *ApJ* , 774, 129

- Deienno, R., Gomes, R. S., Walsh, K. J., Morbidelli, A., & Nesvorný, D. 2016, *Icarus*, 272, 114
- Deienno, R., Izidoro, A., Morbidelli, A., et al. 2018, *ApJ* , 864, 50
- Deienno, R., Morbidelli, A., Gomes, R. S., & Nesvorný, D. 2017, *AJ* , 153, 153
- Delbo', M., Walsh, K., Bolin, B., Avdellidou, C., & Morbidelli, A. 2017, *Science*, 357, 1026
- Delisle, J.-B., Correia, A. C. M., & Laskar, J. 2015, *A&A* , 579, A128
- DeMeo, F. E., & Carry, B. 2013, *Icarus*, 226, 723
- Dermott, S. F., Christou, A. A., Li, D., Kehoe, T. J. J., & Robinson, J. M. 2018, *Nature Astronomy*, 2, 549
- Dominik, C., Blum, J., Cuzzi, J. N., & Wurm, G. 2007, *Protostars and Planets V*, 783
- Drażkowska, J., Alibert, Y., & Moore, B. 2016, *A&A* , 594, A105
- Drażkowska, J., & Dullemond, C. P. 2018, *A&A* , 614, A62
- Duncan, M. J., Levison, H. F., & Lee, M. H. 1998, *AJ* , 116, 2067
- Dwyer, C. A., Nimmo, F., & Chambers, J. E. 2015, *Icarus*, 245, 145
- Ebel, D. S., & Stewart, S. T. 2017, ArXiv e-prints, arXiv:1712.08234
- Elliot, J. L., Kern, S. D., Clancy, K. B., et al. 2005, *AJ* , 129, 1117
- Fabrycky, D. C., & Murray-Clay, R. A. 2010, *ApJ* , 710, 1408
- Fassett, C. I., Head, J. W., Kadish, S. J., et al. 2012, *Journal of Geophysical Research (Planets)*, 117, E00H06
- Fernandes, V. A., Burgess, R., & Turner, G. 2000, *Meteoritics and Planetary Science*, 35, 1355
- Fernandez, J. A., & Ip, W.-H. 1984, *Icarus*, 58, 109
- Fischer, R. A., & Ciesla, F. J. 2014, *Earth and Planetary Science Letters*, 392, 28
- Fressin, F., Torres, G., Charbonneau, D., et al. 2013, *ApJ* , 766, 81
- Fritz, J., Bitsch, B., Kührt, E., et al. 2014, *Planetary and Space Science* , 98, 254
- Genda, H., Kokubo, E., & Ida, S. 2012, *ApJ* , 744, 137
- Gillon, M., Triaud, A. H. M. J., Demory, B.-O., et al. 2017, *Nature* , 542, 456
- Gladman, B., Kavelaars, J. J., Petit, J.-M., et al. 2001, *AJ* , 122, 1051
- Gomes, R., Levison, H. F., Tsiganis, K., & Morbidelli, A. 2005, *Nature* , 435, 466

- Gomes, R., Nesvorný, D., Morbidelli, A., Deienno, R., & Nogueira, E. 2018, *Icarus*, 306, 319
- Gomes, R. S. 2003, *Icarus*, 161, 404
- Gradie, J., & Tedesco, E. 1982, *Science*, 216, 1405
- Gradie, J. C., Chapman, C. R., & Tedesco, E. F. 1989, in *Asteroids II*, ed. R. P. Binzel, T. Gehrels, & M. S. Matthews, 316–335
- Grimm, R. E., & McSween, H. Y. 1993, *Science*, 259, 653
- Grimm, S. L., & Stadel, J. G. 2014, *ApJ* , 796, 23
- Hahn, J. M., & Malhotra, R. 1999, *AJ* , 117, 3041
- Haisch, Jr., K. E., Lada, E. A., & Lada, C. J. 2001, *ApJL* , 553, L153
- Halliday, A. N. 2008, *Philosophical Transactions of the Royal Society of London Series A*, 366, 4163
- . 2013, *Geochimica Cosmochimica Acta* , 105, 146
- Hansen, B. M. S. 2009, *ApJ* , 703, 1131
- Hartmann, W. K., & Davis, D. R. 1975, *Icarus*, 24, 504
- Hauck, S. A., Margot, J.-L., Solomon, S. C., et al. 2013, *Journal of Geophysical Research (Planets)*, 118, 1204
- Hayashi, C. 1981, *Progress of Theoretical Physics Supplement*, 70, 35
- Heiken, G. H., McKay, D. S., & Brown, R. W. 1974, *Geochimica Cosmochimica Acta* , 38, 1703
- Herwartz, D., Pack, A., Friedrichs, B., & Bischoff, A. 2014, *Science*, 344, 1146
- Hirschmann, M. M. 2006, *Annual Review of Earth and Planetary Sciences*, 34, 629
- Hoffmann, V., Grimm, S. L., Moore, B., & Stadel, J. 2017, *MNRAS* , 465, 2170
- Holman, M. J., Fabrycky, D. C., Ragozzine, D., et al. 2010, *Science*, 330, 51
- Izidoro, A., Haghighipour, N., Winter, O. C., & Tsuchida, M. 2014, *ApJ* , 782, 31
- Izidoro, A., Raymond, S. N., Morbidelli, A., & Winter, O. C. 2015, *MNRAS* , 453, 3619
- Izidoro, A., Raymond, S. N., Pierens, A., et al. 2016, *ApJ* , 833, 40
- Jackson, A. P., Gabriel, T. S. J., & Asphaug, E. I. 2018, *MNRAS* , 474, 2924

- Jacobson, S. A., & Morbidelli, A. 2014, *Philosophical Transactions of the Royal Society of London Series A*, 372, 0174
- Jacobson, S. A., Morbidelli, A., Raymond, S. N., et al. 2014, *Nature*, 508, 84
- Jacobson, S. A., Rubie, D. C., Hernlund, J., Morbidelli, A., & Nakajima, M. 2017, *Earth and Planetary Science Letters*, 474, 375
- Jacobson, S. A., & Walsh, K. J. 2015, Washington DC American Geophysical Union Geophysical Monograph Series, 212, 49
- Johnson, B. C., Collins, G. S., Minton, D. A., et al. 2016, *Icarus*, 271, 350
- Jurić, M., & Tremaine, S. 2008a, *ApJ*, 686, 603
- . 2008b, *ApJ*, 686, 603
- Jutzi, M., Asphaug, E., Gillet, P., Barrat, J.-A., & Benz, W. 2013, *Nature*, 494, 207
- Kaib, N. A., & Chambers, J. E. 2016, *MNRAS*, 455, 3561
- Kaib, N. A., & Cowan, N. B. 2015, *Icarus*, 252, 161
- Kennedy, G. M., & Kenyon, S. J. 2008, *ApJ*, 673, 502
- Kenyon, S. J., & Bromley, B. C. 2006, *AJ*, 131, 1837
- . 2009, *ApJL*, 690, L140
- Kinoshita, H., Yoshida, H., & Nakai, H. 1991, *Celestial Mechanics and Dynamical Astronomy*, 50, 59
- Kleine, T., Touboul, M., Bourdon, B., et al. 2009, *Geochimica Cosmochimica Acta*, 73, 5150
- Kley, W., & Nelson, R. P. 2012, *Ann. Rev. Astron. Astrophys.*, 50, 211
- Kobayashi, H., & Dauphas, N. 2013, *Icarus*, 225, 122
- Kokubo, E., & Genda, H. 2010, *ApJL*, 714, L21
- Kokubo, E., & Ida, S. 1996, *Icarus*, 123, 180
- . 1998, *Icarus*, 131, 171
- . 2000, *Icarus*, 143, 15
- Kramer, W., Butler, M., Bauer, G., Chadalavada, K., & Mendes, C. 2015, in *High Performance Parallel I/O*, ed. Prabhat & Q. Koziol (CRC Publications, Taylor and Francis Group), 17–32

- Kruijer, T. S., Kleine, T., Borg, L. E., et al. 2017, *Earth and Planetary Science Letters*, 474, 345
- Kuchynka, P., & Folkner, W. M. 2013, *Icarus*, 222, 243
- Lambrechts, M., Johansen, A., & Morbidelli, A. 2014, *A&A* , 572, A35
- Laskar, J. 1989, *Nature* , 338, 237
- . 1996, *Celestial Mechanics and Dynamical Astronomy*, 64, 115
- . 1997, *A&A* , 317, L75
- . 2000, *Physical Review Letters*, 84, 3240
- . 2008, *Icarus*, 196, 1
- Laskar, J., & Gastineau, M. 2009, *Nature* , 459, 817
- Lecar, M., Podolak, M., Sasselov, D., & Chiang, E. 2006, *ApJ* , 640, 1115
- Lécuyer, C., Grandjean, P., Barrat, J.-A., et al. 1998, *Geochimica Cosmochimica Acta* , 62, 2429
- Lee, M. H., & Peale, S. J. 2002, *ApJ* , 567, 596
- Leinhardt, Z. M., Dobinson, J., Carter, P. J., & Lines, S. 2015, *ApJ* , 806, 23
- Leinhardt, Z. M., & Stewart, S. T. 2012, *ApJ* , 745, 79
- Levison, H. F., & Agnor, C. 2003a, *AJ* , 125, 2692
- . 2003b, *AJ* , 125, 2692
- Levison, H. F., Kretke, K. A., & Duncan, M. J. 2015a, *Nature* , 524, 322
- Levison, H. F., Kretke, K. A., Walsh, K. J., & Bottke, W. F. 2015b, *Proceedings of the National Academy of Science*, 112, 14180
- Levison, H. F., Morbidelli, A., Tsiganis, K., Nesvorný, D., & Gomes, R. 2011, *AJ* , 142, 152
- Levison, H. F., Morbidelli, A., Van Laerhoven, C., Gomes, R., & Tsiganis, K. 2008, *Icarus*, 196, 258
- Lissauer, J. J., Dawson, R. I., & Tremaine, S. 2014, *Nature* , 513, 336
- Lissauer, J. J., Jontof-Hutter, D., Rowe, J. F., et al. 2013, *ApJ* , 770, 131
- Lithwick, Y., & Wu, Y. 2011, *ApJ* , 739, 31
- Lykawka, P. S., & Ito, T. 2013, *ApJ* , 773, 65
- . 2017, *ApJ* , 838, 106

- Maffione, N. P., Darriba, L. A., Cincotta, P. M., & Giordano, C. M. 2013, *MNRAS* , 429, 2700
- Malhotra, R. 1993, *Nature* , 365, 819
- . 1995, *AJ* , 110, 420
- Mamajek, E. E., & Hillenbrand, L. A. 2008, *ApJ* , 687, 1264
- Marchi, S., Bottke, W. F., Elkins-Tanton, L. T., et al. 2014, *Nature* , 511, 578
- Margot, J.-L., Hauck, II, S. A., Mazarico, E., Padovan, S., & Peale, S. J. 2018, ArXiv e-prints, arXiv:1806.02024
- Martin, R. G., & Livio, M. 2012, *MNRAS* , 425, L6
- Marty, B. 2012, *Earth and Planetary Science Letters*, 313, 56
- Marty, B., Avice, G., Sano, Y., et al. 2016, *Earth and Planetary Science Letters*, 441, 91
- Marty, B., Altwegg, K., Balsiger, H., et al. 2017, *Science*, 356, 1069
- Masset, F., & Snellgrove, M. 2001, *MNRAS* , 320, L55
- Mastrobuono-Battisti, A., & Perets, H. B. 2017, *MNRAS* , 469, 3597
- Mastrobuono-Battisti, A., Perets, H. B., & Raymond, S. N. 2015, *Nature* , 520, 212
- Matsumura, S., Thommes, E. W., Chatterjee, S., & Rasio, F. A. 2010, *ApJ* , 714, 194
- Milani, A., & Nobili, A. M. 1992, *Nature* , 357, 569
- Mills, S. M., Fabrycky, D. C., Migaszewski, C., et al. 2016, *Nature* , 533, 509
- Minton, D. A., & Malhotra, R. 2010, *Icarus*, 207, 744
- . 2011, *ApJ* , 732, 53
- Minton, D. A., Richardson, J. E., & Fassett, C. I. 2015, *Icarus*, 247, 172
- Morbidelli, A., Brasser, R., Gomes, R., Levison, H. F., & Tsiganis, K. 2010, *AJ* , 140, 1391
- Morbidelli, A., Brasser, R., Tsiganis, K., Gomes, R., & Levison, H. F. 2009, *A&A* , 507, 1041
- Morbidelli, A., Chambers, J., Lunine, J. I., et al. 2000, *Meteoritics and Planetary Science*, 35, 1309
- Morbidelli, A., & Crida, A. 2007, *Icarus*, 191, 158
- Morbidelli, A., & Henrard, J. 1991a, *Celestial Mechanics and Dynamical Astronomy*, 51, 131
- . 1991b, *Celestial Mechanics and Dynamical Astronomy*, 51, 169

- Morbidelli, A., Levison, H. F., Tsiganis, K., & Gomes, R. 2005, *Nature* , 435, 462
- Morbidelli, A., Lunine, J. I., O'Brien, D. P., Raymond, S. N., & Walsh, K. J. 2012, *Annual Review of Earth and Planetary Sciences*, 40, 251
- Morbidelli, A., Nesvorný, D., Laurenz, V., et al. 2018, *Icarus*, 305, 262
- Morbidelli, A., & Raymond, S. N. 2016, *Journal of Geophysical Research (Planets)*, 121, 1962
- Morbidelli, A., Thomas, F., & Moons, M. 1995, *Icarus*, 118, 322
- Morbidelli, A., Tsiganis, K., Crida, A., Levison, H. F., & Gomes, R. 2007, *AJ* , 134, 1790
- Morbidelli, A., Walsh, K. J., O'Brien, D. P., Minton, D. A., & Bottke, W. F. 2015, *The Dynamical Evolution of the Asteroid Belt*, ed. P. Michel, F. E. DeMeo, & W. F. Bottke, 493–507
- Morbidelli, A., Bitsch, B., Crida, A., et al. 2016, *Icarus*, 267, 368
- Morishima, R., Stadel, J., & Moore, B. 2010, *Icarus*, 207, 517
- Morris, R. V. 1978, in *Lunar and Planetary Science Conference Proceedings*, Vol. 9, *Lunar and Planetary Science Conference Proceedings*, 2287–2297
- Mulders, G. D., Pascucci, I., & Apai, D. 2015, *ApJ* , 814, 130
- Mulders, G. D., Pascucci, I., Apai, D., & Ciesla, F. J. 2018, *AJ* , 156, 24
- Nagasawa, M., Lin, D. N. C., & Thommes, E. 2005, *ApJ* , 635, 578
- Nelson, R. P., & Papaloizou, J. C. B. 2003, *MNRAS* , 339, 993
- . 2004, *MNRAS* , 350, 849
- Nesvorný, D. 2011, *ApJL* , 742, L22
- . 2015a, *AJ* , 150, 73
- . 2015b, *AJ* , 150, 68
- Nesvorný, D., Jenniskens, P., Levison, H. F., et al. 2010, *ApJ* , 713, 816
- Nesvorný, D., & Morbidelli, A. 2012, *AJ* , 144, 117
- Nesvorný, D., Vokrouhlický, D., Bottke, W. F., & Levison, H. F. 2018, *Nature Astronomy*, 2, 878
- Nesvorný, D., Vokrouhlický, D., & Morbidelli, A. 2007, *AJ* , 133, 1962
- . 2013, *ApJ* , 768, 45

- Nimmo, F., & Agnor, C. B. 2006, *Earth and Planetary Science Letters*, 243, 26
- Nittler, L. R., Chabot, N. L., Grove, T. L., & Peplowski, P. N. 2017, ArXiv e-prints, arXiv:1712.02187
- Nomura, R., Hirose, K., Uesugi, K., et al. 2014, *Science*, 343, 522
- O'Brien, D. P., Morbidelli, A., & Bottke, W. F. 2007, *Icarus*, 191, 434
- O'Brien, D. P., Morbidelli, A., & Levison, H. F. 2006, *Icarus*, 184, 39
- O'Brien, D. P., & Sykes, M. V. 2011, *Space and Science Reviews* , 163, 41
- Papaloizou, J. C. B., & Larwood, J. D. 2000, *MNRAS* , 315, 823
- Papaloizou, J. C. B., & Nelson, R. P. 2003, *MNRAS* , 339, 983
- Papaloizou, J. C. B., Nelson, R. P., & Snellgrove, M. D. 2004, *MNRAS* , 350, 829
- Pascucci, I., Apai, D., Luhman, K., et al. 2009, *ApJ* , 696, 143
- Petit, J.-M., Morbidelli, A., & Chambers, J. 2001, *Icarus*, 153, 338
- Pierens, A., & Nelson, R. P. 2008, *A&A* , 482, 333
- Pierens, A., Raymond, S. N., Nesvorny, D., & Morbidelli, A. 2014, *ApJL* , 795, L11
- Poincare, H. 1892, *Les methodes nouvelles de la mecanique celeste*
- Pordes, R., Petravick, D., Kramer, B., et al. 2007, *Journal of Physics: Conference Series*, 78, 012057
- Quarles, B., & Kaib, N. 2019, *AJ* , 157, 67
- Quarles, B. L., & Lissauer, J. J. 2015, *Icarus*, 248, 318
- Quinn, T. R., Tremaine, S., & Duncan, M. 1991, *AJ* , 101, 2287
- Quintana, E. V., Barclay, T., Borucki, W. J., Rowe, J. F., & Chambers, J. E. 2016, *ApJ* , 821, 126
- Rasio, F. A., & Ford, E. B. 1996, *Science*, 274, 954
- Raymond, S. N., Armitage, P. J., & Gorelick, N. 2009a, *ApJL* , 699, L88
- . 2010, *ApJ* , 711, 772
- Raymond, S. N., & Izidoro, A. 2017a, *Icarus*, 297, 134
- . 2017b, *Science Advances*, 3, e1701138
- Raymond, S. N., Izidoro, A., Bitsch, B., & Jacobson, S. A. 2016, *MNRAS* , 458, 2962

- Raymond, S. N., Izidoro, A., & Morbidelli, A. 2018, arXiv e-prints, arXiv:1812.01033
- Raymond, S. N., & Morbidelli, A. 2014, in IAU Symposium, Vol. 310, Complex Planetary Systems, Proceedings of the International Astronomical Union, 194–203
- Raymond, S. N., O’Brien, D. P., Morbidelli, A., & Kaib, N. A. 2009b, *Icarus*, 203, 644
- Raymond, S. N., Quinn, T., & Lunine, J. I. 2004, *Icarus*, 168, 1
- . 2006, *Icarus*, 183, 265
- . 2007, *Astrobiology*, 7, 66
- Raymond, S. N., Schlichting, H. E., Hersant, F., & Selsis, F. 2013, *Icarus*, 226, 671
- Rein, H., & Liu, S.-F. 2012, *A&A*, 537, A128
- Rein, H., & Tamayo, D. 2015, *MNRAS*, 452, 376
- Rivera, E. J., Laughlin, G., Butler, R. P., et al. 2010, *ApJ*, 719, 890
- Roig, F., & Nesvorný, D. 2015, *AJ*, 150, 186
- Roig, F., Nesvorný, D., & DeSouza, S. R. 2016, *ApJL*, 820, L30
- Rubie, D. C., Laurenz, V., Jacobson, S. A., et al. 2016, *Science*, 353, 1141
- Rubie, D. C., Jacobson, S. A., Morbidelli, A., et al. 2015, *Icarus*, 248, 89
- Rufu, R., Aharonson, O., & Perets, H. B. 2017, *Nature Geoscience*, 10, 89
- Sarid, G., Stewart, S. T., & Leinhardt, Z. M. 2014, in Lunar and Planetary Science Conference, Vol. 45, Lunar and Planetary Science Conference, 2723
- Schenk, P., O’Brien, D. P., Marchi, S., et al. 2012, *Science*, 336, 694
- Schmitt, H. H. 2014, in Lunar and Planetary Science Conference, Vol. 45, Lunar and Planetary Science Conference, 2732
- Schmitt, H. H., & Petro, N. E. 2017, AGU Fall Meeting Abstracts
- Schultz, P. H., & Crawford, D. A. 2016, *Nature*, 535, 391
- Sfiligoi, I., Bradley, D. C., Holzman, B., et al. 2009, in (IEEE Publishing), 428–432
- Shukolyukov, A., & Lugmair, G. W. 2002, Chronology of Asteroid Accretion and Differentiation, ed. W. F. Bottke, Jr., A. Cellino, P. Paolicchi, & R. P. Binzel, 687–695
- Siegfried, II, R. W., & Solomon, S. C. 1974, *Icarus*, 23, 192
- Snellgrove, M. D., Papaloizou, J. C. B., & Nelson, R. P. 2001, *A&A*, 374, 1092

- Spudis, P. D., Wilhelms, D. E., & Robinson, M. S. 2011, *Journal of Geophysical Research (Planets)*, 116, E00H03
- Stoer, J., Bartels, R., Gautschi, W., Bulirsch, R., & Witzgall, C. 2002, *Introduction to Numerical Analysis, Texts in Applied Mathematics* (Springer New York)
- Sussman, G. J., & Wisdom, J. 1988, *Science*, 241, 433
- . 1992, *Science*, 257, 56
- Svetsov, V. 2011, *Icarus*, 214, 316
- Tamayo, D., Rein, H., & Shi, P. 2016, in *AAS/Division of Dynamical Astronomy Meeting, Vol. 47, AAS/Division of Dynamical Astronomy Meeting*, 103.02
- Tanaka, H., & Ward, W. R. 2004, *ApJ* , 602, 388
- Tera, F., Papanastassiou, D. A., & Wasserburg, G. J. 1974, *Earth and Planetary Science Letters*, 22, 1
- Thommes, E., Nagasawa, M., & Lin, D. N. C. 2008, *ApJ* , 676, 728
- Thommes, E. W., Duncan, M. J., & Levison, H. F. 1999, *Nature* , 402, 635
- Tisserand, F. 1882, *Annales de l'Observatoire de Paris*, 16, E.1
- Touboul, M., Kleine, T., Bourdon, B., Palme, H., & Wieler, R. 2007, *Nature* , 450, 1206
- Trifonov, T., Kürster, M., Zechmeister, M., et al. 2017, *A&A* , 602, L8
- Tsiganis, K., Gomes, R., Morbidelli, A., & Levison, H. F. 2005, *Nature* , 435, 459
- Šidlichovský, M., & Nesvorný, D. 1996, *Celestial Mechanics and Dynamical Astronomy*, 65, 137
- Volk, K., & Gladman, B. 2015, *ApJL* , 806, L26
- Walker, R. J. 2009, *Chemie der Erde / Geochemistry*, 69, 101
- Walker, R. J., Horan, M. F., Shearer, C. K., & Papike, J. J. 2004, *Earth and Planetary Science Letters*, 224, 399
- Wallace, J., Tremaine, S., & Chambers, J. 2017, *AJ* , 154, 175
- Walsh, K. J., Delbó, M., Bottke, W. F., Vokrouhlický, D., & Lauretta, D. S. 2013, *Icarus*, 225, 283
- Walsh, K. J., & Levison, H. F. 2016, *AJ* , 152, 68
- Walsh, K. J., & Morbidelli, A. 2011, *A&A* , 526, A126

- Walsh, K. J., Morbidelli, A., Raymond, S. N., O'Brien, D. P., & Mandell, A. M. 2011, *Nature* , 475, 206
- Wang, J., Fischer, D. A., Horch, E. P., & Huang, X. 2015, *ApJ* , 799, 229
- Weidenschilling, S. J. 1977, *MNRAS* , 180, 57
- Wetherill, G. W. 1991, *Science*, 253, 535
- . 1992, *Icarus*, 100, 307
- . 1996, *Astrophysics and Space Science*, 241, 25
- Whipple, F. L. 1972, in *From Plasma to Planet*, ed. A. Elvius, 211
- Wisdom, J., & Holman, M. 1991, *AJ* , 102, 1528
- Wisdom, J. L. 1981, PhD thesis, California Institute of Technology, Pasadena.
- Wyatt, M. C., Smith, R., Greaves, J. S., et al. 2007, *ApJ* , 658, 569
- Zellner, N. E. B. 2017, *Origins of Life and Evolution of the Biosphere*, 47, 261

Appendix A

Chapter 2 Supplemental Data

Table A.1: Chaos simulation results

System	τ_L (years)	MEGNO	Inner Planets	Run 1 ¹	Run a ¹	Run b ¹	Run 1 MMRs ²
cjs1	7.09×10^5	100.7	5	Y	Y	Y	
cjs2	1.69×10^7	45.35	4	Y	N	N	7:4
cjs3	2.93×10^5	187.2	5	Y	Y	Y	
cjs4	3.69×10^5	160.9	5	Y	Y	Y	2:1
cjs5	4.63×10^5	183.5	5	Y	Y	Y	
cjs6	3.61×10^5	160.0	5	Y	Y	Y	
cjs7	5.04×10^6	126.0	5	Y	N	Y	7:4,5:1, 7:1 (S), 5:2 (J,S)
cjs8	1.71×10^{10}	2.004	4	N	N	N	
cjs9	5.93×10^{10}	1.997	3	N	N	N	
cjs10	8.28×10^8	1.896	5	N	N	N	
cjs11	7.80×10^{10}	1.999	2	N	N	N	
cjs12	7.14×10^6	90.97	5	Y	Y	Y	

Continued on next page

Table A.1 – *Continued from previous page*

System	τ_L (years)	MEGNO	Inner Planets	Run 1 ¹	Run a ¹	Run b ¹	Run 1 MMRs ²
cjs13	6.10×10^9	2.003	5	N	N	N	
cjs14	1.78×10^{10}	1.988	3	N	N	N	
cjs15	7.61×10^7	8.794	5	Y	Y	Y	7:3 (J)
cjs16	4.89×10^4	212.8	4	Y	Y	Y	
cjs17	5.97×10^8	4.467	4	Y	N	N	3:1 (J)
cjs18	5.16×10^7	21.04	3	Y	N	N	3:1 (J)
cjs19	1.50×10^7	53.36	4	Y	Y	Y	
cjs20	7.23×10^{10}	2.000	2	N	N	N	
cjs21	9.03×10^{10}	1.996	2	N	N	N	
cjs22	3.86×10^{10}	2.000	3	N	N	N	
cjs23	8.83×10^3	169.0	4	Y	Y	Y	
cjs24	1.66×10^6	20.29	4	Y	N	Y	5:2 (J,S)
cjs25	2.16×10^{10}	2.040	4	N	N	N	2:1
cjs26	1.39×10^5	183.2	5	Y	Y	Y	6:1
cjs27	8.50×10^{10}	1.999	3	N	N	N	
cjs28	7.22×10^{10}	1.999	2	N	N	N	
cjs29	9.22×10^7	12.82	4	Y	Y	Y	5:3:1
cjs30	7.50×10^8	4.816	3	Y	N	N	
cjs31	1.58×10^{10}	2.001	2	N	N	N	
cjs32	2.81×10^9	1.966	4	N	N	N	
cjs33	1.31×10^{10}	1.999	2	N	N	N	
cjs34	7.89×10^4	117.0	4	Y	Y	Y	
cjs35	2.26×10^{10}	2.000	3	N	N	N	

Continued on next page

Table A.1 – *Continued from previous page*

System	τ_L (years)	MEGNO	Inner Planets	Run 1 ¹	Run a ¹	Run b ¹	Run 1 MMRs ²
cjs36	3.33×10^6	186.5	4	Y	N	Y	
cjs37	2.14×10^5	193.5	5	Y	Y	Y	
cjs38	3.50×10^8	5.732	3	Y	N	Y	
cjs39	6.30×10^{10}	1.999	4	N	N	N	
cjs40	6.05×10^{10}	1.999	4	N	N	N	
cjs41	6.46×10^6	113.5	4	Y	Y	Y	5:3
cjs42	9.03×10^{10}	1.998	4	N	N	N	5:1
cjs43	1.47×10^7	49.51	4	Y	N	Y	4:1
cjs44	1.93×10^5	189.4	4	Y	Y	Y	
cjs45	1.38×10^5	194.1	4	Y	N	Y	
cjs46	5.10×10^{10}	2.011	4	N	N	N	
cjs47	2.11×10^6	129.4	4	Y	N	Y	
cjs48	1.68×10^8	8.483	4	Y	Y	Y	
cjs49	1.49×10^7	20.44	4	Y	N	Y	
cjs50	5.08×10^8	6.271	4	Y	N	Y	
eejs1	4.36×10^5	178.4	3	Y	N	Y	
eejs2	1.75×10^5	87.08	4	Y	Y	Y	5:3
eejs3	4.55×10^5	202.9	4	Y	N	Y	8:5,7:1
eejs4	9.62×10^5	174.4	1	Y	N	N	
eejs5	1.05×10^{10}	2.000	2	N	N	N	
eejs6	4.11×10^7	29.38	3	Y	Y	Y	3:1,7:1 (S)
eejs7	2.41×10^7	34.65	4	Y	N	Y	
eejs8	1.33×10^{10}	1.988	3	N	N	N	

Continued on next page

Table A.1 – *Continued from previous page*

System	τ_L (years)	MEGNO	Inner Planets	Run 1 ¹	Run a ¹	Run b ¹	Run 1 MMRs ²
eejs9	1.01×10^8	9.676	5	Y	Y	Y	8:3,8:5
eejs10	6.92×10^5	151.8	1	Y	N	N	
eejs11	1.95×10^{10}	2.000	2	N	N	N	
eejs13	9.19×10^8	7.045	4	Y	Y	N	
eejs15	2.57×10^9	1.999	1	N	N	N	
eejs16	3.39×10^{10}	2.002	3	N	N	N	5:2 (J,S)
eejs18	1.87×10^{10}	2.017	4	N	N	N	
eejs19	2.93×10^{10}	2.000	1	N	N	N	
eejs20	1.94×10^9	1.992	3	N	N	N	
eejs21	4.17×10^9	1.919	3	N	N	N	
eejs22	1.05×10^{10}	1.998	2	N	N	N	
eejs23	3.11×10^6	183.4	4	Y	Y	Y	
eejs24	1.21×10^7	57.05	5	Y	Y	Y	8:1 (S)
eejs25	6.18×10^9	2.041	2	N	N	N	
eejs26	6.31×10^9	1.912	3	N	N	N	
eejs27	8.95×10^8	1.813	3	N	N	N	
eejs28	2.48×10^9	4.370	3	Y	N	N	
eejs29	3.43×10^5	173.0	1	Y	N	N	5:2 (J,S)
eejs30	6.32×10^5	158.7	2	Y	N	Y	
eejs31	2.45×10^5	184.6	4	Y	Y	Y	
eejs32	1.96×10^{10}	1.969	3	N	N	N	7:3
eejs33	3.96×10^{10}	2.004	3	N	N	N	7:2,8:5
eejs34	2.67×10^5	196.5	1	Y	Y	N	

Continued on next page

Table A.1 – *Continued from previous page*

System	τ_L (years)	MEGNO	Inner Planets	Run 1 ¹	Run a ¹	Run b ¹	Run 1 MMRs ²
eejs35	4.23×10^6	154.0	2	Y	N	Y	7:3
eejs36	3.39×10^6	180.2	1	Y	N	N	
eejs37	1.06×10^6	183.2	4	Y	Y	Y	
eejs38	2.29×10^5	171.8	2	Y	N	N	
eejs39	1.84×10^9	2.005	2	N	N	N	
eejs40	1.08×10^5	189.1	4	Y	Y	Y	
eejs41	5.27×10^6	33.10	4	Y	Y	Y	5:3
eejs42	1.31×10^{10}	2.511	4	N	N	N	
eejs43	4.94×10^9	1.998	1	N	N	N	
eejs44	7.84×10^4	193.8	3	Y	N	Y	
eejs45	2.09×10^6	178.1	4	Y	N	Y	
eejs46	5.52×10^{10}	2.009	4	N	N	N	
eejs47	5.37×10^8	8.082	3	Y	N	N	8:5
eejs49	3.06×10^{10}	1.996	3	N	N	N	5:2
eejs50	2.10×10^{10}	1.929	2	N	N	N	7:3
ann1	3.64×10^9	2.014	3	N	N	Y	
ann2	3.02×10^{10}	1.998	3	N	N	N	
ann3	3.06×10^{10}	1.988	4	N	N	N	
ann4	4.94×10^{10}	2.000	3	N	N	N	
ann5	4.97×10^7	29.32	3	Y	N	Y	8:5,7:1 (J)
ann6	1.66×10^8	7.441	4	Y	N	N	7:4
ann7	3.91×10^9	3.132	3	Y	N	N	
ann8	2.87×10^5	185.6	3	Y	N	Y	

Continued on next page

Table A.1 – *Continued from previous page*

System	τ_L (years)	MEGNO	Inner Planets	Run 1 ¹	Run a ¹	Run b ¹	Run 1 MMRs ²
ann9	4.67×10^{10}	2.010	3	N	N	N	2:1
ann10	2.06×10^{10}	1.998	2	N	N	N	
ann11	3.17×10^9	2.294	3	N	N	N	
ann12	6.72×10^3	195.1	4	Y	Y	Y	
ann13	2.89×10^6	125.7	2	Y	Y	Y	
ann14	1.68×10^7	60.09	4	Y	N	N	4:1
ann15	9.01×10^9	2.103	3	N	N	N	
ann16	1.85×10^{10}	1.99	2	N	N	N	
ann17	1.05×10^9	4.372	4	Y	N	N	5:2 (J,S)
ann18	8.23×10^8	2.159	3	N	N	N	
ann19	3.61×10^5	183.8	3	Y	Y	Y	
ann20	2.07×10^6	175.4	4	Y	Y	Y	
ann21	4.55×10^6	21.76	3	Y	N	Y	3:1
ann22	2.00×10^7	44.64	3	Y	N	Y	
ann23	2.00×10^7	53.55	3	Y	N	Y	7:4
ann24	2.53×10^{10}	1.999	3	N	N	N	
ann25	3.59×10^7	20.22	4	Y	Y	Y	8:3
ann26	1.08×10^8	9.212	4	Y	Y	Y	5:3
ann27	1.15×10^8	13.65	4	Y	Y	N	5:2,8:5
ann28	1.90×10^8	15.54	5	Y	Y	Y	
ann29	5.97×10^6	115.7	4	Y	N	Y	
ann30	5.10×10^3	193.1	3	Y	Y	Y	
ann31	1.32×10^8	8.47	3	Y	Y	Y	

Continued on next page

Table A.1 – *Continued from previous page*

System	τ_L (years)	MEGNO	Inner Planets	Run 1 ¹	Run a ¹	Run b ¹	Run 1 MMRs ²
ann32	1.85×10^6	182.3	4	Y	Y	Y	
ann33	2.36×10^6	191.6	4	Y	Y	Y	2:1
ann35	3.93×10^7	23.00	3	Y	N	N	
ann36	3.50×10^{10}	1.998	3	N	Y	N	7:3
ann37	2.75×10^5	192.5	4	Y	Y	Y	
ann38	4.23×10^{10}	2.001	3	N	N	N	
ann39	2.50×10^5	189.6	3	Y	Y	Y	
ann40	6.91×10^5	192.9	4	Y	Y	Y	
ann41	4.22×10^{10}	1.998	3	N	N	N	
ann42	1.01×10^{10}	2.000	2	N	N	N	
ann43	1.49×10^{11}	2.000	3	N	N	N	
ann44	2.75×10^8	11.41	3	Y	N	N	
ann45	9.52×10^9	2.000	2	N	N	N	
ann46	4.81×10^6	152.4	3	Y	Y	Y	
ann47	3.71×10^{10}	2.004	3	N	N	N	
ann48	8.07×10^6	54.18	4	Y	Y	Y	5:2 (J,S)
ann49	7.25×10^5	185.7	3	Y	N	Y	7:4
ann50	5.53×10^{10}	2.008	3	N	N	N	

¹“Y” indicates chaos was detected, “N” indicates it was not.²(J) and (S) indicate the resonance was with Jupiter or Saturn respectively.